Title
Defect Passivation towards Highly Efficient and Stable Metal Halide Perovskite Solar Cells

Author
Wang, Rui

Publication Date
2020

Peer reviewed|Thesis/dissertation

UNIVERSITY OF CALIFORNIA

Los Angeles

Defect Passivation towards Highly Efficient and Stable Metal Halide Perovskite Solar Cells

A dissertation submitted in partial satisfaction of the

requirements for the degree Doctor of Philosophy

in Materials Science and Engineering

by

Rui Wang

2020

ABSTRACT OF THE DISSERTATION

Defect Passivation towards Highly Efficient and Stable Metal Halide Perovskite Solar Cells

by

Rui Wang

Doctor of Philosophy in Materials Science and Engineering

University of California, Los Angeles, 2020

Professor Yang Yang, Chair

Metal halide perovskite material had emerged as a rising star in the photovoltaic application due to its excellent optoelectronic properties. Perovskite solar cells with power conversion efficiency of over 25% have been demonstrated within a few years. However, the stability issues of this material still prohibit the commercialization of perovskite solar cells because of the low ion-migration activation energy, phase instability at room temperature, and sensitivity to the external environments. Attacked by the external environments through the defects in the perovskite has been considered one of the most critical issue of the instability of perovskite solar cells. Since the defects are preferred formed at the surface and grain boundaries of the perovskite, developing facile and effective strategies to passivate the defects at surface and grain boundaries is essential to enhance the stability and efficiency of perovskite solar cells.

In Chapter two, 1,3,7-Trimethylxanthine, a commodity chemical with two conjugated carboxyl groups better known by its common name caffeine, improves the performance and thermal stability of perovskite

solar cells based on both $MAPbI_3$ and $CsFAMAPbI_3$ active layers. The strong interaction between caffeine and Pb^{2+} ions serves as a "molecular lock" that increases the activation energy during film crystallization, delivering a perovskite film with preferred orientation, improved electronic properties, reduced ion migration, and greatly enhanced thermal stability. A champion stabilized efficiency of 19.8% and retain over 85% of their efficiency under continuous annealing at 85°C in nitrogen. Later on, in Chapter three, $CuBr_2$ was introduced into the all-inorganic perovskites to control the crystallization and passivate the grain boundary defects, therefore a power conversion efficiency of over 16% was realized.

Apart from grain passivation by modulating the crystallization process of perovskites, a facile surface induced secondary grain growth by utilizing the surface anisotropic was developed to enlarge the grain size to reduce the grain boundaries. As a result, grain size as large as 4 microns was realized through the oleylammonium treatment, the power conversion efficiency of 16.58% was achieved with 4,000-hour shelf stability.

In Chapter 5, the chemical environment of a functional group that is activated for defect passivation was systematically investigated with theophylline, caffeine and theobromine. When N-H and C=O were in an optimal configuration within the molecule, hydrogen-bond formation between N-H and I assisted the primary C=O binding with the antisite Pb defect to maximize surface-defect binding. A stabilized power conversion efficiency of 22.6% of photovoltaic device was demonstrated with theophylline treatment.

The dissertation of Rui Wang is approved.

Jenn-Ming Yang

Yu Huang

Wentai Liu

Yang Yang, Committee Chair

University of California, Los Angeles

2020

Table of Contents

List of Figures

Figure 2.3. a. *J–V* curves of the champion PSC of pristine PVSK and caffeine containing PVSK in reverse scan direction. **b.** EQE spectra and integrated current densities from the EQE spectra of PVSK devices with or without adding caffeine. **c.** Normalized Transient photovoltage (TPV) decay and **d.** Normalized Transient photocurrent (TPC) decay in $MAPbI_3$ and $MAPbI_3$: Caffeine based perovskite solar cells.

Figure 2.4. a. Devices thermal stability upon 85°C continuous annealing in nitrogen box. **b.** XRD patterns of aged device based on pure $MAPbI_3$ and $MAPbI_3$ with caffeine. Thermogravimetric analysis (TGA) analysis of **c.** weight loss and **d.** heat flow of pristine caffeine, MAI-PbI_2-DMSO adduct powder and MAI-PbI_2-DMSO-Caffeine adduct powder.

Figure 2.5. Energy-dispersive X-ray spectra (EDX) mapping of the aged pure PVSK device: **a.** Ag **b.** I and **c.** Pb. And the aged caffeine-containing PVSK device: **d**. Ag **e**. I and **f**. Pb. EDX line scans of **g.** aged pure PVSK device and **h.** aged caffeine-containing PVSK device

Figure 2.6. High resolution transmittance electron microscopy (HRTEM) of **a.** fresh caffeine containing PVSK; **c.** fresh pure PVSK; **e.** aged (5 min 30 s) caffeine containing PVSK and **g.** aged (5 min 30 s) pure PVSK. Corresponding Fast Fourier transforms (FFTs) of **b.** fresh caffeine containing PVSK; **d.** fresh pure PVSK; **f.** aged (5 min 30 s) caffeine containing PVSK and **h.** aged (5 min 30 s) pure PVSK.

Figure 3.1. (a) XPS spectra for Cs 3*d*5, Pb 4*f*, Br 3*d* and I 3*d*5 in $CsPbI_2Br$ and $CsPbI_2Br$:$CuBr_2$ (0.2 wt%) perovskite films. (b) UV-Vis spectra of $CsPbI_2Br$ and $CsPbI_2Br$:$CuBr_2$ (0.2 wt%) perovskite films. (c) Schematic energy level diagram of $CsPbI_2Br$ and $CsPbI_2Br$:$CuBr_2$ -based perovskite solar cells.

Figure 3.2. (a) Top-view SEM images (scale bar, 400 nm) and (b) grain size statistical distribution of $CsPbI_2Br$ films with various $CuBr_2$ ratio (0, 0.1, 0.2 and 0.3 wt%). (c) XRD

Fig. 4.2 Demonstration of the surface induced secondary grain growth.

(**A**) Top-view SEM images of perovskite film with various treatments (IPA, BA, OCA and OLA). (**B**) Grain size statistical distribution of perovskite films with various treatments (IPA, BA, OCA and OLA). (**C**) Schematic demonstration of the process of surface induced secondary grain growth.

Fig. 4.3 Characterization of Perovskite film with the surface induced secondary grain growth by OLA.

(**A**) Evolution of the (100) peak position of perovskite film with OLA extracted from real-time in-situ GIWAXS measurement. (**B** and **C**) 2D GIWAXS patterns of perovskite films (B) without OLA treatment and (C) with OLA treatment. (**D**) Radially integrated intensity plots along (100) crystal plane from the 2D GIWAXS patterns in perovskite films with or without OLA treatment. (**E**) XPS data for Pb 4*f* 7/2 and Pb 4*f* 5/2 core level spectra in perovskite films with or without OLA treatment. (**F**) Time-of-flight secondary ion mass spectroscopy (TOF-SIMS) depth profile of perovskite film with OLA treatment.

Fig. 4.4 Enhanced photovoltaic performance and long-term stability of perovskite film with surface induced secondary grain growth by OLA.

(**A**) Current density–voltage (*J–V*) curves of perovskite solar cells with or without OLA treatment. (**B**) Normalized transient photovoltage decay of perovskite solar cells with or without OLA treatment. (**C**) Nyquist plots of perovskite solar cells with or without OLA treatment measured in the dark and at corresponding open-circuit voltages. (**D**) Normalized transient photocurrent decay of perovskite solar cells with or without OLA treatment. (**E**) Evolution of power conversion efficiency (PCE) of perovskite solar cells with or without OLA treatment. The devices were stored under nitrogen with controlled temperature (85 °C). (**F**) Evolution of power

conversion efficiency (PCE) of perovskite solar cells with or without OLA treatment. The devices were stored under dark with controlled humidity. (**G**) Evolution of the PCEs measured from the encapsulated perovskite solar cells with or without OLA treatment exposed to continuous light (90 ± 5 mW cm^{-2}) under open-circuit condition.

Fig. 5.1 Surface defect identification and constructive configuration of the C=O group in three different chemical environments.

(**A**) Chemical structures of three different passivation molecules. (top to bottom: Theophylline, Caffeine and Theobromine) (**B**) Top view of the various types of surface defects. (**C**) *J-V* curves of perovskite solar cells with or without small molecules treatment under reverse scan direction. (**D**) Theoretical models of perovskite with molecular surface passivation of Pb_I antisite.

Fig. 5.2 Investigation of the interactions between surface defects and the small molecules.

FTIR spectra of (**A**) pure theophylline and theophylline-PbI_2 films; (**B**) pure caffeine and caffeine-PbI_2 films; (**C**) pure theobromine and theobromine-PbI_2 films. (**D**) PL spectra of perovskite films without and with small molecules treatment. (**E**) Trap density of states (*t*DOS) in perovskite solar cells with or without small molecules treatment. (**F**) Nyquist plots of perovskite solar cells with or without small molecules treatment measured in the dark and at corresponding open-circuit voltages.

Fig. 5.3 Characterization of perovskite films and interfaces with theophylline treatment.

(**A**) XPS data for Pb 4*f* 7/2 and Pb 4*f* 5/2 core level spectra in perovskite films with or without theophylline treatment. (**B**) UPS spectra of perovskite films with or without theophylline treatment. (**C**) AFM and KPFM images of perovskite films with (right) or without (left) theophylline treatment. (**D**) Time-resolved PL spectra of perovskite films before and after depositing Spiro-OMeTAD without and with theophylline treatment. (**E**) Cross-section SEM

images and the corresponding EBIC images and line profile of the perovskite solar cells with (right) or without (left) theophylline treatment.

Fig. 5.4 Enhanced photovoltaic performance and long-term stability of perovskite solar cells with theophylline treatment.

(**A**) Current density–voltage (*J–V*) curves of perovskite solar cells with or without theophylline treatment. (**B**) EQE curves of perovskite solar cells with or without theophylline treatment. (**C**) Stabilized maximum power output and the photocurrent density at maximum power point as a function of time for the best performing perovskite solar cells with or without theophylline treatment, as shown in Fig. 4A, recorded under simulated one-sun AM1.5G illumination. (**D**) PCE distribution of perovskite solar cells with or without theophylline treatment. (**E**) Evolution of the PCEs measured from the encapsulated perovskite solar cells with or without theophylline treatment exposed to continuous light (90 ± 10 mW cm^{-2}) under open-circuit condition.

Figure 6.1. Schematic representation of the preparation of $Cs_2AgBiBr_6$ thin films by vacuum-sublimation and solution-processing.

Figure 6.2. Annealing temperature dependent XRD patterns and peak fittings of (a)solution- and (b)vacuum-processed $Cs_2AgBiBr_6$ thin films, respectively. 2D GIXRD patterns of (c) solution- and (d) vacuum-processed $Cs_2AgBiBr_6$ thin films annealed at 280 °C and 220 °C, respectively.

Figure 6.3. Detailed XPS scans of Cs 3d and Br 3d core levels of (a) solution- and (b) vacuum-processed $Cs_2AgBiBr_6$ thin film.

Figure 6.4. (a) UV-Vis absorption spectra, (b) Raman peaks, (c) PL intensity and (d) PL decay dynamics of the optimized $Cs_2AgBiBr_6$ thin films prepared by vacuum-sublimation (purple) and solution-processing (red). Insets of (a) are the Tauc plots extracted from the UV-Vis absorption spectra.

List of Tables

Acknowledgments

The dissertation and the work behind were accomplished with the generous support and supervision of many. I would like to convey my deep appreciation to them and my honest wish that while the dissertation has concluded our friendships continue to bloom.

First, I express my sincerest thanks to Prof. Yang Yang, my Ph.D. research advisor, for the opportunity to participate in the famous research group. His research advice of always thinking deeply has influenced me the greatest. During the years, I have never been lacking in inspiration, trust, and encouragement from my advisor, for which I thank him most.

I also thank my committee members, Prof. Jenn-Ming Yang, Prof. Yu Huang, and Prof. Wentai Liu, for their kindly mentorship.

I would like to thank Ms. Jingjing Xue for her special supports during my research. I thank Dr. Pei Cheng and Dr. Lei Meng who were my mentors for one year in my early-stage research. We had uncountable long and comprehensive discussions about our projects day and night and the device physics of solar cells they taught me have been inspiring and extremely valuable for my career. Dr. Sheng-Yung Chang is also first of the many people who directed me to enter the field.

I will not forget to thank my senior partners in Prof. Yang's Lab during my Ph.D. career: Dr. Jin-Wook Lee, Dr. Wenchao Huang, Dr. En-Ping Yao, Dr. Bowen Zhu, Dr. Qifeng Han, Dr. Dong Meng, Dr. Tae-Hee Han, Dr. Pengyu Sun, Dr. Nicholas De Marco, Dr. Sang-Hoon Bae, Dr. Yao-

Tsung Hsieh, Dr. Jun Yuan, Dr. Yuqiang Liu, Dr. Huanjun Chen, Prof. Zhenxing Li, Prof. Yu Duan and Prof. Zhao-Kui Wang. I also want to thank my collaborators during my Ph.D. study: Ms. Yanqi Luo from UCSD, Dr. Xihan Chen from NREL, Dr. Canglang Yao from U of Toledo, Dr. Rui Wang from Nanjing University, Dr. Kai Zhu from NREL, Dr. Chenhui Zhu from LBNL, Dr. Guangchao Han from ICCAS, Prof. Kendall N. Houk, Prof. Richard B. Kaner from UCLA, Prof. David Fenning from UCSD, Prof. Yanfa Yan from U of Toledo, Prof. Yuanping Yi from ICCAS, Prof. Yingping Zou from CSU and Prof. Chunfeng Zhang from Nanjing University.

I am glad to have the chance to share the joys and hard times together with my fellow colleges: Zhengxu Wang, Haowen Cheng, Tianyi Huang, Shaun Tan, Yepin Zhao, Hao-Cheng Wang, Quantan Wu, Minhuan Wang, Jiahui Zhu, Selbi Nuryyeva, Zhiyu Zhao, Ran Zheng, and Yuan Zhu. I wish them best for their life and career.

At last, I thank my parents, my grandparents and my other family members. I would not have reached this step without their belief in me.

Chapter One is a version of *Adv. Func. Mater,* **2019**, 1808843; Chapter Two is a version of *Joule,* **2019**, 3, 1464; Chapter Three is a version of *Nano Letter,* **2019**, 19, 8, 5176; Chapter Four is a version of *J. Am. Chem. Soc.,* **2019**, 141, 35, 13948; Chapter Five is a version of *Scienc*e, **2019**, 366, 1509; Chapter Six is a version of *Nano Letter,* **2019**, 19, 3, 2066; Chapter Seven is a version of *Adv. Mater.* **2019**, 1904215 All the permissions have been granted by the publishers.

VITA

2011-2015 Bachelor's degree. Materials Science and Engineering, Jilin University, Changchun, China

2015-2016 Master's Degree. Materials Science and Engineering, University of California, Berkeley, Berkeley, CA, USA

2016-2019 Graduate Student Researcher, Department of Materials Science and Engineering, University of California, Los Angeles, CA, USA

Selected Publications

1. Rui Wang†, Jingjing Xue†, Kai-Li Wang†, Zhao-Kui Wang, Yanqi Luo, David Fenning, Guangwei Xu, Selbi Nuryyeva, Tianyi Huang, Yepin Zhao, Jonathan Lee Yang, Jiahui Zhu, Minhuan Wang, Shaun Tan, Ilhan Yavuz, Kendall N. Houk and Yang Yang, Constructive molecular configurations for surface-defect passivation of perovskite photovoltaics, *Science* (2019). (†Equal contributions)
2. Rui Wang†, Jingjing Xue†, Lei Meng, Jin-Wook Lee, Zipeng Zhao, Pengyu Sun, Le Cai, Tianyi Huang, Zhengxu Wang, Zhao-Kui Wang, Yu Duan, Johnathon Lee Yang, Shaun Tan, Yonghai Yuan, Yu Huang, Yang Yang, Caffeine Improves the Performance and Thermal Stability of Perovskite Solar Cells, *Joule* (2019). (†Equal contributions)
3. Rui Wang†, Jun Yuan†, Rui Wang, Guangchao Han, Tianyi Huang, Wenchao Huang, Jingjing Xue, Hao-Cheng Wang, Chunfeng Zhang, Chenhui Zhu, Pei Cheng, Yuanping Yi, Kung-Hwa Wei, Yingping Zou and Yang Yang, Rational Tuning of Molecular Interaction and Energy Level Alignment Enables High-Performance Organic Photovoltaics, *Advanced.*

Materials (2019). (†Equal contributions)

4. Rui Wang, Sheng-Yung Chang, Lei Meng, Wenchao Huang, Jin-Wook Lee, Hao-Wen Cheng, Tianyi Huang, Yuqiang Liu, Jingjing Xue, Pengyu Sun, Chenhui Zhu, Pei Cheng and Yang Yang, Design of a Rigid Scaffold Structure toward Thermal Stable and Thick-film Organic Photovoltaics, *Matter* (2019).
5. Rui Wang†, Jingjing Xue†, Dong Meng, Jun Yuan, Sheng-Yung Chang, Yuqiang Liu, Pei Cheng, Yingping Zou, Xiaowei Zhan and Yang Yang, Molecular Tuning of Titanium Complexes Enabling Electron Transporting Materials with Controllable Work Function for Efficient Organic Photovoltaics, *The Journal of Physical Chemistry: Part C* (2019). (†Equal contributions)
6. Rui Wang†, Muhammad Mujahid†, Yu Duan, Zhao-Kui Wang, Jingjing Xue and Yang Yang, A review of perovskites solar cells stability, *Advanced Functional Materials* (2019). (†Equal contributions)
7. Rui Wang†, Jintao Wang†, Shaun Tan, Yu Duan, Zhao-Kui Wang and Yang Yang, Opportunities and Challenges of Lead-Free Perovskite Optoelectronic Devices, *Trends in Chemistry* (2019). (†Equal contributions)

Chapter 1 Introduction to the stability issues of perovskite solar cells

Global energy consumption has been gradually increasing. Limited sources of fossil fuels are demanding the research on sustainable and renewable energy resources. The conversion of sunlight into electricity is one of the most promising studies to meet the increasing energy demands for future generations without the negative impact of the global climate. Solar cell technology provides an eco-friendly and renewable energy route to convert photon energy into electricity directly.[1] Now a day's scientist intends to design photovoltaic devices with high efficiency, low cost, and large-scale fabrication but unfortunately did not succeed yet. However, the efficient establishment of solar cell technology on a global scale requires an efficient improvement concerning materials and devices to reduce the fabrication cost and increase the power conversion efficiency[1b].

Perovskite solar cells (PSCs) have recently been universally promoted as an economically and environmentally feasible renewable technology option to traditional solar cell technologies for addressing global challenges in the area of energy generation and climate change[2]. The organic-inorganic perovskite with an ABX_3 structure where A is Cesium (Cs), Methyl Ammonium (MA), or formamidinium (FA); B is Pb or Sn; and X is Cl, Br, or I, have recently emerged as an intriguing class of semiconductors.[3] There are various techniques in which perovskites can be processed such as spray coating, a nozzle is used to disperse tiny liquid droplets onto substrates the perovskite layer can also be deposited by ultrasonic spraying.[4] Dip coating, a non-conventional method to create the meniscus edge, is pulling a substrate out of a precursor ink and sheering a cover plate over the deposition substrate,[5] 2-step deposition[6] in which the lead halide thin film is first deposited then converted to the perovskite by reaction with organic halide salts.

[5a] Chemical vapor deposition[7] (CVD) has been used to deposit $FAPbI_3$ thin films on 5 cm × 5 cm substrates and to fabricate 12 cm^2 modules with a PCE of 9%[8]. Ink-jet printing nozzles are used to disperse the precursor ink, with fine control of the droplet size and trajectory. Small-area PSCs (0.04 cm^2) have been fabricated using inkjet printing.[9] PSCs fabricated by blade coating has demonstrated PCEs >19%.[10] And screen printing method has good patterning ability with a lateral resolution of 75~100 μm.[11] Perovskites have exceptional properties such as absorption over a wide spectrum,[12] a direct band gap,[13] charge carrier diffusion lengths in the micrometer range,[14] and defect tolerance.[15] An unprecedented rise in the efficiency from 3.8% to 25.2% was achieved in only a few years, which extremely outperformed many proven commercial photovoltaic technologies, e.g., Si, GaAs, and CdTe-based solar cells.[16]

Massive technologies have been developed to improve the performance of the PSCs, including solvent engineering, interfacial engineering, bandgap engineering, *etc*.[17] Reported by Grätzel group in 1991, Dye-Sensitized Solar Cell (DSSC) has been paid intensive attention in the passing decades. Up to now the certified highest PCE of DSSC has reached 11.9%[18] presenting excellent market competitiveness and commercial prospect. In 1998, M. Grätzel from Switzerland firstly reported a hole-transporting material (HTM), 2, 2, 7, 7-tetrakis (N, N -di-methoxy-phenyl amine)-9, 9-spirobifluorene (spiro-OMeTAD), to replace the conventional liquid-state electrolyte and developed a solid-state DSSC (ss-DSSC).[19] From 1998 to 2011, the PCE of ss-DSSC fast increased from 0.74% to 7.2%, but still much lower than that obtained by liquid-state electrolyte based DSSCs.[20] In late 2012, a remarkable breakthrough was made by using $CH_3NH_3PbI_3$ ($MAPbI_3$) perovskite nanocrystals as the light absorber to fabricate a solid-state mesoporous perovskite solar Cell (MPSC) with a PCE of up to 9.7%.[21] Etgar et al. fabricated an efficient HTM-free TiO_2/$MAPbI_3$/Au solar cell with an efficiency of 10.49%.[22] After that Snaith's group

reported a planar thin-film architecture PSC with a PCE of 12.3%.[23] In 2014, the PCE increased to a certified 17.9% and then 20.1%.[24] And a low-temperature and solution processable ionic liquid, [BMIM]BF_4, is recently utilized to act as an effective electron modification layer and a protective layer for fabricating high-performance indoor and outdoor PSCs. The device delivered an impressive PCE of 19.30% at 1 sun illumination, and a record indoor PCE of 35.20% under a fluorescent lamp with 1000 lux, which was the highest value reported so far for indoor PSCs.[25]

At present, the most challenging issue in perovskite solar cells is the long-term stability, which must be cleared up before putting it into practical applications. As we know that the stability of perovskite solar cells upon the severe environment, e.g., thermal treatment, light illumination, humidity, etc., appears to be the bottleneck that impedes their further commercialized.[26] Amongst them, the humidity is demonstrated to be one of the possible causes for the degradation of perovskites.[27] Zhou et al. reported that exposure to a low level of humidity (RH ≈30%) during solar cell fabrication was capable of controlling the perovskite crystal formation and aided them in enhancing the PCE to 19.3%.[28] Bass et al. reported how humidity could speed up the perovskite crystallization.[29] These studies suggest that rationally controlled amount of H_2O could assist the grain growth of perovskite then result in the film with high quality, carrier mobility and lifetime film, though the excess moisture will damage the crystallinity once the films are prepared.[30] To entirely keep away from any ambient exposure before finishing the device, about all groups performed the perovskite deposition in a dry atmosphere and endeavor to avoide exposure to humidity. Generally, PSCs have two architectures, (i) mesostructured device, and (ii) planar device. In a mesostructured device, the perovskite is used to sensitize the mesoporous Titania (TiO_2) layer.[31] Whereas, the planar device has a comparatively simpler structure and gives better cell performance. Gradual improvement of the perovskite film quality

improved the overall cell efficiency.[31-32]

PCSs have recently attracted much attention due to their high PCE, cheap starting material and ease of fabrication.[33] However, device stability has still been a severe hurdle towards commercialization of perovskite-based solar cells. The instability of the device comes mostly from the degradation of the perovskite materials. the instability has been linked to the organometallic absorber toward humidity[35], and their overall poor long-term thermal stability.[36] Many attempts have been made to achieve better stability of PSCs, such as two-dimensional perovskite structure designing,[37] cation engineering,[38] and an additive in the hole and electron transfer layer was used to enhance the stability of the PCSs.[39] Solving instability problem of perovskite material is the critical strategy to upgrade the long-term stability.

The degradation of PSCs in a humid environment is a challenging issue. Among different factors, moisture has been considered one of the biggest challenges. The moisture instability originates due to the hygroscopic nature of amine salt.[40] Both $MAPbI_{3-x}Cl_x$ and $MAPbI_3$ endure similar moisture assisted degradation process in which the methylamine group is lost via sublimation and PbI_2 is formed.[114] The highly hydrophilic properties of perovskite could lead to the materials to readily absorb water from the surrounding environment and induce the formation of hydrate products similar to $(CH_3NH_3)_4PbI_6.2H_2O$.[27] Previous work reported that PCSs are severely affected due to moisture and oxygen environmental sensitivity since degradation of perovskite by hydrolysis reaction and represented by following chemical equations.

$$CH_3NH_3PbI_3(s) \leftrightarrow PbI_2\ (s) + CH_3NH_3I\ (aq) \qquad (1)$$

$$CH_3NH_3I\ (aq) \leftrightarrow CH_3NH_2\ (aq) + HI\ ((aq). \qquad (2)$$

$$4HI\ (aq) + O_2\ (g) \leftrightarrow 2I_2\ (s) + 2H_2O\ (I) \quad (3)$$

$$2HI\ (aq) \leftrightarrow H_2\ (g) + I_2\ (s) \quad (4)$$

The hydrogen bond between organic and inorganic units in a perovskite, it attributes to the structural ability, and it is strongly affected by the high polarity of a water molecule.[42] Previous works reported that the presence of mesostructured TiO_2 could be helpful for device stability and a device without mp-TiO_2 exhibit profound sensitivity to ambient conditions.

Efforts have been dedicated to developing the moisture tolerance of perovskite materials without degradation of their optoelectronic properties.[43]It is contrary to the thought that water or moisture is harmful to the fabrication of perovskite solar cells. Bass et al. reported better film formation of $MAPbI_3$ and $MAPbBr_3$ while they are spin-coated in the surrounding of air at 58.2% RH.[29] Snaith group reported that the optimal RH of 50% produces a PCE of more than 14% because of the elimination excess of MA^+ [44], the damage of $MAPbI_3$ by water vapor is reversible.[45] This behavior is thought to be due to reversible infiltration of the perovskite lattice during production and postproduction.[46]

In recent years, 2D PSCs have begun to gain attention because of their better stability.[47] Cao et al. studied 2D homologous perovskites $(CH_3(CH_2)_3NH_3)_2(CH_3NH_3)_{n-1}Pb_nI_{3n+1}$ solar cells.[48] Recently, Tsai et al. prepared mixed-dimensional (MD) perovskites $(CH_3(CH_2)_3NH_3)_2(MA)_{n-1}Pb_nI_{3n+1}$ (n==3, 4) which shows a PCE of 12.52% and high light and stability.[49] Organic ammonium salt provides good self-assembly and film reforming properties. The combination of the inorganic framework and different ammonium salt may produce new performances in optical, electrical, and magnetic by changing organic and inorganic components.[50] Although there are

many reports about the high stability of 2D perovskites.[47-49] Dai and his team reported that $(C_6H_5CH_2NH_3)_2(FA)_8Pb_9I_{28}$ quasi-2D perovskite film and the device display high stability in a moist environment. After exposure to RH 80% air for 500 h, the $(C_6H_5CH_2NH_3)_2(FA)_8Pb_9I_{28}$ film only slightly decomposes, and the device maintains 80% of its starting PCE.[51] They also suggest that the hydrophobicity of different ammonium salts can determine moisture resistance of 2D perovskite materials.[51] Adding a small amount of 2D perovskite into 3D perovskite improve not only moisture stability but also suppress nonradioactive recombination via passivating the surface defect and/or bulk tarps of 3D perovskite.[52] Also, negligible hysteresis can also be achieved by grain preferred orientation growth engineering,[49] and in-situ nonstoichiometric precursor engineering.[53] According to the report on $FA_xPEA_{1-x}PbI_3$ used for inverted PSC showing a PCE of 17.7%, bulky organic cations can terminate perovskite lattice and thereby lead to the quantum well (QW) structure. A bulky organic cation can control the number of inorganic perovskite layers (width of QW).[54] The experimental results give important insight into the design of 2D/3D mixed perovskite to have a high carrier transport with less chance of recombination. Wang et al. incorporated BA into $FA_{0.83}Cs_{0.17}Pb(I_yBr_{1-y})_3$ 3D perovskite to produce 2D–3D heterostructured BA–Cs–FA lead halide perovskite for normal planar PSCs. 2D platelets were formed perpendicularly, and these could drive the vertical growth of 3D perovskite. Grain growth perpendicular to the substrate is expected to be favorable for charge transport, accompanied by longer charge diffusion length and lifetime as proved by significantly increased PL studies.[52c] 1D–3D hybrid perovskite materials were also proposed for the improvement of stability, where (1H-pyrazole-1-yr)pyridine (PZPY) was introduced into 3D $Cs_{0.04}MA_{0.16}FA_{0.8}PbI_{0.85}Br_{0.15}$ perovskite.[55]

It is found that 2D perovskites with general formula $(RNH_3)_2A_{n-1}M_nX_{3n+1}$ had appealing

environmental stability.[56] Actually, 2D perovskites are derived from the archetypal AMX_3 3D structure by inserting bulky organic cations between the atomic layers. The hydrophobic nature of the organic spaces and relatively stable structure of 2D perovskite improve the stability of PSCs. Two dimensional $(ZnPc)_{0.5}MA_{n-1}Pb_nI_{3n+1}$ was successfully constructed within the GBs of $MAPbI_3$ film achieving a GBs suture for passivating the defects in GBs.[57] The moisture stabilities of the PSCs were tested in air at room temperature with humidity of about 45% as shown in **Figure 1.1**. The modified perovskite retained over 95% of its original efficiency after 2000 h. In contrast, the device with pure perovskite film first exhibited a fast degradation rate by remaining only <65% of the initial efficiency under the same conditions, and the best efficiency was improved up to 20.3%.[57] Peng et al. reported that the synthesized PCBM/Al_2O_3-ZnO dramatically improves the stability of $CH_3NH_3PbI_3$ against the ambiance and even against liquid water.[58]

The effects of moisture on $CH_3NH_3PbI_3$ is of great interest because of its role in the degradation of perovskite solar cell performance.[59] To avoid exposure to humidity during solar cell fabrication, nearly all groups carry out perovskite deposition in a dry atmosphere and take pains to avoid exposure to humidity following device fabrication. Zhou et al. investigated that exposure to a low level of surrounding humidity (30% RH) during solar cell fabrication process, controlled the perovskite crystal formation, assisted them in boosting PCE to 19.3%.[28] And Bass et al. demonstrated how humidity could facilitate crystallization.[29] Kamat and his team explored the stability of perovskite solar cells stored at 0- 90% RH, to characterize how the PV performance is affected by humidity. [27] The interaction between $CH_3NH_3PbI_3$ and H_2O vapor is investigated by characterizing the ground state and excited state optical absorption properties and probing morphology and crystal structure. **Figure 1.2** shows top-down scanning electron micrographs of films stored in 0%, 50%, and 90% RH for 14 days. Before water exposure, all of the perovskite

films display a somewhat rough surface as seen in Figure 3A-C. After being aged in 90% RH for 14 days, (Figure 1.2F) the perovskite went through a recrystallization process, becoming smooth and highly ordered. Films stored under 0% and 50% RH also show a similar trend, though less severe, structural changes over this period (Figure 1.2D and 1.2E). Same as reported for $CH_3NH_3IPbI_{3-x}Cl_x$ films stored under Ar.[60] Yang co-workers revealed that a mild moisture environment has a positive effect on perovskite film formation, and the devices showed an average PCE of 17.1%.[61]

Niu and his team observed that perovskite is sensitive to moisture, and the degradation process was monitored with UV-vis spectroscopy and XRD.[62] As for as the stability of the device is a concern, Snaith's group showed the enhanced stability of $(HC(NH_2)_2)_{0.83}Cs_{0.17}Pb(I_{0.6}Br_{0.4})_3$ perovskite over 3420 h under continuous 1 sun illumination in the air with an efficiency as high as 18.3%.[63] Chen and his team observed that with optimized casting temperature (70 ºC) and precursor concentration (1.2 M), the best PCE of 19.54% with J_{sc} of 22.70 mA cm^{-2}, V_{oc} of 1.11 V and FF of 0.78 are achieved with the planar PVSC of ITO/NiO_x/$MAPbI_3$/ PCBM/BCP/Ag. The device performance exhibits excellent thickness insensibility and maintains the PCE over 19% in the wide range of the active layer thickness from 700 to 1150 nm. The unsealed device also shows good stability and remained 80% of its initial efficiency after 30 days storage in the air with an RH of 50%.[64] **Table 1.1** portrays the PSCs performance under moisture exposure.

Unlike stability issues associated with moisture, another important factor influencing the stability of perovskite solar cells is UV light exposure. As with multiple solar cell technologies, illumination becomes the reason for degradation in perovskite solar cell.[65] When perovskite films are subjected to both light and dry air the perovskite layer rapidly decompose into

methylamine, PbI_2, and I_2 as reaction products.[66] The photogenerated electrons on the perovskite reacted with molecular oxygen to form superoxide, which further reacts with MA of the perovskite absorber. It suggested that replacing the methylammonium component $CH_3NH_3PbI_3$ with species without acid protons could improve tolerance to oxygen and enhance stability.[67] Leijtens et al. reported that a perovskite solar cell with the TiO_2 layer is susceptible to UV induced degradation. This was investigated by measuring 5h efficiency decay curve, measured under 1 sun AM 1.5G illumination for devices with and without encapsulation and a UV filter. The results showed that encapsulated devices decayed more rapidly than non-encapsulated device, which indicated that the degradation not just start from the active layer but also the meso-TiO_2.[59] The degradation in the film caused by exposure to light has been explained as[42]

$$2I^- \longleftrightarrow I_2+2e^- \quad (5)$$

$$3CH_3NH_3^+ \longleftrightarrow 3CH_3NH_2+3H^+ \quad (6)$$

$$I^-+I_2+3H^++2e^- \longleftrightarrow 3HI \quad (7)$$

First, the TiO_2 extracts the electron from I^- and then breaks the perovskite structure amounting to the production of I_2. Finally, the extracted electrons between TiO_2 and methylammonium lead iodide could return to minimize I_2, and the HI produced evaporates quickly because of its low boiling point.[141]

There are various strategies to retard the UV induced instability of the PVSK devices have been reported. Several groups have demonstrated around 1000 hours stability under illumination with slightly or no drops in performance. Saliba et.al demonstrated MA-free PVSK solar cells with 1000 hours illumination stability via composition engineering.[69] Arora et al. utilized inorganic

material CuSCN as HTL. After aging at 60 ºC under 1 sun illumination for 1000 hours, the corresponding device still preserved its 95% of PCE.[70]

Thermal stability of PSCs also raises a serious concern, that subjects to a high temperature causing degradation of the device.[71] Some researchers say that the instability of perovskite is linked to the grain boundaries (GBs) or surface,[72] to cap these GBs with suitable protective materials is the attractive strategy to improve the stability of perovskites.[73] It is a well-known fact temperature has a great effect on crystal structure and phase of perovskite. Previously reported that phase change from tetragonal to cubic occurs at 54ºC-56ºC. [13] Solar modules will be exposed to elevated temperature during operation as per international standard (IEC 61656 climatic chamber tests). The solar cell must require thermal stability up to 85 ºC that is corresponding to 0.093 eV.[75] Coings et al. found that perovskite could be decomposed into PbI_2 while heated in nitrogen at 85 ºC for 24 hours. They reported the soft matter nature of perovskite layer by investigating morphological, electrical, chemical and optical characteristics of this new class of material. This experiment was performed in pure dry N_2, pure dry O_2 and at ambient atmosphere with 50% relative humidity for 24 h in the dark.[76] The formation energy of $MAPbI_3$ is 0.11-0.14 eV which is very close to 0.093 eV suggesting the possible degradation of $MAPbI_3$ at continuous exposure to 85 ºC.[36] Philippe et al. investigated thermal stability, the measurements were performed at room temperature, 100 ºC, and 200 ºC for 20 minutes. They observed $MAPbl_3$ started to decompose into Pbl_2 with an increase in temperature from room temperature to 100 ºC and then to 200 ºC (given equation show the reaction). The estimated I/Pb and N/Pb ratios gained from hard X-ray photoelectron spectroscopy (HAXPES) results, revealed that $MAPbl_3$ to Pbl_2 ratio modified from 85: 15 to 70: 30 and to 0: 100, respectively.[75] The decomposition temperature of perovskite $CH_3NH_3PBI_2$ has been reported as being between 100 ºC to 140 ºC.[41,

76]

$$CH_3NH_3PbI_3 \longrightarrow PbI_2 + CH_3NH_2 + HI \quad (8)$$

To avoid decomposition due to high temperature, the use of thermally resistant materials is the most suitable option. Researchers are trying to achieve a highly efficient and stable perovskite solar cells. Many attempts have been made to improve the stability of perovskite solar cell. Thus far, scientists have succeeded to achieve the stability of more than one year in perovskite solar cells.[52d] Methylammonium lead tribromide ($CH_3NH_3PbBr_3$ or $MAPbBr_3$) is a light absorber compound with a PCE of 7.11%. It also has attracted geometrical stability, maintaining 93% of its initial PCE even after aging of 1000 h.[77] The $CH_3NH_3PbInBr_{3-n}$ perovskite has reported achieving a PCE of 8.54%, with improved stability compared to $CH_3NH_3PbI_3$.[78] Replacement of MA organic cation with a smaller size (MA: 2.17 Å) by HC $(NH_2)_{2+}$ (FA: 2.53 Å) can push the tolerance factor of 0.99, which could potentially enhance the thermal stability.[79] A substantial effort has been now focused on formamidinium lead iodide ($FAPbI_3$) perovskite which exhibits an ideal bandgap (~1.48 eV) and significantly enhanced thermal stability.[80] Jin et al. reported that $FAPbI_3$ is more thermally stable as compared to $MAPbI_3$ or any other perovskite.[81] Park's team reported good thermal stability in $FAPbI_3$ perovskite at an annealing temperature of 25 ºC for 15 min.[82] Although two-dimensional perovskites have demonstrated over 1000 h device stability.[52d, 83] In a quasi 2D perovskite by controlling the orientation, they produced a thin film of near single crystalline quality, photovoltaic efficiency 12.52% with no hysteresis, improved stability when subjected to light, humidity, and heat stress test. With device encapsulation, the layered devices show a constant value under AM1.5G illumination or humidity for more than 2000 h.[49]

Thermal stability was also explored by thermogravimetric analysis (TGA) measurement.[84] The TGA curves in **Figure 1.3** revealed that both the 3D perovskite $CH_3NH_3PdI_3$ and 2D perovskite $(CH_3NH_3)3Pd_2I_7$ were thermally stable up to 250 °C, comparable to other hybrid perovskites.[72a, 85] Smith et al. reported that a layered 2D perovskite-based on PEA and MA with n = 3 exhibited better stability than the archetypical $MAPbI_3$, with a much lower photovoltaic efficiency (4.7%). This was due to the low carrier mobility on the vertical direction caused by these insulating large organic cation layer supposedly parallel to the electrodes.[86] Dai fabricated three mixed-dimensional (MD) perovskites by non-toxic transition metal cations (Zn_2^+, Mn_2^+, and Ni_2^+) at 3 % to partially replace lead cations in $MAPbI_3$.[87] The MD devices could, respectively, retain 81 %, 80 %, and 74 % of their original PCE values under about 50 % RH for 800 h. The PCE of MD perovskite devices maintained 84 %, 85 %, and 76 % of their starting values at 60°C for 100 h.[87] Leyden demonstrated that solar cells fabricated with $FAPbI_3$ as active layer had better thermal stability than those of $MAPbI_3$. Modules consisted in 6 series connected sub-cells with mesoscopic structure (FTO/Compact-TiO_2/TiO_2-scaffold/$FAPbI_3$/Spiro/Au). FAI (or MAI which was used to fabricate the reference modules) was deposited on PbI_2 films through CVD technique which permits to control the deposition area by masking.[8] The PCE of modules was lower with regards to small cells (from 10.4% to 9.5%, for the best devices) as a result of issues in the patterning of the spray pyrolysis TiO_2 compact layer and growth of the perovskite over large areas. Recently, Lin reported that CSCNT: PEI based device obtained outstanding stability, sustaining over 94% of original efficiencies after 500 h storage in ambient air and 90% of that after 500 h thermal treatment at 60 °C. The devices also showed good stability exposed to moisture under thermal stress (60 °C, 60% RH), remaining over 70% of original PCEs after 500 h, which could be further raised to 85% while encapsulating the devices with PMMA layer.

Kitamura *et al.* studied thermal stresses using an ionic liquid-based electrolyte and a Pt-coated Ti foil as counter-electrode. The performance was not affected by the upscaling processes as demonstrated by comparing cells of both (50 × 50) mm^2 and (55 × 300) mm^2 and sub-module composed by series inter-connecting two or five (55 × 300) mm^2 cells. Accelerated endurance tests were carried out according to JIS-C8938 on the smallest cell. The best cells demonstrated excellent overall stability both in the 1000 h test at (85 °C,85% RH) conditions as shown in **Figure 1.4** and in the 200 cycles thermal stress test (heat-cool cycles, between -40 and 90 °C).[88]

The PSCs with modified perovskite structure ($(ZnPc)_{0.5}MA_{n-1}Pb_nI_{3n+1}$) offered improved heating stability (**Figure 1.5b**), device lost only 10% of its original efficiency beyond 1000 h (Figure 1.5c). The control device with only perovskite film lost over 90% of its original efficiency within 250 h. The color variety of corresponding perovskite films was also prepared to further demonstrate the presence of excellent thermal and moisture stability (Figure 1.5d)[77]

The outdoor environment would be unpredictable,[89] if someone estimates the lifetime of the device from the indoor test.[90] Hole-conductor-free PSCs based on a triple-layer architecture employing carbon as a back contact was subjected to hot weather in Saudi Arabia desert for one week. No degradation was observed during these outdoor tests. Together with heat exposure during three months at 80–85°C these tests were encouraging.[91]

The mixture of organic cations (methylammonium (MA) and formamidinium (FA)) and mixed halides was used to get a more stable and efficient device. Unfortunately, MA/FA compositions were sensitive to the processing conditions because of their intrinsic structural and thermal

instability. Purely inorganic cesium leads trihalide perovskites to exhibit excellent thermal stability.[92] Adding small amounts of inorganic cesium (Cs) in a ‘‘triple cation’’ (Cs/MA/FA) configuration resulted in highly monolithic grains of more pure perovskite. Harvesting this strategy, efficiencies up to 21.1% (stabilized) and an output of 18%, even after 250 hours of aging under operational conditions were achieved. Choi et al. present Cs/MA mixtures which prove, in principle, that embedding small amounts of Cs in a $MAPbI_3$ structure could result in a stable perovskite film reaching 8% in PCE.[93] Yi et al. explained the improved structural stability.[43a]

Among the various factors that can affect the stability of perovskite materials, the crystal structure is also an important parameter. There have been several reports that perovskite compounds with organic molecule were unstable in the presence of moisture, oxygen, light, and heat.[94] Therefore, the improvement in the stability of the crystal structure was a critical issue. Various tools and indicators could facilitate the evaluation of crystal structures. Such as, the concept of tolerance factor was proposed to describe the structural stability of the perovskite materials. Goldsmith tolerance factor (t) is a reliable empirical index to predict which structure is in preference to be formed.[95] Tolerance factor was defined as $t = (R_A + R_X)/\sqrt{2}\ (R_B + R_X)$ where r_A is the radius of the A cation, r_B is the radius of the B cation, and r_X is the radius of the anion. If the value of t is in a certain range, then the crystal present perovskite structure. The value of t should be between 0.8 and 1 for perovskite structure.[96] Nonperovskite structures are formed when the tolerance factor is higher than >1 or lower than <0.71.[95] Advance solar cell technologies towards their maximum efficiency require fragile control over the structural parameters. The rule was developed for oxide perovskite, but the trend is still valid for organic-inorganic hybrid halide perovskite materials. [97] The correlation between the perovskite structure and the tolerance factor is illustrated schematically in **Figure 1.6**. The organic-inorganic hybrid

halide perovskite materials tend to form a hexagonal structure when t >1, orthorhombic structure when t<0.8, cubic structure when 0.8< t < 1[97b].

Recent experimental and theoretical studies showed that the perovskite (FA-Cs)PbI_3 alloying absorbers with effective tolerance factors around 0.94–0.98 have the best device performance.[43c] The most investigated lead halide perovskite is $MAPbI_3$, which offers tolerance factor 0.91. Weber et al. investigated the relationship between temperature and the structure of methylammonium trihalide $MAPbX_3$ (X=Cl, Br, I). At room temperature, both $MAPbBr_3$ and $MAPbCl_3$ present a cubic structure. However, $MAPbI_3$ becomes a tetragonal structure when the temperature increases to 327.4 K.[98] Replacing MA cation (MA: 2.17 Å) by $HC(NH_2)_2^+$ (FA: 2.53 Å) can increase the tolerance factor of 0.99, which could enhance the thermal stability. $FAPbI_3$ does not discolor even at 150 ^oC under ambient conditions, while $MAPbI_3$ discolors in 30 minutes.[79, 99] One of the most interesting things is that the $FAPbI_3$ could be apt to show the yellow phase (δ-phase),[100] and the tolerance factor is larger than 1, which showed instability, to overcome this problem smaller cations should be incorporated like Cs or Rb could be incorporated into the alloy with FA.[101] The doping could lead to the enhancement of thermal stability. The improved stability has been deemed as the enhanced crystallinity of the perovskite layer, the role of tuning the tolerance has not been realized.[11a, 102]

A more stable new kind of perovskite, $(PEA)_2$ $(MA)_2$ Pb_3I_{10} ($PEA=C_6H_5(CH_2)_2NH_3^+$, $MA=CH_3NH_3^+$ has also been reported.[57a] Sargent et al. adopted $(PEA)_2(MA)_{n-1}PbnI_{3n+1}$ structure, which keeps its almost three-dimensional structure also shows significantly improved stability.[103] According to Goldschmidt's rule, it is reasonable to assume that the tolerance factor was larger than 1 for hexagonal δ-$FAPbI_3$. Yamamoto et al. proposed that the stability strongly

depended on the identity of the A-site cation. Cs(B, B′)I_3 structures are stabilized by a mixture of divalent cations, such as Pb, Sn, and Ge, at the B site. Concerning the stabilization mechanisms, Coulomb energy gain seems to be the origin of the structural stability in A=Cs structures. MA(B, B′)I_3 are stabilized by the combination of divalent and trivalent cations, such as the In-Sn and In-Bi systems.[104] The small-size Cs^+ cation results in a tolerance factor too low to sustain a cubic perovskite structure. The photoactive α-$CsPbI_3$ with a bandgap of 1.77 eV is usually attained at a temperature higher than 300 °C.[105] Zhu and co-workers proposed a general chemical composition design protocol to stabilize the perovskite structure, by balancing a material having a large tolerance factor with a material having a small tolerance factor, through solid-state alloying. They reported that the tolerance factor could be tuned by alloying the large-tolerance-factor $FAPbI_3$ and small-tolerance factor $CsPbI_3$ so that α-phase was stabilized in the mixed perovskite. High humidity can trigger the α-to-δH phase transition in $FAPbI_3$ films, but not in the Cs-doped $FA_{0.85}Cs_{0.15}PbI_3$ films, showing the importance of phase stability in $FAPbI_3$-based materials. Due to the stabilized structure, $FA_{0.85}Cs_{0.15}PbI_3$ alloy solar cells showed better performance and device stability against their $FAPbI_3$ counterparts.[43c] Fluorine (F) was introduced into the X-site of ABX_3 to modulate bulk-phase heterostructures and tolerance factors of inorganic $CsPbBrI_{2-x}F_x$ with significantly enhanced PCE and stability.[106]

Given the Goldschmidt tolerance factor, partial substitution of iodine by fluorine in the ABX_3 structure enlarges the low index to stabilize the a-$CsPbBrI_2$ structure. The $CsPbBrI_{1.78}F_{0.22}$ offered superior PCE of up to 10.26% and structural stability. It was also evidenced that $CsPbBrI_{1.5}F_5$ PSCs withstanding constant temperature and humidity retained 69.81% of the initial PCE after 10 days. For lead-free iodide perovskites, $MASnI_3$, $CsSnI_3$, $MASrI_3$, $MABiSI_2$, $MABi_{0.5}Tl_{0.5}I_3$, and $MACaI_3$ have been suggested to be promising candidates by first-principles calculation.[107]

Theoretical results indicated that both $MACaI_3$ and $MASrI_3$ form stable phases with similar formation energies and cell parameters compared to $MAPbI_3$.[107c] Wang et al. investigated the structural reconstruction by the first principle.[181] They calculated that phase stability diagrams concerning the chemical potentials of component elements showed that KO (001), O (110), and KO_2 (111) surface terminations possessed the largest stability domain, indicating that they were more likely to be formed compared with other surface terminations. McMeekin and Yi et al. mixed both cations and halides, delivering the possibility of long-term stability through first principle computations. The majority of blending-ion strategies abide by the tolerance factor within the range of 0.81–1.11. However, the structural stability is still affected by the volatile and hygroscopic nature.[43a, 106, 109] Marshenya et al. reported better structural stability, moderate thermal expansion and high conductivity for the using of $PrBaCo_{1.9}Al_{0.1}O_{6-\delta}$ cobaltite in various high-temperature solid state electrochemical devices.[110] **Table 1.2** illustrate the stability of perovskite solar cells with different tolerance factor.

Unlike traditional photoactive materials such as silicon, the organic-inorganic hybrid perovskite materials show significant ionic characteristics, which restricted the long-term stability of the perovskite materials, owing to the relatively low activation energy for ion migration within perovskite layer.[111] It has been observed that the ion diffusion will become severe when the device subjected to thermal stress, external electric bias or under the illumination.[112] For example, I^- ions will easily migrate through the polycrystalline PVSK grains and even out of the PVSK layer to interfere with the metal electrode, which generates defects which detrimentally function as non-radiative recombination sites at the grain boundaries.[113]

Tremendous strategies have been utilized to mitigate the ion migration to improve the long-term stability of the PSCs. Liao et al. incorporated graphitic carbon nitride into active layer to improve

the crystallinity perovskite layer and minimize the defect density further suppressed ion migration, an average PCE of 19.14% was achieved.[114] Yang et al. utilized phenylethyl ammonium iodide to stabilize the black phase pure $FAPbI_3$, the activation energy of ion migration determined by the temperature-dependent conductivity enhanced within the presence of 2D perovskite in the grain boundary compared with the bare $FAPbI_3$.[115] The suppression of ion diffusion ensured a PCE as high as 21.07% and an operational stability of 500 hours.

References

[1] a) S. N. Habisreutinger, T. Leijtens, G. E. Eperon, S. D. Stranks, R. J. Nicholas, H. J. Snaith, *Nano Lett* **2014**, 14, 5561; b) J. S. Shaikh, N. S. Shaikh, A. D. Sheikh, S. S. Mali, A. J. Kale, P. Kanjanaboos, C. K. Hong, J. H. Kim, P. S. Patil, *Materials & Design* **2017**, 136, 54.

[2] J. Yan, B. R. Saunders, *RSC Adv.* **2014**, 4, 43286.

[3] S. Gholipour, M. Saliba, *Small* **2018**, 14, e1802385.

[4] a) W. C. Chang, D. H. Lan, K. M. Lee, X. F. Wang, C. L. Liu, *Chemsuschem* **2017**, 10, 1405; b) Z. Liang, S. Zhang, X. Xu, N. Wang, J. Wang, X. Wang, Z. Bi, G. Xu, N. Yuan, J. Ding, *RSC Advances* **2015**, 5, 60562; c) D. K. Mohamad, J. Griffin, C. Bracher, A. T. Barrows, D. G. Lidzey, *Advanced Energy Materials* **2016**, 6, 1600994.

[5] a) J. Burschka, N. Pellet, S. J. Moon, R. Humphry-Baker, P. Gao, M. K. Nazeeruddin, M. Gratzel, *Nature* **2013**, 499, 316; b) L. Huang, C. Li, X. Sun, R. Xu, Y. Du, J. Ni, H. Cai, J. Li, Z. Hu, J. Zhang, *Organic Electronics* **2017**, 40, 13.

[6] Z. Xiao, C. Bi, Y. Shao, Q. Dong, Q. Wang, Y. Yuan, C. Wang, Y. Gao, J. Huang, *Energy Environ. Sci.* **2014**, 7, 2619.

[7] P. Luo, Z. Liu, W. Xia, C. Yuan, J. Cheng, Y. Lu, *Journal of Materials Chemistry A* **2015**, 3, 12443.

[8] M. R. Leyden, M. V. Lee, S. R. Raga, Y. Qi, *Journal of Materials Chemistry A* **2015**, 3, 16097.

[9] a) Z. Wei, H. Chen, K. Yan, S. Yang, *Angew Chem Int Ed Engl* **2014**, 53, 13239; b) M. M. Lee, J. Teuscher, T. Miyasaka, T. N. Murakami, H. J. Snaith, *Science* **2012**, 338, 643; c) S.-G. Li, K.-J. Jiang, M.-J. Su, X.-P. Cui, J.-H. Huang, Q.-Q. Zhang, X.-Q. Zhou, L.-M. Yang, Y.-L. Song, *Journal of Materials Chemistry A* **2015**, 3, 9092.

[10] a) K. Hwang, Y. S. Jung, Y. J. Heo, F. H. Scholes, S. E. Watkins, J. Subbiah, D. J. Jones, D. Y. Kim, D. Vak, *Adv Mater* **2015**, 27, 1241; b) S. Tang, Y. Deng, X. Zheng, Y. Bai, Y. Fang, Q. Dong, H. Wei, J. Huang, *Advanced Energy Materials* **2017**, 7, 1700302; c) M. Yang, Z. Li, M. O. Reese, O. G. Reid, D. H. Kim, S. Siol, T. R. Klein, Y. Yan, J. J. Berry, M. F. A. M. van Hest, K. Zhu, *Nature Energy* **2017**, 2, 17038.

[11] a) A. Mei, X. Li, L. Liu, Z. Ku, T. Liu, Y. Rong, M. Xu, M. Hu, J. Chen, Y. Yang, M. Gratzel, H. Han, *Science* **2014**, 345, 295; b) Z. Ku, Y. Rong, M. Xu, T. Liu, H. Han, *Sci Rep* **2013**, 3, 3132.

[12] Y. Liu, Z. Yang, D. Cui, X. Ren, J. Sun, X. Liu, J. Zhang, Q. Wei, H. Fan, F. Yu, X. Zhang, C. Zhao, S. F. Liu, *Adv Mater* **2015**, 27, 5176.

[13] T. Baikie, Y. Fang, J. M. Kadro, M. Schreyer, F. Wei, S. G. Mhaisalkar, M. Graetzel, T. J. White, *Journal of Materials Chemistry A* **2013**, 1, 5628.

[14] V. D'Innocenzo, G. Grancini, M. J. Alcocer, A. R. Kandada, S. D. Stranks, M. M. Lee, G. Lanzani, H. J. Snaith, A. Petrozza, *Nat Commun* **2014**, 5, 3586.

[15] J. R. Poindexter, R. L. Z. Hoye, L. Nienhaus, R. C. Kurchin, A. E. Morishige, E. E. Looney, A. Osherov, J. P. Correa-Baena, B. Lai, V. Bulovic, V. Stevanovic, M. G. Bawendi, T. Buonassisi, *ACS Nano* **2017**, 11, 7101.

[16] E. Klampaftis, B. S. Richards, *Progress in Photovoltaics: Research and Applications* **2011**, 19, 345.

[17] a) Y. Yang, J. Wu, T. Wu, Z. Xu, X. Liu, Q. Guo, X. He, *J Colloid Interface Sci* **2018**, 531, 602; b) L. J. Zuo, H. X. Guo, D. W. deQuilettes, S. Jariwala, N. De Marco, S. Q. Dong, R. DeBlock, D. S. Ginger, B. Dunn, M. K. Wang, Y. Yang, *Sci Adv* **2017**, 3; c) X. Zheng, Z. Wei, H. Chen, Y. Bai, S. Xiao, T. Zhang, S. Yang, *Journal of Energy Chemistry* **2015**, 24, 736; d) P. W. Liang, C. Y. Liao, C. C. Chueh, F. Zuo, S. T. Williams, X. K. Xin, J. Lin, A. K. Jen, *Adv Mater* **2014**, 26, 3748.

[18] a) M. A. Green, K. Emery, Y. Hishikawa, W. Warta, E. D. Dunlop, *Progress in Photovoltaics: Research and Applications* **2015**, 23, 1; b) M. G. Brain O, *Nature* **1991**, 353.

[19] D. L. U. Bach*, P. Comte*, J. E. Moser*, F.Weisso¨ rtel§, J. Salbeck§, H. Spreitzer†&M. Gra¨ tzel*.

[20] a) J. Krüger, R. Plass, L. Cevey, M. Piccirelli, M. Grätzel, U. Bach, *Applied Physics Letters* **2001**, 79, 2085; b) J. Krüger, R. Plass, M. Grätzel, H.-J. Matthieu, *Applied Physics Letters* **2002**, 81, 367; c) L. Schmidt-Mende, S. M. Zakeeruddin, M. Grätzel, *Applied Physics Letters* **2005**, 86, 013504; d) H. J. Snaith, R. Humphry-Baker, P. Chen, I. Cesar, S. M. Zakeeruddin, M. Gratzel, *Nanotechnology* **2008**, 19, 424003.

[21] H. S. Kim, C. R. Lee, J. H. Im, K. B. Lee, T. Moehl, A. Marchioro, S. J. Moon, R. Humphry-Baker, J. H. Yum, J. E. Moser, M. Gratzel, N. G. Park, *Sci Rep* **2012**, 2, 591.

[22] L. Etgar, P. Gao, Z. Xue, Q. Peng, A. K. Chandiran, B. Liu, M. K. Nazeeruddin, M. Gratzel, *J Am Chem Soc* **2012**, 134, 17396.

[23] J. M. Ball, M. M. Lee, A. Hey, H. J. Snaith, *Energy & Environmental Science* **2013**, 6, 1739.

[24] a) W. S. Yang, J. H. Noh, N. J. Jeon, Y. C. Kim, S. Ryu, J. Seo, S. I. Seok, *Science* **2015**, 348, 1234; b) N. J. Jeon, J. H. Noh, W. S. Yang, Y. C. Kim, S. Ryu, J. Seo, S. I. Seok, *Nature* **2015**, 517, 476.

[25] M. Li, C. Zhao, Z.-K. Wang, C.-C. Zhang, H. K. H. Lee, A. Pockett, J. Barbé, W. C. Tsoi, Y.-G. Yang, M. J. Carnie, X.-Y. Gao, W.-X. Yang, J. R. Durrant, L.-S. Liao, S. M. Jain, *Advanced Energy Materials* **2018**, 8, 1801509.

[26] S. R. Raga, M.-C. Jung, M. V. Lee, M. R. Leyden, Y. Kato, Y. Qi, *Chemistry of Materials* **2015**, 27, 1597.

[27] J. A. Christians, P. A. Miranda Herrera, P. V. Kamat, *J Am Chem Soc* **2015**, 137, 1530.

[28] H. P. Zhou, Q. Chen, G. Li, S. Luo, T. B. Song, H. S. Duan, Z. R. Hong, J. B. You, Y. S. Liu, Y. Yang, *Science* **2014**, 345, 542.

[29] K. K. Bass, R. E. McAnally, S. Zhou, P. I. Djurovich, M. E. Thompson, B. C. Melot, *Chem Commun (Camb)* **2014**, 50, 15819.

[30] W. Li, J. Fan, Y. Mai, L. Wang, *Advanced Energy Materials* **2017**, 7, 1601433.

[31] P. Rajput, G. N. Tiwari, O. S. Sastry, B. Bora, V. Sharma, *Solar Energy* **2016**, 135, 786.

[32] a) M. Liu, M. B. Johnston, H. J. Snaith, *Nature* **2013**, 501, 395; b) Q. Fu, X. Tang, B. Huang, T. Hu, L. Tan, L. Chen, Y. Chen, *Adv Sci (Weinh)* **2018**, 5, 1700387; c) D. Wang, M. Wright, N. K. Elumalai, A. Uddin, *Solar Energy Materials and Solar Cells* **2016**, 147, 255.

[33] K. Aitola, K. Domanski, J. P. Correa-Baena, K. Sveinbjornsson, M. Saliba, A. Abate, M. Gratzel, E. Kauppinen, E. M. J. Johansson, W. Tress, A. Hagfeldt, G. Boschloo, *Adv Mater* **2017**, 29.

[34] a) G. Niu, W. Li, F. Meng, L. Wang, H. Dong, Y. Qiu, *J. Mater. Chem. A* **2014**, 2, 705; b) S. Ito, S. Tanaka, K. Manabe, H. Nishino, *The Journal of Physical Chemistry C* **2014**, 118, 16995; c) W. Li, H. Dong, L. Wang, N. Li, X. Guo, J. Li, Y. Qiu, *J. Mater. Chem. A* **2014**, 2, 13587; d) M. Zhang, S. Dai, S. Chandrabose, K. Chen, K. Liu, M. Qin, X. Lu, J. M. Hodgkiss, H. Zhou, X. Zhan, *J Am Chem Soc* **2018**, 140, 14938; e) M. Qin, J. Cao, T. Zhang, J. Mai, T.-K. Lau, S. Zhou, Y. Zhou, J. Wang, Y.-J. Hsu, N. Zhao, J. Xu, X. Zhan, X. Lu, *Advanced Energy Materials* **2018**, 8, 1703399.

[35] J. L. Yang, B. D. Siempelkamp, D. Y. Liu, T. L. Kelly, *Acs Nano* **2015**, 9, 1955.

[36] B. Conings, J. Drijkoningen, N. Gauquelin, A. Babayigit, J. D'Haen, L. D'Olieslaeger, A. Ethirajan, J. Verbeeck, J. Manca, E. Mosconi, F. D. Angelis, H.-G. Boyen, *Advanced Energy Materials* **2015**, 5, 1500477.

[37] Y. Chen, Y. Sun, J. Peng, J. Tang, K. Zheng, Z. Liang, *Adv Mater* **2018**, 30.

[38] a) B. Brunetti, C. Cavallo, A. Ciccioli, G. Gigli, A. Latini, *Sci Rep* **2016**, 6, 31896; b) H. Cho, Y. H. Kim, C. Wolf, H. D. Lee, T. W. Lee, *Adv Mater* **2018**, DOI: 10.1002/adma.201704587.

[39] B. Roose, K. C. Gödel, S. Pathak, A. Sadhanala, J. P. C. Baena, B. D. Wilts, H. J. Snaith, U. Wiesner, M. Grätzel, U. Steiner, A. Abate, *Advanced Energy Materials* **2016**, 6, 1501868.

[40] Y. S. Kwon, J. Lim, H.-J. Yun, Y.-H. Kim, T. Park, *Energy & Environmental Science* **2014**, 7, 1454.

[41] B. Philippe, B.-W. Park, R. Lindblad, J. Oscarsson, S. Ahmadi, E. M. J. Johansson, H. Rensmo, *Chemistry of Materials* **2015**, 27, 1720.

[42] G. Niu, X. Guo, L. Wang, *Journal of Materials Chemistry A* **2015**, 3, 8970.

[43] a) C. Yi, J. Luo, S. Meloni, A. Boziki, N. Ashari-Astani, C. Grätzel, S. M. Zakeeruddin, U. Röthlisberger, M. Grätzel, *Energy & Environmental Science* **2016**, 9, 656; b) D. Q. Bi, W. Tress, M. I. Dar, P. Gao, J. S. Luo, C. Renevier, K. Schenk, A. Abate, F. Giordano, J. P. C. Baena, J. D. Decoppet, S. M. Zakeeruddin, M. K. Nazeeruddin, M. Gratzel, A. Hagfeldt, *Sci Adv* **2016**, 2; c) Z. Li, M. Yang, J.-S. Park, S.-H. Wei, J. J. Berry, K. Zhu, *Chemistry of Materials* **2015**, 28, 284.

[44] G. E. Eperon, S. N. Habisreutinger, T. Leijtens, B. J. Bruijnaers, J. J. van Franeker, D. W. Dequilettes, S. Pathak, R. J. Sutton, G. Grancini, D. S. Ginger, R. A. J. Janssen, A. Petrozza, H. J. Snaith, *Acs Nano* **2015**, 9, 9380.

[45] a) A. M. A. Leguy, Y. Hu, M. Campoy-Quiles, M. I. Alonso, O. J. Weber, P. Azarhoosh, M. van Schilfgaarde, M. T. Weller, T. Bein, J. Nelson, P. Docampo, P. R. F. Barnes, *Chemistry of Materials* **2015**, 27, 3397; b) P. Docampo, T. Bein, *Acc Chem Res* **2016**, 49, 339.

[46] a) A. R. b. M. Yusoff, M. K. Nazeeruddin, *Advanced Energy Materials* **2018**, 8, 1702073; b) Y. Guo, K. Shoyama, W. Sato, Y. Matsuo, K. Inoue, K. Harano, C. Liu, H. Tanaka, E. Nakamura, *J Am Chem Soc* **2015**, 137, 15907; c) A. Wakamiya, M. Endo, T. Sasamori, N. Tokitoh, Y. Ogomi, S. Hayase, Y. Murata, *Chemistry Letters* **2014**, 43, 711.

[47] T. M. Koh, V. Shanmugam, J. Schlipf, L. Oesinghaus, P. Muller-Buschbaum, N. Ramakrishnan, V. Swamy, N. Mathews, P. P. Boix, S. G. Mhaisalkar, *Adv Mater* **2016**, 28, 3653.

[48] D. H. Cao, C. C. Stoumpos, O. K. Farha, J. T. Hupp, M. G. Kanatzidis, *J Am Chem Soc* **2015**, 137, 7843.

[49] H. Tsai, W. Nie, J. C. Blancon, C. C. Stoumpos, R. Asadpour, B. Harutyunyan, A. J. Neukirch, R. Verduzco, J. J. Crochet, S. Tretiak, L. Pedesseau, J. Even, M. A. Alam, G. Gupta, J. Lou, P. M. Ajayan, M. J. Bedzyk, M. G. Kanatzidis, *Nature* **2016**, 536, 312.

[50] a) B. Kundys, A. Lappas, M. Viret, V. Kapustianyk, V. Rudyk, S. Semak, C. Simon, I. Bakaimi, *Physical Review B* **2010**, 81; b) K. Pradeesh, J. J. Baumberg, G. V. Prakash, *Applied Physics Letters* **2009**, 95, 173305.

[51] H. Zheng, G. Liu, L. Zhu, J. Ye, X. Zhang, A. Alsaedi, T. Hayat, X. Pan, S. Dai, *Advanced Energy Materials* **2018**, 8, 1800051.

[52] a) M. I. D. Taiyang Zhang, Ge Li, Feng Xu, Nanjie Guo, Michael Grätzel, Yixin Zhao, *Sci Adv* **2017**, DOI: 10.1126/sciadv.1700841; b) S. Shao, J. Liu, G. Portale, H.-H. Fang, G. R. Blake, G. H. ten Brink, L. J. A. Koster, M. A. Loi, *Advanced Energy Materials* **2018**, 8, 1702019; c) Z. Wang, Q. Lin, F. P. Chmiel, N. Sakai, L. M. Herz, H. J. Snaith, *Nature Energy* **2017**, 2, 17135; d) G. Grancini, C. Roldan-Carmona, I. Zimmermann, E. Mosconi, X. Lee, D. Martineau, S. Narbey, F. Oswald, F. De Angelis, M. Graetzel, M. K. Nazeeruddin, *Nat Commun* **2017**, 8, 15684.

[53] D.-Y. Son, J.-W. Lee, Y. J. Choi, I.-H. Jang, S. Lee, P. J. Yoo, H. Shin, N. Ahn, M. Choi, D. Kim, N.-G. Park, *Nature Energy* **2016**, 1.

[54] N. Li, Z. Zhu, C.-C. Chueh, H. Liu, B. Peng, A. Petrone, X. Li, L. Wang, A. K. Y. Jen, *Advanced Energy Materials* **2017**, 7, 1601307.

[55] J. Fan, Y. Ma, C. Zhang, C. Liu, W. Li, R. E. I. Schropp, Y. Mai, *Advanced Energy Materials* **2018**, 8, 1703421.

[56] a) J. C. Blancon, H. Tsai, W. Nie, C. C. Stoumpos, L. Pedesseau, C. Katan, M. Kepenekian, C. M. M. Soe, K. Appavoo, M. Y. Sfeir, S. Tretiak, P. M. Ajayan, M. G. Kanatzidis, J. Even, J. J. Crochet, A. D. Mohite, *Science* **2017**, 355, 1288; b) Y. Chen, Y. Sun, J. Peng, W. Zhang, X. Su, K. Zheng, T. Pullerits, Z. Liang, *Advanced Energy Materials* **2017**, 7, 1700162; c) C. C. Stoumpos, C. M. M. Soe, H. Tsai, W. Nie, J.-C. Blancon, D. H. Cao, F. Liu, B. Traoré, C. Katan, J. Even, A. D. Mohite, M. G. Kanatzidis, *Chem* **2017**, 2, 427.

[57] J. Cao, C. Li, X. Lv, X. Feng, R. Meng, Y. Wu, Y. Tang, *J Am Chem Soc* **2018**, 140, 11577.

[58] X. Yu, H. Yan, Q. Peng, *ACS Appl Mater Interfaces* **2018**, 10, 28948.

[59] T. Leijtens, G. E. Eperon, S. Pathak, A. Abate, M. M. Lee, H. J. Snaith, *Nat Commun* **2013**, 4, 2885.

[60] B. McKenna, J. R. Troughton, T. M. Watson, R. C. Evans, *RSC Advances* **2017**, 7, 32942.

[61] J. You, Y. Yang, Z. Hong, T.-B. Song, L. Meng, Y. Liu, C. Jiang, H. Zhou, W.-H. Chang, G. Li, Y. Yang, *Applied Physics Letters* **2014**, 105, 183902.

[62] H. Wei, Y. Fang, P. Mulligan, W. Chuirazzi, H.-H. Fang, C. Wang, B. R. Ecker, Y. Gao, M. A. Loi, L. Cao, J. Huang, *Nature Photonics* **2016**, 10, 333.

[63] Z. Wang, D. P. McMeekin, N. Sakai, S. van Reenen, K. Wojciechowski, J. B. Patel, M. B. Johnston, H. J. Snaith, *Adv Mater* **2017**, 29.

[64] J. Chen, L. Zuo, Y. Zhang, X. Lian, W. Fu, J. Yan, J. Li, G. Wu, C.-Z. Li, H. Chen, *Advanced Energy Materials* **2018**, 8, 1800438.

[65] a) M. Jørgensen, K. Norrman, F. C. Krebs, *Solar Energy Materials and Solar Cells* **2008**, 92, 686; b) A. Hinsch, J. M. Kroon, R. Kern, I. Uhlendorf, J. Holzbock, A. Meyer, J. Ferber, *Prog Photovoltaics* **2001**, 9, 425.

[66] N. Aristidou, I. Sanchez-Molina, T. Chotchuangchutchaval, M. Brown, L. Martinez, T. Rath, S. A. Haque, *Angew Chem Int Ed Engl* **2015**, 54, 8208.

[67] D. Bryant, N. Aristidou, S. Pont, I. Sanchez-Molina, T. Chotchunangatchaval, S. Wheeler, J. R. Durrant, S. A. Haque, *Energy & Environmental Science* **2016**, 9, 1655.

[68] B. Salhi, Y. S. Wudil, M. K. Hossain, A. Al-Ahmed, F. A. Al-Sulaiman, *Renewable and Sustainable Energy Reviews* **2018**, 90, 210.

[69] S. H. Turren-Cruz, A. Hagfeldt, M. Saliba, *Science* **2018**, 362, 449.

[70] N. Arora, M. I. Dar, A. Hinderhofer, N. Pellet, F. Schreiber, S. M. Zakeeruddin, M. Gratzel, *Science* **2017**, 358, 768.

[71] J. Wang, Y. Chen, M. Liang, G. Ge, R. Zhou, Z. Sun, S. Xue, *Dyes and Pigments* **2016**, 125, 399.

[72] a) Y.-Y. Zheng, G. Wu, M. Deng, H.-Z. Chen, M. Wang, B.-Z. Tang, *Thin Solid Films* **2006**, 514, 127; b) C. Ran, J. Xu, W. Gao, C. Huang, S. Dou, *Chem Soc Rev* **2018**, 47, 4581; c) N. Ahn, K. Kwak, M. S. Jang, H. Yoon, B. Y. Lee, J. K. Lee, P. V. Pikhitsa, J. Byun, M. Choi, *Nat Commun* **2016**, 7, 13422; d) X. Zheng, B. Chen, J. Dai, Y. Fang, Y. Bai, Y. Lin, H. Wei, Xiao C. Zeng, J. Huang, *Nature Energy* **2017**, 2, 17102; e) Q. Wang, B. Chen, Y. Liu, Y. Deng, Y. Bai, Q. Dong, J. Huang, *Energy & Environmental Science* **2017**, 10, 516.

[73] S. Huang, Z. Li, L. Kong, N. Zhu, A. Shan, L. Li, *J Am Chem Soc* **2016**, 138, 5749.

[74] Y. Rong, L. Liu, A. Mei, X. Li, H. Han, *Advanced Energy Materials* **2015**, 5, 1501066.

[75] H. S. Kim, J. Y. Seo, N. G. Park, *Chemsuschem* **2016**, 9, 2528.

[76] T. Supasai, N. Rujisamphan, K. Ullrich, A. Chemseddine, T. Dittrich, *Applied Physics Letters* **2013**, 103, 183906.

[77] a) H. B. Kim, I. Im, Y. Yoon, S. D. Sung, E. Kim, J. Kim, W. I. Lee, *Journal of Materials Chemistry A* **2015**, 3, 9264; b) H. S. Rao, B. X. Chen, X. D. Wang, D. B. Kuang, C. Y. Su, *Chem Commun (Camb)* **2017**, 53, 5163.

[78] S. Aharon, B. E. Cohen, L. Etgar, *The Journal of Physical Chemistry C* **2014**, 118, 17160.

[79] T. A. Berhe, W.-N. Su, C.-H. Chen, C.-J. Pan, J.-H. Cheng, H.-M. Chen, M.-C. Tsai, L.-Y. Chen, A. A. Dubale, B.-J. Hwang, *Energy & Environmental Science* **2016**, 9, 323.

[80] A. Binek, F. C. Hanusch, P. Docampo, T. Bein, *J Phys Chem Lett* **2015**, 6, 1249.

[81] a) Y. Fu, H. Zhu, A. W. Schrader, D. Liang, Q. Ding, P. Joshi, L. Hwang, X. Y. Zhu, S. Jin, *Nano Lett* **2016**, 16, 1000; b) Z. Wang, Z. Shi, T. Li, Y. Chen, W. Huang, *Angew Chem Int Ed Engl* **2017**, 56, 1190.

[82] J. W. Lee, D. J. Seol, A. N. Cho, N. G. Park, *Adv Mater* **2014**, 26, 4991.

[83] K. A. Bush, A. F. Palmstrom, Z. J. Yu, M. Boccard, R. Cheacharoen, J. P. Mailoa, D. P. McMeekin, R. L. Z. Hoye, C. D. Bailie, T. Leijtens, I. M. Peters, M. C. Minichetti, N. Rolston, R. Prasanna, S. Sofia, D. Harwood, W. Ma, F. Moghadam, H. J. Snaith, T. Buonassisi, Z. C. Holman, S. F. Bent, M. D. McGehee, *Nature Energy* **2017**, 2, 17009.

[84] X. Liu, N. Zhang, B. Tang, M. Li, Y. W. Zhang, Z. G. Yu, H. Gong, *J Phys Chem Lett* **2018**, DOI: 10.1021/acs.jpclett.8b025245862.

[85] Y. Dang, Y. Liu, Y. Sun, D. Yuan, X. Liu, W. Lu, G. Liu, H. Xia, X. Tao, *CrystEngComm* **2015**, 17, 665.

[86] L. Dou, *Journal of Materials Chemistry C* **2017**, 5, 11165.

[87] H. Zheng, G. Liu, X. Xu, A. Alsaedi, T. Hayat, X. Pan, S. Dai, *ChemSusChem* **2018**, 11, 3269.

[88] H. Matsui, K. Okada, T. Kitamura, N. Tanabe, *Solar Energy Materials and Solar Cells* **2009**, 93, 1110.

[89] S. A. Gevorgyan, A. J. Medford, E. Bundgaard, S. B. Sapkota, H.-F. Schleiermacher, B. Zimmermann, U. Würfel, A. Chafiq, M. Lira-Cantu, T. Swonke, M. Wagner, C. J. Brabec, O. Haillant, E. Voroshazi, T. Aernouts, R. Steim, J. A. Hauch, A. Elschner, M. Pannone, M. Xiao, A. Langzettel, D. Laird, M. T. Lloyd, T. Rath, E. Maier, G. Trimmel, M. Hermenau, T. Menke, K. Leo, R. Rösch, M. Seeland, H. Hoppe, T. J. Nagle, K. B. Burke, C. J. Fell, D. Vak, T. B. Singh, S. E. Watkins, Y. Galagan, A. Manor, E. A. Katz, T. Kim, K. Kim, P. M. Sommeling, W. J. H. Verhees, S. C. Veenstra, M. Riede, M. Greyson Christoforo, T. Currier, V. Shrotriya, G. Schwartz, F. C. Krebs, *Solar Energy Materials and Solar Cells* **2011**, 95, 1398.

[90] a) R. Roesch, T. Faber, E. von Hauff, T. M. Brown, M. Lira-Cantu, H. Hoppe, *Advanced Energy Materials* **2015**, 5, 1501407; b) A. Fakharuddin, F. Di Giacomo, A. L. Palma, F. Matteocci, I. Ahmed, S. Razza, A. D'Epifanio, S. Licoccia, J. Ismail, A. Di Carlo, T. M. Brown, R. Jose, *Acs Nano* **2015**, 9, 8420.

[91] K. Leo, *Nat Nanotechnol* **2015**, 10, 574.

[92] M. Kulbak, D. Cahen, G. Hodes, *J Phys Chem Lett* **2015**, 6, 2452.

[93] H. Choi, J. Jeong, H.-B. Kim, S. Kim, B. Walker, G.-H. Kim, J. Y. Kim, *Nano Energy* **2014**, 7, 80.

[94] C. C. Stoumpos, C. D. Malliakas, M. G. Kanatzidis, *Inorg Chem* **2013**, 52, 9019.

[95] Von V. !VI. GOLDSCHMIDT, **1926**.

[96] A. Amat, E. Mosconi, E. Ronca, C. Quarti, P. Umari, M. K. Nazeeruddin, M. Gratzel, F. De Angelis, *Nano Lett* **2014**, 14, 3608.

[97] a) C. C. Stoumpos, M. G. Kanatzidis, *Acc Chem Res* **2015**, 48, 2791; b) G. Kieslich, S. Sun, A. K. Cheetham, *Chem. Sci.* **2014**, 5, 4712.

[98] A. Poglitsch, D. Weber, *The Journal of Chemical Physics* **1987**, 87, 6373.

[99] G. E. Eperon, S. D. Stranks, C. Menelaou, M. B. Johnston, L. M. Herz, H. J. Snaith, *Energy & Environmental Science* **2014**, 7, 982.

[100] J. Xue, J.-W. Lee, Z. Dai, R. Wang, S. Nuryyeva, M. E. Liao, S.-Y. Chang, L. Meng, D. Meng, P. Sun, O. Lin, M. S. Goorsky, Y. Yang, *Joule* **2018**, 2, 1866.

[101] M. Saliba, T. Matsui, K. Domanski, J. Y. Seo, A. Ummadisingu, S. M. Zakeeruddin, J. P. Correa-Baena, W. R. Tress, A. Abate, A. Hagfeldt, M. Gratzel, *Science* **2016**, 354, 206.

[102] G. Liu, H. Zheng, X. Xu, L.-Z. Zhu, X. Zhang, X. Pan, *Chemistry of Materials* **2018**, 30, 7691.

[103] L. N. Quan, M. Yuan, R. Comin, O. Voznyy, E. M. Beauregard, S. Hoogland, A. Buin, A. R. Kirmani, K. Zhao, A. Amassian, D. H. Kim, E. H. Sargent, *J Am Chem Soc* **2016**, 138, 2649.

[104] K. Yamamoto, S. Iikubo, J. Yamasaki, Y. Ogomi, S. Hayase, *The Journal of Physical Chemistry C* **2017**, 121, 27797.

[105] M. R. Filip, G. E. Eperon, H. J. Snaith, F. Giustino, *Nat Commun* **2014**, 5, 5757.

[106] L. Fu, Y. Zhang, B. Chang, B. Li, S. Zhou, L. Zhang, L. Yin, *Journal of Materials Chemistry A* **2018**, 6, 13263.

[107] a) C. Bernal, K. Yang, *The Journal of Physical Chemistry C* **2014**, 118, 24383; b) P. Xu, S. Chen, H.-J. Xiang, X.-G. Gong, S.-H. Wei, *Chemistry of Materials* **2014**, 26, 6068; c) T. J. Jacobsson, M. Pazoki, A. Hagfeldt, T. Edvinsson, *The Journal of Physical Chemistry C* **2015**, 119, 25673; d) Y. Y. Sun, J. Shi, J. Lian, W. Gao, M. L. Agiorgousis, P. Zhang, S. Zhang, *Nanoscale* **2016**, 8, 6284.

[108] Y. Wang, J. Cheng, M. Behtash, W. Tang, J. Luo, K. Yang, *Physical Chemistry Chemical Physics* **2018**, 20, 18515.

[109] D. P. McMeekin, G. Sadoughi, W. Rehman, G. E. Eperon, M. Saliba, M. T. Horantner, A. Haghighirad, N. Sakai, L. Korte, B. Rech, M. B. Johnston, L. M. Herz, H. J. Snaith, *Science* **2016**, 351, 151.

[110] S. N. Marshenya, B. V. Politov, A. Y. Suntsov, I. A. Leonidov, S. A. Petrova, M. V. Patrakeev, V. L. Kozhevnikov, *Journal of Alloys and Compounds* **2018**, 767, 1041.

[111] E. Bi, H. Chen, F. Xie, Y. Wu, W. Chen, Y. Su, A. Islam, M. Gratzel, X. Yang, L. Han, *Nat Commun* **2017**, 8, 15330.

[112] L. Liu, S. Huang, Y. Lu, P. Liu, Y. Zhao, C. Shi, S. Zhang, J. Wu, H. Zhong, M. Sui, H. Zhou, H. Jin, Y. Li, Q. Chen, *Adv Mater* **2018**, DOI: 10.1002/adma.201800544e1800544.

[113] Z. Li, C. Xiao, Y. Yang, S. P. Harvey, D. H. Kim, J. A. Christians, M. Yang, P. Schulz, S. U. Nanayakkara, C.-S. Jiang, J. M. Luther, J. J. Berry, M. C. Beard, M. M. Al-Jassim, K. Zhu, *Energy & Environmental Science* **2017**, 10, 1234.

[114] L.-L. Jiang, Z.-K. Wang, M. Li, C.-C. Zhang, Q.-Q. Ye, K.-H. Hu, D.-Z. Lu, P.-F. Fang, L.-S. Liao, *Advanced Functional Materials* **2018**, 28, 1705875.

[115] J. W. Lee, Z. Dai, T. H. Han, C. Choi, S. Y. Chang, S. J. Lee, N. De Marco, H. Zhao, P. Sun, Y. Huang, Y. Yang, *Nat Commun* **2018**, 9, 3021.

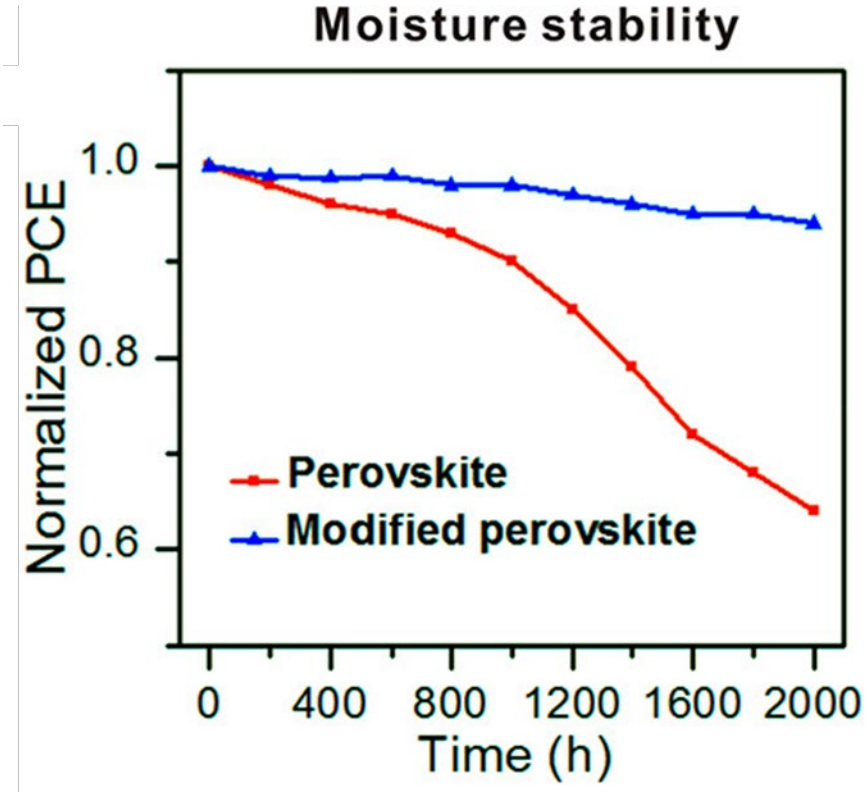

Figure 1.1. Moisture stability measured with a humidity of 45%.

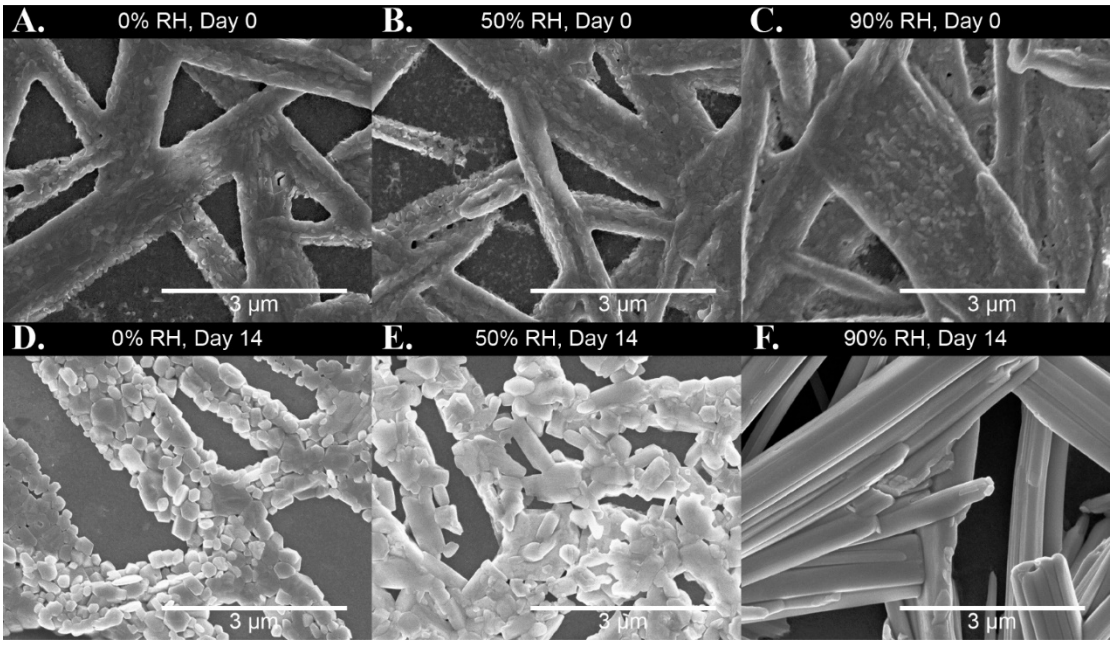

Figure 1.2. Top-down scanning electron micrographs of films stored in 0%, 50%, and 90% RH for 14 days.

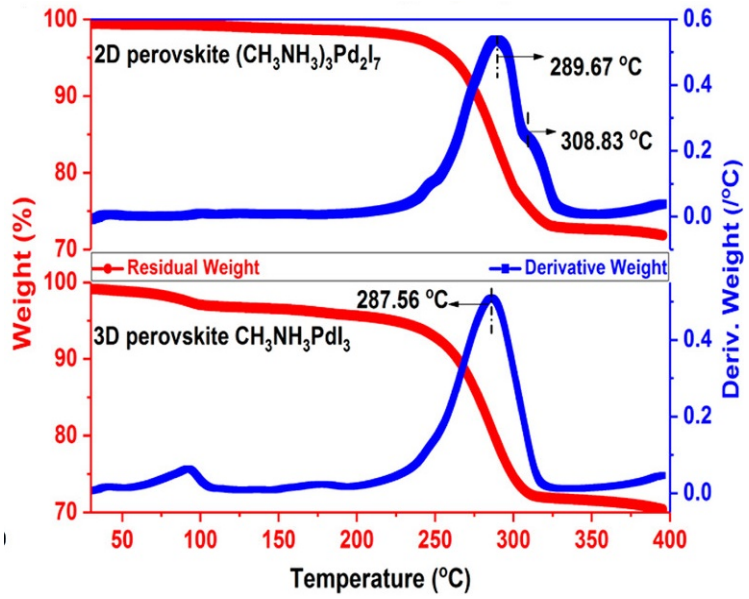

Figure 1.3. TGA curves of the 3D perovskite and the 2D perovskite.

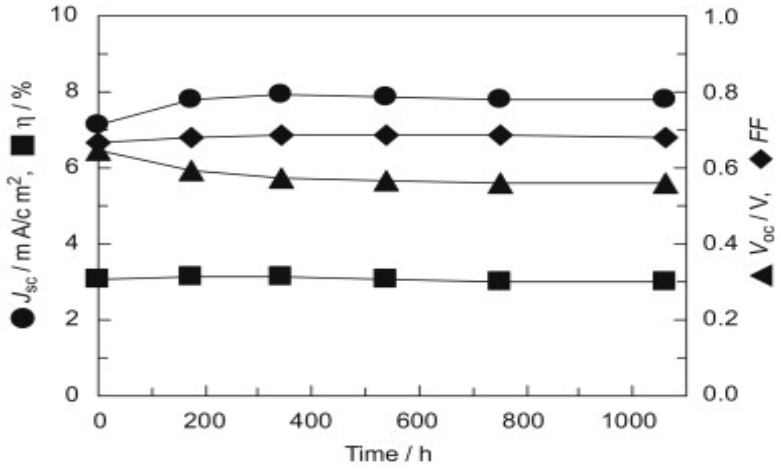

Figure 1.4. Example of stability tests for the best encapsulated DSCs during a thermal stress test (1000h @ 85 °C, 85% RH)

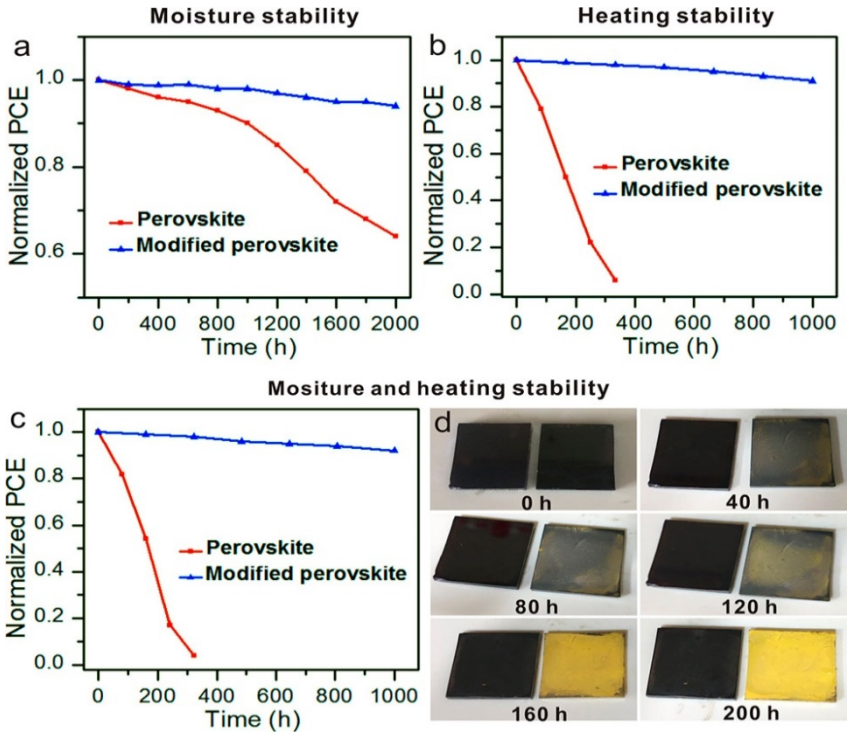

Figure 1.5. (a) Moisture stability measured with a humidity of 45%. (b) Heating stability measured at 85 °C in the N_2 environment. (c) Moisture and heating stability tested at 85 °C with a humidity of 45%. (d) The photos of perovskite films with (left) and without (right) modification stored at 85 °C with a humidity of 45% with different time.

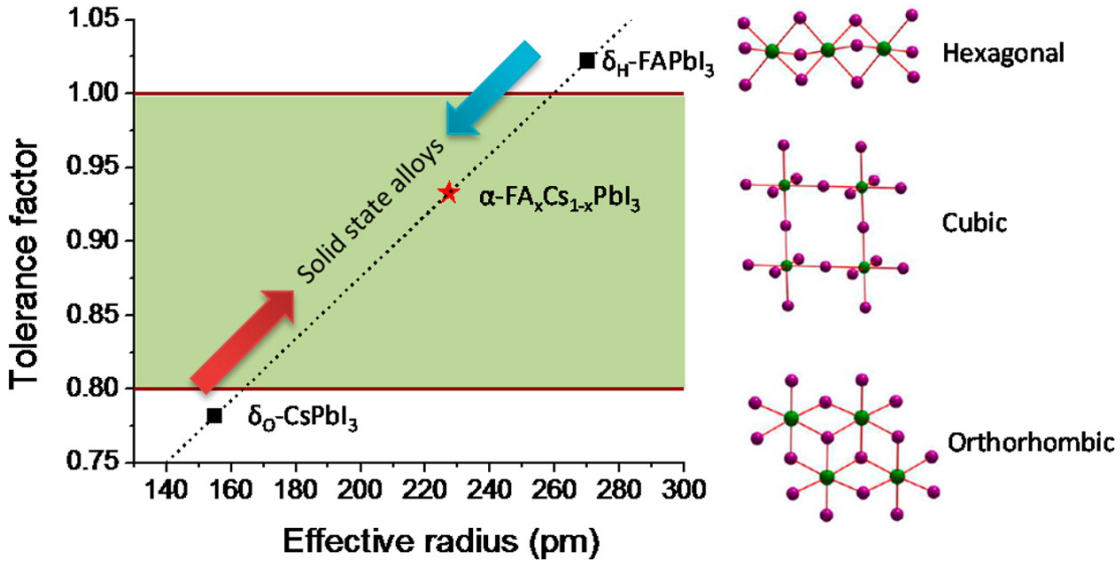

Figure 1.6. Correlations between tolerance factor and crystal structure of perovskite materials.

Device configuration	Test conditions	Stability
FTO/c-TiO_2/meso-TiO_2/$MAPbI_{3-x}Br_x$/Spiro-OMeTAD/Ag	R.H. ≈40%	14 d, 93% PCE remained
FTO/c-TiO_2/meso-TiO_2/$MAPbI_3$/Spiro-OMeTAD/Au	R.H.≈24±2%	7 d, 16% PCE remained
ITO/PEDOT:PSS/$MAPbI_3$/$PC_{61}BM$/Al	R.H. 30–50%	5 d, 0% PCE remained
FTO/c-TiO_2/meso-TiO_2/$MAPbI_3$/Spiro-OMeTAD/Au	R.H. 60%	18 h, 20% PCE remained
ITO/PEDOT:PSS/$MAPbI_{3-x}Cl_x$/$PC_{61}BM$/Ag	Under Ambient conditions	275 min, 0% PCE remained

Table 1.1. PSCs performance under moisture exposure

Materials	Tolerance factor	PCE	Stability
$Cs_x(MA_{0.17}FA_{0.83})_{(1-x)}$ $Pb(I_{0.83}Br_{0.17})_3$	0.911	21.1%	85% for 250 h
$MAPb(I_{1-x}Br_x)_3$	0.919	12.3%	stable for 480 h, 55% humidity
$MAPb(I_{1-x}Br_x)_{3-y}Cl_y$	0.925	11.1%	80% for 720 h
$MAPbI_{3-x}(SCN)_x$	0.834	15.1%	85% for 500 h, 70% humidity
$FAPbI_3$	0.987	16.0%	Thermally stable at 230°C, light stable in humid conditions

Table 1.2. Stability of perovskite solar cell with a different tolerance factor

Chapter 2 Caffeine Improves the Performance and Thermal Stability of Perovskite Solar Cells

Organic-inorganic hybrid halide perovskite (PVSK) materials have attracted considerable attention due to their unique photoelectric properties which can be applied to an extensive variety of applications.[1–6] Particularly, PVSK materials have been applied to photovoltaics with promising results and have shown rapid development.[7–11] Within only a few years, the power conversion efficiency (PCE) of PVSK solar cells has been enhanced from 3.8% to 23.3%.[12–15] Despite the tremendous achievements that have been made towards pushing the efficiency, long-term stability is still the challenge for the commercialization of PVSK solar cells.[16–21] Specifically, the black phase of Cesium (Cs)- and Formamidinium (FA)-based PVSKs are thermodynamically unfavorable at room temperature,[22,23] such that Methylammonium (MA)-based PVSK may be the ideal candidate for the commercialization of PVSK solar cells, since the tetragonal black phase of MA PVSKs are stable at low temperatures.[24] However, the intrinsically volatile nature of the MA organic cation will lead to the rapid decomposition of PVSK and precipitate trigonal PbI_2 at elevated temperatures.[25,26] In the meantime, there are numerous under-coordinated ions in the PVSK as is common in most ionic crystal.[27] For example, I^- ions will easily migrate through the polycrystalline PVSK grains and even out of the PVSK layer to interfere with the metal electrode when exposed to thermal energy.[28] This generates defects which detrimentally function as non-radiative recombination sites at the grain boundaries.[29] Also, the randomly oriented PVSK crystallites may result in poor charge transport in the vertical direction, a consequence of the fast and uncontrollable growth process of the PVSK film.[30,31]

To date, most reported strategies to realize remarkable thermal stability focused on the device architectures.[3233] Park et al. included atomic layer deposition (ALD) aluminum doped zinc oxide,

achieved 500 hours thermal stability at 85°C in air.[34] Seo et al. utilized a novel fluorene-terminated hole transporting materials realizing 500 hours of stability at 85°C in air.[35] Impressed stability has also been shown in architectures that are "hole-conductor free", made by infiltrating porous layers of carbon, ZrO_2, and TiO_2.[36] Studies focus on improving the quality of PVSK layer itself to overcome these demerits.[37,38] Increasing the activation energy for thermal decomposition of the PVSK film is significant to prolong the long-term thermal stability of PVSK solar cells.

On the other hand, many attempts have been made to obtain high-quality PVSK films that mitigate these challenges by utilizing various specific functional group which can interact with PVSK. Park et.al, introduced dimethyl sulfoxide (DMSO) with S=O group to retard the crystal growth via the Lewis base-acid adduct method.[39] Han et. al introduced PCBM to eliminate Pb-I defects by forming fullerene-halide radicals.[40] Niu et.al utilized conjugated small molecule with carboxyl and cyano group to passivate grain boundaries.[41] There are also several studies that incorporated volatile or non-volatile small molecules or polymer additives with similar functional groups to passivate the trap defects and improve the device performance.[42–45] However, it remains difficult to slow down the crystal growth and control the orientated crystals for the purpose of simultaneously boosting the device PCE and long-term stability without sacrificing its electronic properties.[46]

Herein, we introduced a small molecule 1,3,7-Trimethylxanthine (**Figure 2.1a**), popularly known as caffeine, into the MA-based PVSK. By utilizing the carboxyl groups in the different chemistry environment,[47] caffeine served as a "molecular lock" that interacted strongly with Pb^{2+} ions to slow down the PVSK crystal growth and induced a preferred orientation by increasing the activation energy. The superior crystallinity of the PVSK films with caffeine showed a reduced

defect density and better vertical charge transport, achieving a champion PCE as high as 20.25%. In parallel, the excellent film quality suppressed ion migration and the non-volatile caffeine interacted with the PVSK again during the degradation process to improve the thermal stability of the device. Ultimately, the caffeine-based devices were shown to be thermally stable at 85 °C for over 1300 hours.

2.1 Effects of caffeine on the perovskite film crystal growth

Figure 2.1b shows the Fourier transform infrared spectroscopy (FTIR) spectra of caffeine, pristine $MAPbI_3$ and $MAPbI_3$ with caffeine. The stretching vibrations related to the two C=O bonds stretching in pure caffeine appear at 1652 cm^{-1} and 1699 cm^{-1}respectively.[47] Upon adding caffeine into $MAPbI_3$ film, it is observed that only the C=O stretching with lower frequency (due to the conjugation with C=C bond resulting in the electron delocalization) shifted from 1652 cm^{-1} to 1657 cm^{-1}, while the vibration mode of C=O at 1699 cm^{-1} maintain its original value,. This indicates the existence of caffeine in the PVSK film after annealing, and caffeine likely formed an adduct with $MAPbI_3$ via the interaction between Pb^{2+} in perovskite and one of the C=O bonds in caffeine.[48] The FTIR spectra of pure PbI_2 and PbI_2: Caffeine were also measured to further verify that caffeine interacted with the $Pb^{2+}$to form a strong Lewis acid-base adduct.[7] (Figure A2.1, Supporting Information) The shifts of the two characteristic C=O stretches followed the same trend as that of the PVSK case. This interaction was further confirmed by the shift of the Pb 4f orbital in the X-ray photoelectron spectroscopy. (Figure A2.2, Supporting Information) To study the role of caffeine in perovskite crystal growth, we additionally conducted the FTIR on the PbI_2-MAI-DMSO-Caffeine adduct, and observed that the same C=O stretching vibration shifted from 1652 cm^{-1} to 1643 cm^{-1}. (Figure 2.1c) Therefore, this strong interaction of C=O in caffeine with the Pb^{2+} ions is expected to serve as a molecular lock to increase the activation energy of nucleation, which retarded the perovskite crystal growth and improved the crystallinity of the

perovskite films with a preferred orientation. More importantly, the residual molecular lock possibly interacted with the amorphized PVSK again upon heating, which can play a crucial role in prohibiting the thermal-induced decomposition.

Figure 2.2a shows the cross-sectional scanning electron microscopy (SEM) of the caffeine-incorporated PVSK film. Then, we conducted steady-state photoluminescence (PL) and time-resolved photoluminescence (TRPL) decay measurements to study the film quality and charge recombination dynamics, as shown in Figure 2.2b and 2.2c, respectively. The PL intensity of the caffeine-incorporated PVSK film was enhanced by six times compared to that of the pristine PVSK film. Simultaneously, the peak position was blue-shifted from 770 nm to 763 nm, which further confirmed that the number of trap states was reduced upon the addition of caffeine. (Figure S3, Supporting Information) Bi-exponential rate law model was employed to fit the PL decay. Both the pristine $MAPbI_3$ and the caffeine-incorporated $MAPbI_3$ films showed relatively faster decay time (τ_1) and relatively slower decay time (τ_2).[49] The faster decay is likely related to non-radiative recombination induced by charge-trapping defect states. On the other hand, τ_2 represents the bi-molecular recombination in the bulk film. With the addition of caffeine, the fraction of the fast decay phase lifetime decreased from 57.8% to 41.9%, and the lifetime increased from 7.4 ns to 21.98 ns. Notably, the slow decay phase lifetime enhanced from 51.9 ns to 114.3 ns. These results further demonstrate the lower trap density and better electronic properties of the caffeine-incorporated PVSK film.

To examine the crystal structure, we conducted thin-layer X-Ray Diffraction (XRD) measurements for the PVSK films deposited on ITO substrate. (Figure 2.2d) The diffraction peak at 12.5°, assigned to the (001) planes of the hexagonal PbI_2, was not detected for both the $MAPbI_3$ and $MAPbI_3$: Caffeine films. Both films showed the same tetragonal PVSK phase with

the dominant (110) lattice reflection at 13.9°, which is the preferred orientation for the PVSK films. The ratio of the (110) peak intensity at 13.9° to the (222) peak intensity at 31.8° increased from 2.00 to 2.43 upon incorporation of caffeine. This suggests that the (110) grains grew faster by consuming the randomly-oriented neighboring crystals. I calculated the crystallite size using the Scherrer's equation and by taking the full-width half-maximum (FWHM) of the (110) peak. At the optimized ratio of caffeine added, the crystallite size increased from 37.97 nm to 55.99 nm, consistent with the surface SEM images of the PVSK films. (Figure A2.4, Supporting Information) Obviously, the caffeine-incorporated PVSK showed an overall crystallinity enhancement, which was further confirmed by two-dimensional (2D) grazing incidence wide-angle X-ray diffraction (GIWAXS) analysis. Figure 2.2e shows the normalized azimuth angle plots along the (110) plane of pure $MAPbI_3$ and caffeine-incorporated $MAPbI_3$ (1wt%) films, which were integrated from the 2D GIWAXS patterns (Figure A2.5, Supporting Information). At the azimuth angle of 90°, the caffeine-incorporated PVSK film shows a very sharp peak compared with the pristine PVSK film. The narrower FWHM suggests that the incorporation of caffeine assisted the growth of the perovskite grains along the in-plane direction, which would enhance the charge transport of the device.[49]

2.2 Device performance and TPC/TPV analysis

The photovoltaic devices were fabricated with a n-i-p planar structure. Indium tin oxide (ITO) was used as the anode. Tin oxide nano-particles[50] were employed as the electron transporting layer. Pure $MAPbI_3$ and $MAPbI_3$: Caffeine at various concentrations were employed as the active layer. Poly[bis(4-phenyl)(2,4,6-trimethylphenyl)amine] (PTAA) doped with 4-Isopropyl-4'-methyldiphenyliodonium Tetrakis (pentafluorophenyl) borate (TPFB)[51] was employed as the hole transporting layer. Silver (Ag) was used as the cathode. **Figure 2.3a** shows the *J–V* curves of the champion devices based on pure $MAPbI_3$ and $MAPbI_3$: Caffeine measured under reverse

scanning, as illuminated by an AM 1.5G solar simulator with an intensity of 100 mW cm^{-2}. The ratio of caffeine added was varied from 0 wt % to 2 wt%. With increasing amounts of caffeine from 0 (reference) to 1 wt%, the open-circuit voltage (V_{OC}), short-circuit current (J_{sc}), fill factor (FF) and reproducibility were systematically enhanced. (Figure A2.6 Supporting Information). The highest PCE achieved for the pure $MAPbI_3$ devices was 17.59%. (V_{oc}: 1.074 V, J_{sc}: 22.29 mA/cm^2 and FF: 73.46%). In contrast, a PCE of 20.25% (V_{oc}: 1.143 V, J_{sc}: 22.97 mA/cm^2 and FF: 77.13%) was achieved for the optimized devices with 1 wt% caffeine. The enhanced V_{oc} and FF may be associated with decreased non-radiative recombination and crystal defects owing to the passivation effect induced by the incorporation of caffeine, consistent with the PL and TRPL results. The J_{sc} was also enhanced from 22.29 mA/cm^2 to 22.97 mA/cm^2, which was confirmed by the external quantum efficiency (EQE) spectra of devices based on pure $MAPbI_3$ and $MAPbI_3$: Caffeine. (Figure 2.3b) The calculated J_{SC} values obtained from the integration of the EQE spectra were close to the measured values with the AM 1.5G reference spectrum. (Average Mismatch is below 5%, Table 2.1) The quantum efficiency enhancement in the long wavelength region was consistent with the ultraviolet–visible (UV–vis) absorption spectra. (Figure A2.7, Supporting Information). The absorption enhancement may have resulted from the larger crystal size and better crystallinity of the caffeine incorporated devices, which has been proved to enhance the light-harvesting efficiency caused by enhanced light scattering. The steady-state PCEs of the best-performing devices were 17.04% and 19.76% for the devices without and with caffeine, respectively (Figure A2.8). *J-V* hysteresis between the reverse and forward scan directions was also decreased with the addition of caffeine. The hysteresis index ($\frac{PCE_{Reverse}-PCE_{Forward}}{PCE_{Reverse}}$) decreased from 0.157 to 0.097 upon addition of 1 wt% Caffeine (Figure A2.9 and Table B2.1, Supporting Information). To demonstrate the universality of caffeine, we examined the device performance of the devices based on mixed A-site cations and mixed halide

perovskite ($CsFAMAPbI_xBr_{3-x}$). The *J-V* curves under both reverse and forward scan directions and the steady state output efficiency are shown in Figure A2.10 and Table B2.2. The perovskite solar cells with caffeine shown enhanced photovoltaic performance than the reference, which indicates this approach could be effective and universal.

To gain further insight into the performance enhancement resulting from the use of caffeine, we characterized the charge-transfer kinetics and charge recombination in the pure $MAPbI_3$ and $MAPbI_3$: Caffeine solar cells.[9] I used transient photovoltage decay (TPV) under the open-circuit condition to characterize the solar cells and found that the charge-recombination lifetime (τ_r) of the $MAPbI_3$:Caffeine based device was substantially longer than that of the device based on pure $MAPbI_3$ (285 μs versus 157 μs) (Figure 2.3c), consistent with the slowed charge recombination in the $MAPbI_3$: Caffeine film as concluded from the TRPL measurement. This indicates a lower defect concentration and hence superior electronic quality in the caffeine-incorporated perovskite bulk film, consistent with the higher V_{oc} of the corresponding devices. Meanwhile, transient photocurrent decay (TPC) under the short-circuit condition was conducted to investigate the influence of caffeine on the charge transfer in the devices. Although the addition of caffeine did not affect the band structure of the PVSK (Figure A2.11, Supporting Information), the charge transfer lifetime (τ_t) of the caffeine-containing PVSK decreased from 2.67 μs to 2.08 μs. The enhanced charge transfer might have resulted from the reduced interfacial defects and the better crystal orientation of the $MAPbI_3$: Caffeine films.

2.3 Thermal stability and TGA analysis

To prove the molecular locking effect of caffeine on the corresponding PVSK devices during the thermal degradation process, we conducted a continuous thermal stress stability test for the devices based on bare $MAPbI_3$ and $MAPbI_3$: Caffeine at 85°C in a nitrogen atmosphere. The

device with caffeine showed excellent thermal stability, preserving 86% of its original PCE after 1300 hours. The represented *J-V* curves before and after being subjected to the thermal stability test are shown in Figure A2.12, Figure A2.18 and Figure A2.19. The controlled device only retained 60% of its original PCE after 175 hours, which may be due to ion migration, poor crystal quality and phase instability of bare $MAPbI_3$ at high temperatures. Furthermore, to evaluate the operational stability, all the devices were encapsulated under a nitrogen atmosphere and exposed to continuous illumination (90 ±10 mW, without UV filter) under open-circuit condition (Figure A2.13). Caffeine can also effectively enhance the operational stability of the perovskite solar cell. To understand the mechanism of the enhanced thermal stability of the caffeine-incorporated devices in the context of ion migration and phase decomposition, we first conducted XRD analysis on the devices after the thermal stability test. (**Figure 2.4b**) For the reference device, there was a strong peak at 12.5°, attributed to the (001) planes of hexagonal PbI_2. The extremely weak diffraction at 13.9° suggests a complete degradation of the PVSK crystal. Not surprisingly, there was a relatively strong diffraction signal at 38.5°, assigned to the (003) plane of PbI_2. Although there was a peak at 12.5° in the target device, the (110) plane signal was still strong. The superior crystallinity of the caffeine-incorporated PVSK might have resulted in the suppression of ion migration during heating. Thermogravimetric analysis (TGA) on caffeine and the adduct powders was conducted to analyze the phase stability and thermal properties of caffeine and the intermediate adduct phase. Figure 2.4c and 2.4d indicate the weight loss and heat flow of the powders based on caffeine, pure PVSK and caffeine-incorporated PVSK, respectively. Caffeine decomposed completely at around 285 °C, demonstrating its superior thermal stability at temperatures below 200 °C. (Figure A2.14, Supporting Information) From Figure 4c, there are three main steps of the weight loss at around 70 °C, 340 °C and 460 °C for the pure PVSK powders. These three steps are correlated with the sublimation of DMSO, MAI

and PbI_2, respectively.[45] For the caffeine-containing PVSK adduct powders, the sublimation temperature of MAI and PbI_2 were higher than that of the bare PVSK powders, which indicates that more energy is required to break the interaction between caffeine and the PVSK precursors. This is further confirmed by the heat flow diagrams as shown in Figure 2.4d. The strong interaction formed by the caffeine molecular lock may increase the activation energy for the decomposition upon heating.

2.4 Microstructure analysis via cross-sectional STEM and in-situ HRTEM

To further investigate the role of caffeine in suppressing ion migration and thermal decomposition, microstructure analysis was carried out. I first conducted cross-sectional scanning transmission electron microscopy (STEM) and energy-dispersive X-ray (EDX) spectroscopy analysis. (**Figure 2.5**) The samples were directly collected from the devices after the 1300 hours thermal stability test via focused ion beam (FIB). Figure A2.15 shows the EDX mapping of selective regions on both the control and target devices. The spatial distribution of the Pb and I elements determined the PVSK active layer region. The Ag electrode was above the active layer, separated by the PTAA HTL. For the control sample, there were significant silver signals (silver clusters) with a similar intensity as that in the electrode region detected at the interface between the HTL and the active layer region. It is likely that the silver diffused through the whole PVSK region, as confirmed by the observation that the silver signals were detected even in the ITO electrode region. More importantly, the iodine signals were clearly detected in the Ag electrode region. Iodine could accumulate at the electrode and interface. It easily reacted with silver to form AgI, which will negatively impact the device performance. In contrast, there is no obvious indication of such similar ion migration in the caffeine-incorporated PVSK device. To further confirm the result quantitively, line scanning profiles were also measured. As shown in Figure 2.5g, the thickness of the Ag electrode was 50 nm, and that two sharp peaks at both the electrode

and interface were observed, and the Ag signal was detected almost throughout the entire device. However, the thickness of the Ag electrode in the caffeine-incorporated PVSK device maintained its original value of 100 nm. More importantly, a sharp iodine peak was detected in the electrode region of the control device, in agreement with the previous conclusion. Hence, from the STEM results, the suppression of ion migration in the caffeine-containing films ensured the high thermal resistance of the devices. I also conducted real time high resolution transmission electron spectroscopy (HRTEM) to study the effect of caffeine on the phase transformation of the PVSK. The electron beam (E-beam) of the HRTEM instrument was utilized as the source of the thermal energy. **Figure 2.6a-d** show the HRTEM images and the corresponding fast Fourier transforms (FFTs) of the diffraction patterns of both the caffeine-incorporated and pristine PVSKs. $MAPbI_3$ layers with various crystallographic orientations were observed in both samples. The representative spot diffractions (yellow circles) with an interplanar spacing of 3.1 Å, which are well-matched with the (110) diffraction of $MAPbI_3$, are shown in Figure 6b and 6d. After exposure to the E-beam for 5 min 30s, the environmental temperature of the samples was elevated to around 135 °C.[52] Figure 2.6e-h present the HRTEM images and the corresponding FFTs of the diffraction patterns of the aged caffeine-incorporated and pristine PVSKs. Although the intensity of the (110) diffraction spots of the caffeine-incorporated PVSK became weak, no new diffraction peaks appeared. Notably, a critical alteration of the $MAPbI_3$ layer was observed in the control sample, with the (110) diffraction spots observed to split (red circle). On the other hand, there was a new broad ring which appeared in the FFT at 3.9 nm^{-1}, and new diffraction spots were observed at the same place. These morphological characteristics suggests that some crystallized PVSK phase had been transferred to the amorphized phase with precipitated trigonal PbI_2 grains at this region, which agrees with a previous study that the thermal degradation of PVSK is often considered as the reverse process of the perovskite film growth.[53] I also conducted

in-situ TEM measurement on the other regions of the films, the results followed a similar trend as described previously. (Figure A2.16 and A2.17, Supporting Information) From these results, we speculate that the existence of the caffeine additive serves as a molecular lock to interact with the amorphized PVSK phase again to increase the decomposition activation energy of the PVSK, which locks the amorphized phase of the PVSK, thereby preventing the degradation of the PVSK when exposed to high temperatures.

2.5 Conclusion

In conclusion, we employed caffeine, a conjugated Lewis base with two carboxyl groups, to serve as a molecular lock on perovskite. The strong interaction between caffeine and the Pb^{2+} ions increased the growth activation energy of the PVSK film, which facilitated the growth of high-quality films that showed preferred orientation and superior electronic properties. Consequently, a PCE as high as 20.25% was achieved for the champion device. In the meantime, the superior film quality suppressed the migration of ions. Also, the residual conjugated molecular lock effectively prevented any form of thermal degradation (the reverse of the PVSK synthesis process), which realized PVSK: Caffeine-based solar cells that were thermally-stable for over 1300 hours at 85°C.

References

1. Chiba, T., Hayashi, Y., Ebe, H., Hoshi, K., Sato, J., Sato, S., Pu, Y.-J., Ohisa, S., and Kido, J. (2018). Anion-exchange red perovskite quantum dots with ammonium iodine salts for highly efficient light-emitting devices. Nat. Photonics *12*, 681–687.
2. Liu, M., Johnston, M.B., and Snaith, H.J. (2013). Efficient planar heterojunction perovskite solar cells by vapour deposition Many different photovoltaic technologies are being developed for large-scale solar energy conversion. Nature *501*.
3. Cho, H., Jeong, S.H., Park, M.H., Kim, Y.H., Wolf, C., Lee, C.L., Heo, J.H., Sadhanala, A.,

Myoung, N.S., Yoo, S., *et al.* (2015). Overcoming the electroluminescence efficiency limitations of perovskite light-emitting diodes. Science. *350*, 1222–1225.

4. Xue, J., Zhang, Z., Zheng, F., Xu, Q., Xu, J., Zou, G., Li, L., and Zhu, J.J. (2017). Efficient Solid-State Electrochemiluminescence from High-Quality Perovskite Quantum Dot Films. Anal. Chem. *89*, 8212–8216.

5. Wei, H., Desantis, D., Wei, W., Deng, Y., Guo, D., Savenije, T.J., Cao, L., and Huang, J. (2017). Dopant compensation in alloyed CH3NH3PbBr3-xClxperovskite single crystals for gamma-ray spectroscopy. Nat. Mater. *16*, 826–833

6. Kim, Y.C., Kim, K.H., Son, D.Y., Jeong, D.N., Seo, J.Y., Choi, Y.S., Han, I.T., Lee, S.Y., and Park, N.G. (2017). Printable organometallic perovskite enables large-area, low-dose X-ray imaging. Nature *550*, 87–91.

7. Bi, D., Yi, C., Luo, J., Décoppet, J.-D., Zhang, F., Zakeeruddin, S.M., Li, X., Hagfeldt, A., and Grätzel, M. (2016). Polymer-templated nucleation and crystal growth of perovskite films for solar cells with efficiency greater than 21%. Nat. Energy *1*, 16142.

8. Deng, Y., Zheng, X., Bai, Y., Wang, Q., Zhao, J., and Huang, J. (2018). Surfactant-controlled ink drying enables high-speed deposition of perovskite films for efficient photovoltaic modules. Nat. Energy *3*, 560–566.

9. Tan, H., Jain, A., Voznyy, O., Lan, X., De Arquer, F.P.G., Fan, J.Z., Quintero-Bermudez, R., Yuan, M., Zhang, B., Zhao, Y., *et al.* (2017). Efficient and stable solution-processed planar perovskite solar cells via contact passivation. Science *355*, 722–726.

10. Yang, W.S., Noh, J.H., Jeon, N.J., Kim, Y.C., Ryu, S., Seo, J., and Seok, S. Il (2015). High-performance photovoltaic perovskite layers fabricated through intramolecular exchange. Science (80-.). *348*, 1234–1237.

11. Burschka, J., Pellet, N., Moon, S.J., Humphry-Baker, R., Gao, P., Nazeeruddin, M.K., and Grätzel, M. (2013). Sequential deposition as a route to high-performance perovskite-sensitized solar cells. Nature *499*, 316–319.

12. Kojima, A., Teshima, K., Shirai, Y., and Miyasaka, T. (2009). Organometal Halide Perovskites as Visible-Light Sensitizers for Photovoltaic Cells. J. Am. Chem. Soc. *131*, 6050–6051.

13. https://www.nrel.gov/pv/assets/pdfs/pv-efficiencies-07-17-2018.pdf.

14. Yang, W.S., Park, B.-W., Jung, E.H., Jeon, N.J., Kim, Y.C., Lee, D.U., Shin, S.S., Seo, J., Kim, E.K., Noh, J.H., *et al.* (2017). Iodide management in formamidinium-lead-halide-based perovskite layers for efficient solar cells. Science *356*, 1376–1379.

15. Im, J.-H., Lee, C.-R., Lee, J.-W., Park, S.-W., and Park, N.-G. (2011). 6.5% efficient perovskite quantum-dot-sensitized solar cell. Nanoscale *3*, 4088.

16. You, J., Meng, L., Song, T. Bin, Guo, T.F., Chang, W.H., Hong, Z., Chen, H., Zhou, H., Chen, Q., Liu, Y., *et al.* (2016). Improved air stability of perovskite solar cells via solution-processed metal oxide transport layers. Nat. Nanotechnol. *11*, 75–81.

17. Divitini, G., Cacovich, S., Matteocci, F., Cinà, L., Di Carlo, A., and Ducati, C. (2016). In situ observation of heat-induced degradation of perovskite solar cells. Nat. Energy *1*, 15012.

18. Zheng, X., Chen, B., Dai, J., Fang, Y., Bai, Y., Lin, Y., Wei, H., Zeng, X.C., and Huang, J. (2017). Defect passivation in hybrid perovskite solar cells using quaternary ammonium halide anions and cations. Nat. Energy *2*, 17102.

19. Aristidou, N., Sanchez-Molina, I., Chotchuangchutchaval, T., Brown, M., Martinez, L., Rath, T., and Haque, S.A. (2015). The Role of Oxygen in the Degradation of Methylammonium Lead Trihalide Perovskite Photoactive Layers. Angew. Chemie - Int. Ed. *54*, 8208–8212.

20. Zhang, C.C., Li, M., Wang, Z.K., Jiang, Y.R., Liu, H.R., Yang, Y.G., Gao, X.Y., and Ma, H. (2017). Passivated perovskite crystallization and stability in organic-inorganic halide solar cells by doping a donor polymer. J. Mater. Chem. A *5*, 2572–2579.

21. Li, M., Wang, Z.K., Kang, T., Yang, Y., Gao, X., Hsu, C.S., Li, Y., and Liao, L.S. (2018). Graphdiyne-modified cross-linkable fullerene as an efficient electron-transporting layer in organometal halide perovskite solar cells. Nano Energy *43*, 47–54.

22. Xue, J., Lee, J.-W., Dai, Z., Wang, R., Nuryyeva, S., Liao, M.E., Chang, S.-Y., Meng, L., Meng,

D., Sun, P., *et al.* (2018). Surface Ligand Management for Stable FAPbI3 Perovskite Quantum Dot Solar Cells. Joule *2*, 1866–1878.

23. Swarnkar, A., Marshall, A.R., Sanehira, E.M., Chernomordik, B.D., Moore, D.T., Christians, J.A., Chakrabarti, T., and Luther, J.M. (2016). Quantum dot-induced phase stabilization of α-CsPbI3 perovskite for high-efficiency photovoltaics. Science *354*, 92–95.

24. Chen, Q., De Marco, N., Yang, Y., Song, T. Bin, Chen, C.C., Zhao, H., Hong, Z., Zhou, H., and Yang, Y. (2015). Under the spotlight: The organic-inorganic hybrid halide perovskite for optoelectronic applications. Nano Today *10*, 355–396.

25. Berhe, T.A., Su, W.-N., Chen, C.-H., Pan, C.-J., Cheng, J.-H., Chen, H.-M., Tsai, M.-C., Chen, L.-Y., Dubale, A.A., and Hwang, B.-J. (2016). Organometal halide perovskite solar cells: degradation and stability. Energy Environ. Sci. *9*, 323–356.

26. Conings, B., Drijkoningen, J., Gauquelin, N., Babayigit, A., D'Haen, J., D'Olieslaeger, L., Ethirajan, A., Verbeeck, J., Manca, J., Mosconi, E., *et al.* (2015). Intrinsic Thermal Instability of Methylammonium Lead Trihalide Perovskite. Adv. Energy Mater. *5*, 1500477.

27. Yang, Y., and You, J. (2017). Make perovskite solar cells stable. Nature *544*, 155–156.

28. Liu, L., Huang, S., Lu, Y., Liu, P., Zhao, Y., Shi, C., Zhang, S., Wu, J., Zhong, H., Sui, M., *et al.* (2018). Grain-Boundary "Patches" by In Situ Conversion to Enhance Perovskite Solar Cells Stability. Adv. Mater. *30*, 1800544.

29. Lee, J.W., Kim, S.G., Bae, S.H., Lee, D.K., Lin, O., Yang, Y., and Park, N.G. (2017). The Interplay between Trap Density and Hysteresis in Planar Heterojunction Perovskite Solar Cells. Nano Lett. *17*, 4270–4276.

30. McMeekin, D.P., Wang, Z., Rehman, W., Pulvirenti, F., Patel, J.B., Noel, N.K., Johnston, M.B., Marder, S.R., Herz, L.M., and Snaith, H.J. (2017). Crystallization Kinetics and Morphology Control of Formamidinium–Cesium Mixed-Cation Lead Mixed-Halide Perovskite via Tunability of the Colloidal Precursor Solution. Adv. Mater. *29*, 1607039.

31. Guerra, V.L.P., Altamura, D., Trifiletti, V., Colella, S., Listorti, A., Giannuzzi, R., Pellegrino, G.,

Condorelli, G.G., Giannini, C., Gigli, G., *et al.* (2015). Implications of TiO2surface functionalization on polycrystalline mixed halide perovskite films and photovoltaic devices. J. Mater. Chem. A *3*, 20811–20818.

32. Boyd, C.C., Cheacharoen, R., Leijtens, T., and McGehee, M.D. (2018). [ASAP] Understanding Degradation Mechanisms and Improving Stability of Perovskite Photovoltaics. Chem. Rev., acs.chemrev.8b00336.

33. Chen, Y., Yang, Z., Wang, S., Zheng, X., Wu, Y., Yuan, N., Zhang, W.H., and Liu, S.F. (2018). Design of an Inorganic Mesoporous Hole-Transporting Layer for Highly Efficient and Stable Inverted Perovskite Solar Cells. Adv. Mater. *30*, 1805660.

34. Seo, S., Jeong, S., Bae, C., Park, N.G., and Shin, H. (2018). Perovskite Solar Cells with Inorganic Electron- and Hole-Transport Layers Exhibiting Long-Term (≈500 h) Stability at 85 °C under Continuous 1 Sun Illumination in Ambient Air. Adv. Mater. *30*, 1801010.

35. Jeon, N.J., Na, H., Jung, E.H., Yang, T.-Y., Lee, Y.G., Kim, G., Shin, H.-W., Il Seok, S., Lee, J., and Seo, J. (2018). A fluorene-terminated hole-transporting material for highly efficient and stable perovskite solar cells. Nat. Energy *3*, 682–689.

36. Mei, A., Li, X., Liu, L., Ku, Z., Liu, T., Rong, Y., Xu, M., Hu, M., Chen, J., Yang, Y., *et al.* (2014). A hole-conductor-free, fully printable mesoscopic perovskite solar cell with high stability. Science. *345*, 295–298.

37. Wang, R., Mujahid, M., Duan, Y., Wang, Z.-K., Xue, J., and Yang, Y. (2019). A Review of Perovskites Solar Cell Stability. Adv. Funct. Mater., 1808843.

38. Cao, J., Li, C., Lv, X., Feng, X., Meng, R., Wu, Y., and Tang, Y. (2018). Efficient Grain Boundary Suture by Low-Cost Tetra-ammonium Zinc Phthalocyanine for Stable Perovskite Solar Cells with Expanded Photoresponse. J. Am. Chem. Soc. *140*, 11577–11580.

39. Lee, J.W., Kim, H.S., and Park, N.G. (2016). Lewis Acid-Base Adduct Approach for High Efficiency Perovskite Solar Cells. Acc. Chem. Res. *49*, 311–319.

40. Wu, Y., Yang, X., Chen, W., Yue, Y., Cai, M., Xie, F., Bi, E., Islam, A., and Han, L. (2016).

Perovskite solar cells with 18.21% efficiency and area over 1 cm2 fabricated by heterojunction engineering. Nat. Energy *1*, 16148.

41. Niu, T., Lu, J., Munir, R., Li, J., Barrit, D., Zhang, X., Hu, H., Yang, Z., Amassian, A., Zhao, K., *et al.* (2018). Stable High-Performance Perovskite Solar Cells via Grain Boundary Passivation. Adv. Mater. *30*, 1706576.

42. Zuo, L., Guo, H., deQuilettes, D.W., Jariwala, S., De Marco, N., Dong, S., DeBlock, R., Ginger, D.S., Dunn, B., Wang, M., *et al.* (2017). Polymer-modified halide perovskite films for efficient and stable planar heterojunction solar cells. Sci. Adv. *3*, e1700106.

43. Lee, J.W., Dai, Z., Lee, C., Lee, H.M., Han, T.H., De Marco, N., Lin, O., Choi, C.S., Dunn, B., Koh, J., *et al.* (2018). Tuning Molecular Interactions for Highly Reproducible and Efficient Formamidinium Perovskite Solar Cells via Adduct Approach. J. Am. Chem. Soc. *140*, 6317–6324.

44. Xiang, W., Chen, Q., Wang, Y., Liu, M., Huang, F., Bu, T., Wang, T., Cheng, Y.B., Gong, X., Zhong, J., *et al.* (2017). Improved air stability of perovskite hybrid solar cells via blending poly(dimethylsiloxane)-urea copolymers. J. Mater. Chem. A *5*, 5486–5494.

45. Lee, J.W., Bae, S.H., Hsieh, Y.T., De Marco, N., Wang, M., Sun, P., and Yang, Y. (2017). A Bifunctional Lewis Base Additive for Microscopic Homogeneity in Perovskite Solar Cells. Chem *3*, 290–302.

46. Arora, N., Dar, M.I., Hinderhofer, A., Pellet, N., Schreiber, F., Zakeeruddin, S.M., and Grätzel, M. (2017). Perovskite solar cells with CuSCN hole extraction layers yield stabilized efficiencies greater than 20%. Science *358*, 768–771.

47. Singh, B.R., Wechter, M.A., Hu, Y., and Lafontaine, C. (1998). Determination of caffeine content in coffee using fourier transform infra-red spectroscopy in combination with attenuated total reflectance technique: A bioanalytical chemistry experiment for biochemists. Biochem. Educ. *26*, 243–247.

48. Hou, X., Huang, S., Ou-Yang, W., Pan, L., Sun, Z., and Chen, X. (2017). Constructing Efficient and Stable Perovskite Solar Cells via Interconnecting Perovskite Grains. ACS Appl. Mater.

Interfaces *9*, 35200–35208.

49. Lee, J.-W., Dai, Z., Han, T.-H., Choi, C., Chang, S.-Y., Lee, S.-J., De Marco, N., Zhao, H., Sun, P., Huang, Y., *et al.* (2018). 2D perovskite stabilized phase-pure formamidinium perovskite solar cells. Nat. Commun. *9*, 3021.

50. Jiang, Q., Zhang, L., Wang, H., Yang, X., Meng, J., Liu, H., Yin, Z., Wu, J., Zhang, X., and You, J. (2017). Enhanced electron extraction using SnO2for high-efficiency planar-structure HC(NH2)2PbI3-based perovskite solar cells. Nat. Energy *2*, 16177..

51. Han, Q., Hsieh, Y.T., Meng, L., Wu, J.L., Sun, P., Yao, E.P., Chang, S.Y., Bae, S.H., Kato, T., Bermudez, V., *et al.* (2018). High-performance perovskite/ Cu(In,Ga)Se2monolithic tandem solar cells. Science (80-.). *361*, 904–908.

52. Bi, E., Chen, H., Xie, F., Wu, Y., Chen, W., Su, Y., Islam, A., Grätzel, M., Yang, X., and Han, L. (2017). Diffusion engineering of ions and charge carriers for stable efficient perovskite solar cells. Nat. Commun. *8*, 15330.

53. Kim, T.W., Shibayama, N., Cojocaru, L., Uchida, S., Kondo, T., and Segawa, H. (2018). Real-Time In Situ Observation of Microstructural Change in Organometal Halide Perovskite Induced by Thermal Degradation. Adv. Funct. Mater. *28*, 1804039.

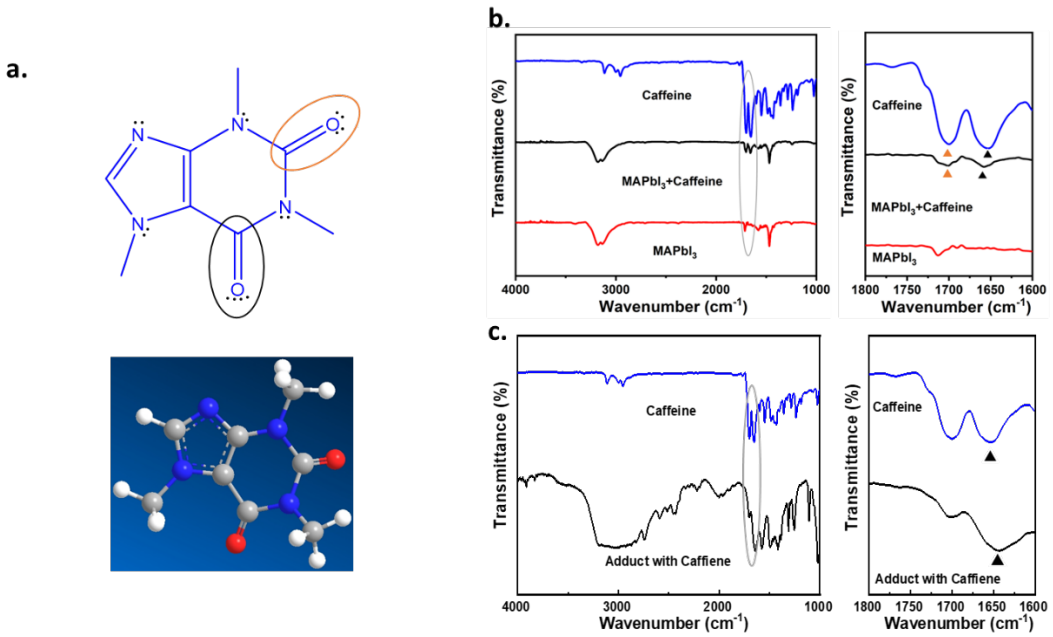

Figure 2.1. a. Lewis Chemical Structure and 3D structure of 1,3,7-Trimethylxanthine (Caffeine) **b**. FTIR spectra and fingerprint regions of pure caffeine, caffeine-PVSK and the pristine PVSK films. The triangles indicate the stretching vibration peaks of C=O in the two films. **c.** FTIR spectra and fingerprint regions of pure caffeine, PbI_2-MAI-DMSO-Caffiene adduct film. The triangles indicate the stretching vibration peaks of C=O in the two films.

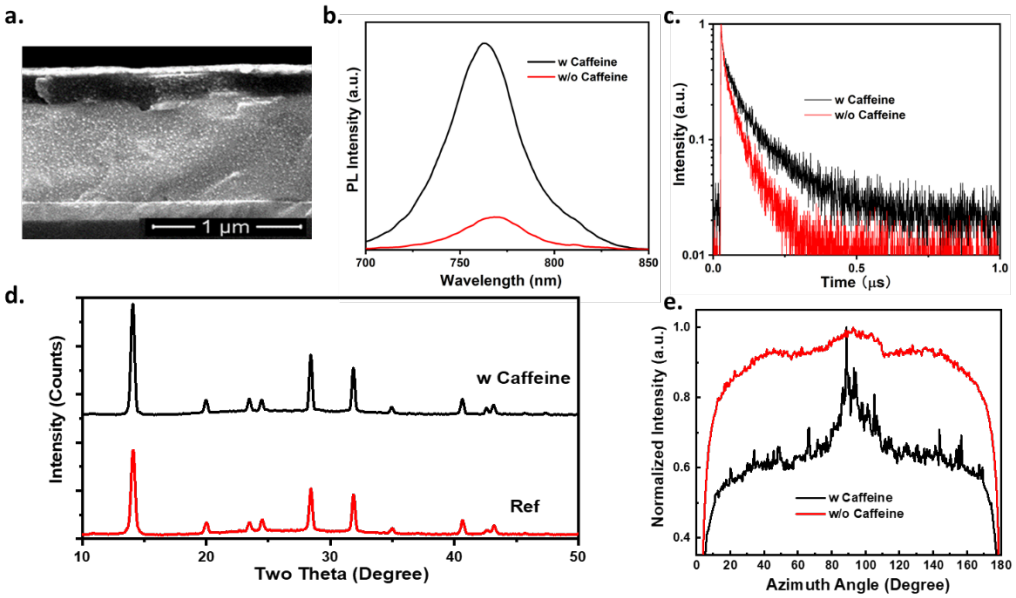

Figure 2.2. a. Cross-sectional SEM of caffeine-containing perovskite film. **b.** Photoluminescence (PL) and **c**. Time-resolved PL spectra of PVSK films without and with caffeine. **d.** X-ray diffraction patterns of as-cast PVSK films with or without caffeine**. e.** Radially integrated intensity plots along (110) crystal plane from the 2D grazing incidence wide angle X-ray diffraction (GIWAXS) patterns in $MAPbI_3$ and $MAPbI_3$: Caffeine films.

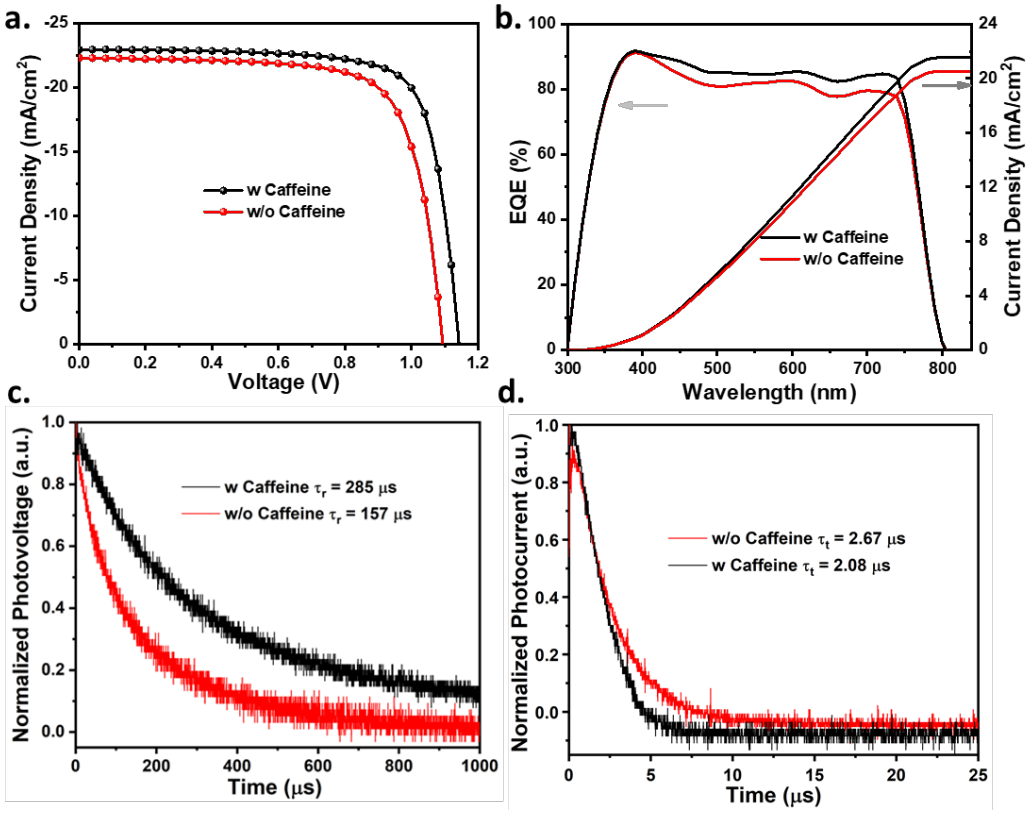

Figure 2.3. a. *J–V* curves of the champion PSC of pristine PVSK and caffeine containing PVSK in reverse scan direction. **b.** EQE spectra and integrated current densities from the EQE spectra of PVSK devices with or without adding caffeine. **c.** Normalized Transient photovoltage (TPV) decay and **d.** Normalized Transient photocurrent (TPC) decay in $MAPbI_3$ and $MAPbI_3$: Caffeine based perovskite solar cells.

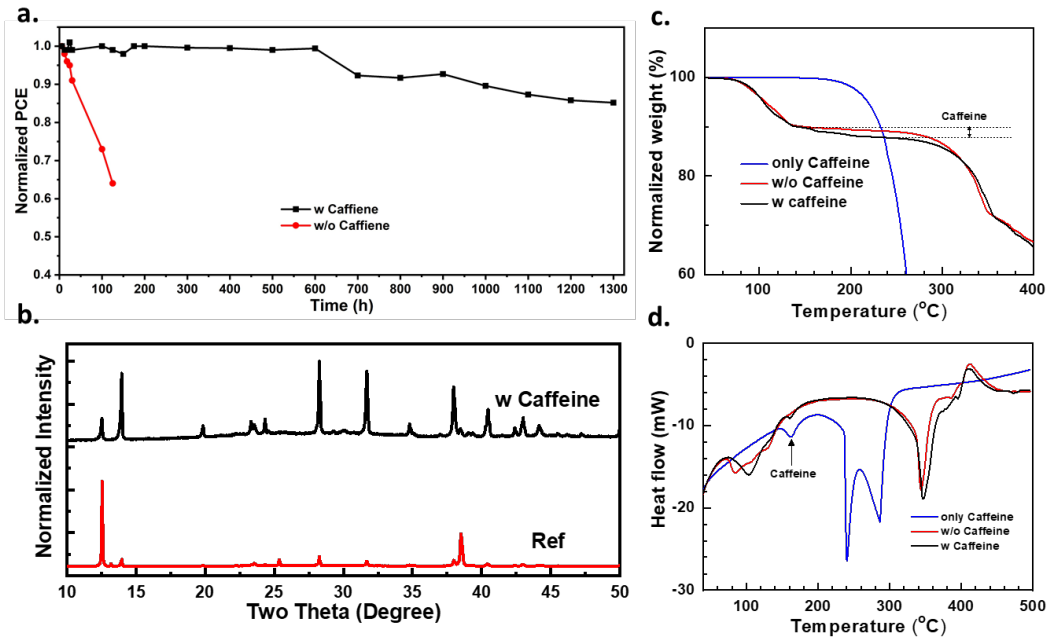

Figure 2.4. a. Devices thermal stability upon 85°C continuous annealing in nitrogen box. **b.** XRD patterns of aged device based on pure $MAPbI_3$ and $MAPbI_3$ with caffeine. Thermogravimetric analysis (TGA) analysis of **c.** weight loss and **d.** heat flow of pristine caffeine, MAI-PbI_2-DMSO adduct powder and MAI-PbI_2-DMSO-Caffeine adduct powder.

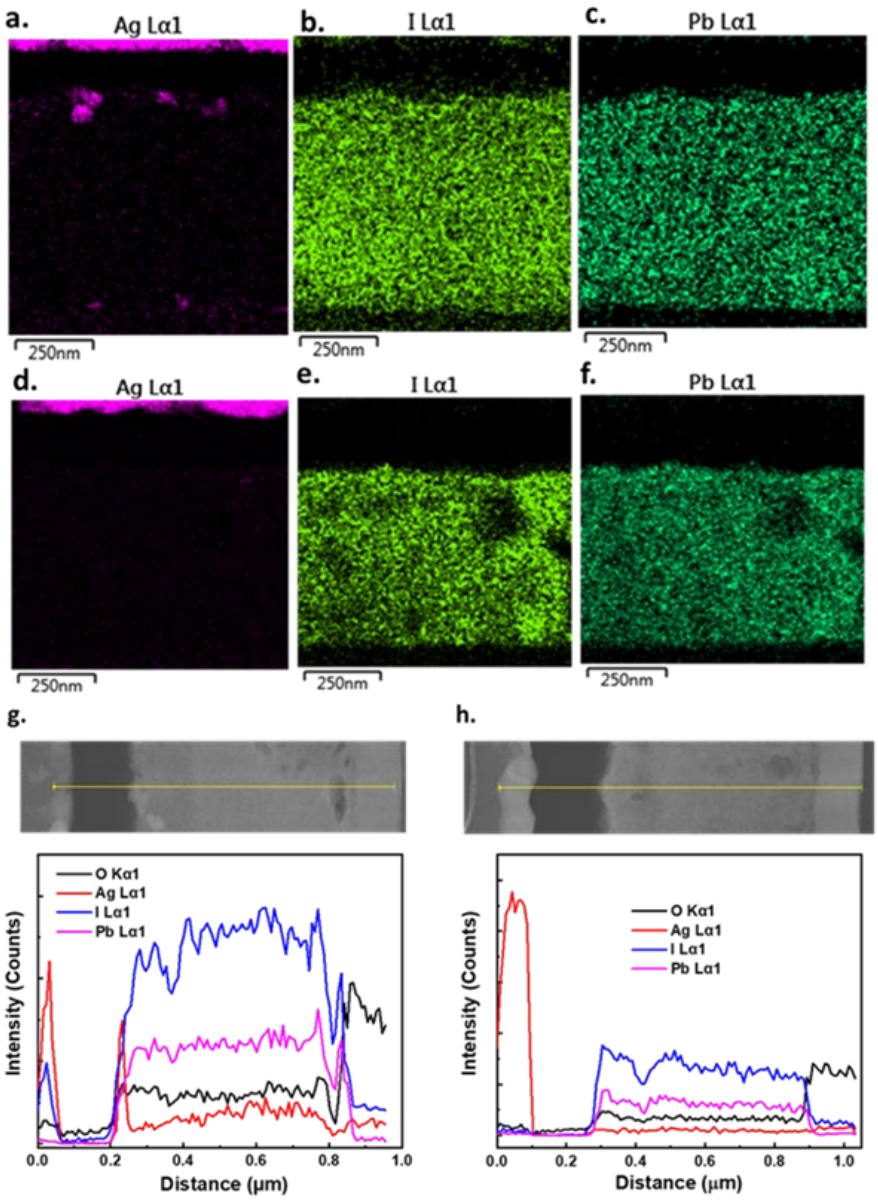

Figure 2.5. Energy-dispersive X-ray spectra (EDX) mapping of the aged pure PVSK device: **a.** Ag **b.** I and **c.** Pb. And the aged caffeine-containing PVSK device: **d**. Ag **e**. I and **f**. Pb. EDX line scans of **g.** aged pure PVSK device and **h.** aged caffeine-containing PVSK device

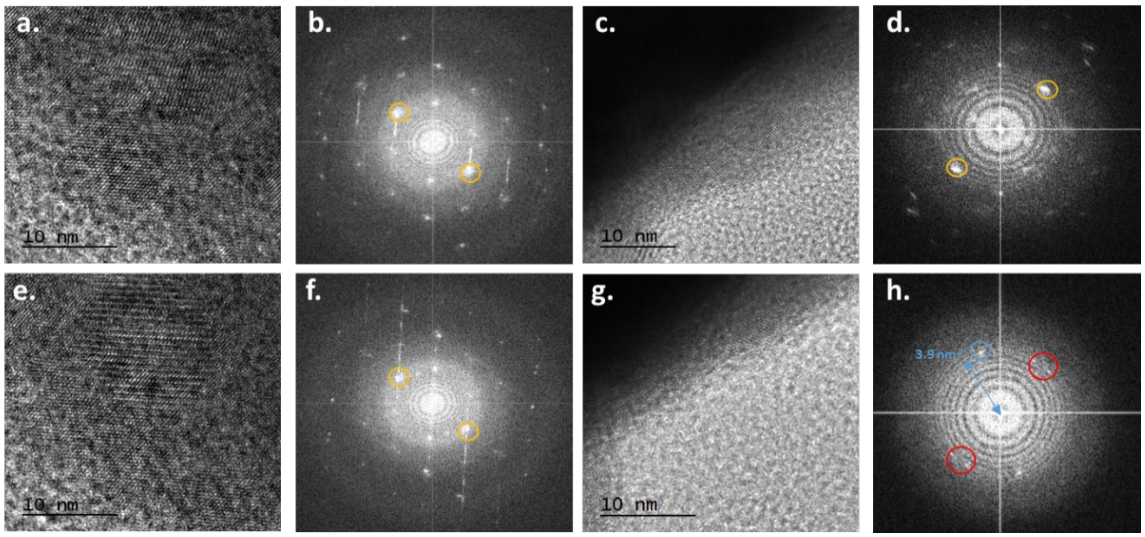

Figure 2.6. High resolution transmittance electron microscopy (HRTEM) of **a.** fresh caffeine containing PVSK; **c.** fresh pure PVSK; **e.** aged (5 min 30 s) caffeine containing PVSK and **g.** aged (5 min 30 s) pure PVSK. Corresponding Fast Fourier transforms (FFTs) of **b.** fresh caffeine containing PVSK; **d.** fresh pure PVSK; **f.** aged (5 min 30 s) caffeine containing PVSK and **h.** aged (5 min 30 s) pure PVSK.

Table 2.1. Average and the best device data based on $MAPbI_3$ with various concentration of caffeine.

Caffeine Concetraion	V_{OC} (V)	J_{SC} (mA cm^{-2})	Calculated J_{SC} (mA cm^{-2})	FF (%)	PCE (%)	
					average	best
0 wt%	1.071±0.01	21.78±0.31	20.58	72.52±1.32	16.92±0.40	17.59
0.5 wt%	1.107±0.01	21.77±0.54	20.89	73.60±1.48	17.74±0.17	17.98
1 wt%	1.134±0.01	22.77±0.30	21.53	76.90±1.13	19.87±0.22	20.25
2 wt%	1.132±0.01	22.16±0.26	21.24	73.21±1.22	18.40±0.37	18.82

Chapter 3 Tailored Phase Transformation of $CsPbI_2Br$ Films by Copper (II) Bromide for High-Performance All-Inorganic Perovskite Solar Cells

Organic-inorganic hybrid perovskites are regarded as promising next-generation photovoltaic materials owing to their excellent semiconducting properties such as suitable band gap, high carrier mobility and long charge diffusion length. With these merits, the power conversion efficiency (PCE) of organic-inorganic hybrid perovskite solar cells (PSCs) has skyrocketed from 3.8% to 23.3% within the past decade.[1,2] However, the organic parts such as methylammonium (MA) and formamidinium (FA) make the hybrid perovskite materials ~~to~~ suffer from poor thermal, optical and moist stabilities.[3-5] Although the instability issue could be partially addressed by substitution,[6-8] cation-exchange,[9,10] additives,[11-13] and encapsulation,[14,15] the intrinsic instability of organic-inorganic hybrid perovskite materials is still a serious challenge for commercial application of PSCs. Recently, all-inorganic based perovskites by replacing the organic component with cesium (Cs) have drawn much attention owing to their intrinsic stability.[16-18]

For example, the inorganic perovskite $CsPbX_3$ (X= Cl, Br, I) are reported to exhibit better thermal stability than the organic-inorganic based one.[16,18] Particularly, $CsPbI_3$ in the cubic phase (α phase) possesses an appropriate optical energy band gap (E_g) of 1.73 eV,[19] which is beneficial to configure a tandem device by combining it with other low band gap solar cells.[20-24] Recently, several groups have reported $CsPbI_3$-based PSCs with PCE exceeding 15%.[25,26] Unfortunately, $CsPbI_3$ film suffers from serious phase instability since α-$CsPbI_3$ is just stable over 330 °C and prone to be converted into a non-perovskite phase (δ-$CsPbI_3$) at room temperature.[27] In contrast, $CsPbBr_3$ has a stable orthorhombic phase at room temperature. It can be easily transformed into high-symmetry tetragonal and cubic phase by annealing at 88 and 130 °C, respectively. [28] However, the larger bandgap (~2.3 eV) restricts its absorption in the visible light region. This

causes low short-circuit current density (J_{sc}) and thus low PCE in single-junction cells.[29] Alternatively, mixed-halide inorganic perovskites, $CsPbI_{3-x}Br_x$ are feasible materials to possess low phase transition temperature and tunable band gap by a I/Br composition engineering.[30-34] For examples, Lau *et al*. reported a PCE of 6.3 % in all-inorganic PSCs based on $CsPbIBr_2$ with an E_g of 2.05 eV.[30] Yang *et al*. developed a polymer-passivated $CsPbI_2Br$ film with an E_g of 1.82 eV, giving an PCE over 12% in corresponding PSCs with a large V_{oc} up to 1.32 V.[31] Liu *et al*. designed inorganic PSCs based on 3D-2D-0D $CsPbI_2Br$ multiple graded heterojunction with a PCE of 12.39%.[32] These promising achievements indicate that the mixed-halide inorganic perovskites have great potential in realizing highly-efficient and long-term stable all-inorganic PSCs.

High-quality polycrystalline all-inorganic perovskite films with good morphology and large grain size are desirable for realizing high-performance devices. Unfortunately, defects and traps are inevitable in most solution-processed perovskite films.[35,36] Similar with the organic-inorganic hybrid perovskites,[37-42] various methods for traps passivation among grain boundaries and/or on surfaces, such as partial substitution and/or incorporation of metal cations anions, have been developed in mixed-halide inorganic PSCs.[43-47] However, the cell efficiency in mixed-halide inorganic PSCs is still far below that of organic-inorganic hybrid based ones. Therefore, further strategies of reducing the defects and traps in mixed-halide inorganic perovskite films are necessary. Herein, we reported a facial passivation route for $CsPbI_2Br$ films by a direct incorporating of copper bromide ($CuBr_2$) into perovskite precursor. Bromine salt is selected to avoid additional incorporation of impurities into the perovskite films. $CuBr_2$ incorporation plays an important role in improving the $CsPbI_2Br$ crystallization with large grain size and full film coverage by retarding the crystalline dynamics process. As a result, the fabricated all-inorganic

perovskite solar cells employing $CsPbI_2Br$:$CuBr_2$ as the absorber layer exhibit a maximum PCE of 16.15% with a V_{oc} of 1.18 V, a J_{sc} of 16.95 mA cm^{-2} and a FF of 0.80.

3.1 $CuBr_2$-Doped $CsPbI_2Br$ films

$CsPbI_2Br$ precursor solution was prepared by dissolving CsI:CsBr:PbI_2:$PbBr_2$ (1:0.5:1:0.5) in dimethylsulfoxide (DMSO) with a 0.8 M concentration. $CsPbI_2Br$:$CuBr_2$ composite perovskite films were deposited in N_2 glovebox by spin-coating $CuBr_2$-incorporated $CsPbI_2Br$ precursor onto compact TiO_2 layer with desired doping ratios. The samples were treated with chlorobenzene drop-casting during spin-coating and subsequently annealed at 260 °C for 10 min.

To clarify the effect of $CuBr_2$ incorporation on the electrical structure and chemical states of $CsPbI_2Br$, X-ray photoelectron spectra (XPS) of corresponding pristine and composite perovskite films are evaluated. **Figure 3.1a** plots the XPS results of Cs 3d*5*, Pb 4*f*, Br 3*d* and I 3*d*5 core levels in pristine $CsPbI_2Br$ and $CsPbI_2Br$:$CuBr_2$ (0.2 wt%) films. Compared to the pristine $CsPbI_2Br$ film, the core level peaks of all four elements in $CsPbI_2Br$: $CuBr_2$ composite film are seen slightly blue shifted by 0.36 eV, 0.47 eV, 0.39 eV and 0.41 eV for Cs 3*d*5, Pb 4*f*, Br 3*d* and I 3*d*5, respectively. I ascribe these shifts to the doping of $CsPbI_2Br$ by $CuBr_2$ since simple blending would not cause a large change of chemical state.[44,48] To further inspect the electronic structure of the $CsPbI_2Br$:$CuBr_2$ (0.2 wt%) perovskite, the perovsite film was scraped off and the obtained power was put onto a copper gird for evaluation. The selected area electron diffraction (SAED) patterns of $CsPbI_2Br$ and $CsPbI_2Br$:$CuBr_2$ (0.2 wt%) perovskites are shown in Figure A3.1a and A3.1b, respectively. It is found that the both samples are composed of some single crystals due to their distinct electron diffraction patterns. Figure A3.1c and 1d shows the high-resolution transmission electron microscope (HRTEM) images of dispersed $CsPbI_2Br$ and $CsPbI_2Br$:$CuBr_2$

(0.2 wt%) perovskite scraped form their films. The lattice parameter of $CsPbI_2Br$ films was determined to be 0.31 nm, matching well the spacing of (100) crystal planes in the cubic $CsPbBrI_2$ crystal structure.[49] In contrast, $CsPbI_2Br$:$CuBr_2$ (0.2 wt%) sample has a slightly decreased lattice parameter of 0.30 nm, which is correlative with the lattice distortion caused by the smaller atomic radius of Cu compared with Pb. Meanwhile, the imperceptible change in lattice parameter resulted from insufficient $CuBr_2$ doping.

A comparison of photophysical properties of pristine $CsPbI_2Br$ and composite $CsPbI_2Br$:$CuBr_2$ films was further investigated. Figure 3.1b presents the absorbance spectra of $CsPbI_2Br$ and $CsPbI_2Br$:$CuBr_2$ (0.2 wt%) films. $CsPbI_2Br$:$CuBr_2$ film showed obviously enhanced optical absorption in the whole region beyond 630 nm compared to the pristine perovskite film. The Tauc plot shown in the inset of Figure 3.1b indicated that the band gap of $CsPbI_2Br$ was increased from 1.88 eV to 1.95 eV after doping 0.2 wt% $CuBr_2$. To further clarify the doping effect of $CuBr_2$ on the electronic structure of $CsPbI_2Br$, density functional theory (DFT) calculations based on the exchange-correlation functions of Generalized Gradient Approximation (GGA) with Perdew-Burke-Ernzerhof (PBE) were executed. The calculation was carried out based on $CsPbI_2Br$ orthorhombic phase with space group of Pnma. One Cu atom substitutes one Pb atom from 16 equivalent sites is shown in Supporting Information Figure A3.2. The simulation results give a similar trend of increased band gap in $CsPbI_2Br$ by $CuBr_2$ doping. Interestingly, this phenomenon is different from the case of organic-inorganic hybrid perovskite in which Cu^{2+} doping reduced the band gap of $CH_3NH_3PbI_3$.[50] In planar structure PSCs, the band gap of perovskite absorber layer and the energy levels of interfacial layers are the main factors to determine the V_{oc} of the devices. Figure 3.1c presents a schematic of the energy levels of used materials in pristine $CsPbI_2Br$ and $CsPbI_2Br$:$CuBr_2$ based PSCs. Obviously, the V_{oc} is expected to be increased owing to the enlarged E_g by $CuBr_2$ doping.

The effects of $CuBr_2$ doping on the crystalline and morphological properties of $CsPbI_2Br$ films were further evaluated. **Figure 3.2a** shows the top-view scanning electron microscopy (SEM) images of $CsPbI_2Br$:$CuBr_2$ films with varied doping ratios (0-0.3 wt%). Compared to pristine $CsPbI_2Br$ film, the grain size in $CsPbI_2Br$:$CuBr_2$ films is enlarged with $CuBr_2$ doping ratio. The statistical distribution of the grain size in each film is plotted in Figure 3.2b. The average grain size in pristine $CsPbI_2Br$, $CsPbI_2Br$:$CuBr_2$ (0.1 wt%), $CsPbI_2Br$:$CuBr_2$ (0.2 wt%), and $CsPbI_2Br$:$CuBr_2$ (0.3 wt%) films was 643, 848, 1051 and 1255 nm, respectively. Although the grain size was enlarged, the $CuBr_2$ doping did not deteriorate the film morphology largely (Supporting Information, **Figure A3.3**).

Figure 3.2c shows the X-ray diffraction (XRD) patterns of corresponding $CsPbI_2Br$:$CuBr_2$ films. All samples exhibited a typical perovskite after a high temperature annealing process at 260 °C. The main diffraction peaks at 15.37° and 30.18° were assigned to (100) and (200) planes of $CsPbI_2Br$ δ-phase.[32] Obviously, the diffraction peak intensities in $CsPbI_2Br$:$CuBr_2$ films were stronger than that in pristine $CsPbI_2Br$ film, indicating an improved crystalline quality by $CuBr_2$ doping. The diffraction peak of PbI_2 was clearly observed in the magnified illustration shown in the right of Figure 3.2c. Furthermore, the intensity of PbI_2 was increased with the $CuBr_2$ doping ratio. According to previous studies,[51,52] appropriate amount of PbI_2 could effectively passivate the perovskite film with reduced defects and traps, whereas excessive PbI_2 would lower the crystalline quality of perovskite films. In addition, (100) peak was shifted to higher degree, indicating an incorporation of smaller Cu atoms into the lattice sites of $CsPbI_2Br$.[53,54] The high crystalline quality of $CsPbI_2Br$:$CuBr_2$ film was further revealed by grazing incidence X-ray diffraction (GIXRD) measurements. The inset of Figure 3.2d plots the 2D GIXRD profiles of pristine $CsPbI_2Br$ and $CsPbI_2Br$:$CuBr_2$ (0.2 wt%) films. Compared to the pristine film, the appearance of strongly scattered secondary spots and rings in $CsPbI_2Br$:$CuBr_2$ film suggests that

the polycrystalline film was grown with good orientation relative to the substrate plane. The preferred orientation in the $CsPbI_2Br$:$CuBr_2$ film was further proven by the plots of azimuthally integrated scattering intensities for two samples as shown in Figure 3.2d. Obviously, the peak intensity at 90° azimuth in $CsPbI_2Br$:$CuBr_2$ film was higher than that in pristine $CsPbI_2Br$ perovskite film, indicating a highly ordered orientation along (100) plane.[55-59] The preferred crystalline orientation means less defects and traps, which would improve the charge transport along the preferred direction and reduce the carrier recombination.

Furthermore, combined evaluation of SEM and XRD on typical steps during the formation of perovskite films is carried out to investigate the role of $CuBr_2$ in assisting the crystallization dynamics process of $CsPbI_2Br$. As shown in **Figure 3.3**, the freshly spin-coated $CsPbI_2Br$:$CuBr_2$ film presented poor crystalline quality with smaller grain size compared with pristine $CsPbI_2Br$ film. At a yellow phase before annealing, two new peaks at 12° and 32° were observed in both samples, indicating that the samples possess an intermediate phase. Noticeably, $CsPbI_2Br$:$CuBr_2$ film showed improved crystallization with larger grain size. However, more pinholes and voids were observed. After annealing, both films demonstrated compact morphology with excellent crystallization. Similar with Figure 3.2, $CsPbI_2Br$:$CuBr_2$ film exhibited superior crystallization with larger grain size compared with pristine $CsPbI_2Br$ film. The growing of perovskite film from initial small grain size to final large grain size suggests a slower crystallization dynamic process in $CsPbI_2Br$:$CuBr_2$ film. It means that $CuBr_2$ played an important role in retarding the crystallization rate of $CsPbI_2Br$ film. The direct comparison of photographs between the colors of $CsPbI_2Br$ and $CsPbI_2Br$:$CuBr_2$ films further revealed the slow crystallization process in $CuBr_2$-doped $CsPbI_2Br$ film (Supporting Information, Figure A3.4). To further understanding the effect of $CuBr_2$ doping on the stability of perovskite phase, Figure 3.3 shows the XRD patterns of perovskite films with or without $CuBr_2$ doping after exposure to ambient for more than 24 hours.

Exposure to ambient restores the films to the yellow phase. Nevertheless, $CsPbI_2Br$: $CuBr_2$ film kept part δ-phase with weak intensities of (100) and (200) peaks, indicating improved stability in $CsPbI_2Br$ by $CuBr_2$ doping.

3.2 Photovoltaic Performance

To investigate the effect of $CuBr_2$ doping on photovoltaic performance, n-i-p PSCs with a structure of FTO/TiO_2 /$CsPbI_2Br$:$CuBr_2$/Spiro-OMeTAD/MoO_3/Ag were fabricated (the area of device is 0.09 cm^2). **Figure 3.4a** shows the $CuBr_2$ ratio dependent *J-V* characteristics of $CsPbI_2Br$:$CuBr_2$ based PSCs under the AM 1.5G illumination with the light intensity of 100 mW cm^{-2}. The main cell parameters are summarized in **Table 3.1**. The reference device without $CuBr_2$ doping presented a PCE of 13.24%, a short-circuit current density (J_{sc}) of 16.18 mA cm^{-2}, a V_{oc} of 1.12 V and a fill factor (FF) of 0.73. The positive effect of $CuBr_2$ incorporation was very obvious even at very small amount. By doping 0.1 wt% $CuBr_2$, V_{oc} and J_{sc} were increased to 1.16 V and 16.92 mA cm^{-2}, respectively. At an optimized doping ratio of 0.2 wt%, the device approached a maximum PCE of 16.15% with a V_{oc} of 1.18 V, a J_{sc} of 16.95 mA cm^{-2} and an FF of 0.80. In addition, the cell was aged for 150 hours under continuous illumination with full intensity and maximum power point tracking (MPPT) in a nitrogen atmosphere (Figure A3.5), the device retained more than 80% of its initial performance. Figure 3.4b plots the changes of V_{oc} and J_{sc} with $CuBr_2$ doping ratio. J_{sc} achieved the maximum at the optimized doping ratio of 0.2 wt%. However, V_{oc} reached a maximum of 1.19 V when the doping ratio was further increased to 0.3 wt%. The incident-photon-to-current efficiency (IPCE) spectra of the reference device and the champion device are displayed in Figure 3.4c. In the absorbance range from 420 to 640 nm, almost all of EQE values are exceeding 85%. From IPCE values, the integrated current density is 16.78 mA cm^{-2}, which agrees well with the value from *J-V* curve. Figure 3.4d gives the steady-

state photocurrent and PCE values measured over a period of 900 s at the maximum power point of 0.87 V, these devices are very stable with the PCE of 15.93% for over 900 s in ambient. To verify the reproducibility of high efficiency, 40 individual $CsPbI_2Br$:$CuBr_2$ based devices were fabricated. The histograms of PCE distributions are plotted in Figure 3.4e. The PCE distribution exhibits a small deviation with an average value of 14.6%, indicating a better device reproducibility.

Besides the device efficiency, the cell stability is another critical concern for perovskite solar cells. The device reliabilities of $CsPbI_2Br$ and $CsPbI_2Br$:$CuBr_2$ based PSCs were evaluated without encapsulation in ambient at room temperature and < 20% relative humidity. Figure 3.4f shows PCE decay as a function of time for one month. The reference device presents a poor stability during the test. The PCE reduces to 92% of the initial value after 18 days' aging. After that, the degradation rate increased with a rapid drop in PCE. It further deteriorated to 73% after 30 days continuous degradation. In contrast, $CsPbI_2Br$:$CuBr_2$ based device exhibits an excellent stability by remaining 95% of the initial value after one month aging. This means that the incorporation of $CuBr_2$ could play a very positive role in improving the cell stability of $CsPbI_2Br$ based all-inorganic PSC.

To clarify the positive influence of $CuBr_2$ on the cell performance, a detailed investigation on the elements distributions and carrier dynamic process in the device was executed. **Figure 3.5a** and **3.5b** gives the time-of-flight secondary ion mass spectroscopy (TOF-SIMS) depth profiles including CN, Ag, Pb, Cs and Cu elements in $CsPbI_2Br$ and $CsPbI_2Br$:$CuBr_2$ based PSCs. The insets show the 3D distribution for these elements. As expected, Cu elements are distributed homogeneously throughout the perovskite film similar as Pb and Cs elements. The energy-dispersive X-ray spectroscopy (EDS) mapping of Cu and Br elements further verifies the uniform distribution of $CuBr_2$ in $CsPbI_2Br$:$CuBr_2$ film (Supporting Information, Figure A3.6). In addition,

there was no evident shift of the TOF-SIMS depth profiles of Pb and Cs elements in two devices, suggesting that the incorporation of $CuBr_2$ did not change the distribution of other elements. To explore the degradation origin of $CsPbI_2Br$:$CuBr_2$ film during a long-time operation, TOF-SIMS was performed to detect changes chemical composition in a sample of FTO/TiO_2/$CsPbI_2Br$:$CuBr_2$. The sample was kept in ambient with 60% humidity over 24 h until it completely transformed into a yellow phase. As shown in Supporting Information Figure A3.7, there is no obvious diffusion of Cu element as the sample transforms into a yellow phase on aging. The depth profiles of TOF-SIMS provided the direct information of key elemental distributions in the device before and after degradation.

The diode behavior was evaluated by getting rid of other possible interference induced by light, typical dark *J-V* characteristics in $CsPbI_2Br$ and $CsPbI_2Br$:$CuBr_2$ PSCs are shown in **Figure 3.6a**. Compared to the reference device, the $CuBr_2$-doped device exhibited lower leakage current. In the exponential behavior regime, the ideal factor *n* can be derived from[60]

$$ln(J) = ln(J_0) + (\frac{1}{n})\frac{q}{k_BT}V \quad \ldots\ldots\ldots\ldots\ldots\ldots (1)$$

where *J* is the current density, J_0 is the reverse saturation current density, *q* is elemental charge, k_B is the Boltzmann constant, *T* is the temperature. By fitting the dark *J-V* curve, the ideal factor *n* is extrapolated to be 3.4 and 2.5 for $CsPbI_2Br$ and $CsPbI_2Br$:$CuBr_2$ based device, respectively. The large decrease of ideal factor indicates that the incorporation of $CuBr_2$ could enable the device deliver a better diode junction quality.[60] The electron extraction dynamics process in $CsPbI_2Br$ and $CsPbI_2Br$:$CuBr_2$ films were further investigated by steady-state photoluminescence (PL) and time-resolved photoluminescence (TRPL) spectra (Supporting Information, Figure A3.8). $CsPbI_2Br$:$CuBr_2$ film demonstrated stronger PL quenching than the pristine $CsPbI_2Br$ film. The blue-shift of PL emission peak and the decreased Stokes shift in the $CsPbI_2Br$:$CuBr_2$ film

suggests the positive role of $CuBr_2$ incorporation.[31,62] The shortened PL lifetime from 14.93 to 3.16 ns further confirmed the fast charge extraction in $CsPbI_2Br$:$CuBr_2$ film compared with the pristine $CsPbI_2Br$ film. I ascribe it to an excellent grain boundary passivation by $CuBr_2$ with reduced defect states.

To compare the trap states in $CsPbI_2Br$ and $CsPbI_2Br$:$CuBr_2$ based devices, the charge transport characteristics in two devices were evaluated. Figure 3.6b shows the *J-V* curves by double-logarithmic plots of $CsPbI_2Br$- and $CsPbI_2Br$:$CuBr_2$-based hole-only and electron-only devices. Typical *J-V* shapes with three regions, Ohmic current, trap-fill limited (TFL) current and space charge limited current (SCLC),[63-66] were observed in four devices. The trap densities (n) could be calculated by $n = (2V_{TFL}\varepsilon\varepsilon_0)/eL^2$, where V_{TFL} is the trap-fill limit voltage, L is the thickness of $CsPbI_2Br$ active layer, ε is the relative dielectric constant of $CsPbI_2Br$, ε_0 is the vacuum permittivity, and e is the electron charge. As shown in **Table 3.2**, $CuBr_2$-doped $CsPbI_2Br$ films show significantly reduced trap density regardless in hole-only or electron-only devices. The hole and electron mobilities were further calculated according to Mott-Gurney's equation $\mu = (8JL^3)/(9\varepsilon\varepsilon_0V^2)$[67-69] in the SCLC region. By $CuBr_2$ doping, the hole and electron mobilities were increased from 0.92 to 1.55 $cm^2\,V^{-1}\,S^{-1}$ and from 0.23 to 0.99 $cm^2\,V^{-1}\,S^{-1}$, respectively. The reduced trap states and improved carrier mobilities were attributed to the improved crystal quality of $CsPbI_2Br$ films by $CuBr_2$ doping. I see this as the main reason for the largely improved device performance in $CsPbI_2Br$:$CuBr_2$ based devices.

3.3 CONCLUSION

I have demonstrated a high-performance all-inorganic perovskite solar cell by using $CuBr_2$-mediated $CsPbI_2Br$ film as the absorber layer. $CuBr_2$ is directly incorporated into the $CsPbI_2Br$

precursor by controlling the perovskite crystallization with suppressed nucleation rate during the annealing process. The retarded crystalline dynamics process results in a high quality all-inorganic perovskite film with enlarged grain size, improved carrier mobilities and reduced trap states. Accordingly, the cell efficiency is largely increased from 13.24% to 16.15% owing to simultaneous enhancements in the cell parameters of V_{oc}, J_{sc} and FF. In addition, the resulting devices also present an excellent stability by retaining 95% of the initial value after one month~~'s~~ aging. This simple strategy opens a new route to realizing highly efficient and stable all-inorganic perovskite solar cells.

References

(1) Kojima, A.; Teshima, K.; Shirai, Y.; Miyasaka, T. *J. Am. Chem. Soc.* **2009,** *131*, 6050-6051.

(2) Jeon, N. J.; Na, H.; Jung, E. H.; Yang, T.-Y.; Lee, Y. G.; Kim, G.; Shin, H.-W.; Seok, S. I.; Lee, J.; Seo, Jeon N J, Na H, Jung E H, et al. *Nat. Energy* **2018,** *3*, 682.

(3) Song, T.-B.; Yokoyama, T.; Stoumpos, C. C.; Logsdon, J.; Cao, D. H.; Wasielewski, M. R. *J. Am. Chem. Soc.* **2017,** *139*, 836-842.

(4) Yang, Y.; You, J. *Nature* **2017,** *544*, 155.

(5) Tsai, H.; Nie, W.; Blancon, J.-C.; Stoumpos, C. C.; Asadpour, R.; Harutyunyan, B.; Neukirch, A. J.; Verduzco, R.; Crochet, J. J.; Tretiak, S. *Nature* **2016,** *536*, 312.

(6) Li, W.; Zhang, C.; Ma, Y.; Liu, C.; Fan, J.; Mai, Y.; & Schropp, R. E. *Energy Environ. Sci.* **2018**, *11*, 286-293.

(7) Wang, Z. K.; Li, M.; Yang, Y. G.; Hu, Y.; Ma, H.; Gao, X. Y.; Liao, L. S. *Adv. Mater.* **2016,** *28*, 6695-6703.

(8) Li, M.; Wang, Z. K.; Zhuo, M. P.; Hu, Y.; Hu, K. H.; Ye, Q. Q.; Jain, S. M.; Yang, Y. G.; Gao, X. Y.; Liao, L. S. *Adv. Mater.* **2018,** *30*, 1800258.

(9) Zhang, H.; Wang, H.; Williams, S. T.; Xiong, D.; Zhang, W.; Chueh, C. C.; Chen, W.; Jen, A. K. Y. *Adv. Mater.* **2017,** *29*, 1606608.

(10) Chen, Q.; Chen, L.; Ye, F.; Zhao, T.; Tang, F.; Rajagopal, A.; Jiang, Z.; Jiang, S.; Jen, A. K.-Y.; Xie, Y. *Nano lett.* **2017,** *17*, 3231-3237.

(11) Gong, X.; Li, M.; Shi, X. B.; Ma, H.; Wang, Z. K.; Liao, L. S. *Adv. Funct. Mater.* **2015,** *25*, 6671-6678.

(12) Liu, C.; Li, W.; Zhang, C.; Ma, Y.; Fan, J.; & Mai, Y. *J. Am. Chem. Soc*. **2018**,*140*, 3825-3828.

(13) Yang, Z.; Chueh, C. C.; Zuo, F.; Kim, J. H.; Liang, P. W.; Jen, A. K. Y. *Adv. Energy Mater.* **2015,** *5*, 1500328.

(14) Huang, J.; Tan, S.; Lund, P. D.; Zhou, H. *Energy Environ. Sci.* **2017,** *10*, 2284-2311.

(15) Chen, S.; Duan, J.; Tang, Y.; Jin, B.; Qiao, S. Z. *Nano Energy* **2015,** *11*, 11-18.

(16) Wang, Q.; Dong, Q.; Li, T.; Gruverman, A.; Huang, J. *Adv. Mater.* **2016,** *28*, 6734-6739.

(17) Liu, C.; Li, W.; Zhang, C.; Ma, Y.; Fan, J.; & Mai, Y. *J. Am. Chem. Soc.* **2018**, *140*, 3825-3828.

(18) Kulbak, M.; Cahen, D.; Hodes, G. *J. Phys. Chem. lett.* **2015,** *6*, 2452-2456.

(19) Liang, J.; Wang, C.; Wang, Y.; Xu, Z.; Lu, Z.; Ma, Y.; Zhu, H.; Hu, Y.; Xiao, C.; Yi, X. *J. Am. Chem. Soc.* **2016,** *138*, 15829-15832.

(20) Kulbak, M.; Gupta, S.; Kedem, N.; Levine, I.; Bendikov, T.; Hodes, G.; Cahen, D. *J. Phys.Chem. Lett.* **2015,** *7*, 167-172.

(21) Wang, Q.; Zheng, X.; Deng, Y.; Zhao, J.; Chen, Z.; Huang, J. *Joule* **2017,** *1*, 371-382.

(22) Zhao, D.; Yu, Y.; Wang, C.; Liao, W.; Shrestha, N.; Grice, C. R.; Cimaroli, A. J.; Guan, L.; Ellingson, R. J.; Zhu, K. *Nat. Energy* **2017,** *2*, 17018.

(23) McMeekin, D. P.; Sadoughi, G.; Rehman, W.; Eperon, G. E.; Saliba, M.; Hörantner, M. T.; Haghighirad, A.; Sakai, N.; Korte, L.; Rech, B. *Science* **2016,** *351*, 151-155.

(24) Bush, K. A.; Palmstrom, A. F.; Zhengshan, J. Y.; Boccard, M.; Cheacharoen, R.; Mailoa, J. P.; McMeekin, D. P.; Hoye, R. L.; Bailie, C. D.; Leijtens, T. *Nat. Energy* **2017,** *2*, 17009.

(25) Eperon, G. E.; Leijtens, T.; Bush, K. A.; Prasanna, R.; Green, T.; Wang, J. T.-W.; McMeekin, D. P.; Volonakis, G.; Milot, R. L.; May, R. *Science* **2016,** *354*, 861-865.

(26) Ahmad, W.; Khan, J.; Niu, G.; Tang, J. *Solar RRL* **2017,** *1*, 1700048.

(27) Wang, Y.; Zhang, T.; Kan, M.; Zhao, Y. *J. Amer. Chem. Soc.* **2018**, *140*,12345-12348.

(28) Wang, P.; Zhang, X.; Zhou, Y.; Jiang, Q.; Ye, Q.; Chu, Z.; Li, X.; Yang, X.; Yin, Z.; You, J. *Nat. Commun.* **2018,** *9*, 2225.

(29) Stoumpos, C. C.; Malliakas, C. D.; Kanatzidis, M. G. *Inorg. Chem.* **2013,** *52*, 9019-9038.

(30) Akkerman, Q. A.; Gandini, M.; Di Stasio, F.; Rastogi, P.; Palazon, F.; Bertoni, G.; Ball, J. M.; Prato, M.; Petrozza, A.; Manna, L. *Nat. Energy* **2017,** *2*, 16194.

(31) Chen, W.; Zhang, J.; Xu, G.; Xue, R.; Li, Y.; Zhou, Y.; Hou, J.; Li, Y. *Adv. Mater.* **2018,** *30*, 1800855.

(32) Lau, C. F. J.; Deng, X.; Ma, Q.; Zheng, J.; Yun, J. S.; Green, M. A.; Huang, S.; Ho-Baillie, A. W. *ACS Energy Lett.* **2016,** *1*, 573-577.

(33) Zeng, Q.; Zhang, X.; Feng, X.; Lu, S.; Chen, Z.; Yong, X.; Redfern, S. A.; Wei, H.; Wang, H.; Shen, H. *Adv. Mater.* **2018,** *30*, 1705393.

(34) Zhang, J.; Bai, D.; Jin, Z.; Bian, H.; Wang, K.; Sun, J.; Wang, Q.; Liu, S. *Adv. Energy Mater.* **2018,** *8*, 1703246.

(35) Sutton, R.; Eperon, G.; Miranda, L.; Parrott, E.; Kamino, B.; Patel, J.; Hörantner, M.; Johnston, M.; Haghighirad, A.; Moore, D., Adv. Energy Mater. **2016**, *6*, 1502458.

(36) Chen, C. Y.; Lin, H. Y.; Chiang, K. M.; Tsai, W. L.; Huang, Y. C.; Tsao, C. S.; Lin, H. W. *Adv. Mater.* **2017,** *29*, 1605290.

(37) Weissbuch, I.; Lahav, M.; Leiserowitz, L. *Cryst. Growth Des.* **2003,** *3*, 125.

(38) Chung, S.-Y.; Kim, Y.-M.; Kim, J.-G.; Kim, Y.-J. *Nature Phys.* **2009,** *5*, 68.

(39) Burschka, J.; Pellet, N.; Moon, S.-J.; Humphry-Baker, R.; Gao, P.; Nazeeruddin, M. K.; Grätzel, M. *Nature* **2013,** *499*, 316.

(40) Liang, P. W.; Chueh, C. C.; Xin, X. K.; Zuo, F.; Williams, S. T.; Liao, C. Y.; Jen, A. K. Y. *Adv. Energy Mater.* **2015,** *5*, 1400960.

(41) Zhao, Y.; Wei, J.; Li, H.; Yan, Y.; Zhou, W.; Yu, D.; Zhao, Q. *Nat. Commun.* **2016,** *7*, 10228.

(42) Wang, Z.-K.; Gong, X.; Li, M.; Hu, Y.; Wang, J.-M.; Ma, H.; Liao, L.-S. *ACS Nano* **2016,** *10*, 5479-5489.

(43) Jiang, L. L.; Wang, Z. K.; Li, M.; Zhang, C. C.; Ye, Q. Q.; Hu, K. H.; Lu, D. Z.; Fang, P. F.; Liao, L. S. *Adv.Funct. Mater.* **2018,** *28*, 1705875.

(44) Yamashita, Y. *Sci Technol. Adv. Mater.* **2009,** *10*, 024313.

(45) Nam, J. K.; Chai, S. U.; Cha, W.; Choi, Y. J.; Kim, W.; Jung, M. S.; Kwon, J.; Kim, D.; Park, J. H. *Nano Lett.* **2017,** *17*, 2028-2033.

(46) Appukkuttan, P.; Dehaen, W.; Fokin, V. V.; Van der Eycken, E. *Org. Lett.* **2004,** *6*, 4223-4225.

(47) Baradarani, M. M.; Farshi, H.; Khodaie, M.; Fazlelahi, H. Z.; Rashidi, A.; Joule, J. A. *J. Hetero. Chem.* **2018,** *55*, 91.

(48) Zeng, Z.; Zhang, J.; Gan, X.; Sun, H.; Shang, M.; Hou, D.; Lu, C.; Chen, R.; Zhu, Y.; Han, L. *Adv. Energy Mater.* **2018,** *8*, 1801050.

(49) Zeng, Q.; Zhang, X.; Feng, X.; Lu, S.; Chen, Z.; Yong, X.; Zhang, W. *Adv. Mater.* **2018**, 30, 1705393.

(50) Lau, C. F. J.; Zhang, M.; Deng, X.; Zheng, J.; Bing, J.; Ma, Q.; Kim, J.; Hu, L.; Green, M. A.; Huang, S. *ACS Energy Lett.* **2017,** *2*, 2319-2325.

(51) Xu, W.; Zheng, L.; Zhang, X.; Cao, Y.; Meng, T.; Wu, D.; Liu, L.; Hu, W.; Gong, X. *Adv. Energy Mater.* **2018,** *8*, 1703178.

(52) Jahandar, M.; Heo, J. H.; Song, C. E.; Kong, K.-J.; Shin, W. S.; Lee, J.-C.; Im, S. H.; Moon, S.-J. *Nano Energy* **2016,** *27*, 330-339.

(53) Wang, H. Y.; Hao, M. Y.; Han, J.; Yu, M.; Qin, Y.; Zhang, P.; Guo, Z. X.; Ai, X. C.; Zhang, J. P. *Chem. A Europ. J.* **2017,** *23*, 3986-3992.

(54) Liu, F.; Dong, Q.; Wong, M. K.; Djurišić, A. B.; Ng, A.; Ren, Z.; Shen, Q.; Surya, C.; Chan, W. K.; Wang, J. *Adv. Energy Mater.* **2016,** *6*, 1502206.

(55) Arunkumar, P.; Gil, K. H.; Won, S.; Unithrattil, S.; Kim, Y. H.; Kim, H. J.; Im, W. B. *J. Phys. Chem. Lett.* **2017,** *8*, 4161-4166.

(56) De, A.; Mondal, N.; Samanta, A. *Nanoscale* **2017,** *9*, 16722-16727.

(57) Wu, Z.; Bai, S.; Xiang, J.; Yuan, Z.; Yang, Y.; Cui, W.; Gao, X.; Liu, Z.; Jin, Y.; Sun, B. *Nanoscale* **2014,** *6*, 10505-10510.

(58) Feng, S.; Yang, Y.; Li, M.; Wang, J.; Cheng, Z.; Li, J.; Ji, G.; Yin, G.; Song, F.; Wang, Z.; Li, J.; Gao, X. *ACS Appl. Mater. Interfaces* **2016,** *8*., 14503-14512.

(59) Grancini, G.; Marras, S.; Prato, M.; Giannini, C.; Quarti, C.; De Angelis, F.; De Bastiani, M.; Eperon, G. E.; Snaith, H. J.; Manna, L.; Petrozza, A. *J. Phys. Chem. Lett.* **2014,** *5*, 3836-3842.

(60) Yang, Y.; Feng, S.; Xu, W.; Li, M.; Li, L.; Zhang, X.; Ji, G.; Zhang, X.; Wang, Z.; Xiong, Y.; Cao, L.; Sun, B.; Gao, X. *ACS Appl. Mater. Interfaces* **2017,** *9*, 23141-23151.

(61) Yang, Y.; Feng, S.; Li, M.; Li, F.; Zhang, C.; Han, Y.; Li, L.; Yuan, J.; Cao, L.; Wang, Z.; Sun, B.; Gao, X. *Nano Energy* **2018,** *48*, 10-19.

(62) Liao, P.; Zhao, X.; Li, G.; Shen, Y.; Wang, M. *Nano-Micro Lett.* **2018,** *10*, 5.

(63) Kim, J.; Yun, J.-H.; Kim, H.; Cho, Y.; Park, H.-H.; Kumar, M. M. D.; Yi, J.; Anderson, W. A.; Kim, D.-W. *Sci. Rep.* **2015,** *5*, 9256.

(64) Shao, Y.; Xiao, Z.; Bi, C.; Yuan, Y.; Huang, J. *Nat. Commun.* **2014,** *5*, 5784.

(65) Ruppel, W. *Helv. Phys. Acta* **1958,** *31*, 311-313.

(66) Lou, Y.; Xu, M.; Zhang, L.; Wang, Z.; Naka, S,; Okada, L.; Liao, L. *Org. Electron*. **2013**, *14,* 2698-2704.

(67) Adinolfi, V.; Yuan, M.; Comin, R.; Thibau, E.; Shi, D.; Saidaminov, M.; Kanjanaboos, P.; Kopilovic, D.; Hoogland, S.; Lu, Z. *Adv. Mater*. **2016**, *28*, 3406-3410.

(68) Li, M.; Wang, Z.; Yang, Y.; Hu, Y.; Feng, S.; Wang, J.; Gao, X.; Liao, L. *Adv. Mater.* **2016**, *6*, 1601156.

(69) Saidaminov, M.; Haque, M.; Almutlaq, J.; Sarmah, S.; Miao, X.; Begum, R.; Zhumekenov, A.; Dursun, I.; Cho, N.; Murali, B. *Adv. Mater*. **2017**, *5*, 1600704.

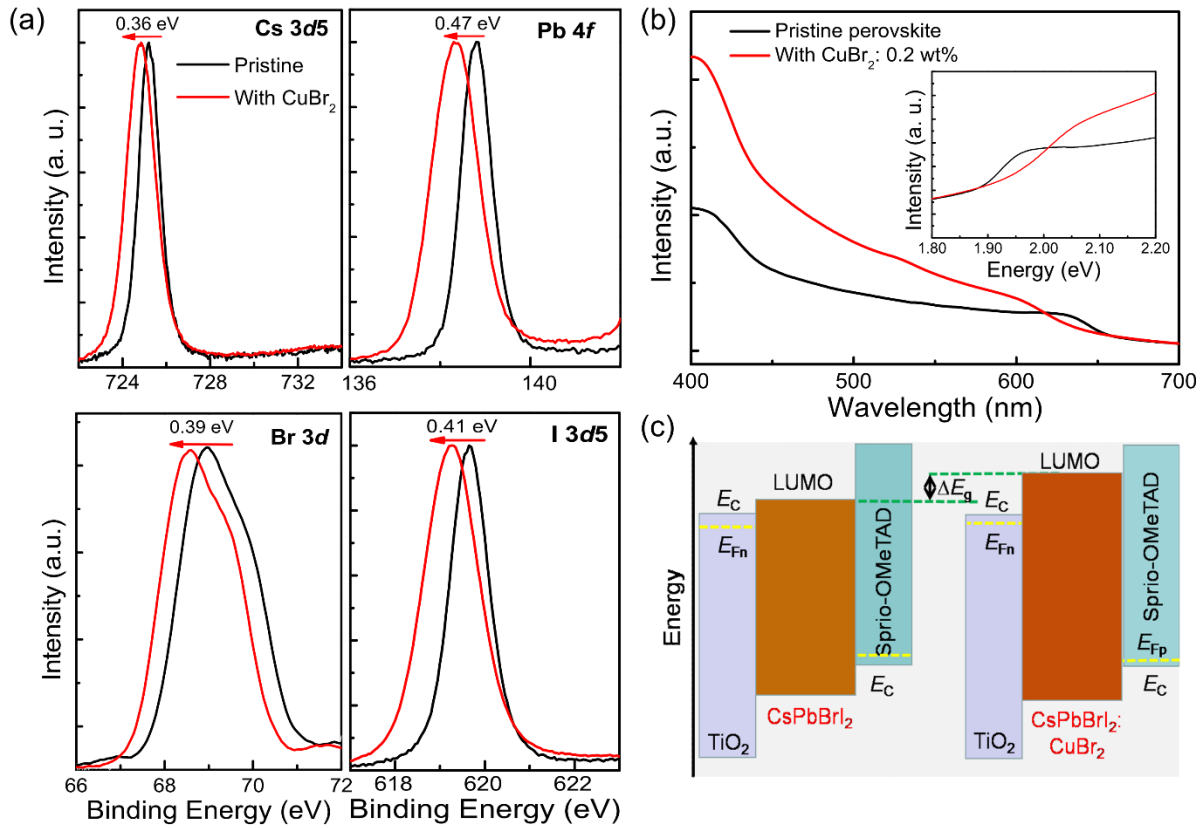

Figure 3.1. (a) XPS spectra for Cs 3*d*5, Pb 4*f*, Br 3*d* and I 3*d*5 in $CsPbI_2Br$ and $CsPbI_2Br$:$CuBr_2$ (0.2 wt%) perovskite films. (b) UV-Vis spectra of $CsPbI_2Br$ and $CsPbI_2Br$:$CuBr_2$ (0.2 wt%) perovskite films. (c) Schematic energy level diagram of $CsPbI_2Br$ and $CsPbI_2Br$:$CuBr_2$ -based perovskite solar cells.

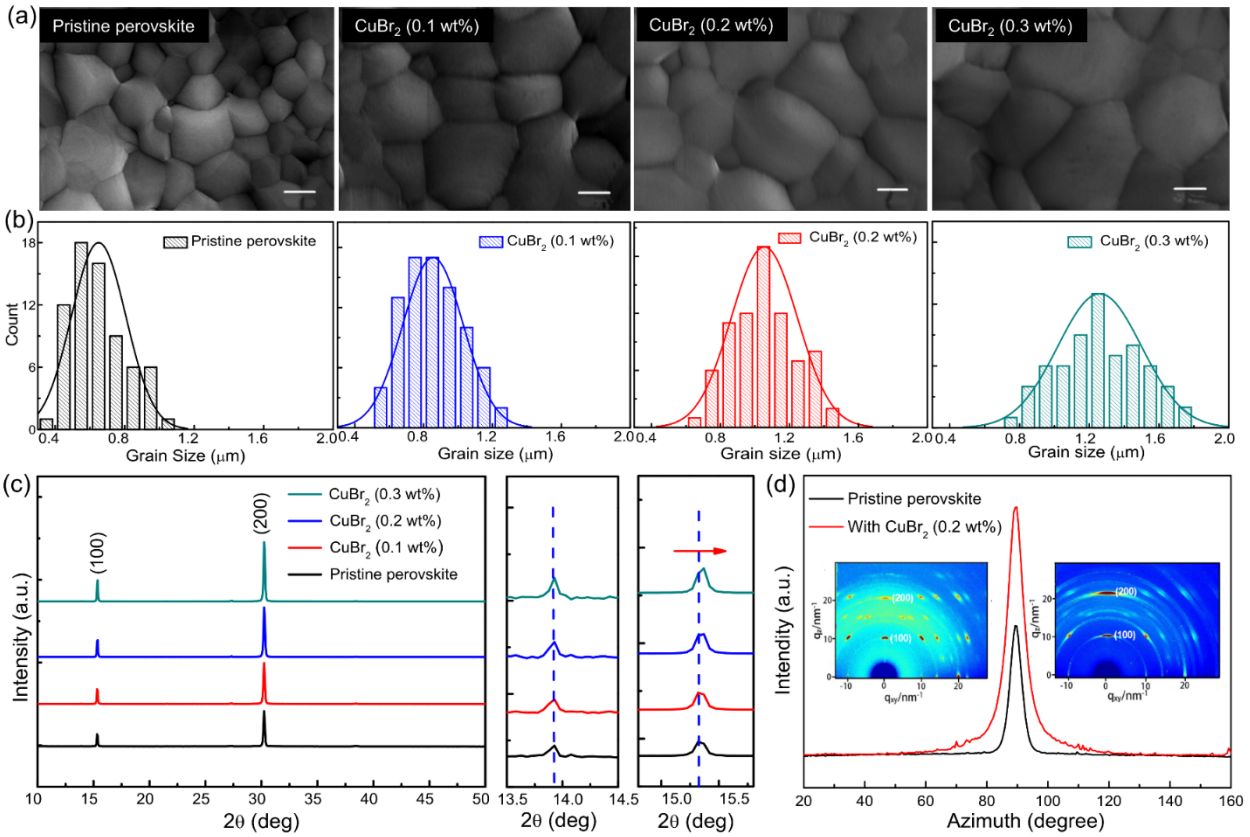

Figure 3.2. (a) Top-view SEM images (scale bar, 400 nm) and (b) grain size statistical distribution of $CsPbI_2Br$ films with various $CuBr_2$ ratio (0, 0.1, 0.2 and 0.3 wt%). (c) XRD profiles of corresponding $CsPbI_2Br$:$CuBr_2$ perovskite films. (d) Radially integrated intensity plots along the ring assigned to the (100) planes of $CsPbI_2Br$ and $CsPbI_2Br$: $CuBr_2$ (0.2 wt%) films. Insets are the corresponding GIXRD patterns.

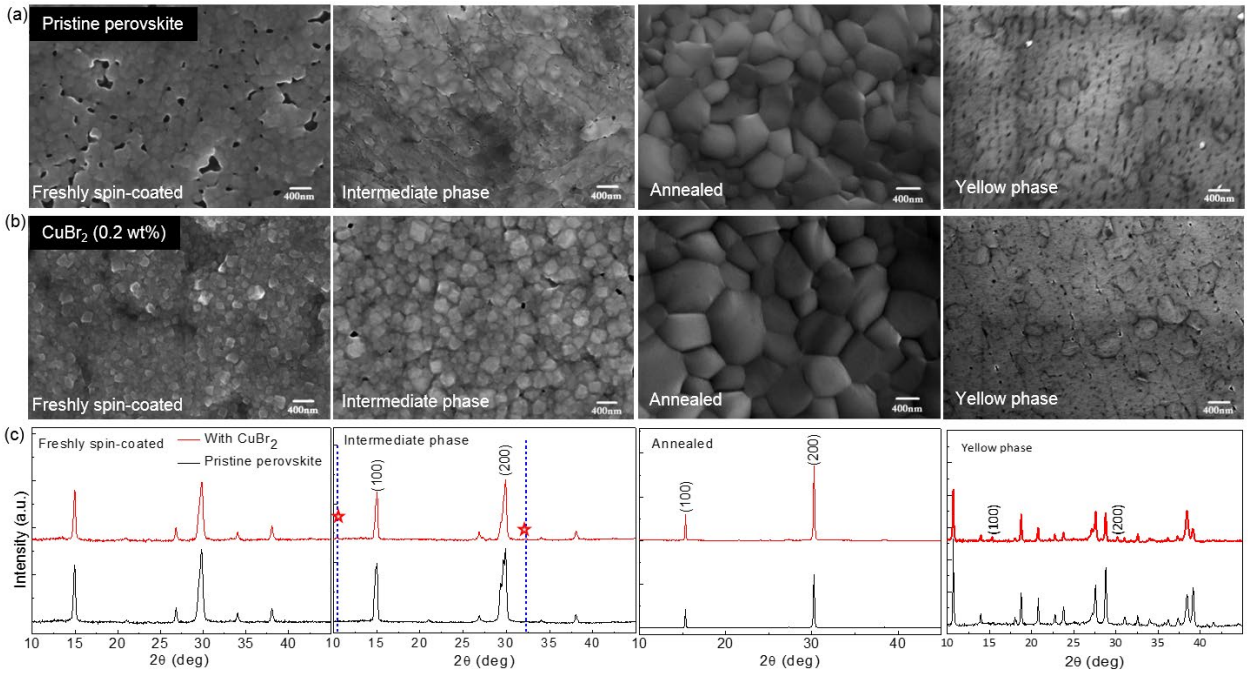

Figure 3.3. Top SEM images of (a) $CsPbI_2Br$ and (b) $CsPbI_2Br$:$CuBr_2$ (0.2 wt%) films at typical steps during perovskite formation. (c) XRD patterns of $CsPbI_2Br$ and $CsPbI_2Br$:$CuBr_2$ (0.2 wt%) films at corresponding steps.

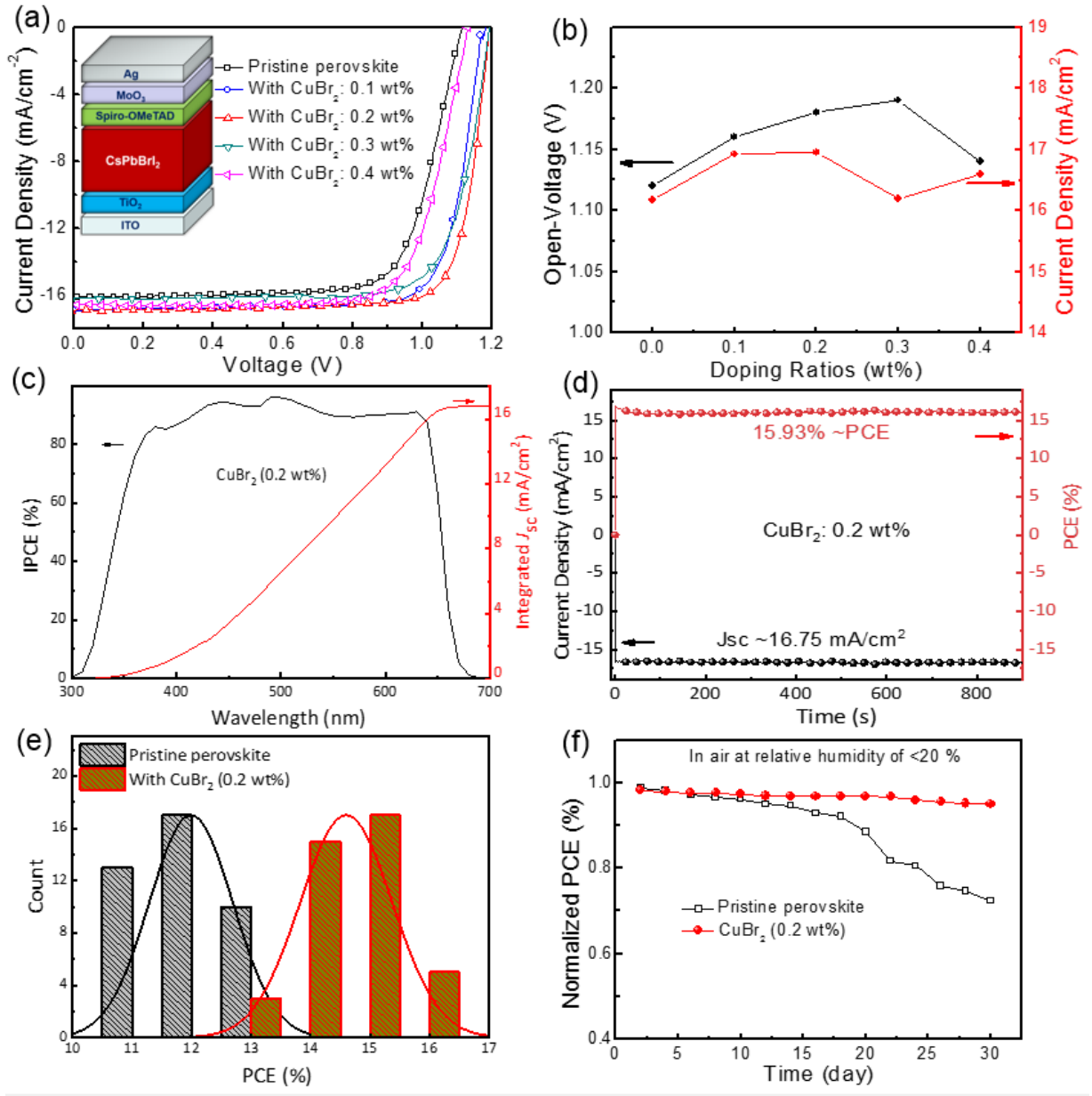

Figure 3.4. (a) *J-V* curves of perovskite solar cells measured under simulated AM 1.5 sunlight of 100 mW cm^{-2}. (b) Doping ratio dependence of open voltage and current density in devices with $CsPbI_2Br$ and $CsPbI_2Br$:$CuBr_2$ (0.2 wt%) films. c) IPCE spectra and d) steady power output curves for $CsPbI_2Br$:$CuBr_2$ (0.2 wt%)-based device and their corresponding photocurrent output at 0.87 V. e) A histogram of PCEs measured from $CsPbI_2Br$ and $CsPbI_2Br$:$CuBr_2$ (0.2 wt%)-based device. (f) Long-term stability of $CsPbI_2Br$:$CuBr_2$ (0.2 wt%) based devices without encapsulation.

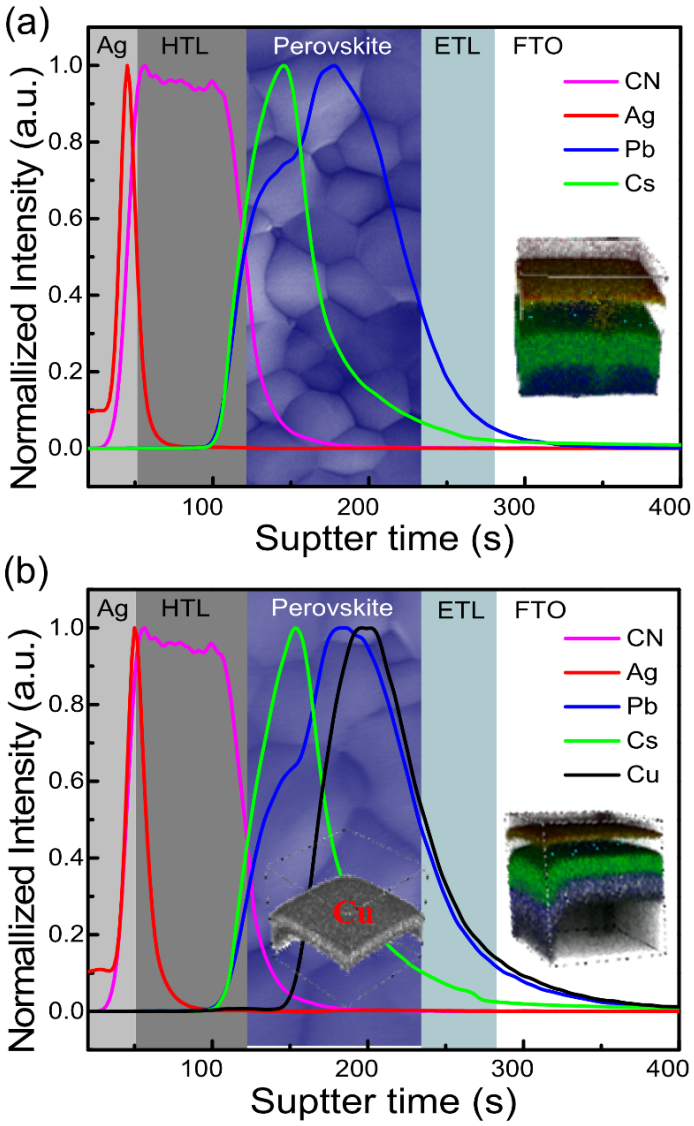

Figure 3.5. Time-of-flight secondary ion mass spectroscopy (TOF-SIMS) depth profiles of (a) $CsPbI_2Br$ and (b) $CsPbI_2Br$:$CuBr_2$ (0.2 wt%) based perovskite solar cells.

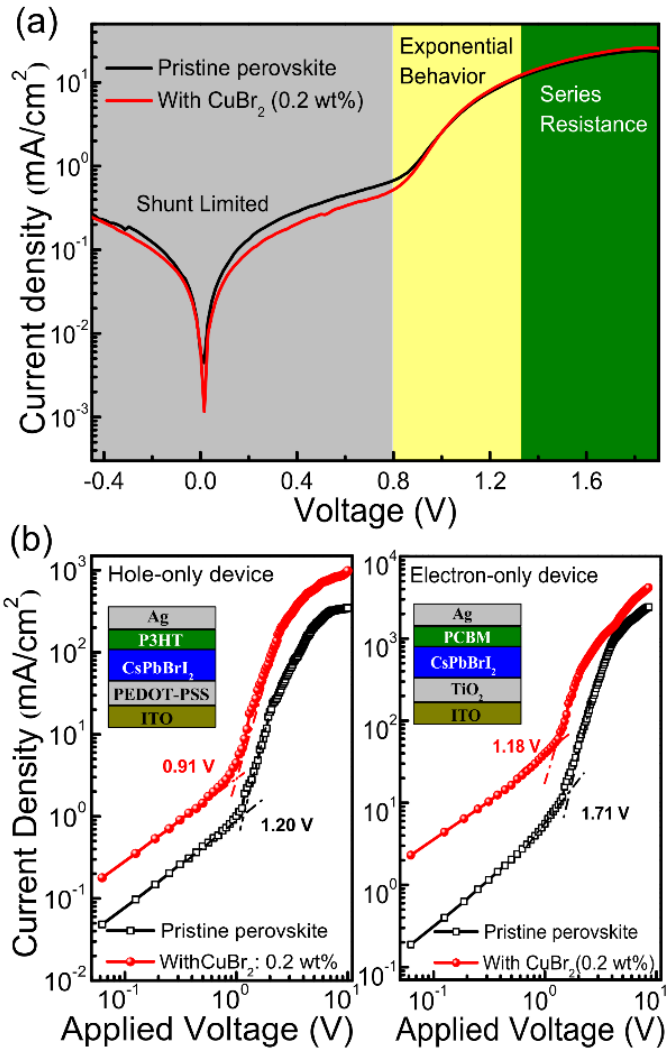

Figure 3.6. (a) Dark *J-V* curves in $CsPbI_2Br$ and $CsPbI_2Br$: $CuBr_2$ (0.2 wt%) based perovskite solar cells. (b) Dark *J-V* characteristics of hole-only and electron-only devices with or without $CuBr_2$ (0.2 wt%) doping.

Table 3.1. Cell parameters of $CsPbI_2Br$:$CuBr_2$ based perovskite solar cells with various $CuBr_2$ doping ratio.

Perovskites	V_{oc} **(V)**	J_{sc} **(mA/cm^2)**	**FF**	**PCE (%)**
Pristine perovskite	1.12	16.18	0.73	13.24
With $CuBr_2$: 0.1 wt%	1.16	16.92	0.79	15.45
With $CuBr_2$: 0.2 wt%	1.18	16.95	0.80	16.15
With $CuBr_2$: 0.3 wt%	1.19	16.20	0.77	14.89
With $CuBr_2$: 0.4 wt%	1.14	16.59	0.74	13.99

Table 3.2. Electronic properties of $CsPbI_2Br$ and $CsPbI_2Br$:$CuBr_2$ (0.2 wt%) based perovskite solar cells.

Device	τ_{ave} (ns)	τ_{t-e} (cm^{-3})	τ_{t-h} (cm^{-3})	u_e ($cm^2V^{-1}s^{-1}$)	u_h ($cm^2V^{-1}s^{-1}$)
Pristine perovskite	14.93	8.60×10^{16}	8.60×10^{16}	0.23	0.92
With $CuBr_2$: .2 wt%	3.16	5.90×10^{16}	4.55×10^{16}	0.99	1.55

Chapter 4 Crystalline Liquid-like Behavior: Surface-Induced Secondary Grain Growth of Photovoltaic Perovskite Thin Film

Surface effects play a dominant role in regulating the properties of a solid when the size reaches the nanoscale regime [1–4]. For micron or submicron thin films, which are the most commonly employed thicknesses in microelectronics industry, the surface effect on the internal properties of the entire film will usually be negligible. However, for "soft" matters such as polymers, or taking the extreme, liquids, due to their highly deformable or flowable character, they can be highly responsive to an external field, upon which the depth scale affected by the surface can dramatically increase to the microscale or even larger [5–7]. Halide perovskite semiconductor materials were recently reported to be inherently "soft"-structured [8–11], which can be described as a crystalline liquid with both crystalline solid and liquid-like behaviors. The soft nature of halide perovskites offers the possibility of regulating their micron-scale thin film behavior via a simple tuning of surface features. Among typical industrial electronic device fabrication techniques, secondary grain growth is a powerful strategy for the fabrication of polycrystalline thin films with grain sizes much larger than the film thickness or even towards single crystal thin films [12–16]. The resulting reduced grain boundaries not only improve the electronic or photoelectronic behavior but also suppress device degradation pathways resulting from grain boundaries [17–20]. The driving force (ΔF) of secondary grain growth stems from the existence of one or a set of crystallographic textures that minimize the surface free energy such that the grains will grow larger along the orientation to minimize the free energy of the system, which is shown below [13]:

$$\Delta F = F_f - F_i = -\frac{2(\Delta\gamma)}{h} + \frac{\beta\gamma_{gb}}{r}$$

where F_i and F_f is the energy per unit volume before and after the secondary grain growth, respectively; $\Delta\gamma$ is defined as surface energy anisotropy $(\bar{\gamma} - \gamma_{min})$; h is the film thickness; β is

a geometric factor (typically equals to 0.85 when using a cylinder geometry model); γ_{gb} is an average grain boundary energy per unit area. The state-of-art techniques for secondary grain growth commonly involve harsh and complicated conditions, such as elevated and/or cyclic temperature annealing, chemical doping, and high-pressure plastic straining, to obtain the driving force to trigger grain boundary migration [21–25]. The "soft" liquid-like nature of perovskite offers a way to take advantage of the surface effect on the inner film properties for secondary grain growth. Hence, here we demonstrate a surface-induced secondary grain growth (SISG) technique, where surface modification induces post-crystallization grain growth in the entire perovskite thin film. This strategy sheds light on a new perspective for the perovskite research community, offering a novel methodology for property manipulation of perovskite thin films: changing the surface can induce the property evolution of the perovskite thin film as a whole.

4.1 Theoretical modeling of the driving force

For investigation of SISG in perovskite thin films, we chose the $CsPbI_2Br$ perovskite as a model compound, since it is a relatively pure and simple system that contains only inorganic components. Organic components were left out because they will interfere with the elemental analysis and add complexity to the study of chemical interactions in the system, which will obfuscate the investigation of the underlying mechanism. Furthermore, compared with the pure iodine-based $CsPbI_3$ perovskite, $CsPbI_2Br$ shows an enhanced phase stability rendering it more promising towards commercialization. For surface manipulation, we chose three organic ammoniums with varying carbon lengths, i.e. n-butylammonium (BA), octyl ammonium (OCA), and oleylammonium (OLA), all of which potentially can lower the surface energy of the perovskite (100) plane when anchored to the void of the corner-sharing PbI_6^{4-} octahedron. I first

used density functional theory (DFT) to examine the surface energies of the organic ammonium terminated low-index planes of the perovskite based on a slab model (**Fig. 4.1** and Table B4.1. The detailed calculation method can be found in the Supporting Information). The surface free energies of the Cs, BA, OCA, and OLA-terminated (111) planes were found to be similar, while those of (100) plane were determined to be 4.30, 3.23, 2.14, and 1.97 eV/nm^{-2}, respectively. The surface energy differences between (100) and (111) planes are summarized in Fig. A4.1, demonstrating an increasing surface energy anisotropy in the following order: Cs, BA, OCA, and OLA. This indicated a corresponding increasing driving force for the secondary grain formation.

4.2 Characterizations of the grain growth and film properties

Following theoretical predictions, the three organic ammoniums were evaluated in the preparation of perovskite films via a sequential two-step procedure. $CsPbI_2Br$ perovskite film was fabricated using a one-step method consisting of spin-coating $PbI_2/PbBr_2/CsI$ mixed perovskite precursors on the substrate followed by annealing at 300 °C for 10 min. The substrate was then cooled down to room temperature, yielding black perovskite thin film, which indicates the formation of the $CsPbI_2Br$ cubic phase. For the targeted film, an ammonium iodide isopropanol solution was subsequently spin-coated onto the crystallized perovskite thin film followed by heating to 100 °C for 5 min to remove the excess solvent. For the reference film, pure isopropanol was spin-coated onto perovskite film followed by the same annealing process as the organic ammoniums to examine the effect of isopropanol and heat. The scanning electron microscopy (SEM) images of the fabricated films are shown in **Fig. 4.2A**. Crystal grains in the reference film were of almost the same size as the ones in the as-fabricated film without any post treatment (Fig. A4.2), indicating that isopropanol and heat did not induce the grain growth of

perovskite. However, films that underwent surface treatment using organic ammoniums showed much enlarged grains. The average grain sizes of films with different post-treatment conditions shown in Fig. 4.2B are 769 nm, 1277 nm, 1287 nm, and 1846 nm for reference, BA, OCA and OLA, respectively. I attribute this secondary grain growth process to the decrease in surface energy of a crystal facet that provides the driving force of surface anisotropy $\Delta\gamma$. On the one hand, the grain had an orientation, *i.e.* plane (100), that could minimize the surface energy of the film due to the existence of the organic ammonium on the surface. On the other hand, the low activation barrier of ion diffusion in perovskite facilitated by soft lattice modes can facilitate the grain boundaries rearrangement during the out-of-plane crystalline reorientation process (the orientation will be further discussed in detail) [10]. From another aspect, the highly anharmonic lattice with low-frequency modes and small elastic modulus renders the perovskite highly "flowable" and, thus, highly responsive to the influence from the surface [10,26]. Thus, the original perovskite grains were able to grow further in that favorable direction to reduce the energy of the whole system (Fig. 4.2C). The lower the surface energy, the larger the grain could grow. As a result, OLA, which gave the lowest surface energy, induced secondary grain growth with the largest resulting average grain size of up to 4 μm (Fig. A4.3). Muti-phase field model was also employed to simulate the grain growth for the film with and without OLA, which showed a significant increase of the grain size for the film with OLA (Fig. A4.4). This demonstrates that SISG is a powerful strategy towards precise control of perovskite grain size or even perovskite single crystal thin film given that the surface energy is rationally manipulated.

In situ real time Grazing-Incidence Wide-Angle X-ray Scattering (GIWAXS) was performed to obtain an in-depth insight into the SISG of the perovskite thin film. The X-ray diffraction signal measurement was initiated once the organic ammonium isopropanol solution was drop-cast onto the pristine perovskite thin film triggering the SISG (Fig. A4.5). **Fig. 4.3A** shows the time-

dependent diffraction peak evolution at q_z value of around 10 nm^{-1}, which is a characteristic peak corresponding to the (100) plane of the cubic phase of perovskite [27]. During the SISG process, the peak position gradually shifted to a lower q_z value, indicating a gradual decrease in lattice constant that possibly results from the strain relaxation during the grain growth. The initial peak splitting phenomenon can be attributed to the partial halide segregation in perovskite, which was commonly observed in the $CsPbI_2Br$ film [28]. At a later stage, the dual-peak behavior gradually disappeared, suggesting that the SISG that caused the strain relaxation, as well as, better crystallinity of the secondary perovskite grains, might also suppress the halide segregation, which could be beneficial to the long-term stability of the perovskite device (more details will be provided in the device description part) [28]. Such phenomenon was not observed in the reference film eliminating the effect of solvent and heat on the grain size growth in the perovskite film (Fig. A4.6). Fig 4.3B and 4.3C show the two-dimensional GIWAXS patterns of the perovskite film with and without SISG, respectively. The azimuth angle plots in Fig. 4.3D were obtained from the patterns by cutting along the (100) plane of the perovskite films. At the azimuth angle of 90°, the perovskite film with SISG showed a very sharp peak with a half peak width of 9.30°, much lower than that of the reference film (10.66°), demonstrating that SISG produced a more preferred out-of-plane orientation of the secondary perovskite grains. This is consistent with the growth mechanism we proposed earlier suggesting that the presence of organic ammonium on the surface lowers the surface energy of the (100) plane of perovskite and generates a driving force for the grain growth in that direction to minimize the energy of the system. High-resolution X-ray photoelectron spectroscopy (XPS) patterns of the Pb 4f of the reference and targeted films are shown in Fig. 4.3E. For the targeted film, two main peaks located at 138.14 and 143.00 eV were observed corresponding to the Pb 4*f* 7/2 and Pb 4*f* 5/2, respectively. For comparison, the reference film showed two main peaks at 138.76 and 143.42 eV. The peaks from Pb 4*f* shifted to

higher binding energies in the film after the SISG process based on OLA, indicating the interaction between organic ammonium on the surface and the Pb in the perovskite lattice [29]. The spatial distribution of OLA in the perovskite film with SISG was characterized by time-of-flight secondary-ion mass spectrometry (TOF-SIMS) with a device structure of ITO/SnO_2/perovskite/MoO_x/Au. As shown in Fig. 4.3F, the C and N profiles, which are the characteristic signals of OLA, exhibited a very narrow distribution (similar to the depth profile of Mo) with little overlap with the depth profile of Pb, which is a representative signal of perovskite. This signifies the existence of OLA only on the surface of the perovskite. The resulting organic ammonium-terminated perovskite film with SISG was further confirmed to have a lower surface energy (38.38 mN/m) than the reference film (59.78 mN/m) via contact angle measurements (Fig. A4.7, and Table B4.2). In order to further evaluate the perovskite film quality, the X-ray diffraction patterns of the perovskite film after the SISG process based on OLA were obtained (Fig. A4.8). They exhibited much higher peak intensity than that of the reference, suggesting enhanced crystallinity of the secondary perovskite grains. UV-Vis absorption spectrum (Fig. A4.9) demonstrates that the perovskite film with SISG showed higher absorption than the reference, which can be attributed to the enlarged grain sizes and thus enhanced light scattering [30]. The perovskite film after the SISG process exhibits much improved film quality necessary for enhancing the device performance.

4.3 Device performance and stability

I further assessed the photovoltaic performance of the perovskite films prepared with and without the SISG process by fabricating devices with the ITO/SnO_2/perovskite/PTAA/Au configuration, wherein PTAA refers to poly[bis(4-phenyl)(2,4,6-trimethylphenyl) amine]. Current density-

voltage (*J-V*) curves of the photovoltaic devices with and without SISG are compared in **Fig. 4.4A**, in which the highest power conversion efficiency (PCE) of the target device reached 16.58% with negligible hysteresis (open circuit voltage (V_{OC}): 1.23 V, short circuit current (J_{SC}): 16.85 mA cm^{-2}, fill factor (FF): 0.80), while a PCE of only 13.09% was achieved with the control device (V_{OC}: 1.11V, J_{SC}: 15.32 mA cm^{-2}, FF: 0.77). To the best of our knowledge, this is the highest PCE reported in the $CsPbI_2Br$ system. External quantum efficiency (EQE) spectra of the devices were compared in Fig. A4.10A. An integrated J_{SC} of 16.44 mA cm^{-2} from the target device matched well with the value measured from the *J-V* scan (<5% discrepancy), while a control device showed an integrated J_{SC} of 14.98 mA cm^{-2}. A stabilized PCE of 16.04% was achieved with the target device when biased at 1.06 V, while that of the control device was 12.36% when biased at 0.94 V (Fig. A4.10B). The remarkably enhanced V_{OC} (by up to 0.12 V) in the device based on SISG can be attributed to the enlarged grain size and, thus, decreased grain boundaries, which usually provide a non-radiative recombination pathway for the carriers due to trap states [20,31]. This is consistent with the transient photovoltage measurements (TPV) under open circuit condition. As shown in Fig. 4.4B, the device based on SISG exhibited a photovoltage decay time constant of 2.16 ms, which was longer than that of the reference device (1.31 ms), indicating less non-radiative recombination sites [32]. In addition, electrochemical impedance spectroscopy (EIS) characterization was performed to demonstrate the carrier transport processes under illumination at the interface (Fig. 4.4C). The middle frequency zone of the EIS semicircle should be dominated by the junction capacitance and recombination resistance related to the interfaces between the transport materials and the perovskite. According to Fig. 4.4C, the SISG-based device has a smaller impedance than that of the reference, signifying a substantial suppressed recombination at the interface, which most probably originates from the preferred orientation of the perovskite secondary grains that enable improved carrier flow between

perovskites and carrier transport layers [33]. Moreover, the hydrophobic tails of the OLAs on the surface of the perovskite could enhance the compatibility of the surface with the upper layer, PTAA, resulting in a better interfacial contact. The improved carrier dynamics can also be reflected in the measurement of transient photocurrent decay. As shown in Fig. 4.4D, the device with SISG had a shorter decay time constant of 0.91 μs compared to that of the reference device (1.23 μs), suggesting a faster carrier collection efficiency, which is consistent with the improved J_{SC} in the targeted device [32].

Not only does the photovoltaic efficiency significantly benefit from the SISG strategy, but also the device stability showed remarkable improvement in all aspects, including thermal stability, phase stability and, thus, operational stability. In Fig. 4.4E, the changes in PCE of the unencapsulated devices in a nitrogen atmosphere at 85 °C were tracked over time to test the long-term thermal stability. While the reference device degraded by 30% in 500 h, the target device maintained 90% of its initial efficiency during this time. Although the all-inorganic perovskite has been reported to show superior thermal and light stability to that of their organic-inorganic counterparts, it is well-known to suffer from a rapid phase transition to the non-perovskite phase, especially when exposed to moisture in ambient atmosphere [28]. However, the phase stability of the device based on SISG was noticeably enhanced, maintaining over 90% of its original PCE when stored under ambient conditions with 20-30% humidity at 25 °C for 4000 h. In contrast, the reference device lost >50% of its initial efficiency within 900 h (Fig. 4.4F). The operational stability of the devices was also compared in Fig. 4G. The reference device underwent fast degradation, while the device based on SISG maintain >90% of its initial efficiency over the course of 1000 h. Generally, we attribute the dramatically improved stability to two factors resulting from the SISG processing. On the one hand, high-quality perovskite films with reduced grain boundaries and higher crystallinity suppresses the degradation pathways either through

grain boundaries or ion migration, which is also one of the motivations towards single crystal perovskite thin films[34]. On the other hand, the hydrophobic nature of the small molecules shields the interface from moisture. Therefore, the SISG strategy demonstrates a good example of the possibility to affect and regulate the properties of the entire thin film by tuning of surface states. The surface agents can play a dual functional role of enabling the evolution of the underlying film properties and regulating the interface at the same time to produce improved interfacial contact with the upper layer and thus enabling improvement in both device performance and stability.

To demonstrate the universality of this strategy, we further applied it to the organic-inorganic hybrid perovskite system. As shown in Fig. A4.11, the post-treatment of OLA can induce the secondary grain growth in the formamidinium (FA)-based perovskite thin film as well. The surface energies of the low-index planes of FA-based perovskite with and without OLA were investigated computationally to confirm that the (100) plane became more energy favorable after the surface treatment (Fig. A4.12). The resulted photovoltaic devices showed an improved PCE from 20.04% to 22.13% (Fig. A4.13).

4.4 Conclusion

The demonstration of surface-state-tuning enabling secondary grain growth over the entire perovskite thin film sheds light on a new research angle in the area of perovskite thin films in regard to surface states by taking advantage of the unique soft nature of perovskites. In contrast to the widely reported strategies of regulating the properties of perovskite thin films via composition tuning, additive incorporation, solvent engineering and so on, a new methodology basis is proposed: changing the surface is a powerful tool to induce the property evolution of the entire perovskite thin film. Since the surface treatment process is after the formation of the perovskite

film, it strategically avoids the limitation of conventional methods in choosing agents/additives that are appropriate with high annealing temperatures of crystallization. Additionally, many of the additives incorporated into perovskite precursors to control the nucleation/growth kinetics, which is often a requirement for high quality films, always serve as a carrier recombination or degradation centers due to the heterogeneous microstructure In contrast, the surface agents that did not penetrate into the perovskite bulk film will not induce the formation of these undesirable centers within the perovskite film. Furthermore, the surface agents provide a versatile platform to tune the interface between the perovskite film and the top layer, which can be regarded as a bi-functional interfacial agent. On the one hand, they induce the evolution of the perovskite layer at the bottom, and on the other hand, they serve as an interconnecting layer that improves the contact with the upper layer. Moreover, the utilization of our methodology does not have to be limited to mechanical properties, in which perovskites exhibit low elastic modulus as a reflection of their "soft" nature as demonstrated in this report. I expect the reach of this strategy to extend to the properties in all aspects, such as electronic properties, in which perovskites exhibit low electric modulus rendering them highly vulnerable to an electric field [35]. A possible example might be introducing surface dipoles to modify the internal electric field and, thus, change the energy levels/band structures of the thin films as a whole. Hence, we hope this strategy will provide a new direction towards high-quality perovskite thin films with tunable and desirable properties and pave the way to the commercialization of perovskite photoelectric devices.

References

1. Boles, M. A., Ling, D., Hyeon, T. & Talapin, D. V. The surface science of nanocrystals. *Nature Materials* **15,** 141–153 (2016).

2. Carey, G. H. *et al.* Colloidal Quantum Dot Solar Cells. *Chem Rev* **115,** 12732–12763 (2015).

3. Milliron, D. J. Quantum dot solar cells: The surface plays a core role. *Nat. Mater.* **13,** 772–773 (2014).

4. Diao, J., Gall, K. & Dunn, M. L. Surface-stress-induced phase transformation in metal nanowires. *Nat. Mater.* **2,** 656–660 (2003).

5. Ding, Y., Niu, X. R., Wang, G. F., Feng, X. Q. & Yu, S. W. Surface effects on nanoindentation of soft solids by different indenters. *Mater. Res. Express* **3,** (2016).

6. Thomas Brunet, Jacques Leng, O. M.-M. Soft Acoustic Metamaterials. *Science (80-.).* **342,** 323–324 (2013).

7. Xu, X. *et al.* Gravity and surface tension effects on the shape change of soft materials. *Langmuir* **29,** 8665–8674 (2013).

8. Zhu, H. *et al.* Screening in crystalline liquids protects energetic carriers in hybrid perovskites. *Science (80-.).* **353,** 1409–1413 (2016).

9. Joshi, P. P., Maehrlein, S. F. & Zhu, X. Dynamic Screening and Slow Cooling of Hot Carriers in Lead Halide Perovskites. *Adv. Mater.* **1803054,** 1–10 (2019).

10. Lai, M. *et al.* Intrinsic anion diffusivity in lead halide perovskites is facilitated by a soft lattice. *Proc. Natl. Acad. Sci.* **115,** 201812718 (2018).

11. Miyata, K., Atallah, T. L. & Zhu, X. Y. Lead halide perovskites: Crystal-liquid duality, phonon glass electron crystals, and large polaron formation. *Science Advances* **3,** e1701469 (2017).

12. Omori, T. *et al.* Abnormal grain growth induced by cyclic heat treatment. *Science (80-.).*

341, 1500–1502 (2013).

13. Thompson, C. V. Secondary grain growth in thin films of semiconductors: Theoretical aspects. *J. Appl. Phys.* (1985). doi:10.1063/1.336194

14. Ye, Z. G. *Handbook of Advanced Dielectric, Piezoelectric and Ferroelectric Materials: Synthesis, Properties and Applications*. *Handbook of Advanced Dielectric, Piezoelectric and Ferroelectric Materials: Synthesis, Properties and Applications* (2008). doi:10.1533/9781845694005

15. Thompson, C. V. Grain Growth in Thin Films. *Annu. Rev. Mater. Sci.* (1990). doi:10.1146/annurev.ms.20.080190.001333

16. Kang, S.-J. L. *Sintering: Densification, Grain Growth, and Microstructure*. *Sintering* (2005). doi:http://dx.doi.org/10.1016/B978-075066385-4/50009-1

17. Adam W. Tsen, Lola Brown, Mark P. Levendorf, Fereshte Ghahari, Pinshane Y. Huang, Robin W. Havener, Carlos S. Ruiz-Vargas, David A. Muller, Philip Kim, J. P. Tailoring Electrical Transport Across Grain Boundaries in Polycrystalline Graphene. *Science.* **336,** 1143–1146 (2012).

18. Seager, C. H. & Ginley, D. S. Passivation of grain boundaries in polycrystalline silicon. *Appl. Phys. Lett.* **34,** 337–340 (1979).

19. Liu, Y. *et al.* Thinness- and Shape-Controlled Growth for Ultrathin Single-Crystalline Perovskite Wafers for Mass Production of Superior Photoelectronic Devices. *Adv. Mater.* **28,** 9204–9209 (2016).

20. Son, D. Y. *et al.* Self-formed grain boundary healing layer for highly efficient $CH_3NH_3PbI_3$perovskite solar cells. *Nat. Energy* **1,** 16081 (2016).

21. Thompson, C. V. Structure Evolution During Processing of Polycrystalline Films. *Annu. Rev. Mater. Sci.* (2000). doi:10.1146/annurev.matsci.30.1.159

22. Miller, D. L. *et al.* Giant secondary grain growth in Cu films on sapphire. *AIP Adv.* (2013). doi:10.11646/phytotaxa.311.2.4

23. Palmer, J. E., Thompson, C. V. & Smith, H. I. Grain growth and grain size distributions in thin germanium films. *J. Appl. Phys.* (1987). doi:10.1063/1.339460

24. Ciulik, J. & Taleff, E. M. Dynamic abnormal grain growth: A new method to produce single crystals. *Scr. Mater.* **61,** 895–898 (2009).

25. Omori, T. *et al.* Abnormal grain growth induced by cyclic heat treatment. *Science (80-.).* **341,** 1500–1502 (2013).

26. Ferreira, A. C. *et al.* Elastic Softness of Hybrid Lead Halide Perovskites. *Phys. Rev. Lett.* **121,** (2018).

27. Nam, J. K., Chun, D. H., Rhee, R. J. K., Lee, J. H. & Park, J. H. Methodologies toward Efficient and Stable Cesium Lead Halide Perovskite-Based Solar Cells. *Advanced Science* **5,** 1800509 (2018).

28. Zeng, Q. *et al.* Inorganic $CsPbI_2Br$ Perovskite Solar Cells: The Progress and Perspective. *Sol. RRL* **3,** 1800239 (2018).

29. Liu, L. *et al.* Grain-Boundary "Patches" by In Situ Conversion to Enhance Perovskite Solar Cells Stability. *Adv. Mater.* **30,** 1800544 (2018).

30. Im, J. H., Jang, I. H., Pellet, N., Grätzel, M. & Park, N. G. Growth of $CH_3NH_3PbI_3$ cuboids with controlled size for high-efficiency perovskite solar cells. *Nat. Nanotechnol.* **9,** 927–932 (2014).

31. Niu, T. *et al.* Stable High-Performance Perovskite Solar Cells via Grain Boundary Passivation. *Adv. Mater.* **30,** 1706576 (2018).

32. Meng, L. *et al.* Tailored phase conversion under conjugated polymer enables thermally stable perovskite solar cells with efficiency exceeding 21%. *J. Am. Chem. Soc.* (2018). doi:10.1021/jacs.8b10520

33. Zheng, G. *et al.* Manipulation of facet orientation in hybrid perovskite polycrystalline films by cation cascade. *Nat. Commun.* **9,** 2793 (2018).

34. Shao, Y. *et al.* Grain boundary dominated ion migration in polycrystalline organic-inorganic halide perovskite films. *Energy Environ. Sci.* **9,** 1752–1759 (2016).

35. Huang, J., Yuan, Y., Shao, Y. & Yan, Y. Understanding the physical properties of hybrid perovskites for photovoltaic applications. *Nature Reviews Materials* **2,** (2017).

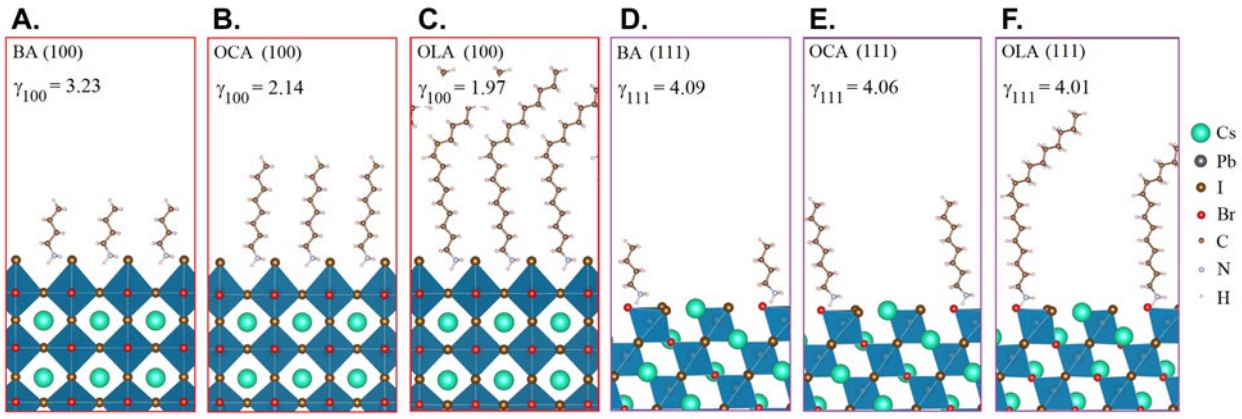

Fig. 4.1. The effect of organic ammoniums on surface servicing as the driving force of surface induced secondary grain growth.

Optimized (100) slab model of perovskite with (**A**) BA, (**B**) OCA, (**C**) OLA termination by DFT-D3 method; Optimized (111) slab model of perovskite with (**D**) BA, (**E**) OCA, (**F**) OLA termination by DFT-D3 method.

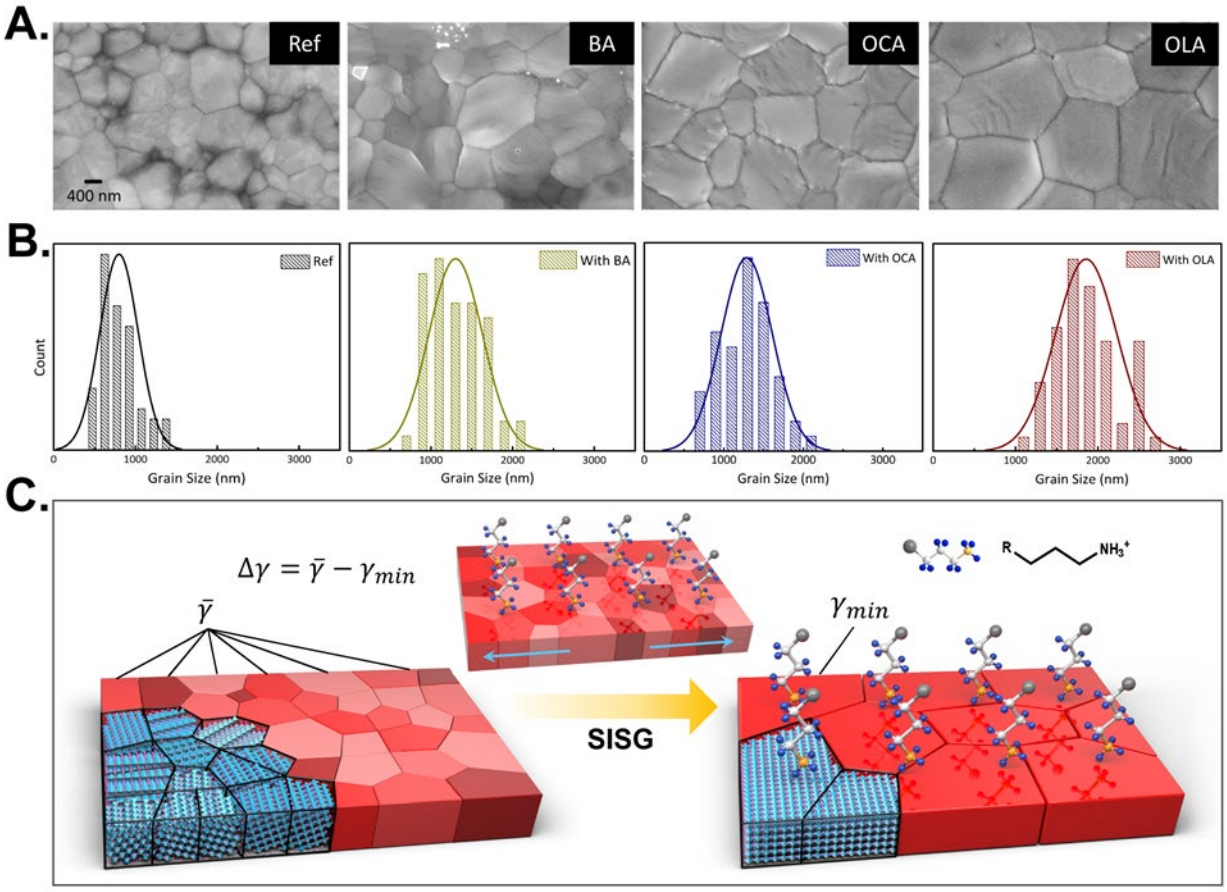

Fig. 4.2 Demonstration of the surface induced secondary grain growth.

(**A**) Top-view SEM images of perovskite film with various treatments (IPA, BA, OCA and OLA). (**B**) Grain size statistical distribution of perovskite films with various treatments (IPA, BA, OCA and OLA). (**C**) Schematic demonstration of the process of surface induced secondary grain growth.

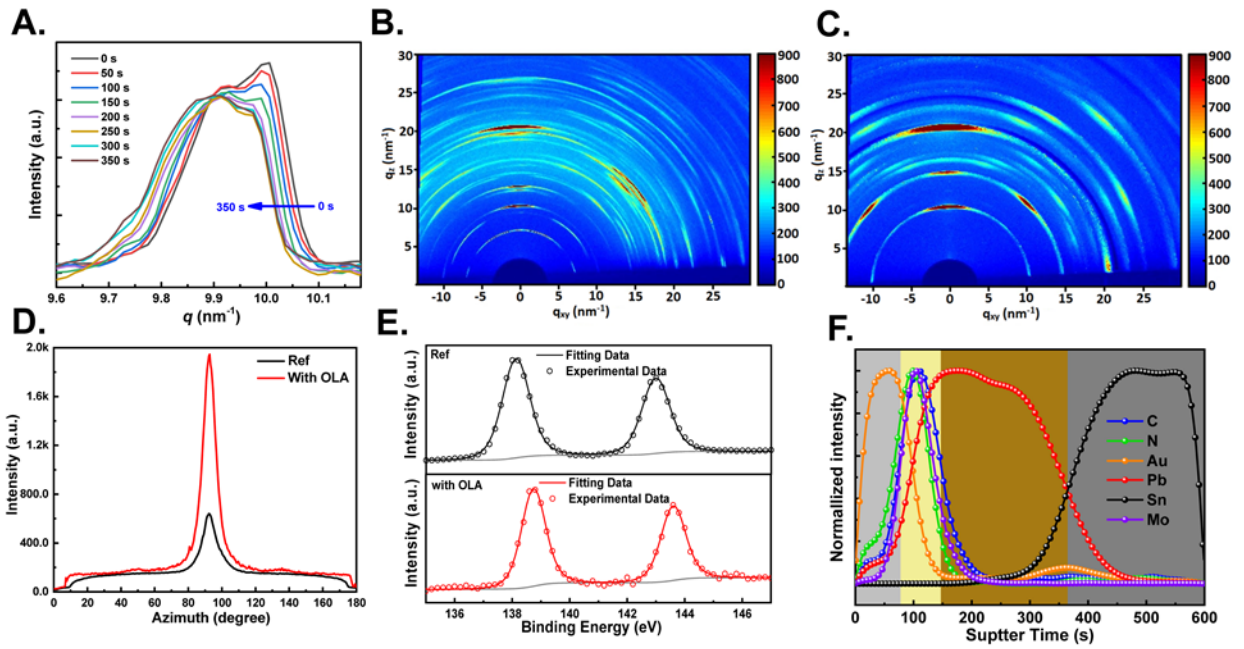

Fig. 4.3 Characterization of Perovskite film with the surface induced secondary grain growth by OLA.

(**A**) Evolution of the (100) peak position of perovskite film with OLA extracted from real-time in-situ GIWAXS measurement. (**B** and **C**) 2D GIWAXS patterns of perovskite films (B) without OLA treatment and (C) with OLA treatment. (**D**) Radially integrated intensity plots along (100) crystal plane from the 2D GIWAXS patterns in perovskite films with or without OLA treatment. (**E**) XPS data for Pb 4*f* 7/2 and Pb 4*f* 5/2 core level spectra in perovskite films with or without OLA treatment. (**F**) Time-of-flight secondary ion mass spectroscopy (TOF-SIMS) depth profile of perovskite film with OLA treatment.

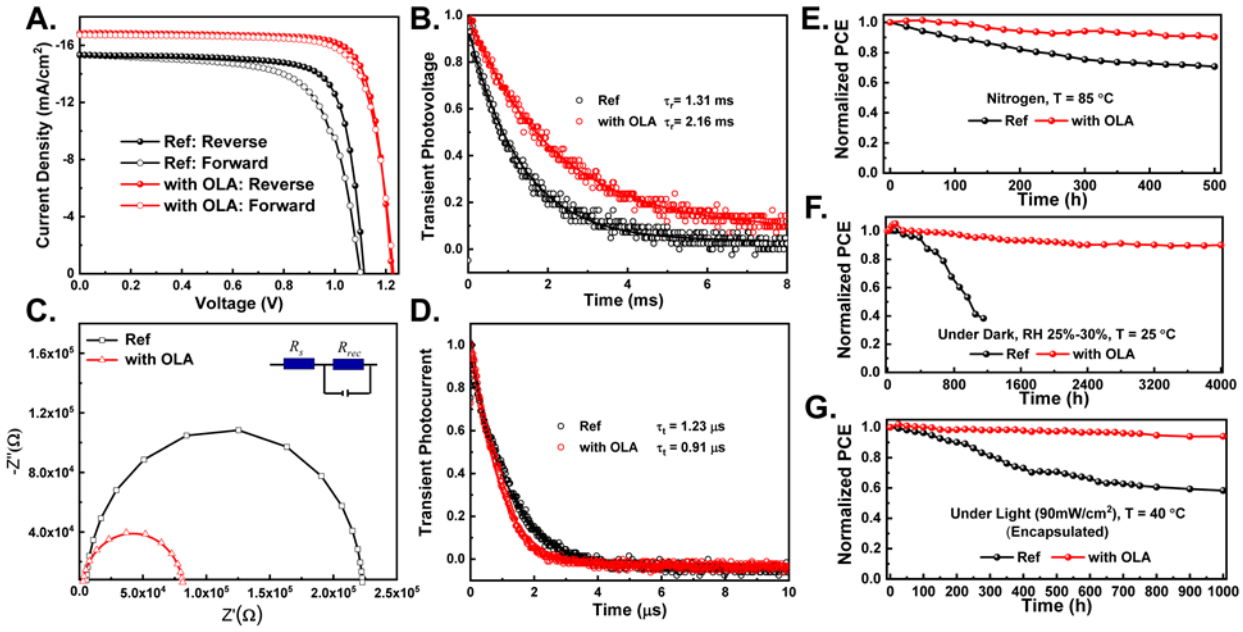

Fig. 4.4 Enhanced photovoltaic performance and long-term stability of perovskite film with surface induced secondary grain growth by OLA.

(**A**) Current density–voltage (*J–V*) curves of perovskite solar cells with or without OLA treatment. (**B**) Normalized transient photovoltage decay of perovskite solar cells with or without OLA treatment. (**C**) Nyquist plots of perovskite solar cells with or without OLA treatment measured in the dark and at corresponding open-circuit voltages. (**D**) Normalized transient photocurrent decay of perovskite solar cells with or without OLA treatment. (**E**) Evolution of power conversion efficiency (PCE) of perovskite solar cells with or without OLA treatment. The devices were stored under nitrogen with controlled temperature (85 °C). (**F**) Evolution of power conversion efficiency (PCE) of perovskite solar cells with or without OLA treatment. The devices were stored under dark with controlled humidity. (**G**) Evolution of the PCEs measured from the encapsulated perovskite solar cells with or without OLA treatment exposed to continuous light (90 ± 5 mW cm^{-2}) under open-circuit condition.

Chapter 5 Constructive molecular configurations for surface-defect passivation of perovskite photovoltaics

Metal-halide perovskite has emerged as a promising photovoltaic absorber due to its intriguing optoelectronic properties.(*1–5*) The long standing efforts towards the power conversion efficiency (PCE) enhancement have witnessed the significance of effective defect passivation in the reduction of the charge recombination in polycrystalline perovskite thin film photovoltaics.(*6–11*) The ionic nature of the perovskite lattice gives rise to unique passivation approaches such as molecular passivation through coordinate binding based on Lewis acid-base chemistry.(*12–15*) A variety of organic molecules containing functional groups interacting with the defects have been reported to enhance the PCE and stability of perovskite solar cells *via* defect passivation.(*16–18*) However, selection of the correct configuration within a tremendously large molecule pool and the lack of in-depth understanding of the corresponding passivation mechanism pose a significant challenge to perovskite research community: the dire need for molecular design rules for effective defect passivation.(*19*) For instance, molecules containing the carbonyl group, well-known as a Lewis base, have been reported as effective passivation agents in perovskites.(*20*, *21*) However, while the rich chemistry in organic molecules enables the structural tunability, it also adds up to the complexity to finding the most effective passivating molecules.(*22*) A problem arises that there are a variety of molecules containing carbonyl groups, but what kind of molecular structure will show the most effectiveness is often difficult to judge. This brings out the significance of investigation on the chemical environment of the effective functional groups and its effect on defect passivation.

Herein, we demonstrate high efficiencies for $FA_xMA_{1-x}PbI_xBr_{3-x}$ perovskite photovoltaic devices *via* rational design and comprehensive investigation of the chemical environment around the active functional group for defect passivation. A set of small molecules sharing the identical functional groups but with strategically varying chemical structure were designed: namely theophylline, caffeine and theobromine, which are the commonly found components in tea, coffee and chocolate, respectively. These molecules are easily accessible and therefore it is another step towards perovskite commercialization. The chemical structures of the molecules are shown in **Fig. 5.1A**. In order to investigate the properties of defect passivation, defect identification is the prerequisite.(*23*) After intensive studies, the interior defects of perovskite have become negligible compared to the surface ones due to now available high-quality perovskite polycrystalline thin film fabrication of monolayered perovskite grains.*(24-26)* Utilizing the first-principles density-functional theory calculations, we first compared the formation energies of selected native defects that form on the perovskite surface. Pb and I involving point defects, Pb vacancy (V_{Pb}), I vacancy (V_I) and Pb-I antisite (Pb_I and I_{Pb}, corresponding to I site substitution by Pb, and Pb site substitution by I, respectively) were particularly taken into consideration because the band edges of perovskite were reported to be composed of Pb and I orbitals.(*27*, *28*) As confirmed by X-ray photoelectron spectroscopy (XPS), the surface of the as-fabricated perovskite thin film using a two-step method was Pb-rich. (Fig. A5.1) Therefore, we focused on the (100) surface with PbI_2 termination in a Pb-rich condition. The types of surface defects studied, and their corresponding top layer view of atomic structures are shown in Fig. 5.1B. The formation energies of the defects were calculated using PDE-D3 method and are summarized in Table B5.1. The defect formation energies (DFE) of V_{Pb}, V_I, Pb_I, and I_{Pb} on the surface were calculated to be 3.20 eV, 0.51 eV, 0.57 eV and 3.15 eV, respectively. Compared to the values reported in bulk perovskite, V_{Pb}, V_I and I_{Pb} defects show similar DFE,(*29*) while the Pb_I antisite defect exhibited particularly lower

formation energy than that in the bulk. This indicated that Pb_I antisite defect is more easily formed and becomes more dominant when it is on the surface. V_I was not considered even though the DFE is as low as Pb_I, because the interaction of molecules with the V_I turned out to be not energy favorable. (Fig. B5.2) Based on that, we focused on the interaction between the surface Pb_I antisite defect and candidate molecules for defect passivation.

I incorporated theophylline onto the surface of perovskite thin film using a post-treatment method, and a PCE enhancement from 21.02% to 23.48% was observed in the photovoltaic devices with ITO/SnO_2/perovskite/Spiro-OMeTAD/Ag structure. The current density-voltage (*J-V*) curves of the photovoltaic devices with and without theophylline treatment are compared in Fig. 5.1C and Table B5.2, in which the control device showed an open circuit voltage (V_{OC}) of 1.164 V, a short circuit current (J_{SC}) of 24.78 mA cm^{-2}, a fill factor (FF) of 72.88%, while the target device showed a V_{OC} of 1.191 V, a J_{SC} of 25.24 mA cm^{-2}, a FF of 78.11%. The significant enhancement in the V_{OC} is attributed to the surface passivation by theophylline *via* the Lewis base-acid interaction between C=O group and the antisite Pb. As shown in the surface structure model of perovskite with theophylline (Fig 5.1B), the C=O group on theophylline showed a strong interaction with the antisite Pb. Noticeably, the neighboring N-H on the imidazole ring also interact with the I of PbI_6^{2-} octahedron through a hydrogen bond, which strengthened the absorption of theophylline onto the Pb_I defect, resulting in an interaction energy (defined as $E_{molecule\text{-}perovskite}$-$E_{perovskite}$-$E_{molecule}$) as strong as -1.7 eV. This observation suggested that the neighboring hydrogen bond between the xanthene molecule and the PbI_6^{2-} octahedron can contribute to the defect passivation. A methyl group was added to the N on the imidazole ring of theophylline (resulting in caffeine) to eliminate the effect from hydrogen bond between the N-H

and I. The interaction of caffeine with surface Pb_I defect is shown in Fig 5.1B. While the C=O of caffeine still interacted with the Pb antisite, as in the case of theophylline, the missing hydrogen bond between N-H and PbI_6^{2-} octahedron resulted in a weakened interaction resulting in a less favorable interaction energy of -1.3 eV. This leads to a lesser PCE enhancement with caffeine-treated perovskite photovoltaic device compared to that of the theophylline (Fig 5.1C). A lower PCE of 22.32% along with a lower V_{OC} of 1.178 V, J_{SC} of 25.04 mA cm^{-2}, FF of 75.76% was observed due to less effective surface defect passivation. As comparison, when the N-H is located next to the C=O group on the same six-membered ring, producing a shorter distance between the C=O and the N-H (i.e. theobromine), the spatially effective interaction between the N-H and I was disabled as C=O is bound to antisite Pb, resulting in an even weaker interaction energy of -1.1 eV (Fig. 5.1B). Although both C=O and N-H are coexisting, the lack of appropriate coordination of I to the molecule leads to 'spatially destructive' molecular configuration. In this configuration, the theobromine-treated devices showed a decrease in PCE to 20.24% with a lower V_{OC} of 1.163 V, J_{SC} of 24.27 mA cm^{-2} and FF of 71.58% compared with the reference device. This emphasizes the significance of not only the co-existence of N-H with C=O, but also the constructive configuration of the relative position of them to enable the cooperative multi-site interaction and synergistic passivation effect.

The variation in the C=O and the PbI_2-terminated perovskite surface interaction with different molecular configurations was further studied using Fourier Transform Infrared Spectroscopy (FTIR). As shown in **Fig. 5.2A**, the C=O in pure theophylline showed a typical stretching vibration mode at 1660 cm^{-1}, while it shifted to 1630 cm^{-1} upon binding to PbI_2. The downwards shift of 30 cm^{-1} of the C=O stretching vibration frequency resulted from the electron

delocalization in C=O when a Lewis base-acid adduct was formed, demonstrating a strong interaction between PbI_2 and C=O in theophylline. The atomic distance between the O in C=O and the Pb in PbI_2 based on theoretical modeling was as low as 2.28 Å. When the H was replaced by a methyl group on the N of imidazole to eliminate the effect of a hydrogen bond, the vibration frequency of C=O in caffeine showed a shift of only 10 cm^{-1} upon addition of PbI_2, indicating a weakened interaction between the C=O and PbI_2 (Fig. 5.2B). The atomic distance between the corresponding O and Pb also increased to 2.32 Å, further confirming the weakened interaction due to the missing assistance of hydrogen bonding. In the case of theobromine, when the N-H was in a closer position to C=O, the interaction between the molecule and PbI_2 became comparable to that in theophylline, as evidenced by the large shift of C=O stretching vibration frequency from 1655^{-1} to 1620 cm^{-1} and the short distance between O and Pb (Fig. 5.2C). However, this strong interaction is enabled by the free rotation of PbI_2, which results in a different configuration than that in theophylline and caffeine. Hence, when the configuration of PbI_2 is fixed and shows a 90° angle between Pb and I atom as that on perovskite surface, i.e. PbI_6^{2-} octahedron, the N-H in a 'wrong' position becomes unfavorable for the interaction with I. This would either cause weakened interaction between the molecule and the perovskite surface or distorted PbI_6^{2-} octahedron, resulting in the ineffectiveness of defect passivation and perhaps causing even more defects due to the lattice distortion (Fig. A5.3). The surface passivation effects of the three molecules with different configuration were further studied by photoluminescence (PL). As shown in Fig. 5.2D, the PL intensity increased noticeably with the treatment by theophylline, implying the suppressed non-radiative charge recombination sites from defects.(*20*) With the caffeine treatment, an enhancement of PL intensity was also observed, but not as strong as that with the theophylline, suggesting a less effective passivation effect when the hydrogen bond between N-H and PbI_6^{2-} octahedron is missing. In the case of theobromine, however, a

decrease in PL intensity was observed compared with the reference one, which can be attributed to the destructive molecular configuration of the passivation agents causing more charge recombination sites. The trap density of states (*t*DOS) of the as-fabricated devices were also deduced from the angular frequency dependent capacitance. As shown in Fig. 5.2E, the *t*DOS as a function of the defect energy demonstrated a reduction in trap states for theophylline- and caffeine- treated perovskite compared with the reference device. In contrast, theobromine treatment induced more trap states, which is consistent with the decrease in PCE. The change in *t*DOS with different surface treatments was also confirmed by theoretical modeling (Fig. A5.4). In addition, electrochemical impedance spectroscopy (EIS) characterization was performed to demonstrate the carrier transport processes under illumination at the interface. The middle frequency zone of EIS semicircle should be dominated by junction capacitance and recombination resistance related to the interfaces between transport materials and perovskite. According to Fig. 5.2F, the device with theophylline surface treatment has the smallest impedance, signifying a substantially suppressed charge recombination at the interface, which originated from the reduced surface defect states. A larger impedance was observed in caffeine-treated device and an even larger impedance was measured in theobromine-treated device demonstrated the significance of the co-existing N-H bond and its constructive configuration to enable effective defect passivation.

Further characterizations were performed to better understand the perovskite interface with theophylline and gain more insights on the device behavior. High-resolution XPS patterns of the Pb 4*f* of the reference and theophylline-treated films are shown in **Fig. 5.3A** for surface chemistry comparison. For the theophylline-treated film, two main peaks located at 138.48 and 143.38 eV

were observed corresponding to the Pb 4*f* 7/2 and Pb 4*f* 5/2, respectively. The reference film, on the other hand, showed two main peaks at 138.27 and 143.13 eV. The peaks from Pb 4*f* shifted to higher binding energies in the film with theophylline surface treatment, indicating the interaction between the theophylline and the Pb on perovskite surface. The Ultraviolet photoelectron spectroscopy (UPS) was employed to measure the surface band structure with and without the theophylline surface treatment. As shown in Fig. 5.3B, the work function was determined to be -4.77 eV and -4.96 eV with the valance band maximum (VBM) of -5.66 eV and -5.73 eV for reference and theophylline, respectively, indicating a less n-type surface after theophylline treatment, which might be beneficial for the hole extraction of the device. Atomic Force Microscopy combined with Kelvin Probe Force Microscopy (KPFM) was further applied to probe the effect of theophylline on the surface morphology and surface potential. As shown in Fig. 5.3C, the theophylline-treated surface exhibited a higher electronic chemical potential than that of reference film, while keeping the surface morphology unchanged. The transient photoluminescence (TRPL) of the perovskite films with hole transporting layer was compared in Fig. 5.3D to delineate the carrier dynamics of the devices. The perovskite film with theophylline treatment showed a slightly longer carrier lifetime than the reference film, while a faster decay profile was observed when adding the hole transporting layer on top of the perovskite film. This demonstrated a better hole extraction with theophylline treatment,(*25*) most likely arising from lesser recombination sites at the interface and the slightly shallower work function of the perovskite film with theophylline. The improved carrier dynamics originating from the effective surface passivation by theophylline was further characterized by cross-sectional electron-beam-induced current (EBIC) measurement. In EBIC measurement, the e-beam excited carriers were collected based on the collection probability CP (x, L_d), where x is the distance between junction and incident beam position, and L_d is the diffusion length of the carriers (Fig. A5.5). As shown in

Fig. 5.3E, the device with theophylline treatment exhibits higher EBIC current as compared to the reference device. The average intensity extracted from these EBIC maps demonstrates a general increase in the EBIC signal after treated with theophylline (Fig. A5.6), indicating an enhanced carrier collection efficiency.(*30*) Specifically in Fig. 5.3E, a representative EBIC line profile of the reference device shows a current decay from the HTL/perovskite to the SnO_2/perovskite interface. The decay indicates that carrier collection is limited by the hole diffusion length as the beam position moves away from the HTL/perovskite interface. In contrast, the device with theophylline treatment displays minimal decay within the perovskite layer in the EBIC line profile. This suggests that a longer diffusion length of holes is present in theophylline-treated sample and balanced electron and hole charge transport and collection is achieved, which is likely due to the reduced recombination sites at the surface of perovskite (Fig. 5.3E).

Further assessment of the performance of the photovoltaic devices based on the theophylline surface passivation was performed. As shown in **Fig. 5.4A**, the devices showed a negligible hysteresis (4.1%) due to the balanced charge collection originated from the effective surface passivation via rational molecule design, while the reference device showed a large hysteresis up to 7.6% (Table B5.3). External quantum efficiency (EQE) spectra of the devices were compared in Fig. 5.4B. An integrated J_{SC} of 24.42 mA cm^{-2} from the target device matched well with the value measured from the *J-V* scan (<5% discrepancy), while control device showed an integrated J_{SC} of 23.56 mA cm^{-2}. A stabilized PCE of 22.64% was achieved with the target device when biased at 1.00 V while that of control device was 20.36% when biased at 0.98 V (Fig. 5.4C). The histogram of solar cell efficiencies for 40 devices is shown in Fig. 5.4D, which confirms good reproducibility of the performance improvement with theophylline (11.1% improvement in an

average PCE from 20.36±0.53% to 22.61±0.58% with the incorporation of the theophylline). In Fig. 5.4E, the changes in PCE of the encapsulated devices at a relative humidity of 30-40% and temperature of 40 ℃ were tracked over time to test the long-term operational stability. While the reference device degraded by more than 80% in 500 h, the target device maintained over 90% of its initial efficiency during this time. Also, as shown in Fig. A5.7, the shelf stability of the device based on theophylline treatment was noticeably enhanced, maintaining over 95% of its original PCE when stored under ambient conditions with 20-30% humidity at 25 °C for 60 days. In contrast, the reference device lost over 35% of its initial efficiency. The improvement in the operational stability could be attributed to the strong interaction between the theophylline and the surface defects. This stabilized the perovskite surface and suppressed the ion migration, which usually emanates from the defect sites.(*31–33*)

In conclusion, we demonstrated the so far largely ignored chemical environment around the effective functional group for defect passivation in perovskite surfaces. The hydrogen bond formation between N-H and I was investigated to be secondary assistance with the primary C=O binding with Pb to maximize the surface defect passivation in perovskite. This synergistic effect can be enabled only when the N-H and C=O are in a constructive configuration in the molecular structure: the sole influence of C=O is insufficient, a neighboring N-H is needed; the co-existence of C=O and N-H is insufficient, a constructive structural configuration is needed. This provides new insights on the molecular design of effective defect passivation strategy for achieving highly efficient and stable perovskite optoelectronics.

References and Notes:

1. H. S. Kim, C. R. Lee, J. H. Im, K. B. Lee, T. Moehl, A. Marchioro, S. J. Moon, R. Humphry-Baker, J. H. Yum, J. E. Moser, M. Grätzel, N. G. Park, Lead iodide perovskite sensitized all-solid-state submicron thin film mesoscopic solar cell with efficiency exceeding 9%. *Sci. Rep.* **2**, 591 (2012).

2. S. D. Stranks, H. J. Snaith, Metal-halide perovskites for photovoltaic and light-emitting devices. *Nat. Nanotechnol.* **10**, 391–402 (2015).

3. H. Zhu, K. Miyata, Y. Fu, J. Wang, P. P. Joshi, D. Niesner, K. W. Williams, S. Jin, X. Y. Zhu, Screening in crystalline liquids protects energetic carriers in hybrid perovskites. *Science.* **353**, 1409–1413 (2016).

4. M. Xiao, F. Huang, W. Huang, Y. Dkhissi, Y. Zhu, J. Etheridge, A. Gray-Weale, U. Bach, Y. B. Cheng, L. Spiccia, A fast deposition-crystallization procedure for highly efficient lead iodide perovskite thin-film solar cells. *Angew. Chemie - Int. Ed.* **53**, 9898–9903 (2014).

5. W. Nie, H. Tsai, R. Asadpour, J. C. Blancon, A. J. Neukirch, G. Gupta, J. J. Crochet, M. Chhowalla, S. Tretiak, M. A. Alam, H. L. Wang, A. D. Mohite, High-efficiency solution-processed perovskite solar cells with millimeter-scale grains. *Science.* **347**, 522–525 (2015).

6. J. Tong, Z. Song, D. H. Kim, X. Chen, C. Chen, A. F. Palmstrom, P. F. Ndione, M. O. Reese, S. P. Dunfield, O. G. Reid, J. Liu, F. Zhang, S. P. Harvey, Z. Li, S. T. Christensen, G. Teeter, D. Zhao, M. M. Al-Jassim, M. F. A. M. Van Hest, M. C. Beard, S. E. Shaheen, J. J. Berry, Y. Yan, K. Zhu, Carrier lifetimes of >1 μs in Sn-Pb perovskites enable efficient all-perovskite tandem solar cells. *Science.* **364**, 475–479 (2019).

7. H. Tan, A. Jain, O. Voznyy, X. Lan, F. P. G. De Arquer, J. Z. Fan, R. Quintero-Bermudez, M. Yuan, B. Zhang, Y. Zhao, F. Fan, P. Li, L. N. Quan, Y. Zhao, Z. H. Lu, Z. Yang, S. Hoogland, E. H. Sargent, Efficient and stable solution-processed planar perovskite solar cells via contact passivation. *Science.* **355**, 722–726 (2017).

8. X. Zheng, B. Chen, J. Dai, Y. Fang, Y. Bai, Y. Lin, H. Wei, X. C. Zeng, J. Huang, Defect passivation in hybrid perovskite solar cells using quaternary ammonium halide anions and cations. *Nat. Energy*. **2**, 17102 (2017).

9. J. J. Yoo, S. Wieghold, M. Sponseller, M. Chua, S. N. Bertram, N. T. P. Hartono, J. Tresback, E. Hansen, J.-P. Correa-Baena, V. Bulovic, T. Buonassisi, S. S. Shin, M. G. Bawendi, An Interface Stabilized Perovskite Solar Cell with High Stabilized Efficiency and Low Voltage Loss. *Energy Environ. Sci.* **12**, 2192–2199 (2019).

10. Q. Jiang, Y. Zhao, X. Zhang, X. Yang, Y. Chen, Z. Chu, Q. Ye, X. Li, Z. Yin, J. You, Surface passivation of perovskite film for efficient solar cells. *Nat. Photonics*. **13**, 460–466 (2019).

11. N. Li, S. Tao, Y. Chen, X. Niu, C. K. Onwudinanti, C. Hu, Z. Qiu, Z. Xu, G. Zheng, L. Wang, Y. Zhang, L. Li, H. Liu, Y. Lun, J. Hong, X. Wang, Y. Liu, H. Xie, Y. Gao, Y. Bai, S. Yang, G. Brocks, Q. Chen, H. Zhou, Cation and anion immobilization through chemical bonding enhancement with fluorides for stable halide perovskite solar cells. *Nat. Energy*. **4**, 408–415 (2019).

12. J. S. Manser, J. A. Christians, P. V Kamat, Intriguing Optoelectronic Properties of Metal Halide Perovskites. *Chem. Rev.* **116**, 12956–13008 (2016).

13. H. Zhang, H. Chen, C. C. Stoumpos, J. Ren, Q. Hou, X. Li, J. Li, H. He, H. Lin, J. Wang, F. Hao, M. G. Kanatzidis, Thiazole-Induced Surface Passivation and Recrystallization of

$CH_3NH_3PbI_3$ Films for Perovskite Solar Cells with Ultrahigh Fill Factors. *ACS Appl. Mater. Interfaces*. **10**, 42436–42443 (2018).

14. J. W. Lee, H. S. Kim, N. G. Park, Lewis Acid-Base Adduct Approach for High Efficiency Perovskite Solar Cells. *Acc. Chem. Res.* **49**, 311–319 (2016).

15. Y. Zong, Y. Zhou, Y. Zhang, Z. Li, L. Zhang, M. G. Ju, M. Chen, S. Pang, X. C. Zeng, N. P. Padture, Continuous Grain-Boundary Functionalization for High-Efficiency Perovskite Solar Cells with Exceptional Stability. *Chem*. **4**, 1404–1415 (2018).

16. D. Bi, C. Yi, J. Luo, J. D. Décoppet, F. Zhang, S. M. Zakeeruddin, X. Li, A. Hagfeldt, M. Grätzel, Polymer-templated nucleation and crystal growth of perovskite films for solar cells with efficiency greater than 21%. *Nat. Energy*. **1**, 16142 (2016).

17. B. Chen, P. N. Rudd, S. Yang, Y. Yuan, J. Huang, Imperfections and their passivation in halide perovskite solar cells. *Chem. Soc. Rev.* **48**, 3842–3867 (2019).

18. T. Wu, Y. Wang, X. Li, Y. Wu, X. Meng, D. Cui, X. Yang, L. Han, Efficient Defect Passivation for Perovskite Solar Cells by Controlling the Electron Density Distribution of Donor-π-Acceptor Molecules. *Adv. Energy Mater.* **9**, 1803766 (2019).

19. W. Xu, Q. Hu, S. Bai, C. Bao, Y. Miao, Z. Yuan, T. Borzda, A. J. Barker, E. Tyukalova, Z. Hu, M. Kawecki, H. Wang, Z. Yan, X. Liu, X. Shi, K. Uvdal, M. Fahlman, W. Zhang, M. Duchamp, J. M. Liu, A. Petrozza, J. Wang, L. M. Liu, W. Huang, F. Gao, Rational molecular passivation for high-performance perovskite light-emitting diodes. *Nat. Photonics*. **13**, 418–424 (2019).

20. R. Wang, J. Xue, L. Meng, J. W. Lee, Z. Zhao, P. Sun, L. Cai, T. Huang, Z. Wang, Z. K. Wang, Y. Duan, J. L. Yang, S. Tan, Y. Yuan, Y. Huang, Y. Yang, Caffeine Improves the

Performance and Thermal Stability of Perovskite Solar Cells. *Joule*. **3**, 1464–1477 (2019).

21. T. Niu, J. Lu, R. Munir, J. Li, D. Barrit, X. Zhang, H. Hu, Z. Yang, A. Amassian, K. Zhao, S. F. Liu, Stable High-Performance Perovskite Solar Cells via Grain Boundary Passivation. *Adv. Mater.* **30**, 1706576 (2018).

22. H. Zhang, M. K. Nazeeruddin, W. C. H. Choy, Perovskite Photovoltaics: The Significant Role of Ligands in Film Formation, Passivation, and Stability. *Adv. Mater.* **31**, 1805702 (2019).

23. W. J. Yin, T. Shi, Y. Yan, Unusual defect physics in $CH_3NH_3PbI_3$ perovskite solar cell absorber. *Appl. Phys. Lett.* **104**, 063903 (2014).

24. W. S. Yang, B. W. Park, E. H. Jung, N. J. Jeon, Y. C. Kim, D. U. Lee, S. S. Shin, J. Seo, E. K. Kim, J. H. Noh, S. Il Seok, Iodide management in formamidinium-lead-halide-based perovskite layers for efficient solar cells. *Science.* **356**, 1376–1379 (2017).

25. N. J. Jeon, H. Na, E. H. Jung, T. Y. Yang, Y. G. Lee, G. Kim, H. W. Shin, S. Il Seok, J. Lee, J. Seo, A fluorene-terminated hole-transporting material for highly efficient and stable perovskite solar cells. *Nat. Energy*. **3**, 682–689 (2018).

26. E. H. Jung, N. J. Jeon, E. Y. Park, C. S. Moon, T. J. Shin, T. Y. Yang, J. H. Noh, J. Seo, Efficient, stable and scalable perovskite solar cells using poly(3-hexylthiophene). *Nature*. **567**, 511–515 (2019).

27. M. A. Green, A. Ho-Baillie, H. J. Snaith, The emergence of perovskite solar cells. *Nat. Photonics*. **8**, 506–514 (2014).

28. Z. Xiao, Z. Song, Y. Yan, From Lead Halide Perovskites to Lead-Free Metal Halide Perovskites and Perovskite Derivatives. *Adv. Mater.*, 1803792 (2019).

29. N. Liu, C. Y. Yam, First-principles study of intrinsic defects in formamidinium lead triiodide perovskite solar cell absorbers. *Phys. Chem. Chem. Phys.* **20**, 6800–6804 (2018).

30. E. Edri, S. Kirmayer, S. Mukhopadhyay, K. Gartsman, G. Hodes, D. Cahen, Elucidating the charge carrier separation and working mechanism of $CH_3NH_3PbI_{3-x}Cl_x$ perovskite solar cells. *Nat. Commun.* **5**, 3461 (2014).

31. R. Wang, M. Mujahid, Y. Duan, Z. K. Wang, J. Xue, Y. Yang, A Review of Perovskites Solar Cell Stability. *Adv. Funct. Mater.*, 1808843 (2019).

32. J. A. Christians, P. Schulz, J. S. Tinkham, T. H. Schloemer, S. P. Harvey, B. J. Tremolet De Villers, A. Sellinger, J. J. Berry, J. M. Luther, Tailored interfaces of unencapsulated perovskite solar cells for >1,000 hour operational stability. *Nat. Energy*. **3**, 68–74 (2018).

33. Y. Hou, X. Du, S. Scheiner, D. P. McMeekin, Z. Wang, N. Li, M. S. Killian, H. Chen, M. Richter, I. Levchuk, N. Schrenker, E. Spiecker, T. Stubhan, N. A. Luechinger, A. Hirsch, P. Schmuki, H. P. Steinrück, R. H. Fink, M. Halik, H. J. Snaith, C. J. Brabec, A generic interface to reduce the efficiency-stability-cost gap of perovskite solar cells. *Science.* **358**, 1192–1197 (2017).

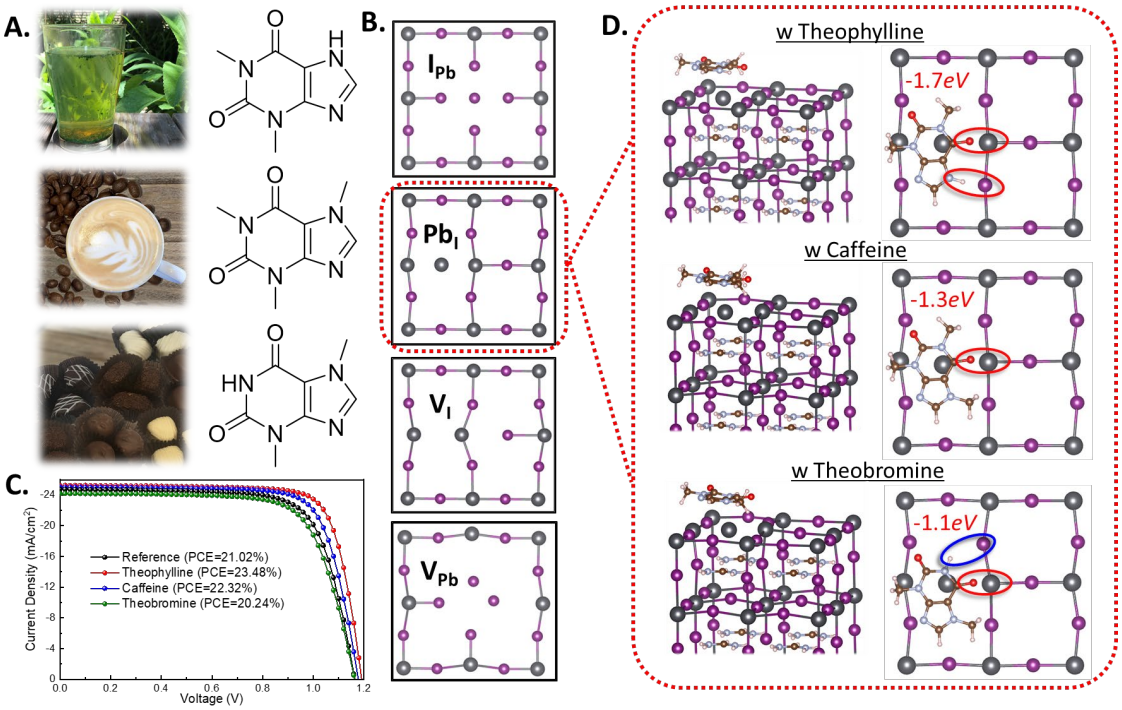

Fig. 5.1 Surface defect identification and constructive configuration of the C=O group in three different chemical environments.

(**A**) Chemical structures of three different passivation molecules. (top to bottom: Theophylline, Caffeine and Theobromine) (**B**) Top view of the various types of surface defects. (**C**) *J-V* curves of perovskite solar cells with or without small molecules treatment under reverse scan direction. (**D**) Theoretical models of perovskite with molecular surface passivation of Pb_I antisite.

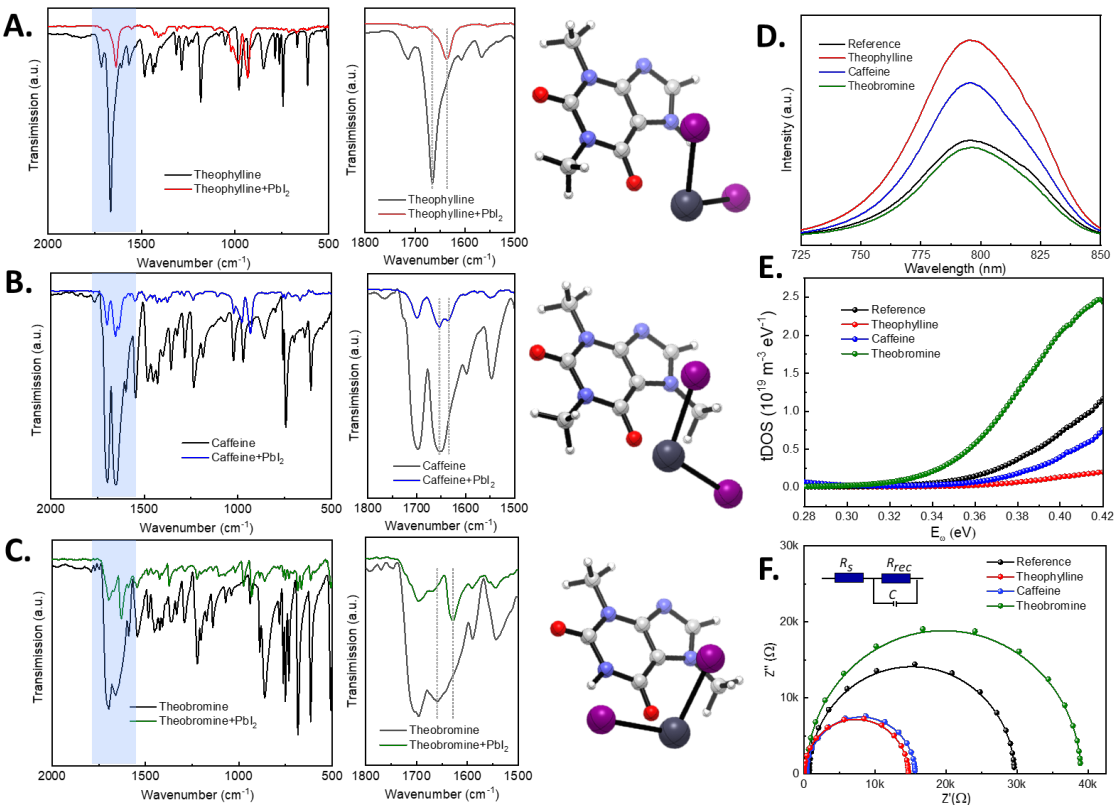

Fig. 5.2 Investigation of the interactions between surface defects and the small molecules.

FTIR spectra of (**A**) pure theophylline and theophylline-PbI_2 films; (**B**) pure caffeine and caffeine-PbI_2 films; (**C**) pure theobromine and theobromine-PbI_2 films. (**D**) PL spectra of perovskite films without and with small molecules treatment. (**E**) Trap density of states (*t*DOS) in perovskite solar cells with or without small molecules treatment. (**F**) Nyquist plots of perovskite solar cells with or without small molecules treatment measured in the dark and at corresponding open-circuit voltages.

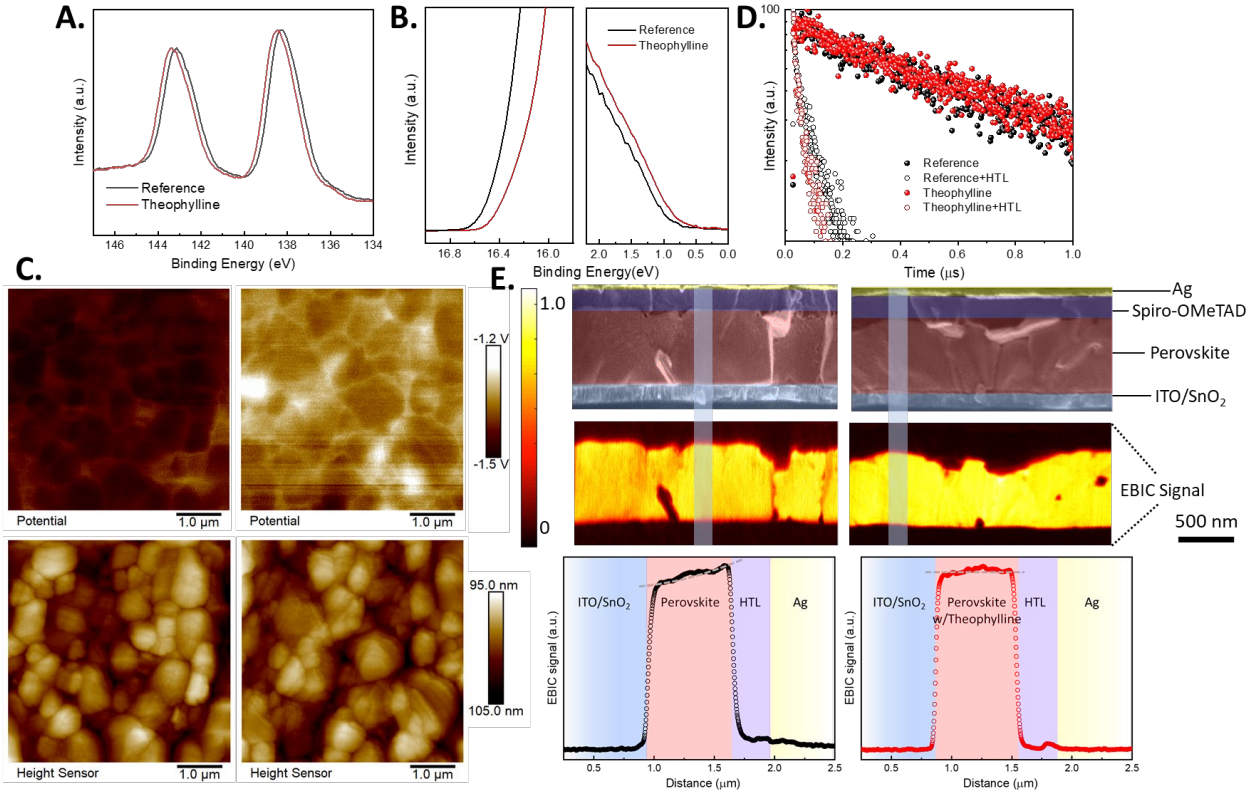

Fig. 5.3 Characterization of perovskite films and interfaces with theophylline treatment.

(**A**) XPS data for Pb 4*f* 7/2 and Pb 4*f* 5/2 core level spectra in perovskite films with or without theophylline treatment. (**B**) UPS spectra of perovskite films with or without theophylline treatment. (**C**) AFM and KPFM images of perovskite films with (right) or without (left) theophylline treatment. (**D**) Time-resolved PL spectra of perovskite films before and after depositing Spiro-OMeTAD without and with theophylline treatment. (**E**) Cross-section SEM images and the corresponding EBIC images and line profile of the perovskite solar cells with (right) or without (left) theophylline treatment.

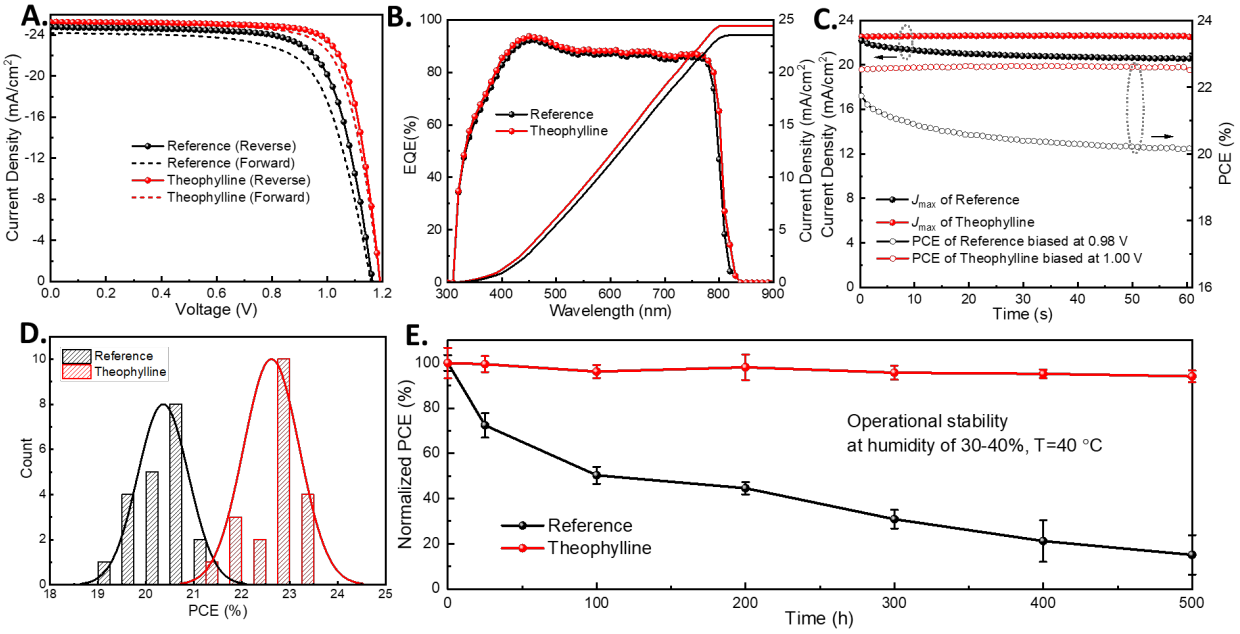

Fig. 5.4 Enhanced photovoltaic performance and long-term stability of perovskite solar cells with theophylline treatment.

(**A**) Current density–voltage (*J–V*) curves of perovskite solar cells with or without theophylline treatment. (**B**) EQE curves of perovskite solar cells with or without theophylline treatment. (**C**) Stabilized maximum power output and the photocurrent density at maximum power point as a function of time for the best performing perovskite solar cells with or without theophylline treatment, as shown in Fig. 4A, recorded under simulated one-sun AM1.5G illumination. (**D**) PCE distribution of perovskite solar cells with or without theophylline treatment. (**E**) Evolution of the PCEs measured from the encapsulated perovskite solar cells with or without theophylline treatment exposed to continuous light (90 ± 10 mW cm^{-2}) under open-circuit condition.

Chapter 6 Composition Stoichiometry of $Cs_2AgBiBr_6$ Films for Highly Efficient Lead-Free Perovskite Solar Cells

Although the power conversion efficiency (PCE) of lead (Pb) based hybrid organic-inorganic halide perovskite solar cells (PSCs) has exceeded 23 %,[1] issues such as stability and the toxicity of Pb have limited the real life consumption of this technology.[2,3] Therefore, it is imperative to address these issues by replacing the Pb content with a non-toxic element and by achieving an all-inorganic compound in which the A-site of the unit cell is occupied by inorganic elements such as Cesium (Cs). Of all the approaches reported to date,[4-11] lead-free halide double perovskites show the best promise of realizing non-toxic and stable PSCs.[8-11] This class of compounds allows the expansion of the perovskite crystal lattice and the substitution of the Pb occupying the B site with two heterovalent cations such as Ag^+ and Bi^{3+}.[12-16] The approach yields a double perovskite crystal lattice with a general representation of $A_2B^+B^{3+}X_6$. However, inferior performance has been reported so far for photovoltaic (PV) devices based on these materials.[17-20] This has been traced to some inherent factors such as electronic band structure which involves a wide bandgap ~1.98 eV and an indirect bandgap character.[12-14] Beyond such inherent factors, an important external factor which has also contributed to the poor PV performance is the film quality of the halide double perovskite layer.[18,20] Various approaches, such a metal alloying,[15,16] lower dimension (0D, 1D and 2D) compounds [21,22] and incorporation of mixed cations and halides,[23] have been reported to address the aforementioned intrinsic factors. However, the alteration of the intrinsic nature of the compounds is a complicated process. Also, the maintenance of the double perovskite crystal lattice while taking these measures cannot be guaranteed.[24] Therefore, a focus on the external factor by optimizing the thin film deposition techniques could give an insight into advancing the PV performance of halide double perovskite based PSCs.

Vapor deposition and solution processing have been reported in the preparation of halide double perovskite compounds for PV applications. For instance, two-step vapor deposition was used in the preparation of Cs_2TiBr_6 perovskites[25]. Ke *et al.* prepared the Cs_2SnI_6 film via an aerosol

assisted chemical vapor deposition technique.[26] Very recently, Wang *et al.* prepared the $Cs_2AgBiBr_6$ films by a sequential vapor deposition technique.[20] Furthermore, solution processing involving low pressure assisted annealing was utilized by Wu *et al.* for the preparation of $Cs_2AgBiBr_6$ films.[17] Due to the merits of easy processibility, impressive stability and non-toxicity, $Cs_2AgBiBr_6$ stands out as the most studied halide double perovskites. The optoelectronic properties of halide double perovskites are strongly affected by the film deposition methods.[12,14,17,20,27] However, to date, there are no empirical reports on how different preparation methods affect the film quality of these compounds and corresponding device performance. Herein, we compared the pristine $Cs_2AgBiBr_6$ thin films deposited by vacuum sublimation and solution processing with a goal of achieving the precise composition stoichiometry in $Cs_2AgBiBr_6$. The solution-processed $Cs_2AgBiBr_6$ film showed higher crystallinity, narrower electronic bandgap, longer photoexcitation lifetime and higher mobility than the vacuum-sublimated one. Quantitative X-ray photoelectron spectra (XPS) analysis revealed the origin of the superior performance of the solution processed films to be a near-stiochiometric existence of its chemical composition. The resulting perovskite solar cells delivered a champion PCE as high as 2.51 %. To the best of our knowledge, the PCE presented in this work is the highest efficiency in $Cs_2AgBiBr_6$-based PSCs.

6.1 Preparation of Solution- and Vacuum-Processed $Cs_2AgBiBr_6$ films

The orange crystalline powder of $Cs_2AgBiBr_6$ (Figure A6.1a,b,c) was synthesized by keeping the ratio 2:1:1 of CsBr:AgBr:$BiBr_3$ in HBr with the processes of reflux, evaporation, crystal growth, decanting and washing. Solution-processed $Cs_2AgBiBr_6$ film was deposited on TiO_2 layer by spin-coating of 0.5 M $Cs_2AgBiBr_6$ solution in dimethyl sulfoxide (DMSO). Vacuum-sublimated $Cs_2AgBiBr_6$ film was obtained via a multiple cycles of sequentially deposition of CsBr, AgBr and

$BiBr_3$ precursor materials at a base pressure of 5.0×10^{-4} Pa (Figure A6.1d,e,f). Both the vacuum sublimation and solution processing deposition methods yielded $Cs_2AgBiBr_6$ films with a translucent yellow appearance (Figure A6.1c,g). For the vacuum sublimation process, CuBr/AgBr/$BiBr_3$ stacks with a 2:1:1 molar ratio were sequentially deposited onto the TiO_2 layer by repeating five cycles. The solution-processed films were achieved on the TiO_2 layer by spin-coating 0.5 M $Cs_2AgBiBr_6$ solution onto the TiO_2 layer. Subsequent annealing at optimized temperatures of 220 °C and 280 °C yielded optimized $Cs_2AgBiBr_6$ absorber layers for the vacuum sublimation and solution processing methods, respectively. The thickness of both films was approximately 200 nm. A schematic diagram showing a comparison of the two different deposition processes is given in **Figure 6.1**. For the vacuum sublimation process, the multilayer stack of CuBr/AgBr/$BiBr_3$ yielded $Cs_2AgBiBr_6$ absorber layer by a thermally induced diffusion reaction. This diffusion reaction was facilitated by the ultrathin nature of each precursor layer deposited.

6.2 Crystalline Properties of $Cs_2AgBiBr_6$ films

To understand the morphological properties of the $Cs_2AgBiBr_6$ thin films based on vacuum sublimation and solution processing, their crystallinity and surface morphology were investigated. XRD patterns were obtained for the vacuum-processed films annealed at 180 °C, 200 °C, 220 °C and 240 °C, and solution-processed films annealed at 240 °C, 260 °C, 280 °C and 300 °C. The solution-processed films were annealed for 5 min at the given temperatures to improve the film crystallinity while a more prolonged annealing time of 30 min was required for the vacuum-processed films to allow a nano-scale solid state reaction. XRD results presented in **Figure 6.2**a and 2b showed that the annealed thin films obtained from both deposition processes possessed the same patterns as those previously reported.[20,28,29] There was an increase in peak

intensity as the annealing temperature increased in both cases. The highest peak intensities were observed at 220 °C and 280 °C for the vacuum- and solution-processed film, respectively. To further confirm the optimum annealing temperature, the grain sizes of the crystallites making up the thin films were determined by calculating the crystalline domain sizes. Full width at half maximum (FWHM) values, obtained from the Gaussian fit of the most intense peaks of each XRD pattern, were substituted into the Scherrer equation.

A gradual increase in crystalline domain size was observed from 180 °C to 220 °C and from 240 °C to 280 °C while the domain sizes decreased at higher temperatures of 240 °C and 280 °C for the vacuum-and solution-processed film, respectively. Furthermore, higher degree of crystallinity was seen in the solution-processed $Cs_2AgBiBr_6$ film compared to the vacuum-processed one. The realization of $Cs_2AgBiBr_6$ phase with difference in crystallinity was further confirmed by two-dimensional grazing incidence X-ray diffraction (GIXRD), which can evaluate the crystallinity of thin films without interference with the underlyer (Figure 6.2c,d). The indexed lines agreed well with the $Cs_2AgBiBr_6$ peaks on the XRD patterns (Figure 6.2a,b). This gradual increase in crystallite size followed by a size decrease and the creation of pin-hole defects was further observed from the SEM top images (Figure A6.2**)**. Full coverage of vacuum- and solution-processed $Cs_2AgBiBr_6$ films were observed upto the optimized annealing temperatures of 220 °C and 280 °C. AFM images showing the surface morphologies (Figure A6.3**)** further revealed the larger crystallite grain size in the solution-processed $Cs_2AgBiBr_6$ film than the vacuum-processed one.

6.3 Electronic Structure of $Cs_2AgBiBr_6$ films

To investigate the origin of the superior crystalline and morphological properties of the solution-processed $Cs_2AgBiBr_6$ film, the actual molar ratios of the elemental compositions in the vacuum-

and solution-processed films were determined via post-annealing XPS analysis. **Figure 6.3** and Figure A6.4 present the XPS spectra of Cs 3d, Ag 3d, Bi 4f and Br 3d core levels in the vacuum- and solution-processed $Cs_2AgBiBr_6$ films. The composition ratios were obtained by processing the data of Cs 3d, Ag 3d, Bi 4f and Br 3d core levels with XPSPEAK software and Casa XPS program (Casa Software Ltd, UK). The relative sensitivity factors (RSF) provided in the Casa XPS software library were utilized to quantify constituent elements. **Table 6.1** summarizes the detailed parameters for calculating the atomic ratios of the chemical composition of solution- and vacuum-processed $Cs_2AgBiBr_6$ thin films. Figure A6.5 plots the actual atomic component ratios in the vacuum- and solution-processed $Cs_2AgBiBr_6$ films. It can be seen that the vacuum-processed film exhibited a wider deviation from the 2:1:1:6 ratio of Cs:Ag:Bi:Br expected for the $Cs_2AgBiBr_6$ compound. Although partial Br maybe lost in the form of gaseous bromine during annealing, the larger loss of gaseous Br in the vacuum-processed film may have resulted from the transformation of the precursor material into vapor form during vacuum deposition. An annealing of the vacuum-processed $Cs_2AgBiBr_6$ films in a Br vapor atmosphere may mitigate this loss. However, it should be noted that a careful modulation of the Br composition is required to achieve high-quality $Cs_2AgBiBr_6$ films with reduced low-energy-forming deep level defects. This stems from the conflicting reports on the best crystal growth conditions for this compound. For instances, Xiao *et al.*[24] predicted a Br-poor/Bi-rich condition while Li *et al.*[35] reported a Br-rich/Bi-poor condition. Furthermore, the XRD patterns of vacuum- and solution-processed $Cs_2AgBiBr_6$ films were investigated by heating them at 100 °C in ambient for 300 hrs. Although there was a slight reduction in the intensities for both films, no appearance of new crystal phase and no changes of the XRD peak patterns were observed after a long time and high temperature aging (Figure A6.6).

6.4 Photophysical properties of $Cs_2AgBiBr_6$ films

For the thin films to be suitable for PV application, it is important to understand the photophysical properties of $Cs_2AgBiBr_6$ films. Therefore, UV-Vis absorption, steady state photoluminescent (PL) spectra and time-resolved PL (TRPL) spectra of $Cs_2AgBiBr_6$ films were conducted to study their photophysical properties. **Figure 6.4**a shows the UV-Vis absorption spectra for both samples. Insets are the Tauc plots extracted from the UV-Vis absorption spectra. A sharp peak could be seen at 438 nm and 442 nm on the absorption spectra of the solution- and vacuum-processed $Cs_2AgBiBr_6$ films, respectively. Since there is no monotonic variation between crystallite size and peak shape, the existence of such peaks did not result from quantum confined excitonic transitions. Therefore, the peaks are ascribed to *s-p* transitions occurring in bismuth (Bi). Furthermore, the Tauc plots confirmed the indirect bandgap character in the two films. Values of phonon assisted transition energies of 1.83 eV and 2.12 eV were obtained for the solution-processed film, indicating a bandgap of 1.98 eV. Whereas, the vacuum-processed film presented phonon assisted energies of 1.89 eV and 2.27 eV, giving a bandgap of 2.08 eV. These results mean that the transitions in the solution- and vacuum-processed $Cs_2AgBiBr_6$ films were assisted by phonon energies of 0.29 eV and 0.38 eV, respectively. Although the two films were made of the same compound, the bandgaps extracted from their Tauc plots had different values. This stemmed from the difference in the pattern of their absorption spectra. Higher absorbance could be seen in the solution-processed film compared with the vacuum-processed one. Such difference in pattern affected the corresponding Tauc plot parameters. Therefore, the difference in bandgap values was associated with the difference in film deposition method. Factors such as the differences in preparation method,[13,36] characterization techniques[12,13,37] structural models[38,39] and disorder in atomic arrangements[40] have been previously reported to be responsible for the wide range of bandgap values of $Cs_2AgBiBr_6$. Figure 6.4b shows the Raman spectroscopies of two

samples. The similarity in Raman peak positions indicated that both films possessed the same elemental components.[30,31] However, the observed difference in peak intensities revealed a gradation in degree of crystallinity in the films.[32-34] The variation in peak intensity was ascribed to the variation in phonon energies in the crystal lattice. There exists a monotonic relationship between degree of crystallinity, phonon energy and peak intensity.[33]

The PL spectra of the solution- and vacuum-processed $Cs_2AgBiBr_6$ films are presented in Figure 6.4c. Bandgap values of 2.01 eV and 1.99 eV were obtained from the probe wavelengths of 616 nm and 624 nm for the vacuum- and solution-processed $Cs_2AgBiBr_6$ films, respectively. The values are within the range of those obtained from the Tauc plots. The PL decay kinetics of the two films are shown in Figure 6.4d. The curves can be separated into initial rapid decay followed by an intermediate decay and a prolonged decay. Therefore, corresponding three different lifetime components; τ_1, τ_2, and τ_3, can be assigned to the photoexcited charges in the thin films. For the solution processed film, the values obtained for τ_1, τ_2 and τ_3 were 0.16±0.02 ns (8 %), 5.8±1.14 ns (29 %) and 56.3±4.0 ns (63 %), respectively. Whereas, the vacuum-processed film yielded 0.16±0.01 ns (9 %), 6.7±0.5 ns (33 %) and 39.0±8 ns (58 %), respectively. The lifetimes of the rapid PL decay components of the solution- and vacuum-processed films are comparable. The same is also seen for the intermediate decay components of both films. However, their prolonged PL decay components exhibited a wide difference in lifetime. The rapid and intermediate decay components likely resulted from the defects such as surface traps and/or recombination involving less mobile excitons. However, the long PL decay component was ascribed to the intrinsic charge carrier recombination. As a result, the long PL decay component would give the fundamental recombination lifetime of the films.[12] Therefore, using Fick's first law of diffusion (Equation 6.1), the room temperature diffusion coefficients (D) for both films

were estimated from their prolonged PL decay components.

$$J = -D\frac{dc}{dx} \quad \text{.....(1)}$$

where J is the diffusion flux, D is the diffusion coefficient and dc/dx is the charge carrier concentration gradient. Subsequent calculations using D yielded mobility values of 0.39 cm^2/Vs and 0.74 cm^2/Vs for the vacuum- and solution-processed films, respectively. Compared to the vacuum-processed film, the solution-processed film exhibited higher mobility. Moreover, the extracted mobility values were far lower than those exhibited by the standard $MAPbI_3$ perovskites.[41,42] This, among other factors, is responsible for the low-performance commonly reported for $Cs_2AgBiBr_6$-based solar cells.

6.5 Photovoltaic performance

The planar perovskite solar cells with an n-i-p structure of FTO/TiO_2/perovskite/Spiro-OMeTAD/MoO_3/Ag (**Figure 6.5**a) were fabricated to investigate the photovoltaic performance of solution- and vacuum-processed $Cs_2AgBiBr_6$ films. The annealing temperature was optimized to be 220 °C and 280 °C for vacuum- and solution-processed devices, respectively (Figure A6.7). As shown in Figure 6.5b and **Table 6.2**, the champion solution- and vacuum-processed devices presented PCEs of 2.51% and 1.41 %, respectively. The eighty devices fabricated, in each case, confirmed the reproducibility of efficiency (Figure A6.8), producing the average PCEs of 2.48±0.03 % and 1.35±0.06 % for solution- and vacuum-processed devices, respectively. The obtained photovoltaic parameters were far inferior to those already possessed by the lead-based perovskites. This can be attributed to the less suitable electronic and photophysical properties of the $Cs_2AgBiBr_6$ thin film which has wide bandgap ≥ 0.95 eV with indirect character and low charge carrier mobility. Interestingly, there was a 78% increase in the PCE when the vacuum sublimation method was replaced with solution processing technique to deposit the $Cs_2AgBiBr_6$

film. As aforementioned, owing to the accurate composition stoichiometry of $Cs_2AgBiBr_6$, the solution-processed $Cs_2AgBiBr_6$ film exhibited excellent optoelectronic and photophysical properties with higher crystallinity, narrower electronic bandgap, longer photoexcitation lifetime and higher mobility. These merits enable the corresponding perovskite solar cells to deliver a champion power conversion efficiency (PCE) of 2.51 %. Furthermore, the external quantum efficiency (EQE) of both devices are presented in Figure 6.5c. The EQE is the ratio of the amount of current created by the solar cell to the amount of photons of a given energy from the incident photons. It can be seen that the higher current was generated in the solution-processed device for the same photon energy. The overall generation of current by high energy photons (with shorter wavelength $\leq$ 550 nm) was ascribed to the wide and indirect bandgap character of the absorber layers. Figure 6.5d shows the results for the stability tests of vacuum- and solution-processed PSCs. The devices were kept in ambient without encapsulation for 15 days. Both devices were able to retain over 90 % of their initial PCEs. The ambient stability obtained for the two devices are greater than those of standard $MAPbI_3$ based devices and can be traced to the stability of the $Cs_2AgBiBr_6$ absorber layers.

6.6 Conclusion

In summary, a comparison has been executed by preparing $Cs_2AgBiBr_6$ halide double perovskite via vacuum-sublimation and solution-processing. The solution-processed film exhibited higher crystallinity, lower bandgap, longer charge carrier lifetime and higher mobility compared to the vacuum-processed one. Optimized power conversion efficiencies of 2.51 % and 1.41 % were obtained for the solution- and vacuum-processed films, respectively, as a result of the differences in their optoelectronic and photophysical properties. Although, immense research is still required to improve the performance of halide double perovskite based devices, the finding in this work

gives a hint that a wide deviation from ideal stoichiometry is responsible for lower film quality and device performance, whereas solution-processing film deposition technique could guarantee a precise composition stoichiometry to form high quality multicomponent perovskite films.

Reference

1. Zhao, D.; Wang, C.; Song, Z.; Yu, Y.; Chen, C.; Zhao, X.; Zhu, K.; Yan, Y. Four-Terminal All-Perovskite Tandem Solar Cells Achieving Power Conversion Efficiencies Exceeding 23%. *ACS Energy Lett.* **2018**, *3*, 305-206.
2. Babayigit, A.; Ethirajan, A.; Muller, M.; Conings, B. Toxicity of Organometal Halide Perovskite Solar Cells. *Nat. Mater.* **2016**, *15***,** 247-251.
3. Liu, F.; Dong, Q.; Wong, M. K.; Djurisic, A. B.; Ng, A.; Ren, Z.; Shen, Q.; Surya, C.; Chan, W. K.; Wang, J.; Ng, A. M. C.; Liao, C.; Li, H.; Shih, K.; Wei, C.; Su, H.; Dai, J. Is Excess PbI_2 Beneficial for Perovskite Solar Cell Performance? *Adv. Energy Mater.* **2016**, *6*, 1502206.
4. Gao, W.; Ran, C.; Li, J.; Dong, H.; Jiao, B.; Zhang, L.; Lan, X.; Hou, X.; Wu, Z. Robust Stability of Efficient Lead-Free Formamidinium Tin Iodide Perovskite Solar Cells Realized by Structural Regulation. *J. Phys. Chem. Lett.* **2018**, *9*, 6999-7006.
5. Konstantakou, M.; Stergiopoulos, T. A Critical Review on Tin Halide Perovskite Solar Cells. *J. Mater. Chem. A* **2017**, *5*, 11518-11549.
6. Krishnamoorthy, T.; Ding, H.; Yan, C.; Leong, W. L.; Baikie, T.; Zhang, Z. Y.; Sherburne, M.; Li, S.; Asta, M.; Mathews, N.; Mhaisalkar, S. G. Lead-Free Germanium Iodide Perovskite Materials for Photovoltaic Applications. *J. Mater. Chem. A* **2015**, *3*, 23829-23832.

7. Shi, Z. J.; Guo, J.; Chen, Y. H.; Li, Q.; Pan, Y. F.; Zhang, H. J.; Xia, Y. D.; Huang, W. Lead-Free Organic–Inorganic Hybrid Perovskites for Photovoltaic Applications: Recent Advances and Perspectives. *Adv. Mater.* **2017**, *29*, 1605005.
8. Heo, J. H.; Kim, J.; Kim, H.; Moon, S. H.; Im, S. H.; Hong, K.-H. J. Roles of SnX_2 (X = F, Cl, Br) Additives in Tin-Based Halide Perovskites toward Highly Efficient and Stable Lead-Free Perovskite Solar Cells. *Phys. Chem. Lett.* **2018**, *9*, 6024-6031.
9. Stoumpos, C.C.; Frazer, L.; Clark, D.J.; Kim, Y.S.; Rhim, S.H.; Freeman, A.J.; Ketterson, J.B.; Jang, J.I.; Kanatzidis, M.G. Hybrid Germanium Iodide Perovskite Semiconductors: Active Lone Pairs, Structural Distortions, Direct and Indirect Energy Gaps, and Strong Nonlinear Optical Properties. *J. Am. Chem. Soc.* **2015**, *137*, 6804-6819.
10. Zhang, Q.; Hao, F.; Li, J.; Zhou, Y.; Wei, Y.; Lin, H.; Perovskite Solar Cells: Must Lead be Replaced- and Can It be Done? *Sci. Technol. Adv. Mater.* **2018**, *19*, 425-442.
11. Marshall, K. P.; Walker, M.; Walton, R. I.; Hatton, R. A. Enhanced Stability and Efficiency in Hole-Transport-Layer-Free $CsSnI_3$ Perovskite Photovoltaics. *Nat. Energy* **2016**, 1, 1.
12. Slavney, A. H.; Hu, T.; Lindenberg, A. M.; Karunadasa, H. I. A Bismuth-Halide Double Perovskite with Long Carrier Recombination Lifetime for Photovoltaic Applications. *J. Am. Chem. Soc.* **2016**, *138*, 2138-2141.
13. McClure, E. T.; Ball, M. R.; Windl, W.; Woodward, P. M. Cs_2AgBiX_6 (X = Br, Cl): New Visible Light Absorbing, Lead-Free Halide Perovskite Semiconductors. *Chem. Mater.* **2016**, *28*, 1348-1354.
14. Volonakis, G.; Filip, M. R.; Haghighirad, A. A.; Sakai, N.; Wenger, B.; Snaith, H. J.; Giustino, F. Lead-Free Halide Double Perovskites via Heterovalent Substitution of Noble Metals. *J. Phys. Chem. Lett.* **2016**, *7*, 1254-1259.

15. Du, K.-Z.; Meng, W.; Wang, X.; Yan, Y.; Mitzi, D. B. Bandgap Engineering of Lead-Free Double Perovskite Cs_2 $AgBiBr_6$ through Trivalent Metal Alloying. *Angew. Chem. Int. Ed.* **2017**, *56*, 8158-8162.

16. Du, K.-Z.; Wang, X.; Han, Q.; Yan, Y.; Mitzi, D. B. Heterovalent B-Site Co-Alloying Approach for Halide Perovskite Bandgap Engineering. *ACS Energy Lett.* **2017**, *2*, 2486-2490.

17. Wu, C.; Zhang, Q.; Liu, Y.; Luo, W.; Guo, X.; Huang, Z.; Ting, H.; Sun, W.; Zhong, X.; Wei, S.; Wang, S.; Chen, Z.; Xiao, L. The Dawn of Lead-Free Perovskite Solar Cell: Highly Stable Double Perovskite $Cs_2AgBiBr_6$ Film. *Adv. Sci.* **2017**, *5*, 1700759.

18. Ning, W.; Wang, F.; Wu, B.; Lu, J.; Yan, Z.; Liu, X.; Tao, Y.; Liu, J.-M.; Huang, W.; Fahlman, M.; Hultman, L.; Sum, T. C.; Gao, F. Long Electron-Hole Diffusion Length in High-Quality Lead-Free Double Perovskite Films. *Adv. Mater.* **2018**, 1706246.

19. Greul, E.; Petrus, M. L.; Binek, A.; Docampo, P.; Bein, T. Highly Stable, Phase Pure $Cs_2AgBiBr_6$ Double Perovskite Thin Films for Optoelectronic Applications. *J. Mater. Chem. A* **2017**, *5*, 19972-19981.

20. Wang, M.; Zeng, P.; Bai, S.; Gu, J.; Li, F.; Yang, Z.; Liu, M. High-Quality Sequential-Vapor-Deposited $Cs_2AgBiBr_6$ Thin Films for Lead-Free Perovskite Solar Cells. *Sol. RRL* **2018**, 1800217.

21. Connor, B. A.; Leppert, L.; Smith, M. D.; Neaton, J. B.; Karunadasa, H. I. Layered Halide Double Perovskites: Dimensional Reduction of $Cs_2AgBiBr_6$. *J. Am. Chem. Soc.* **2018**, *140*, 5235-5240.

22. Tang, G.; Xiao, Z.; Hosono, H.; Kamiya, T.; Fang, D.; Hong, J. Layered Halide Double Perovskites $Cs_{3+n}M(II)_nSb_2X_{9+3n}$ (M = Sn, Ge) for Photovoltaic Applications. *J. Phys. Chem. Lett.* **2018**, *9*, 43-48.

23. Volonakis, G.; Haghighirad, A. A.; Snaith, H. J.; Giustino, F. Route to Stable Lead-Free Double Perovskites with the Electronic Structure of $CH_3NH_3PbI_3$: A Case for Mixed-Cation $[Cs/CH_3NH_3/CH(NH_2)_2]_2InBiBr_6$. *J. Phys. Chem. Lett.* **2017**, *8*, 3917-3924.

24. Xiao, Z.; Meng, W.; Wang, J.; Yan, Y. Thermodynamic Stability and Defect Chemistry of Bismuth-Based Lead-Free Double Perovskites. *ChemSusChem.* **2016**, *9*, 2628-2633.

25. Chen, M.; Ju, M.-G.; Carl, A. D.; Zong, Y.; Grimm, R. L.; Gu, J.; Zeng, X. C.; Zhou, Y.; Padture, N. P. Cesium Titanium(IV) Bromide Thin Films Based Stable Lead-free Perovskite Solar Cells. *Joule* **2018**, *2*, 558-570.

26. Ke, J. C.-R.; Lewis, D. J.; Walton, A. S.; Spencer, B. F.; O'Brien, P.; Thomas, A. G.; Flavell, W. R. Ambient-Air-Stable Inorganic Cs_2SnI_6 Double Perovskite Thin Films via Aerosol-Assisted Chemical Vapour Deposition. *J. Mater. Chem. A* **2018**, ***6,*** 11205-11214.

27. Gao, W.; Ran, C.; Xi, J.; Jiao, B.; Zhang, W.; Wu, M.; Hou, X.; Wu, Z. High-Quality $Cs_2AgBiBr_6$ Double Perovskite Film for Lead-Free Inverted Planar Heterojunction Solar Cells with 2.2 % Efficiency. *Chem. Phys. Chem.* **2018**, *19*, 1696-1700.

28. Yang, B.; Chen, J.; Yang, S.; Hong, F.; Sun, L.; Han, P.; Pullerits, T.; Deng, W.; Han, K. Lead-Free Silver-Bismuth Halide Double Perovskite Nanocrystals. *Ange. Chem. Int. Ed. Engl.* **2018**, *57*, 5359-5363.

29. Zhou, L.; Xu, Y.-F.; Chen, B.-X.; Kuang, D.-B.; Su, C.-Y. Synthesis and Photocatalytic Application of Stable Lead-Free Cs2AgBiBr6 Perovskite Nanocrystals. *Small* **2018**, 1703762.

30. Ha, S. T.; Liu, X.; Zhang, Q.; Giovanni, D.; Sum, T. C.; Xiong, Q. Synthesis of Organic-Inorganic Lead Halide Perovskite Nanoplatelets: Towards High-Performance Perovskite Solar Cells and Optoelectronic Devices. *Adv. Optical Mater.* 2014, *2*, 838-844.

31. Xie, L.-Q.; Zhang, T.-Y.; Chen, L.; Guo, N.; Wang, Y.; Liu, G.-K.; Wang, J.-R.; Zhou, J.-Z.; Yan, J.-W.; Zhao, Y.-X.; Mao, B.-W.; Tian, Z.-Q. Organic-Inorganic Interactions of Single Crystalline Organolead Halide Perovskites Studied by Raman Spectroscopy. *Phys. Chem. Chem. Phys.* **2016**, *18*, 18112-18118.

32. Edinger, M.; Knopp, M. M.; Kerdoncuff, H.; Rantanen, J.; Rades, T.; Löbmann, K. Quantification of Microwave-Induced Amorphization of Celecoxib in PVP Tablets using Transmission Raman Spectroscopy. *Eur. J. Pharm. Sci.* **2018***, 117,* 62-67.

33. Joya, M. R.; Fonseca, K.M.; Barba-Ortega, J. Difference in the Relative Intensities Raman of the Perovskite PLT with Temperature. *AIP Conf. Pro*. **2014**, *1627*, 42-45.

34. Quarti, C.; Grancini, G.; Mosconi, E.; Bruno, P.; Ball, J. M.; Lee, M. M.; Snaith, H. J.; Petrozza, A.; De Angelis, F. The Raman Spectrum of the $CH_3NH_3PbI_3$ Hybrid Perovskite: Interplay of Theory and Experiment. *J. Phys. Chem. Lett.* **2014**, *5*, 279-284.

35. Li, T.; Zhao, X.; Yang, D.; Du, M.-H.; Zhang, L. Intrinsic Defect Properties in Halide Double Perovskites for Optoelectronic Applications. *Phys. Rev. Appl.* **2018**, *10*, 041001.

36. Filip, M. R.; Hillman, S.; Haghighirad, A.-A.; Snaith, H. J.; Giustino, F. Band Gaps of the Lead-Free Halide Double Perovskites $Cs_2BiAgCl_6$ and $Cs_2BiAgBr_6$ from Theory and Experiment. *J. Phys. Chem. Lett.* **2016**, *7*, 2579-2585.

37. Bartesaghi, D.; Slavney, A. H.; Gelvez-Rueda, M. C.; Connor, B. A.; Grozema, F. C.; Karunadasa, H. I; Savenije, T. J. Charge Carrier Dynamics in $Cs_2AgBiBr_6$ Double Perovskite. *J. Phys. Chem. C* **2018**, *122*, 4809-4816.

38. Savory, C. N.; Walsh, A.; Scanlon, D. O. Can Pb-Free Halide Double Perovskites Support High-Efficiency Solar Cells? *ACS Energy Lett.* **2016**, *1*, 949-955.

39. Han, D.; Zhang, T.; Huang, M.; Sun, D.; Du, M.-H.; Chen, S. Predicting the Thermodynamic Stability of Double-Perovskite Halides from Density Functional Theory. *APL Mater.* **2018**, *6*, 084902.

40. Zhao, X.; Yang, J.; Fu, Y.; Yang, D.; Xu, Q.; Yu, L.; Wei, S.-H.; Zhang, L. Design of Lead-Free Inorganic Halide Perovskites for Solar Cells via Cation-Transmutation. *J. Am. Chem. Soc.* **2017**, *139*, 2630-2638.

41. Hutter, E. M.; Eperon, G. E.; Stranks, S. D.; Savenije, T. J. Charge, Carriers in Planar and Meso-Structured Organic–Inorganic Perovskites: Mobilities, Lifetimes, and Concentrations of Trap States. *J. Phys. Chem. Lett.* **2015**, *6*, 3082-3090.

42. Guo, Z.; Manser, J. S.; Wan, Y.; Kamat, P. V.; Huang, L. Spatial and Temporal Imaging of Long-Range Charge Transport in Perovskite Thin Films by Ultrafast Microscopy. *Nat. Commun.* **2015**, *6*, 7471.

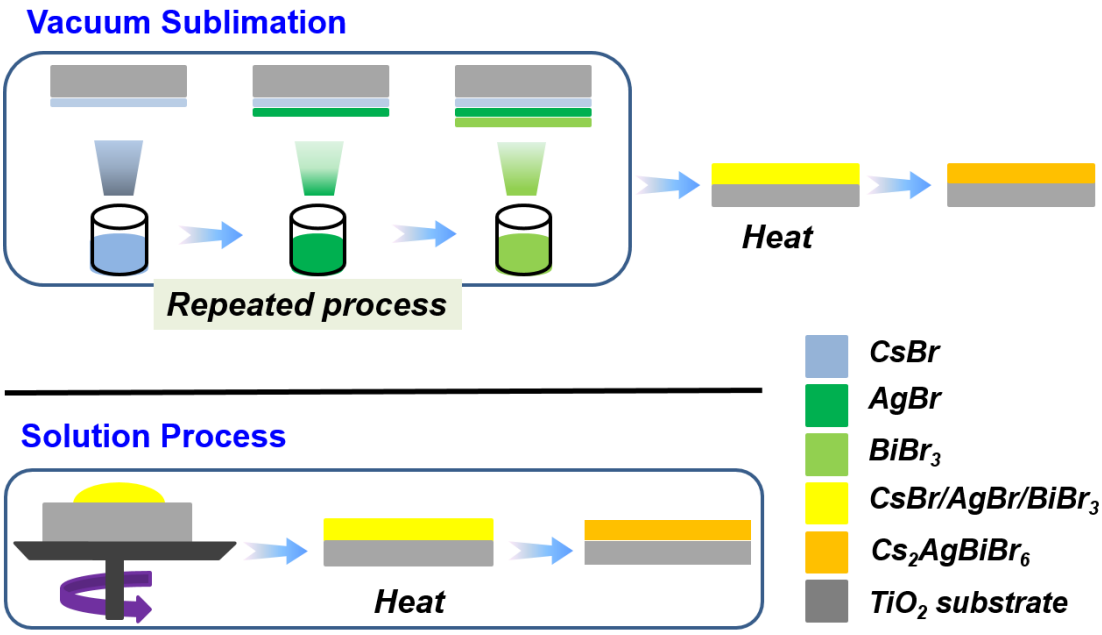

Figure 6.1. Schematic representation of the preparation of $Cs_2AgBiBr_6$ thin films by vacuum-sublimation and solution-processing.

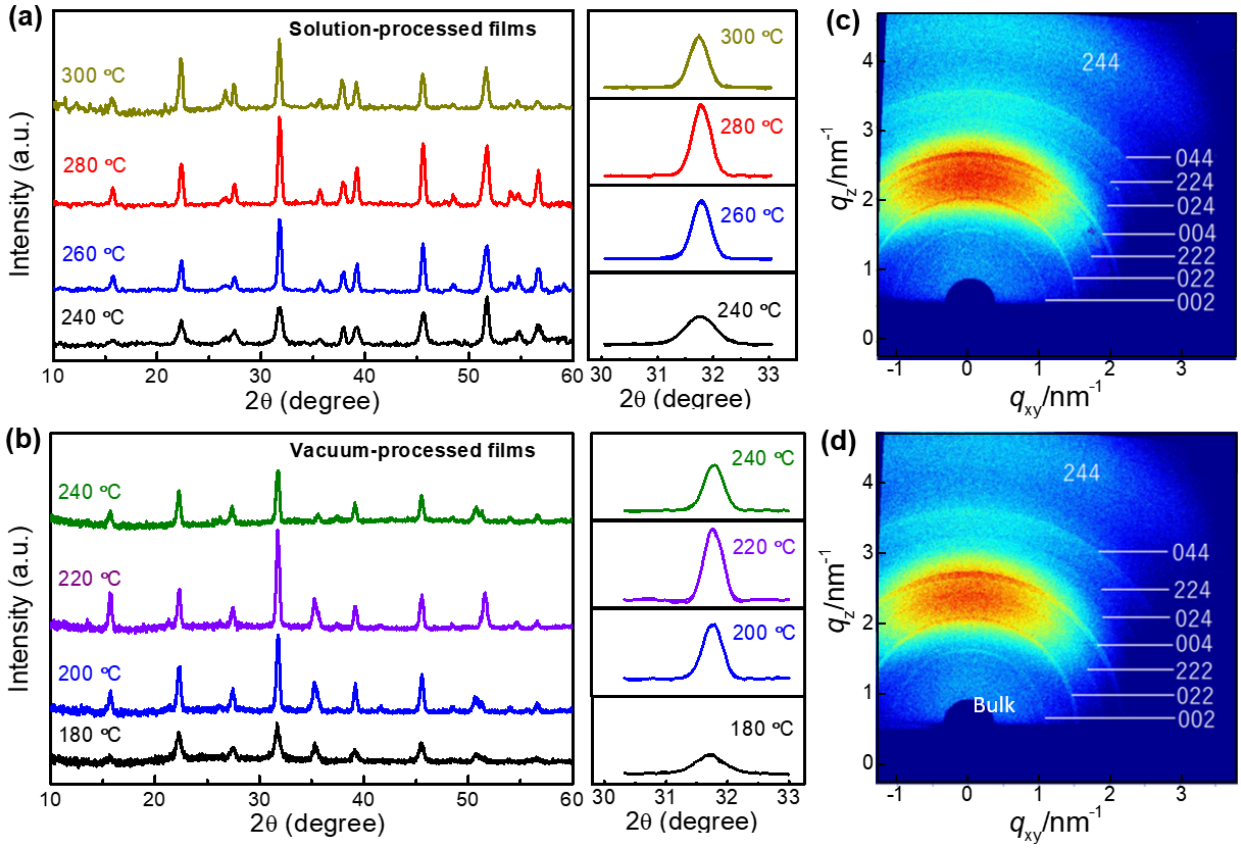

Figure 6.2. Annealing temperature dependent XRD patterns and peak fittings of (a)solution- and (b)vacuum-processed $Cs_2AgBiBr_6$ thin films, respectively. 2D GIXRD patterns of (c) solution- and (d) vacuum-processed $Cs_2AgBiBr_6$ thin films annealed at 280 °C and 220 °C, respectively.

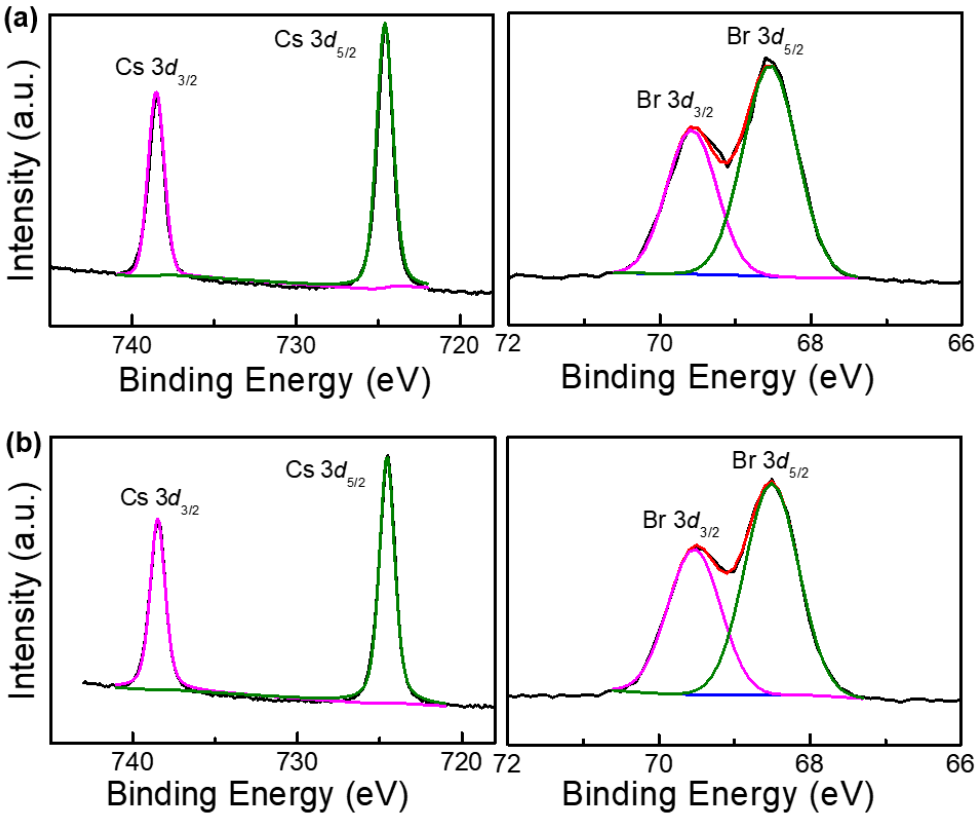

Figure 6.3. Detailed XPS scans of Cs 3d and Br 3d core levels of (a) solution- and (b) vacuum-processed $Cs_2AgBiBr_6$ thin film.

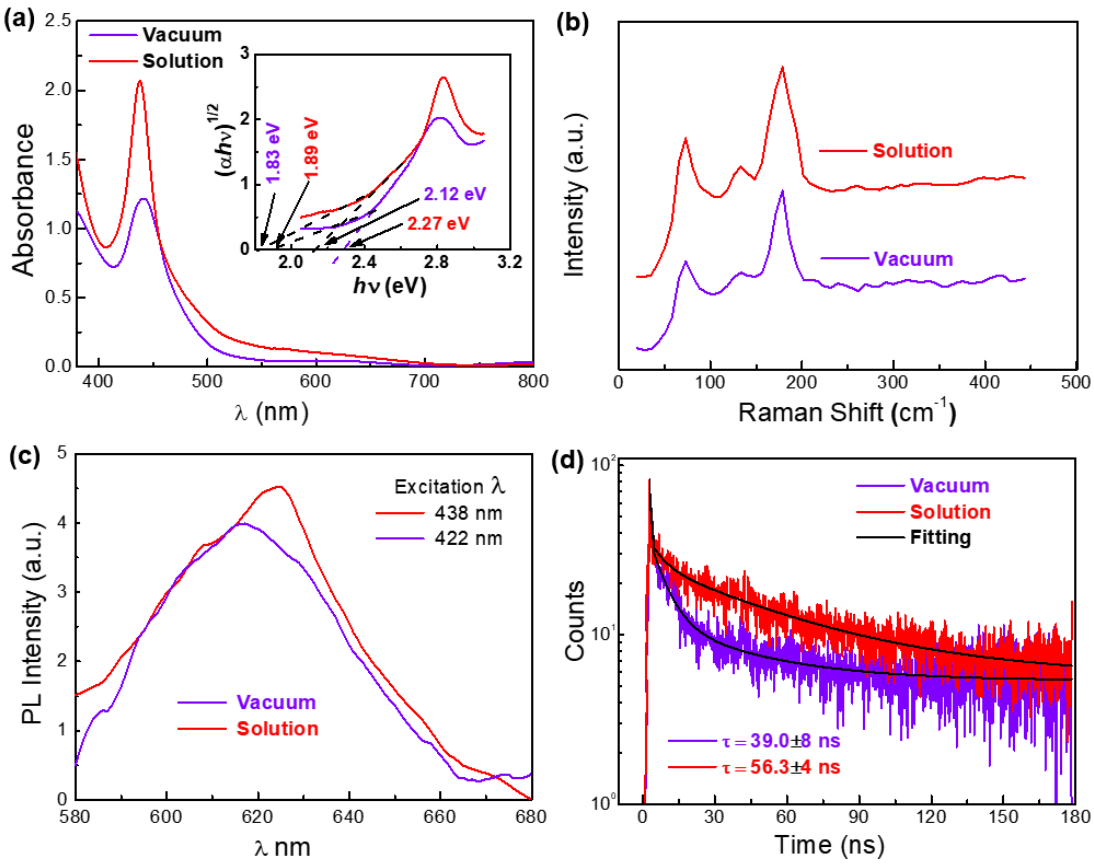

Figure 6.4. (a) UV-Vis absorption spectra, (b) Raman peaks, (c) PL intensity and (d) PL decay dynamics of the optimized $Cs_2AgBiBr_6$ thin films prepared by vacuum-sublimation (purple) and solution-processing (red). Insets of (a) are the Tauc plots extracted from the UV-Vis absorption spectra.

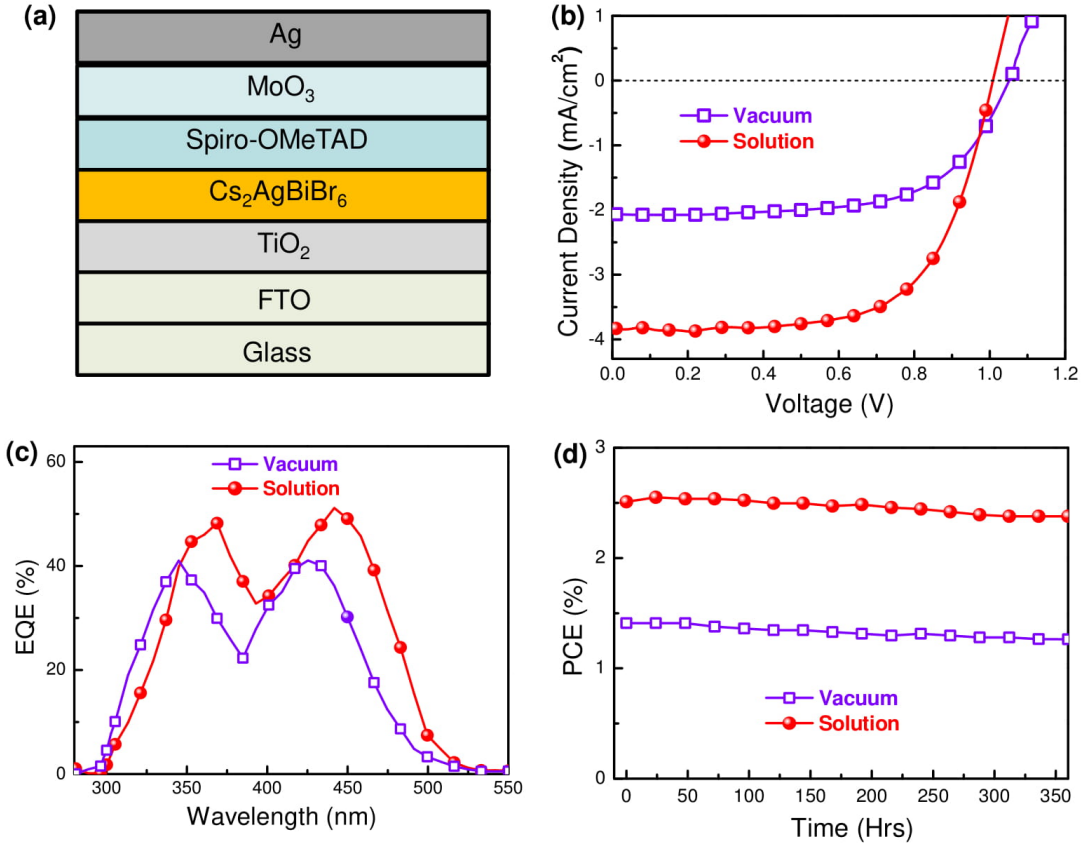

Figure 6.5. (a) Device structure: FTO/TiO_2/$Cs_2AgBiBr_6$/Spiro-OMeTAD/MoO_3/Ag. (b)*J-V* curves, (c) EQE spectra and (d) ambient stability characteristics of the perovskite solar cells fabricated with optimized solution- and vacuum-processed $Cs_2AgBiBr_6$ thin films.

Table 6.1. Atomic ratios of the chemical composition of solution- and vacuum-processed $Cs_2AgBiBr_6$ thin films.

	Element	Core Level	Binding Energy	Area	Scofield sensitivity	Effective Area	Composition (%)	Atom Ratio
Solution	Cs	$3d_{5/2}$	724.00	23826.66	23.80	1001.12	20.50	2.01
		$3d_{3/2}$	738.50	19286.85	16.50	1168.90		
	Ag	$3d_{5/2}$	368.10	5773.72	10.70	539.60	10.30	1.01
		$3d_{3/2}$	374.10	4064.17	7.38	550.70		
	Bi	$4f_{7/2}$	159.18	8314.56	13.90	598.17	10.20	1.00
		$4f_{5/2}$	164.58	5248.90	10.90	481.55		
	Br	$3d_{5/2}$	68.50	5319.54	1.68	3166.39	59.00	5.78
		$3d_{3/2}$	69.50	3571.68	1.16	3079.03		
Vacuum	Cs	$3d_{5/2}$	724.60	27559.92	23.80	1157.98	25.20	2.03
		$3d_{3/2}$	738.50	16570.62	16.50	1004.28		
	Ag	$3d_{5/2}$	368.10	5989.86	10.70	559.80	12.50	1.01
		$3d_{3/2}$	374.10	3784.17	7.38	512.76		
	Bi	$4f_{7/2}$	159.18	8347.09	13.90	600.51	12.40	1.00
		$4f_{5/2}$	164.58	5051.71	10.90	463.46		
	Br	$3d_{5/2}$	68.50	3757.19	1.68	2236.42	49.90	4.02
		$3d_{3/2}$	69.50	2372.42	1.16	2045.19		

Table 6.2. Cell parameters of $Cs_2AgBiBr_6$-based PSCs using different deposition method.

	Deposition Method	J_{sc} (mA/cm^2)	V_{oc} (V)	FF	PCE (%)
Champion	Solution	3.82	1.01	0.65	2.51
	Vacuum	2.06	1.05	0.65	1.41
Average	Solution	3.81±0.01	1.00±0.03	0.63±0.02	2.48±0.03
	Vacuum	2.05±0.02	1.03±0.02	0.62±0.03	1.35±0.06

Chapter 7 Rational Tuning of Molecular Interaction and Energy Level Alignment Enables High-Performance Organic Photovoltaics

Organic photovoltaics (OPVs) are promising as an alternative to fossil fuels due to their light weight, flexibility and roll-to-roll processability.[1–4] However, the commercialization potential of OPVs is still limited by their relatively low efficiency and instability under operational conditions.[5–9] So far, tremendous efforts have been made to improve the power conversion efficiencies (PCEs) of OPVs.[10–13]

Rational design of the donor and acceptor materials to realize high-performance OPV needs to consider absorption profiles to maximize the coverage of the solar spectrum, efficient charge separation and transport.[14–16]. Introducing the fluorine (F) atom into the end-group of the NFAs is one of the most successful strategies to enlarge the absorption, however, the energy levels of NFAs will downshift.[17,18] Meanwhile, the F atom will lead to a change in the molecular interaction behavior to further influence the morphology.[19] Therefore, for the rational design of the high-performance donor/acceptor blend with fluorinated materials, apart from broadening the absorption, to achieve efficient charge separation/transfer, two main issues need to be carefully considered: morphology of the donor and acceptor blend and the energy level alignment between them.

The microstructural morphology of a polymer donor and small molecule acceptor bulk heterojunction (BHJ) was mostly related to the molecular interaction between the donor and acceptor, the miscibility of the materials.[20] An optimized morphology will be crucial for increased charge separation and transport, and therefore higher short-circuit current (J_{sc}) and fill

factor (FF).[21–23] It is significant to understand the design rule of the BHJ blend from the perspective of the chemical structure to attain the excellent morphology desired.

On the other hand, due to the relatively low dielectric constant of organic materials, such that the electron-hole pair formed following charge transfer at the interface experiences a Coulombic attraction, which indicates that a driving force is necessary to overcome the Coulomb force to realize efficient charge dissociation.[24] The driving force is needed to ensure efficient charge separation/transfer, hence, the energy level alignment of the donor and acceptor is needed to be in consideration to achieve high-performance solar cells.[25] However, the deep LUMO and HOMO levels of most NIR acceptors will result in difficulties to match the energy levels of the wide bandgap donors to attain the efficient driving force of charge separation and charge transfer.[26] Therefore, rational selection of the HOMOs and LUMOs of the blend should be seriously considered.

Herein, a new NIR fluorinated small molecule with an absorption offset at 953 nm, named Y1-4F, was synthesized. To systematically study the role of fluorine on the morphology and energy level alignment and provide a general guideline towards a rational design rule of highly efficient donor/acceptor blends, the well-known wide gap donor PBDB-T, a corresponding fluorinated donor PBDB-T-F and a non-fluorinated small molecule Y1 were selected as candidates in this study. **Figure 7.1a** shows the chemical structures of the materials. After rationally tuning the molecular interaction and energy level alignments of the donors and acceptors, we found that when both donor and acceptor are fluorinated, or both are not fluorinated, high-performance OPVs can be realized. Due to the optimized morphology and sufficient driving force for charge separation, a PCE as high as 14.8% was achieved for the fluorinated blend (PBDB-T-F/Y1-4F).

7.1 Selection of the Donor/Acceptor pairs and Photovoltaic Properties

In this study, four active layer blends with fluorinated or non-fluorinated materials were selected to investigate the role of the fluorine in the microstructural morphology and the energy level alignment, and to then envisage a selection rule to deliver high-performance OPVs. The absorption spectra of PBDB-T, PBDB-T-F, Y1, and Y1-4F in solution (chloroform) and in thin films are shown in Figure A7.2 and Figure A7.3, respectively. In going from solution to film, the maximum absorption of Y1 and Y1-4F was redshifted from 738 to 802 nm and from 758 nm to 851 nm, respectively. Compared to the Y1 film, a larger redshift (93 nm) can be observed in the Y1-4F film, signifying that much stronger π-π intermolecular interactions are formed when introducing the fluorine atom into the end-group. The absorption onset of Y1 and Y1-4F films are located at 910 and 953 nm with the optical bandgaps of 1.36 and 1.31 eV, respectively. As shown in Figure A7.2, the polymer donors of PBDB-T and PBDB-T-F showed very analogous absorption profiles in thin films, corresponding to the approximate optical bandgap of 1.82 eV. The electrochemical properties of polymer donors and non-fullerene acceptors were measured by cyclic voltammetry (CV) in anhydrous acetonitrile solutions with ferrocene/ferrocenium (Fc/Fc+) redox couple as an internal reference. From the onset oxidation/reduction potentials in Figure A7.4b, the highest occupied molecular orbital (HOMO) and lowest unoccupied molecular orbital (LUMO) energy levels of PBDB-T, Y1, PBDB-T-F, and Y1-4F were -5.39/-3.48 eV, -5.45/-3.95 eV, -5.50/-3.50 eV and -5.56/-4.11 eV, respectively. Fluorination of the polymer donors and non-fullerene acceptors were found to result in both deeper HOMO and LUMO levels. The energy level alignments of these materials are illustrated in Figure 1b.

Figure7. 2a and 7.**2b** show the *J-V* curves under forward scan direction and the external quantum efficiency (EQE) spectra of devices based on PBDB-T/Y1, PBDB-T/Y1-4F, PBDB-T-F/Y1 and

PBDB-T-F/Y1-4F under the illumination of an AM 1.5G solar simulator, 100 mW cm^{-2}. The average and the best device characteristics of PBDB-T/Y1, PBDB-T/Y1-4F, PBDB-T-F/Y1, and PBDB-T-F/Y1-4F are summarized in **Table 7.1**. The average device data are calculated from 10 individual devices. (Figure S5) The average PCE of 13.0% for both the non-fluorinated OPV (PBDB-T/Y1) with an open circuit voltage (V_{oc}) of 0.88V, a J_{sc} of 21.4 mA/cm^2 and an FF of 69.5% was achieved. However, for the PBDB-T/Y1-4F based device, even though an enhanced J_{sc} (22.7 mA/cm^2) was observed corresponding to the broaden absorption, the low FF of 57% and V_{oc} of 0.74V limited the overall PCE (9.6%). The approximate 140 mV decrease of V_{oc} may correspond to the down-shift of the LUMO level of the acceptor. Furthermore, the PBDB-T-F/Y1 delivered the lowest PCE of 6.6%. Although the highest V_{oc} of 0.92 V was achieved due to the deeper HOMO and LUMO level of the donor materials compared with PBDB-T, the lowest J_{sc} (12.9 mA/cm^2) and FF (55.5%) finally resulted in the poor performance. Ultimately, both fluorinated OPVs exhibited a remarkable average PCE of 14.4%, with the champion PCE as high as 14.8% with a V_{oc} of 0.838 V, a J_{sc} of 24.80 mA/cm^2 and an FF of 71.21%. As shown in Figure 7.2b, the trend observed in the EQE is similar to the one in the J_{SC}. Moreover, the *J-V* curves under both reverse and forward scanning directions were performed on the PBDB-T-F/Y1-4F devices (Figure 7.2c), and a mismatch behavior of PCEs under different scanning directions was observed. Since no hysteresis behavior has ever been reported for OPVs, we speculate that the mismatch of the PCEs is due to the metastable nature of the active layer.[5] Therefore, to investigate the "real" PCE of the OPVs, we performed the steady-state output measurement on the corresponding device, and a PCE of 13.3% was measured. (Figure 7.2d) Notably, the PCE mismatch behavior disappeared, which indicated the reliability of this measurement. (Figure 7.2e) More importantly, the PBDB-T-F/Y1-4F device was sent to Newport Corporation for

certification. A certified quasi-steady-state PCE of 12.86 ± 0.33% was obtained, which is consistent with our result measured in our lab. (Figure A7.6).

7.2 Miscibility and Microstructure Morphology of the Active Materials

To investigate the role of fluorine on the microstructural morphology of the donor/acceptor blend, we first utilized the Flory-Huggins model via contact angle measurements to study the miscibility and interaction between the fluorinated and non-fluorinated materials.[27] As shown in **Figure 7.3** and **Table 7.2**, we obtained the values of the surface free energy (γ_s) from the contact angles on water and diiodomethane (DIM) of 38.74, 46.32, 32.86 and 44.03 mNm^{-1} for Y1, Y1-4F, PBDB-T, and PBDB-T-F, respectively. Moreover, the solubility parameters (δ) for Y1, Y1-4F, PBDB-T, and PBDB-T-F are calculated based on the previous literature,[28] which are 22.84, 24.97, 21.03 and 24.35 $MPa^{1/2}$. Finally, the Flory-Huggins interaction parameters are calculated to be 0.54 for $\chi_{PBDB\text{-}T/Y1,}$ 1.30 for $\chi_{PBDB\text{-}T/Y1\text{-}4F,}$ 0.48 for $\chi_{PBDB\text{-}T\text{-}F/Y1}$ and 0.36 for $\chi_{PBDB\text{-}T\text{-}F/Y1\text{-}4F}$, respectively. These results suggest that Y1 shows the better miscibility between PBDB-T as compared with Y1-4F, and Y1-4F shows better miscibility between PBDB-T-F than Y1, which may result in a poor microstructural morphology for PBDB-T/Y1-4F and PBDB-T-F/Y1, and hence the relatively low PCEs.[20] To further study the effect of the poor miscibility, transmission electron microscopy (TEM) was performed to obtain the information about the phase separation. (Figure A7.7). Notably, the relatively large phase separation behavior was observed for PBDB-T/Y1-4F and PBDB-T-F/Y1, which agrees with the results of the Flory-Huggins model. It has been reported that non-ideal phase separation may result in low carrier mobility,[29] to further confirm that space charge limited current (SCLC)[30] was conducted. As shown in Figure A7.8 and Table B7.1, both PBDB-T/Y1-4F and PBDB-T-F/Y1 show relatively low carrier mobilities compared

with the one for PBDB-T-F/Y1-4F and PBDB-T/Y1. The relatively low mobility may be correlated with the low FF that we obtained from the photovoltaics performance.

To obtain detailed information regarding the molecular packing orientation and domain size, grazing-incidence wide angle and small angle X-ray scattering (GIWAXS and GISAXS) measurements were carried out. **Figure 7.4a** shows the 2D GIWAXS patterns of PBDB-T/Y1, PBDB-T/Y1-4F, PBDB-T-F/Y1, and PBDB-T-F/Y1-4F, respectively. In all blends, a broad peak corresponding to the π-π stacking was observed along the out-of-plane direction at q= 1.7 $Å^{-1}$, which is assigned to the polymer donors, while the scattering peak at q= 0.3 $Å^{-1}$ is assigned to the small molecule acceptors. Although the molecular packing behaviors of all the blends are similar, the crystallinity and crystallite size of PBDB-T/Y1 and PBDB-T-F/Y1-4F are slightly larger than the others, which is beneficial for photon absorption and charge transport.[31] (Figure A7.8). **Figure 7.4b** presents the corresponding 2D GISAXS patterns. The in-plane scattering intensity profiles are shown in Figure A7.10. The Cylinder model[32] was chosen to fit the profiles to roughly estimate the average domain size of the non-fullerene acceptor cluster. The fitted parameters are summarized in Table B7.2. In this model, comparing the length of the cylinder, the radius is more critical to the charge transfer in the vertical direction.[33] A relatively small radius for PBDB-T/Y1 (27.80 Å) and PBDB-T-F/Y1-4F (27.95 Å) was observed, which could be beneficial to charge transfer. However, a large domain size was observed for PBDB-T/Y1-4F (40.95 Å) and PBDB-T-F/Y1 (29.35 Å), and a relatively poor morphology may result from the unbalanced molecular interaction induced by the fluorine atom. The faulty morphologies of the PBDB-T/Y1-4F and PBDB-T-F/Y1 films explain the low performance of their corresponding devices.

7.3 Driving Force of Charge Transfer and Charge Dynamics

In parallel with the morphological investigation, the driving force for charge transfer has to be considered as well. I first conducted density functional theory (DFT) calculations using the ωB97XD functional and 6-31G** basis set to get the optimized molecular geometries of PBDB-T, PBDB-T-F, Y1 and Y1-4F, and then to find their respective energy levels. (**Figure 7.5**) Based on the optimized geometries, the frontier molecular orbital energy levels were then obtained at the same level of theory as the geometry optimizations while the range separation parameter (ω) of the functional was optimally tuned with the implicit consideration of the dielectric environment via the polarizable continuum model (the dielectric constant ε = 4.0).[34] The hole transfer driving force (ΔG_{HT}) is equal to the difference between the lowest excited state (S_1) of the acceptor and the lowest charge transfer state (CT_1). Thus, $\Delta G_{HT} = |HOMO_A| - |HOMO_D| - \Delta E_b$ was calculated based on the theoretical values of HOMOs of donor and acceptor, where ΔE_b is the difference of the binding energies of an acceptor exciton and of a charge pair. Here, we set ΔE_b = 0.15 eV as with the previous work,[35] and the resultant values of the driving forces are summarized in Table B7.3. Compared with the other three blends, the driving force of hole transfer for PBDB-T-F/Y1 was approximately zero, which may have led to the lowest J_{sc} of the corresponding device.

To extract the charge dynamics of the blends, we measured the transient absorption spectra of the blends with a temple resolution of ~100 fs. The pump wavelength is selected at 800 nm, which matches the absorption of the acceptors. To avoid the effect of exciton-exciton annihilation, we keep the excitation density in a week regime below 3 μJ/cm^2. The samples are preserved in a nitrogen atmosphere, and no degeneration is observed during the measurements. I show the transient absorption spectra of the PBDB-T-F/Y1-4F blend in **Figure 7.6a**. A bleaching signal

around 850 nm co-exists in the neat film of Y1-4F at the same excitation condition (Figure A7.11). This signal is consistent with the absorption peak of Y1-4F and can be naturally assigned to the ground state bleaching (GSB) of the acceptor Y1-4F. Besides, the transient absorption spectra of the blend also show two bleaching peaks around 630 nm and 585 nm, which match the absorption peak of the donor PBDB-T-F. In addition, the spectra feature is also observed from the transient absorption of neat PBDB-T-F film at 500 nm excitation (Figure A7.12), confirming the GSB signals of the donor at 630 nm and 585 nm. The bleaching signals at 630 nm and 585 nm are built up with the decays of bleaching signal at 850 nm (Figure 7.6b), indicating the transfer of excitations from Y1-4F to PBDB-T-F. Considering the type-II arrangement of the HOMO and LUMO levels between the donor and acceptor, the excitation transfer will probably create charge transfer states with electrons in the acceptor and holes in the donor. Together with the bleaching signals, we also observe a long-lasting excited state absorption (ESA) signal around 1000 nm, which is not present in both the neat films of the donor and acceptor (Figure A7.11&7.12). The ESA band around 1000 nm shows a delayed rise in the first 10 ps, which is corresponding to the GSB signal rising of the donor (Figure 7.6b). The similar dynamics of the ESA signal and GSB signal of the donor suggests the ESA band around 1000 nm comes from the absorption of the charge transfer state to higher levels and can be used to exhibit the charge transfer dynamics in the blends. The transient absorption spectra of the other three blends are shown in Figure A7.13. Following the same analysis, the ESA bands around 1000 nm of the charge transfer state exist in all the blends and can be used to compare the charge generation and decay dynamics of the four blends.

I compare the generation dynamics of the four blends in Figure 7.6c. The blends of PBDB-T/Y1-4F and PBDB-T-F/Y1-4F show comparable transfer rates with a lifetime of ~ 2 ps. The efficient

charge transfer process is consistent with the large J_{sc} of PBDB-T/Y1-4F and PBDB-T-F/Y1-4F devices. The charge transfer of PBDB-T-F/Y1 is much slower than the other three blends, which probably accounts for the lowest J_{sc} of PBDB-T-F/Y1. In addition, to determine the decay lifetime of the charge transfer state in the four blends, we measure the nanosecond transient absorption spectra of the four blends at an excitation of 532 nm. The extracted decay dynamics of the charge transfer state at the probe wavelength of ~ 1000 nm are plotted in Figure 7.6d. The blend of PBDB-T/Y1-4F shows dramatically longer charge transfer lifetime compared to the other three blends, which may be attributed to the larger hole transfer driving force. Besides, the charge transfer state decays very fast in 10 ns, consistent with the poor J_{sc} measured. Nevertheless, the high J_{sc} measured for the other blends with different charge transfer lifetime suggests a lifetime of > 40 ns may be enough for efficient charge collection in non-fullerene OPV devices. In fullerene-based OPV devices, a driving force of > 0.3 eV is generally accepted for efficient charge transfer.[36] However, recent work has shown that this is inaccurate in non-fullerene OPV devices.[24,37] In this work, we find that even though the driving force is very small for PBDB-T-F/Y1-4F, the charge transfer can still be very efficient, on the other hand, for the PBDB-T-F/Y1 blend, the approximately zero driving force will lead to deficient charge transfer, which may guide the design of new donors and acceptors for higher efficiency organic solar cells.

7.4 Conclusion

In summary, we successfully synthesized a new fluorinated NIR non-fullerene acceptor with a broadened absorption onset of 953 nm, Y1-4F. After rationally tuning the molecular interaction and energy level alignment, the blend with the fluorinated polymer donor PBDB-T-F achieved a champion PCE as high as 14.8% with steady-state PCE of 13.3%. Moreover, a certified Quasi-Steady state PCE of 12.9% was obtained from Newport Corporation, which is in excellently consistency with the result measured in our lab. The unique energy level alignment enables a

small but sufficient driving force of charge transfer, which could lead to an enhanced photocurrent without sacrificing V_{oc}. In addition, a relatively low Flory-Huggins molecular interaction parameter of 0.36 was realized. Due to this well-matched miscibility of fluorinated materials, an optimized morphology with desired phase separation and crystallinity was realized. Our work provides insights into the rational design of donor/acceptor blends by considering the morphology and energy level simultaneously.

References

1. Graetzel, M., Janssen, R. A. J., Mitzi, D. B. & Sargent, E. H. Materials interface engineering for solution-processed photovoltaics. *Nature* **488,** 304–312 (2012).
2. Li, G., Zhu, R. & Yang, Y. Polymer solar cells. *Nature Photonics* **6,** 153–161 (2012).
3. Cheng, P., Li, G., Zhan, X. & Yang, Y. Next-generation organic photovoltaics based on non-fullerene acceptors. *Nature Photonics* **12,** 131–142 (2018).
4. Zhang, G. *et al.* Nonfullerene Acceptor Molecules for Bulk Heterojunction Organic Solar Cells. *Chem. Rev.* **118,** 3447–3507 (2018).
5. Cheng, P. & Zhan, X. Stability of organic solar cells: challenges and strategies. *Chem. Soc. Rev.* **45,** 2544–2582 (2016).
6. Cheng, P. *et al.* Alloy Acceptor: Superior Alternative to PCBM toward Efficient and Stable Organic Solar Cells. *Adv. Mater.* **28,** 8021–8028 (2016).
7. Dou, L. *et al.* 25th Anniversary Article: A Decade of Organic/Polymeric Photovoltaic Research. *Adv. Mater.* **25,** 6642–6671 (2013).
8. Janssen, R. A. J. & Nelson, J. Factors Limiting Device Efficiency in Organic Photovoltaics. *Adv. Mater.* **25,** 1847–1858 (2013).
9. Jørgensen, M. *et al.* Stability of polymer solar cells. *Advanced Materials* **24,** 580–612 (2012).

10. Li, W. *et al.* A High-Efficiency Organic Solar Cell Enabled by the Strong Intramolecular Electron Push–Pull Effect of the Nonfullerene Acceptor. *Adv. Mater.* **30,** 1707170 (2018).

11. Zhang, S., Qin, Y., Zhu, J. & Hou, J. Over 14% Efficiency in Polymer Solar Cells Enabled by a Chlorinated Polymer Donor. *Adv. Mater.* **30,** 1800868 (2018).

12. Liu, Y. *et al.* Aggregation and morphology control enables multiple cases of high-efficiency polymer solar cells. *Nat. Commun.* **5:5293,** doi: 10.1038/ncomms6293 (2014).

13. Zhao, J. *et al.* Efficient organic solar cells processed from hydrocarbon solvents. *Nat. Energy* **1,** 15027 (2016).

14. Hou, J., Inganäs, O., Friend, R. H. & Gao, F. Organic solar cells based on non-fullerene acceptors. *Nat. Mater.* **17,** 119–128 (2018).

15. Xu, W. & Gao, F. The progress and prospects of non-fullerene acceptors in ternary blend organic solar cells. *Mater. Horizons* **5,** 206–221 (2018).

16. Yan, C. *et al.* Non-fullerene acceptors for organic solar cells. *Nature Reviews Materials* **3,** (2018).

17. Li, Y. Molecular design of photovoltaic materials for polymer solar cells: Toward suitable electronic energy levels and broad absorption. *Accounts of Chemical Research* **45,** 723–733 (2012).

18. Bin, H. *et al.* Non-Fullerene Polymer Solar Cells Based on Alkylthio and Fluorine Substituted 2D-Conjugated Polymers Reach 9.5% Efficiency. *J. Am. Chem. Soc.* **138,** 4657–4664 (2016).

19. Zhao, W. *et al.* Molecular Optimization Enables over 13% Efficiency in Organic Solar Cells. *J. Am. Chem. Soc.* **139,** 7148–7151 (2017).

20. Ye, L. *et al.* Quantitative relations between interaction parameter, miscibility and function in organic solar cells. *Nat. Mater.* **17,** 253–260 (2018).

21. Chen, G., Sasabe, H., Igarashi, T., Hong, Z. & Kido, J. Squaraine dyes for organic photovoltaic cells. *J. Mater. Chem. A* **3,** 14517–14534 (2015).

22. Wang, Z. *et al.* Highly efficient organic p–i–n photovoltaic cells based on tetraphenyldibenzoperiflanthene and fullerene C 70. *Energy Environ. Sci.* **6,** 249–255 (2013).

23. Huang, Y., Kramer, E. J., Heeger, A. J. & Bazan, G. C. Bulk heterojunction solar cells: Morphology and performance relationships. *Chemical Reviews* **114,** 7006–7043 (2014).

24. Liu, J. *et al.* Fast charge separation in a non-fullerene organic solar cell with a small driving force. *Nat. Energy* **1,** 16089 (2016).

25. Cheng, P. *et al.* Unique Energy Alignments of a Ternary Material System toward High-Performance Organic Photovoltaics. *Adv. Mater.* **30,** 1801501 (2018).

26. Fan, B. *et al.* Fine-tuning of the chemical structure of photoactive materials for highly efficient organic photovoltaics. *Nat. Energy* **3,** 1 (2018).

27. Holliday, S. *et al.* High-efficiency and air-stable P3HT-based polymer solar cells with a new non-fullerene acceptor. *Nat. Commun.* **7,** 11585 (2016).

28. Lin, Y. L., Fusella, M. A. & Rand, B. P. The Impact of Local Morphology on Organic Donor/Acceptor Charge Transfer States. *Adv. Energy Mater.* **1702816,** 1–16 (2018).

29. Sharenko, A., Kuik, M., Toney, M. F. & Nguyen, T. Q. Crystallization-induced phase separation in solution-processed small molecule bulk heterojunction organic solar cells. *Adv. Funct. Mater.* **24,** 3543–3550 (2014).

30. Malliaras, G., Salem, J., Brock, P. & Scott, C. Electrical characteristics and efficiency of single-layer organic light-emitting diodes. *Phys. Rev. B - Condens. Matter Mater. Phys.* **58,** R13411–R13414 (1998).

31. Huang, W. *et al.* Unraveling the morphology of high efficiency polymer solar cells based

on the donor polymer PBDTTT-EFT. *Adv. Energy Mater.* **5,** 1401259 (2015).

32. Rice, S. A. Small angle scattering of X-rays. A. Guinier and G. Fournet. Translated by C. B. Wilson and with a bibliographical appendix by K. L. Yudowitch. Wiley, New York, 1955. 268 pp. $7.50. *J. Polym. Sci.* **19,** 594–594 (1956).

33. Lin, Y. C. *et al.* Energy transfer within small molecule/conjugated polymer blends enhances photovoltaic efficiency. *J. Mater. Chem. A* **5,** 18053–18063 (2017).

34. Sun, H. *et al.* Ionization Energies, Electron Affinities, and Polarization Energies of Organic Molecular Crystals: Quantitative Estimations from a Polarizable Continuum Model (PCM)-Tuned Range-Separated Density Functional Approach. *J. Chem. Theory Comput.* **12,** 2906–2916 (2016).

35. Ward, A. J. *et al.* The Impact of Driving Force on Electron Transfer Rates in Photovoltaic Donor – Acceptor Blends. *Adv. Mater* **27,** 2496–2500 (2015).

36. Brédas, J. L., Beljonne, D., Coropceanu, V. & Cornil, J. Charge-transfer and energy-transfer processes in π-conjugated oligomers and polymers: A molecular picture. *Chem. Rev.* **104,** 4971–5003 (2004).

37. Bin, H. *et al.* 11.4% Efficiency non-fullerene polymer solar cells with trialkylsilyl substituted 2D-conjugated polymer as donor. *Nat. Commun.* **7,** 13651 (2016).

38. Feng, L. *et al.* Thieno[3,2-b]pyrrolo-Fused Pentacyclic Benzotriazole-Based Acceptor for Efficient Organic Photovoltaics. *ACS Appl. Mater. Interfaces* **9,** 31985–31992 (2017).

39. Kawabata, K., Takeguchi, M. & Goto, H. Optical activity of heteroaromatic conjugated polymer films prepared by asymmetric electrochemical polymerization in cholesteric liquid crystals: Structural function for chiral induction. *Macromolecules* **46,** 2078–2091 (2013)

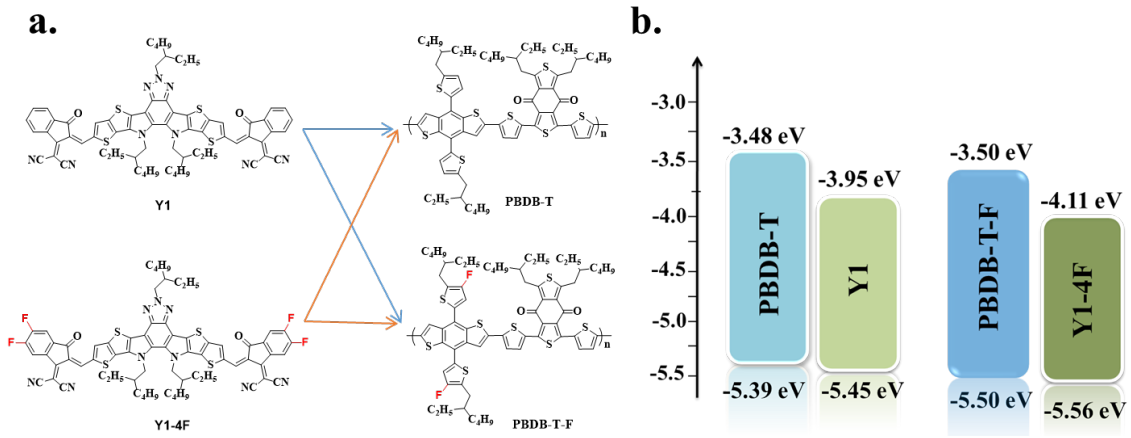

Figure 7.1. a. Chemical structures and **b.** energy level diagrams of donors (PBDB-T, PBDB-T-F), acceptors (Y1, Y1-4F).

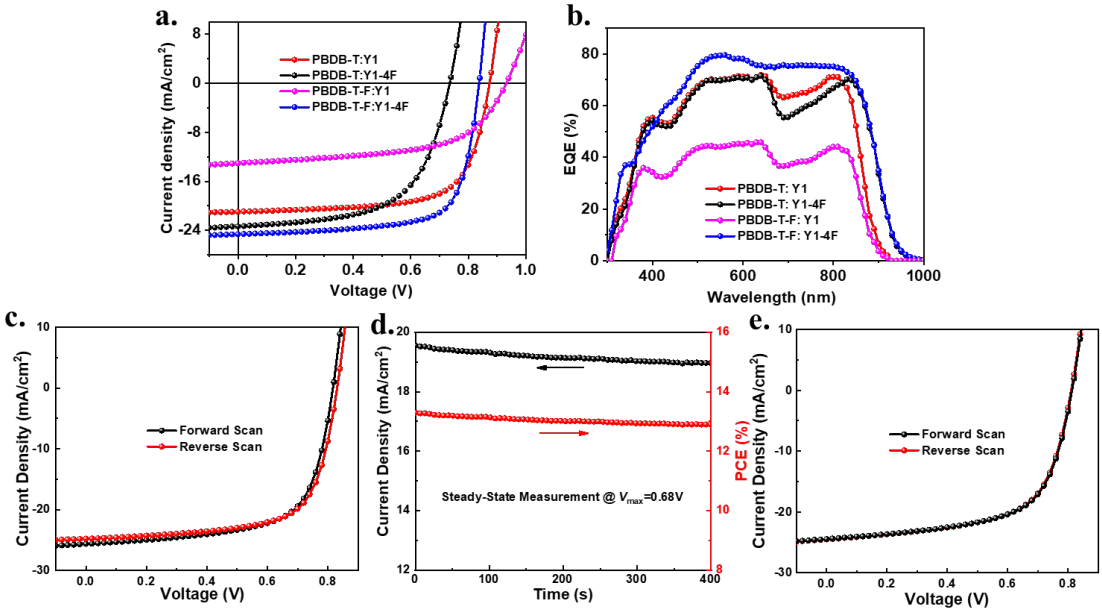

Figure 7.2. a. *J–V* curves and **b.** EQE spectra of devices based on PBDB-T/Y1, PBDB-T/Y1-4F, PBDB-T-F/Y1 and PBDB-T-F/Y1-4F under the illumination of an AM 1.5G solar simulator, 100 mW cm^{-2}. **c.** *J-V* curves of the device based on PBDB-T-F/Y1-4F under reverse and forward scan before Steady-State measurement. **d.** Steady-State measurement of PBDB-T-F/Y1-4F at V_{bias}= 0.68V. **e.** *J-V* curves of the device based on PBDB-T-F/Y1-4F under reverse and forward scan after Steady-State measurement.

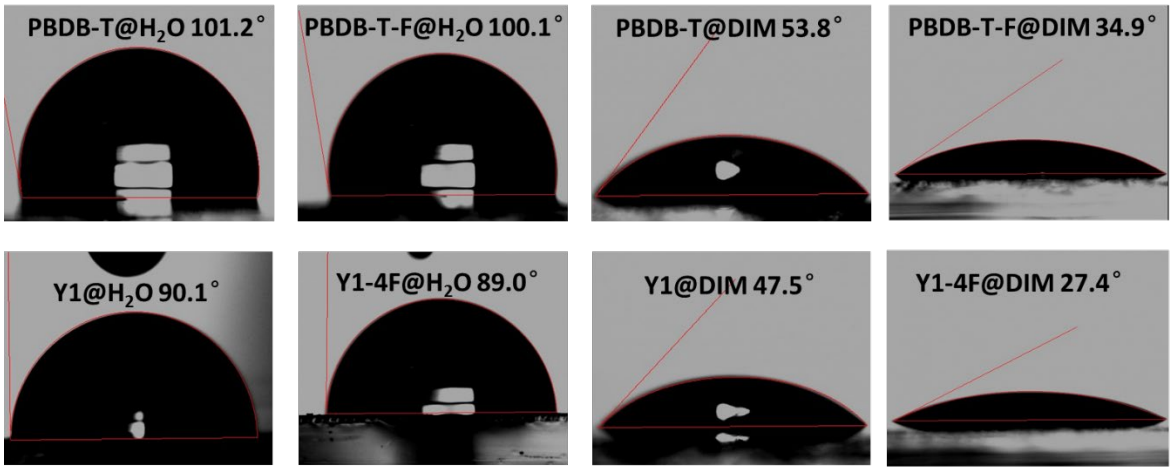

Figure 7.3. Contact angles of PBDBT, PBDB-T-F, Y1 and Y1-4F on H_2O and DIM.

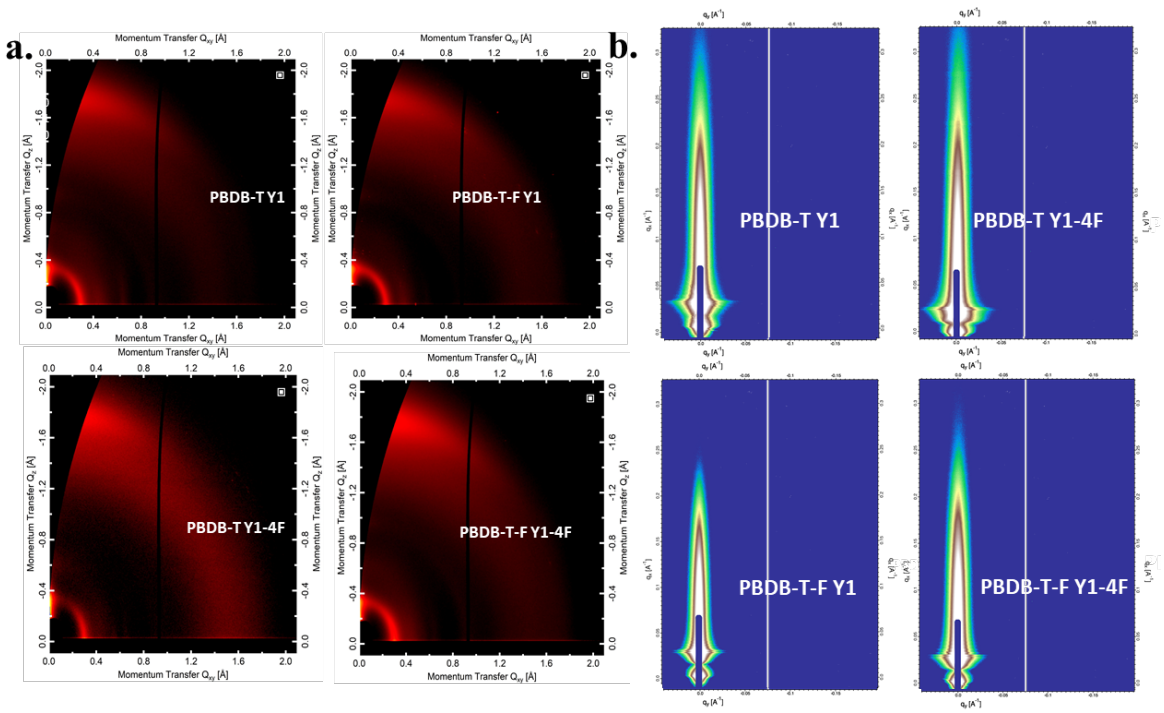

Figure 7.4. a. 2D GIWAXS patterns. **b.** 2D GISAXS patterns of PBDB-T/Y1, PBDB-T/Y1-4F, PBDB-T-F/Y1 and PBDB-T-F/Y1-4F films.

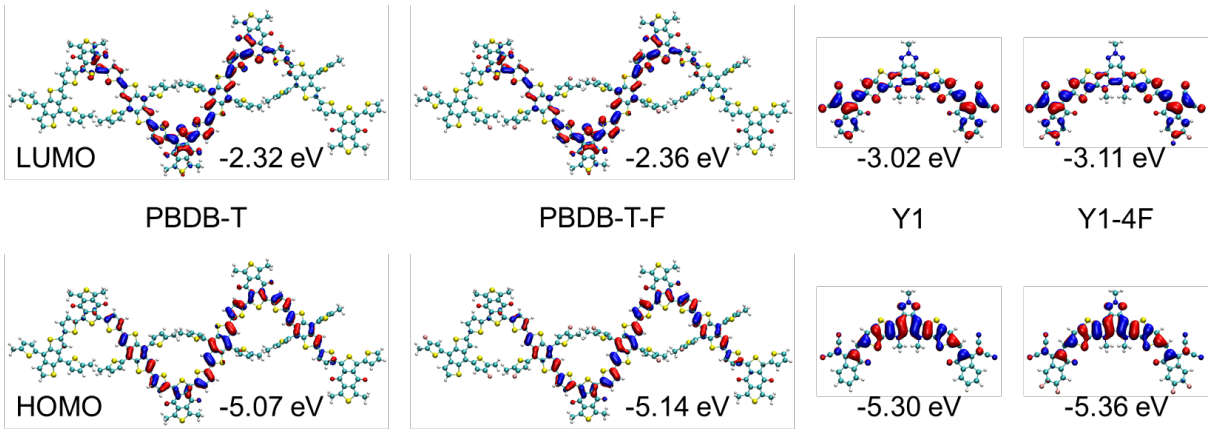

Figure 7.5. Frontier molecular orbitals and corresponding energy levels of PBDB-T, PBDB-T-F, Y1 and Y1-4F calculated by DFT at the PCM-tuned-ωB97XD/6-31G** level based on DFT-ωB97XD/6-31G** optimized geometries.

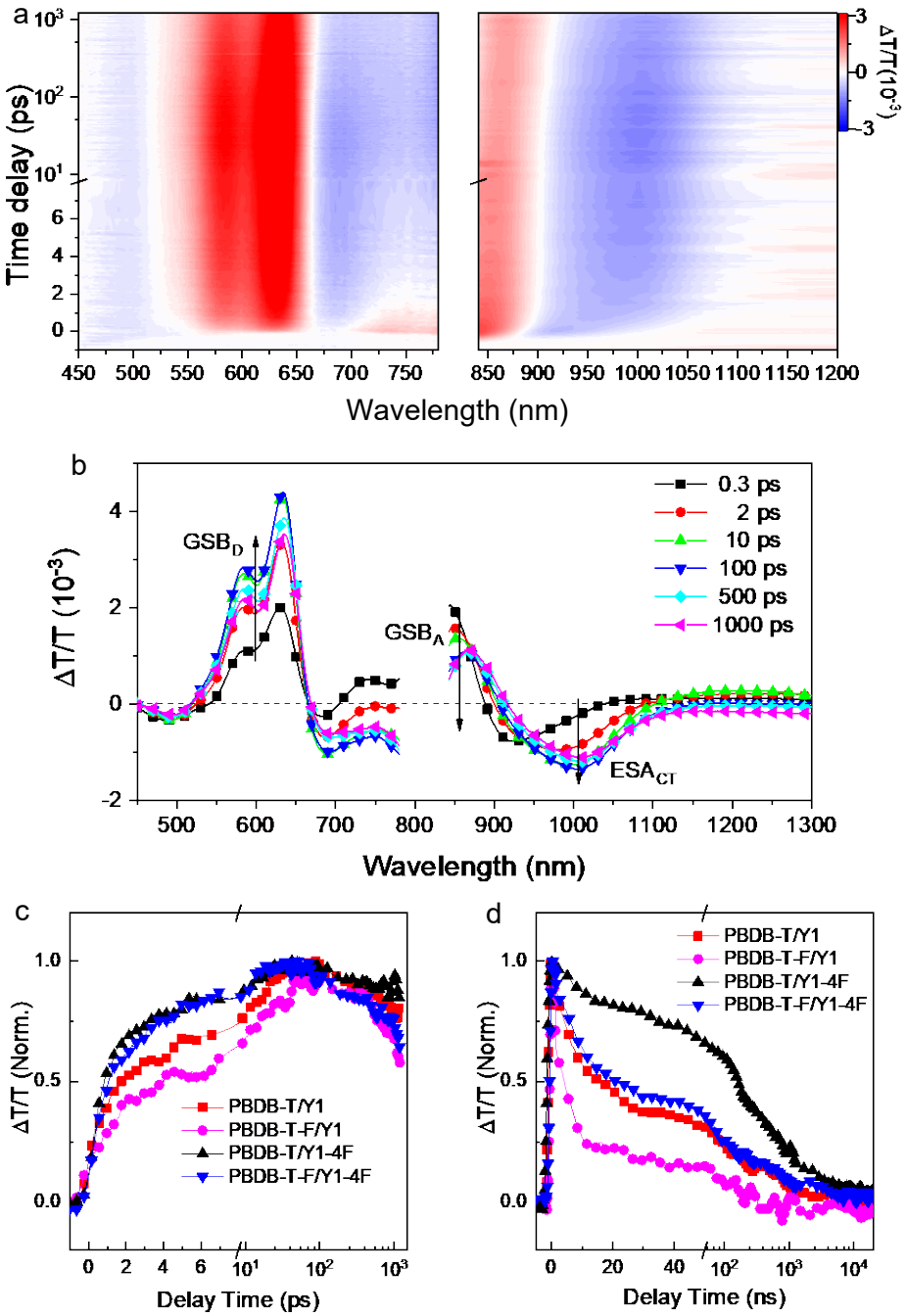

Figure 7.6. Transient absorption measurements. (a) Transient absorption signal recorded from PBDB-T-F/Y1-4F (63) blend excited at 800 nm. (b) Slices of the transient absorption spectra from (a) at different time delays. (c,d) The extracted charge transfer state generation and decay dynamics of PBDB-T/Y1, PBDB-T-F/Y1, PBDB-T/Y1-4F and PBDB-T-F/Y1-4F, respectively.

Table 7.1. Average and the best device data based on PBDB-T/Y1, PBDB-T/Y1-4F, PBDB-T-F/Y1 and PBDB-T-F/Y1-4F

Active layer	V_{OC} (V)	J_{SC} (mA cm^{-2})	Calculated J_{SC} (mA cm^{-2})	FF (%)	PCE (%)	
					average	best
PBDB-T/Y1	0.88±0.01	21.4±0.5	20.7	69.5±1.5	13.0±0.4	13.4
PBDB-T/Y1-4F	0.74±0.01	22.7±0.5	21.9	57.4±1.8	9.6±0.2	9.9
PBDB-T-F/Y1	0.92±0.01	12.9±0.4	12.8	55.5±2.3	6.6±0.4	7.1
PBDB-T-F/Y1-4F	0.83±0.00	25.2±0.6	24.1	68.5±2.1	14.4±0.4	14.8

Table 7.2. The summarized surface free energy, solubility parameters and Flory–Huggins interaction parameters of Y1, Y1-4F, PBDB-T and PBDB-T-F

i	γ_s [mNm^{-1}]	δ [$MPa^{1/2}$]	χ [PBDB-T, *i*]	χ [PBDB-T-F, *i*]
Y1	38.74	22.84	0.54	0.48
Y1-4F	46.32	24.97	1.30	0.36
PBDB-T	32.86	21.03	N/A	N/A
PBDB-T-F	44.03	24.35	N/A	N/A

Appendix A

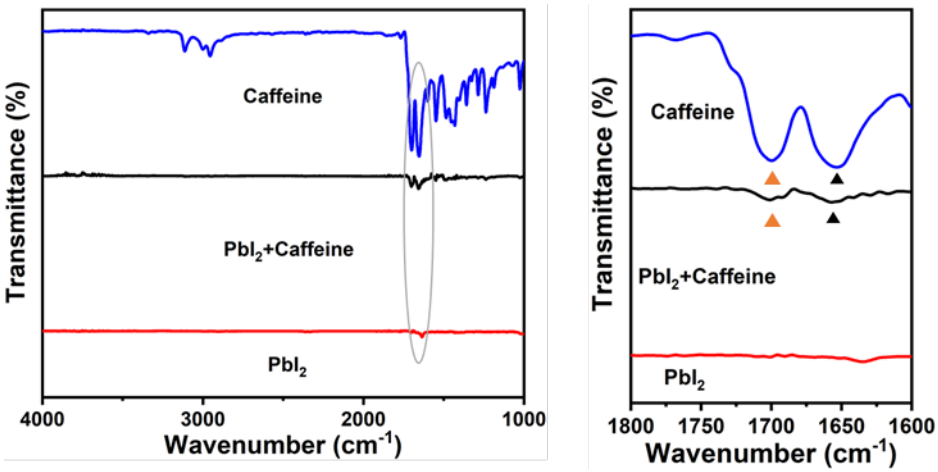

Figure A2.1 FTIR spectra and fingerprint regions of pure caffeine, caffeine-PbI_2 and the pristine PbI_2 films. The triangles indicate the stretching vibration peaks of C=O in the two films.

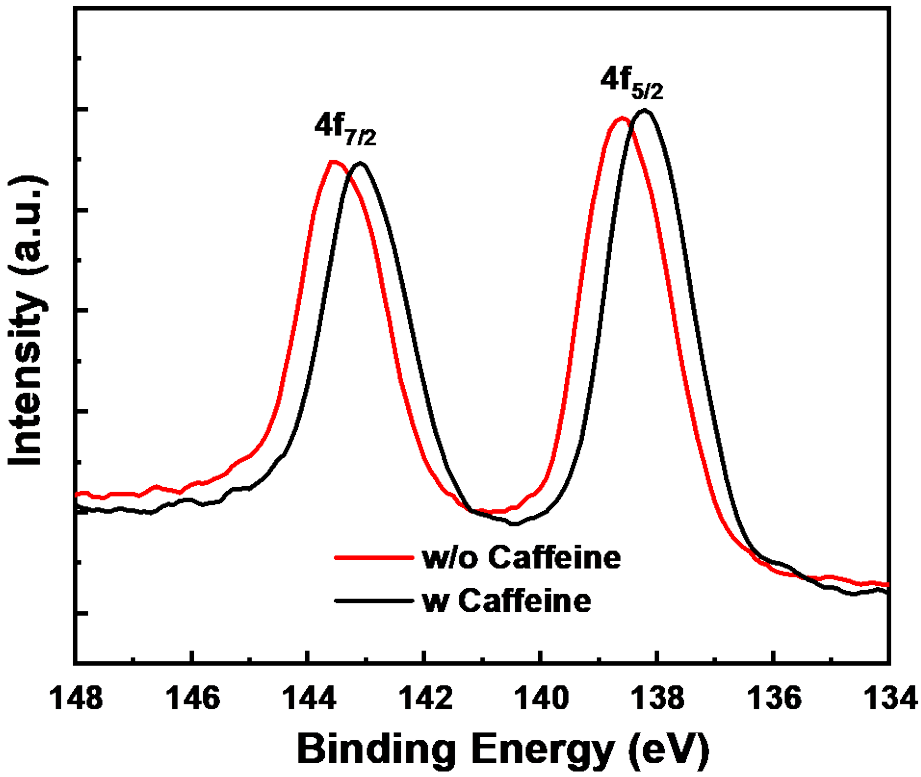

Figure A2.2. XPS data for Pb 4f 7/2 and Pb 4f 5/2 core level spectra in $MAPbI_3$ and $MAPbI_3$: Caffeine films.

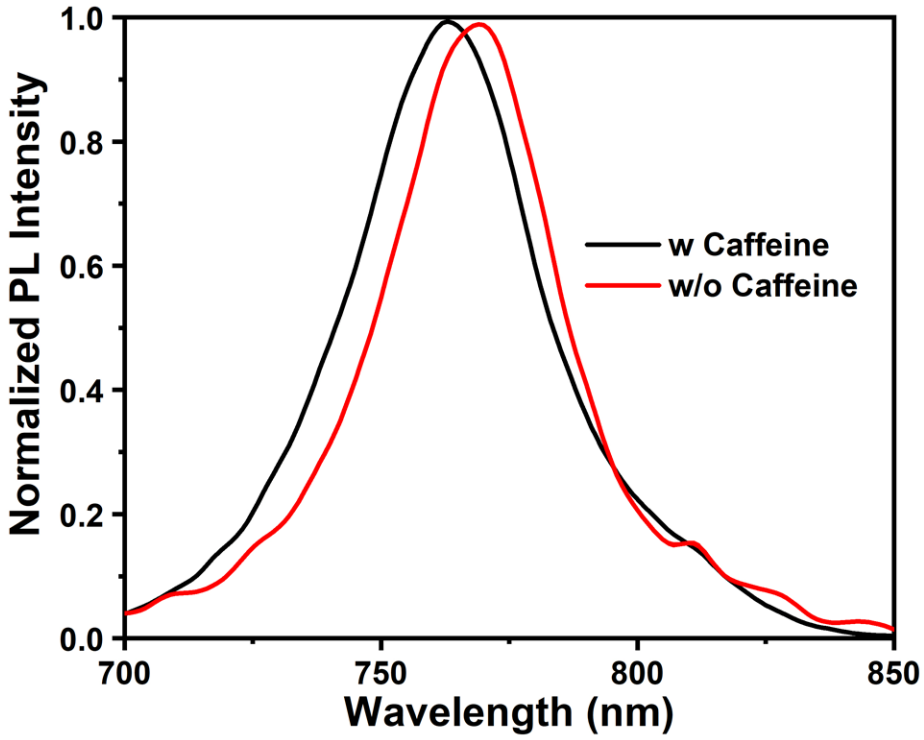

Figure A2.3 Normalized Steady-State PL spectra of PVSK films without and with caffeine.

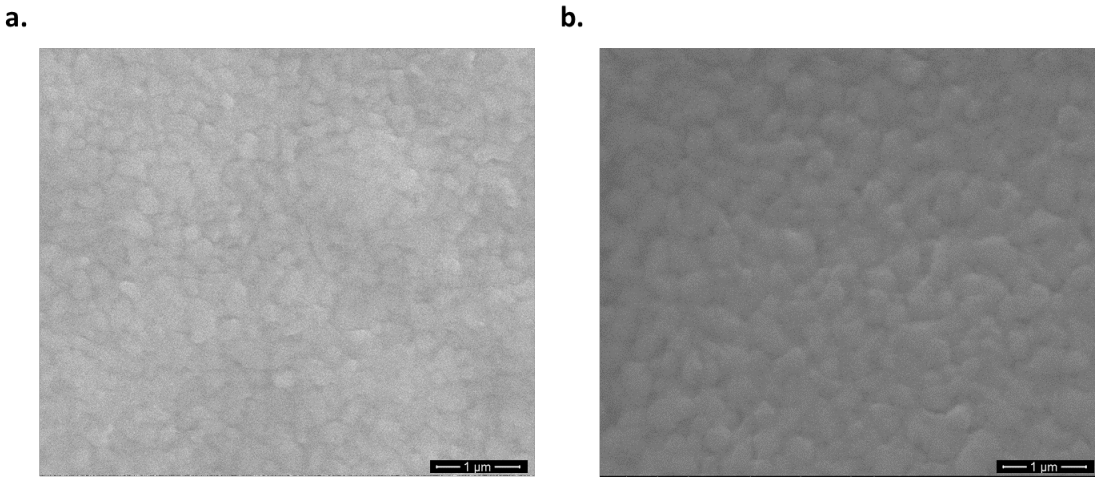

Figure A2.4 Top-view SEM of the a. Pure PVSK film and b. PVSK-Caffeine film

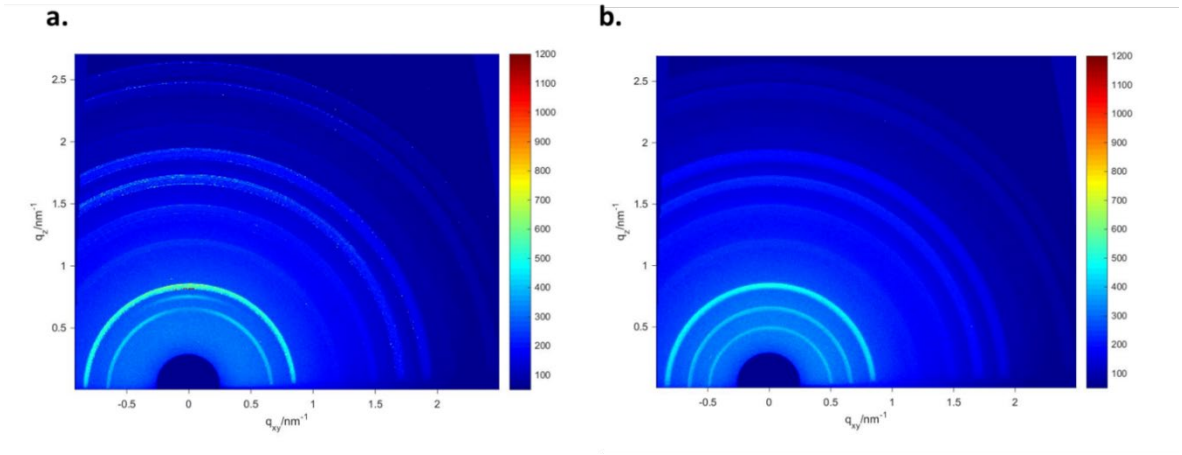

Figure A2.5 2D GIWAXS Patterns of the PVSK films: a. without caffeine; b. with caffeine.

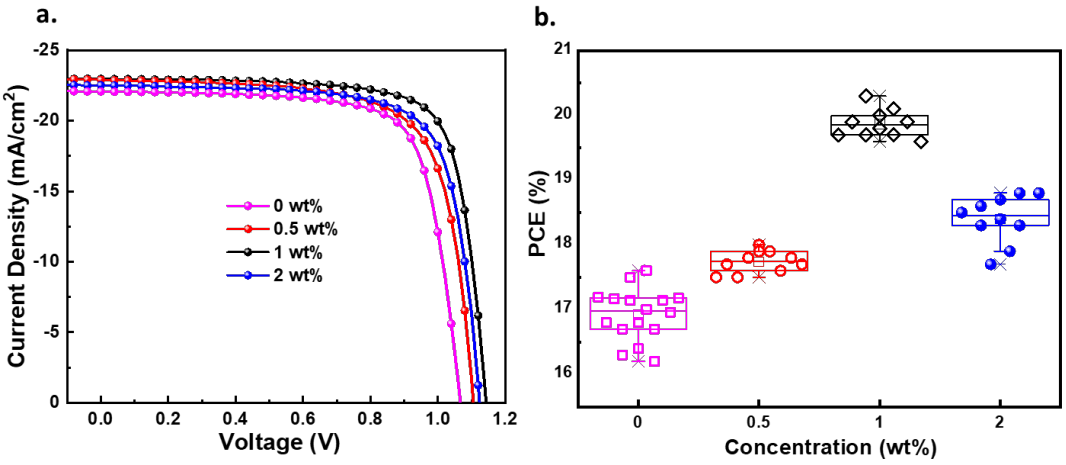

Figure A2.6 a. *J-V* curves of the PVSK with different concentration of caffeine in reverse scan direction. b. The statistic distribution of PCEs versus the concentaion of caffeine.

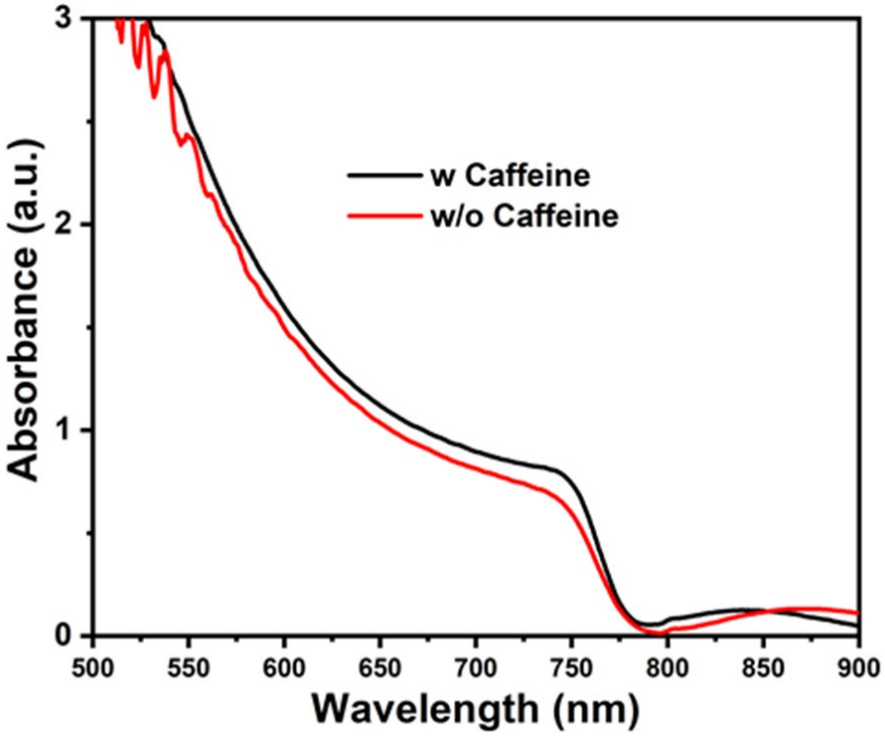

Figure A2.7 UV-vis spectra of PVSK films with or without caffeine.

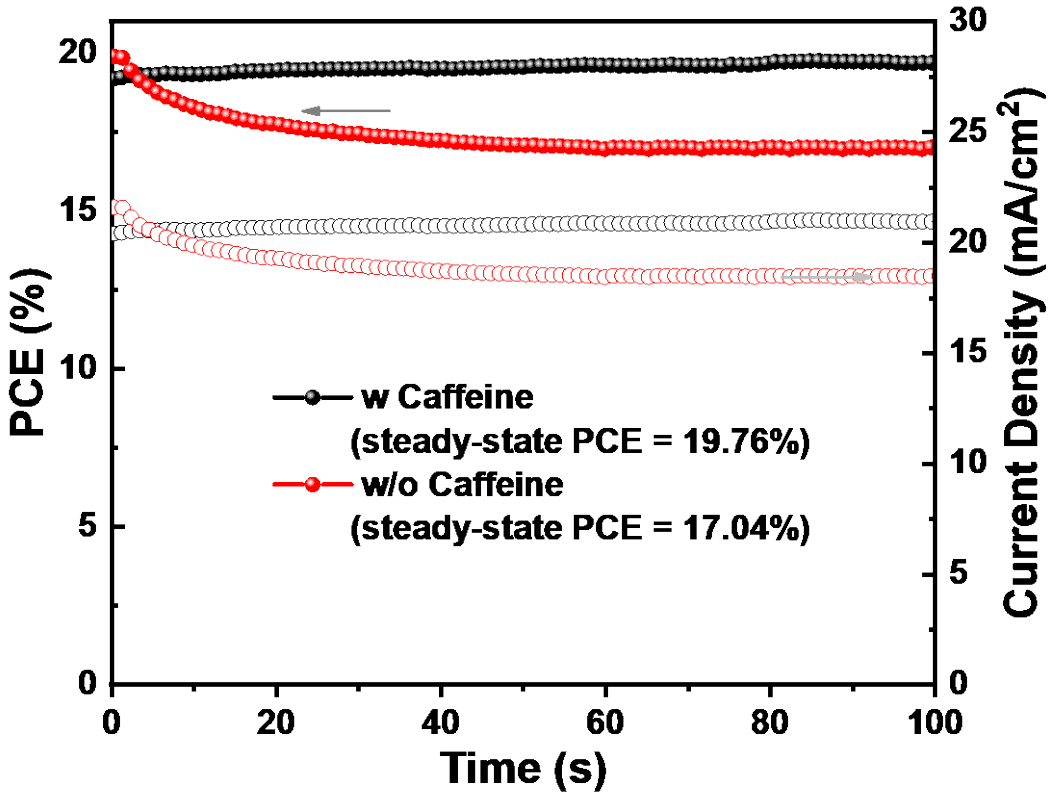

Figure A2.8 Steady-state PCE of the champion device based on $MAPbI_3$ and $MAPbI_3$-Caffeine

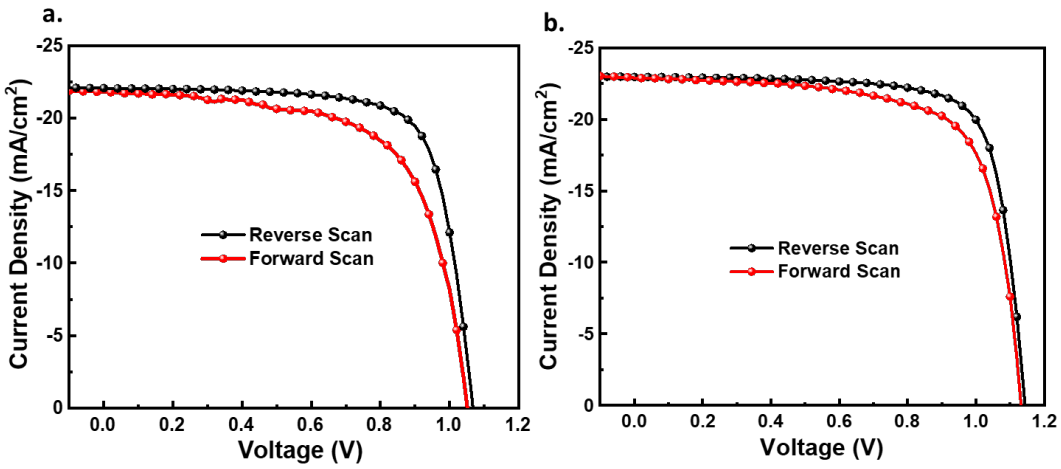

Figure A2.9 *J-V* curves of a. Pure $MAPbI_3$ device and b. Caffeine containing $MAPbI_3$ device on both reverse and forward scan directions.

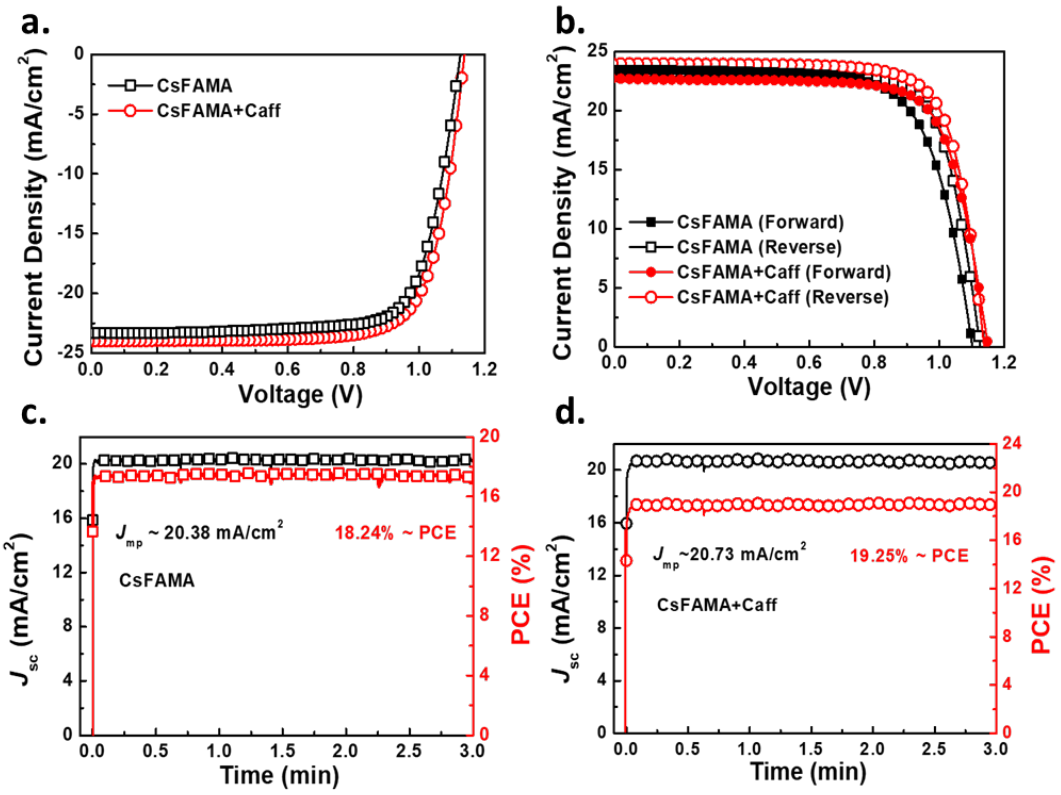

Figure A2.10 a. *J-V* curves under Reverse Scan of the CsFAMA based devices with or without caffeine. b. Hysteresis behaviors of the CsFAMA based devices with or without caffeine. Steady-State output efficiencies of CsFAMA based devices c. without caffeine and d. with caffeine.

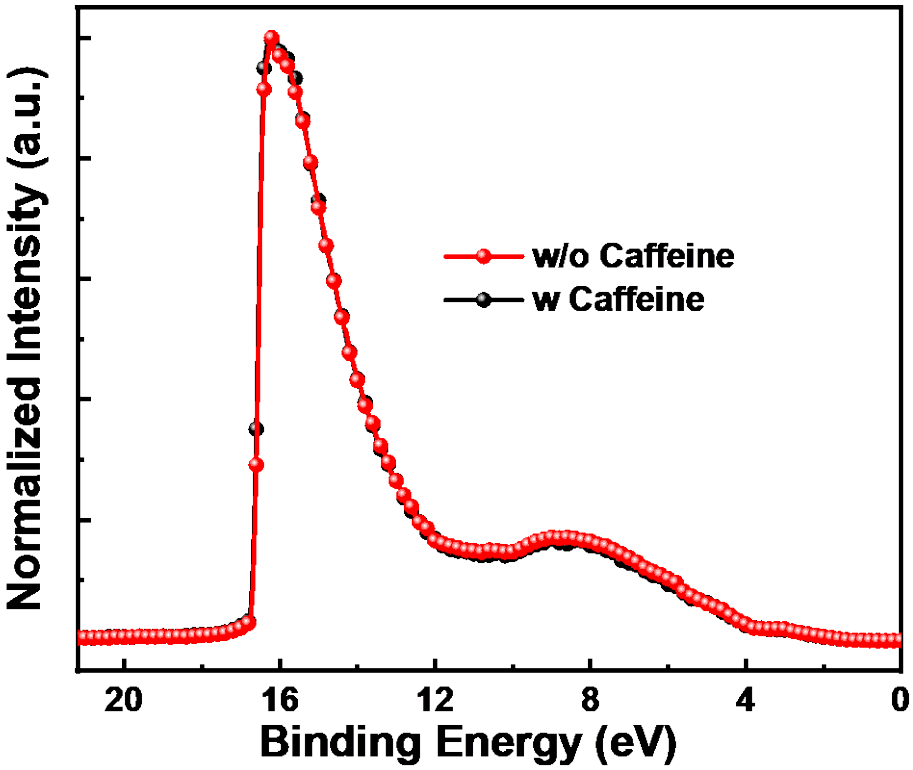

Figure A2.11 UPS spectra of PVSK films with or without caffeine.

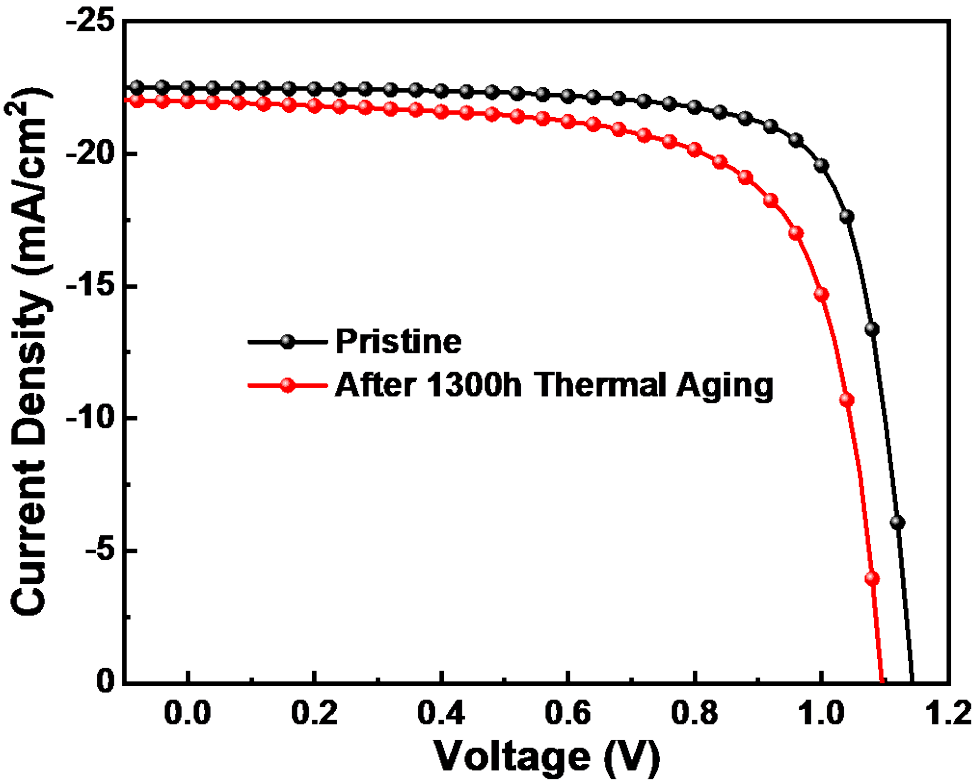

Figure A2.12 *J-V* curves of the selected device before and after subjected to the thermal stability test

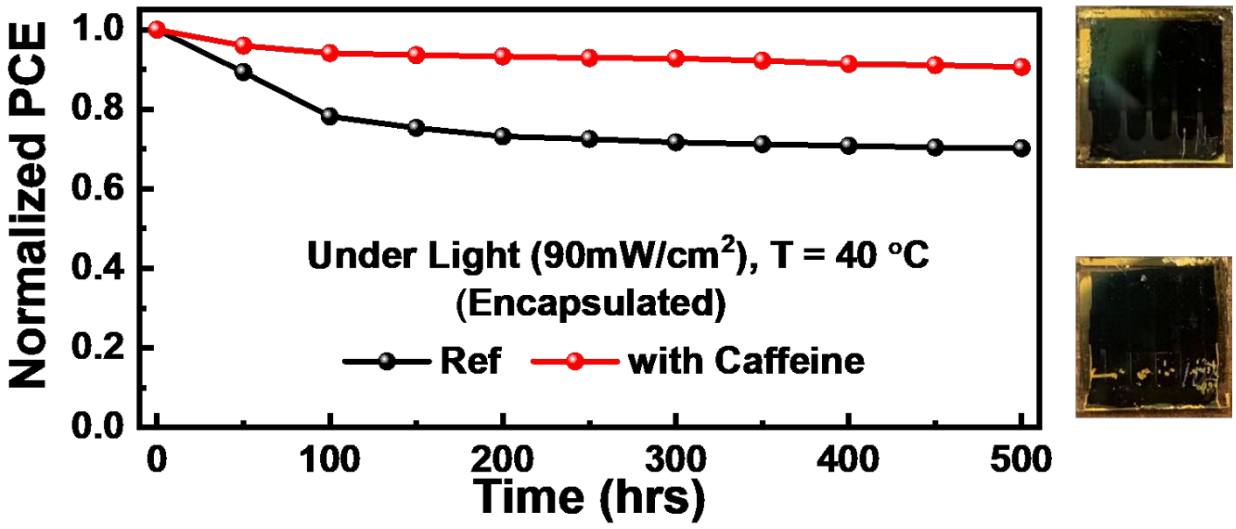

Figure A2.13 Evolution of the PCEs measured from the encapsulated perovskite solar cells with or without caffeine exposed to continuous light (90 ± 5 mW cm^{-2}) under open-circuit condition.

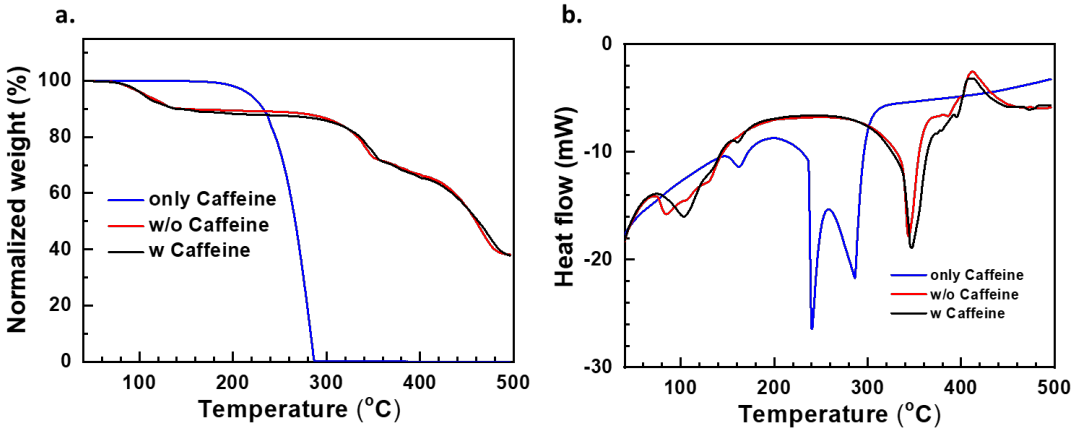

Figure A2.14 Full data of the TGA analysis on the pristine caffeine, MAI-PbI_2-DMSO adduct powder and MAI-PbI_2-DMSO-Caffeine adduct powder.

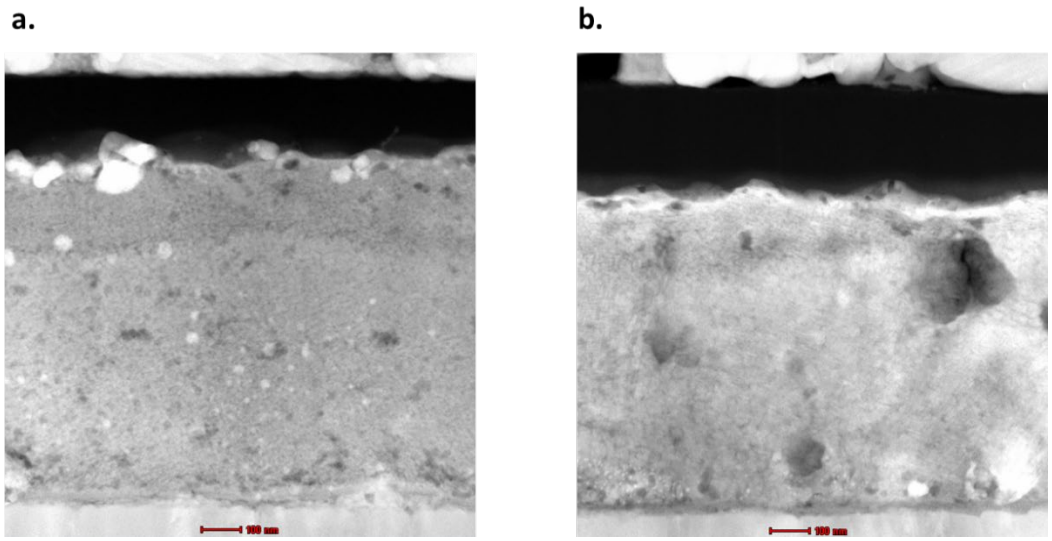

Figure A2.15 HAADF TEM data on the EDX mapping region of a. Pure PVSK device and b. PVSK-Caffeine device.

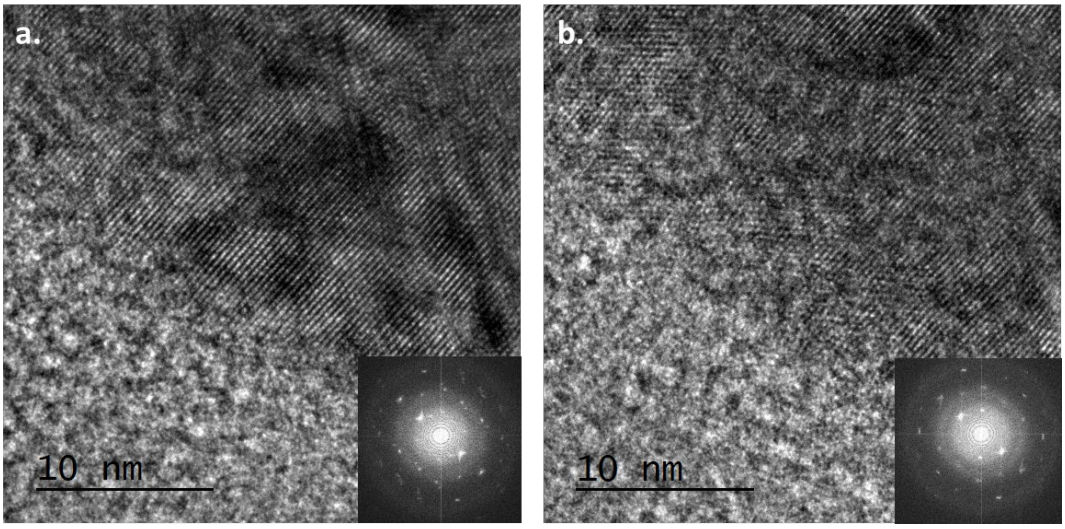

Figure A2.16 HRTEM data of different Region of the PVSK-caffeine film a. before and b. after subjected to in-situ heating test.

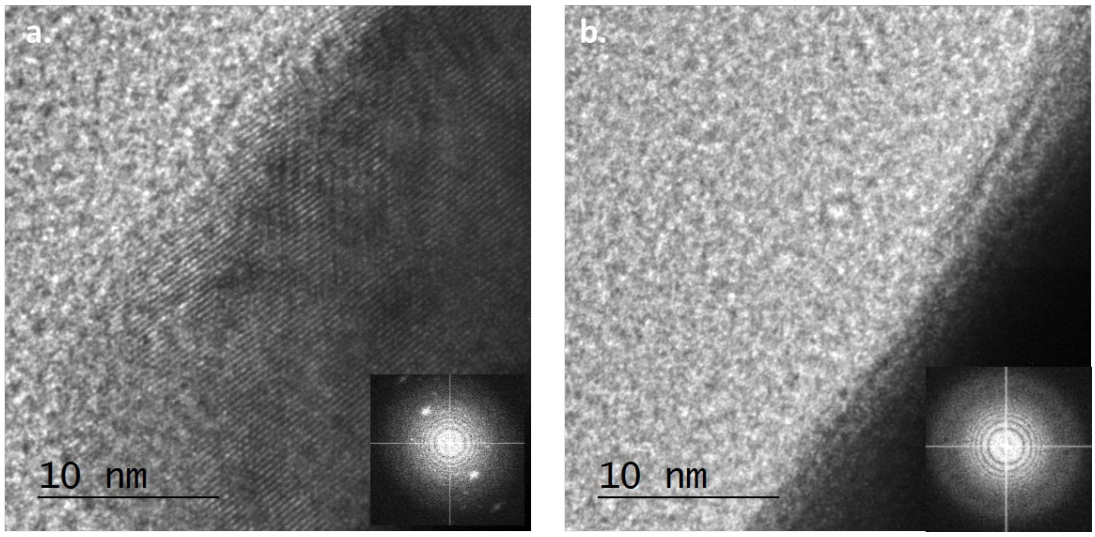

Figure A2.17 HRTEM data of different Region of the pure PVSK film a. before and b. after subjected to in-situ heating test.

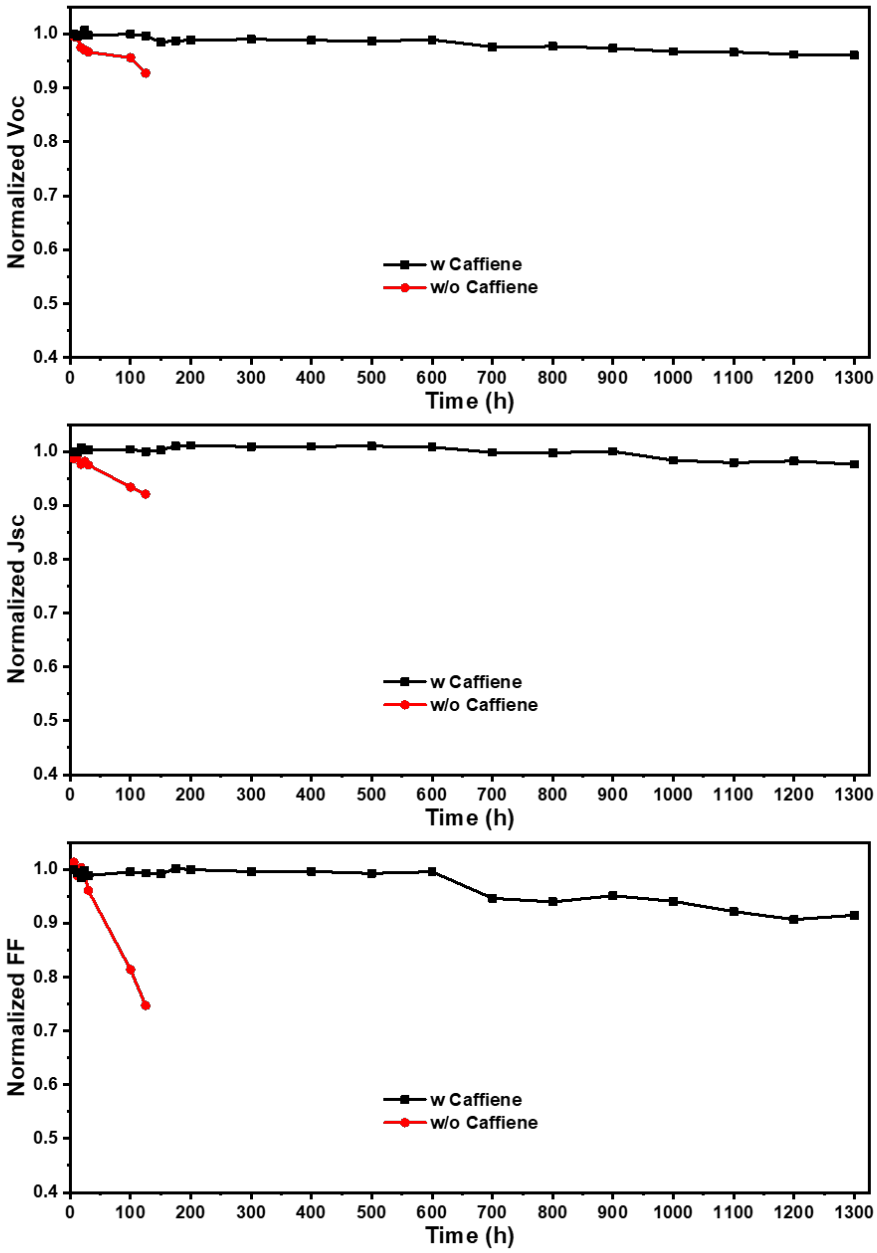

Figure A2.18 Evolution of the photovoltaic parameters of the device thermal stability upon 85°C continuous annealing in nitrogen box.

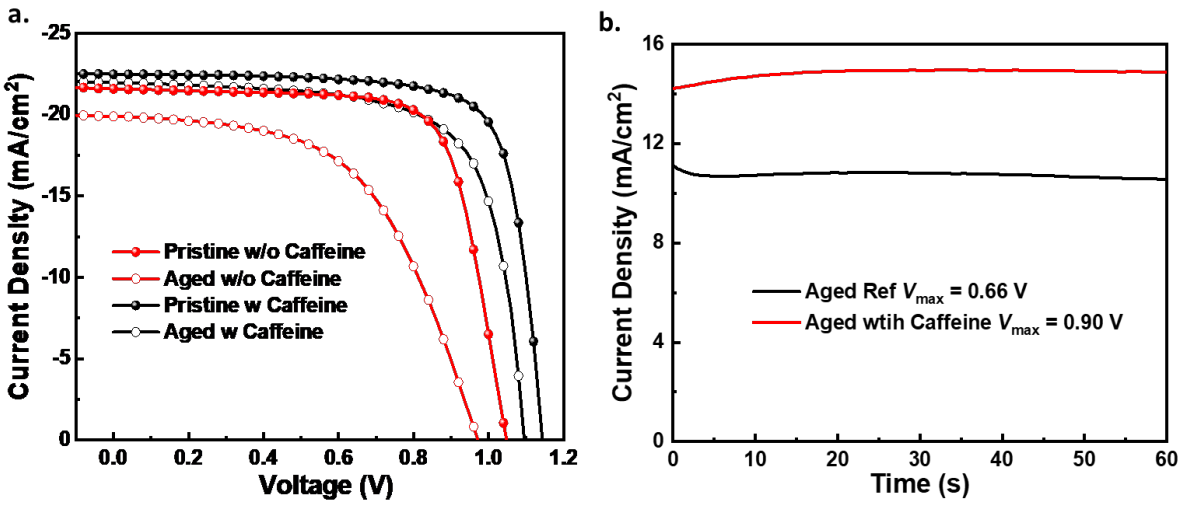

Figure A2.19 a. *J-V* curves under reverse scan of fresh and aged control or caffeine devices. b. Stabilized efficiency of aged control or caffeine devices.

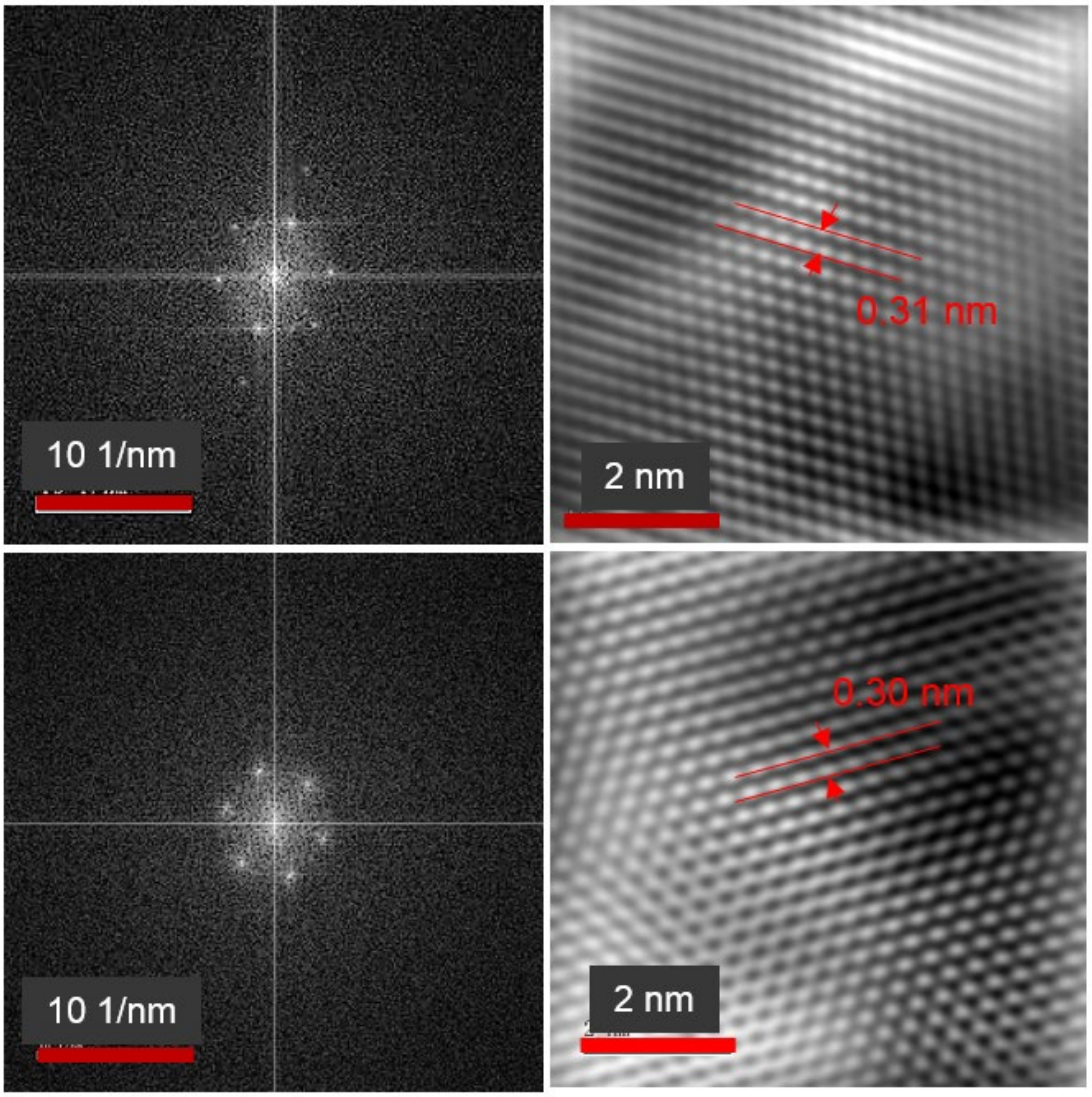

Figure A3.1. (a) $CsPbI_2Br$ and (b) $CsPbI_2Br$: $CuBr_2$ perovskites TEM images (c) $CsPbI_2Br$ and (d) $CsPbI_2Br$: $CuBr_2$ perovskites HRTEM images.

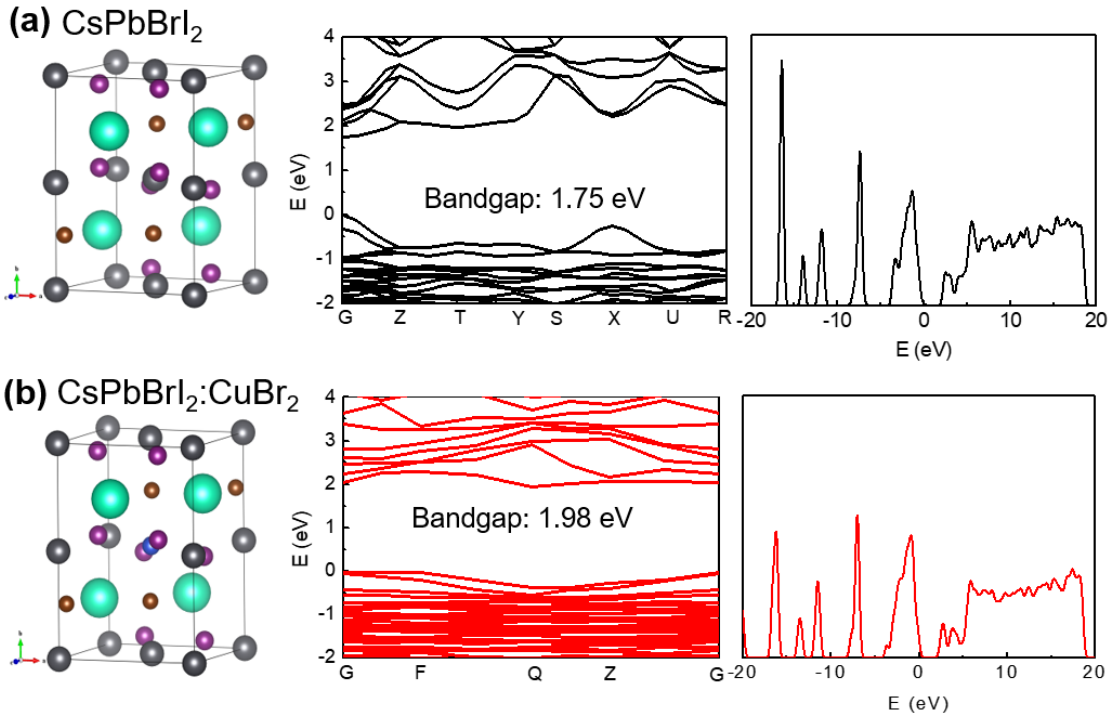

Figure A3.2. Unit cell structures, calculated band gaps and densities of states of (a) $CsPbI_2Br$ and (b) $CsPbI_2Br$: $CuBr_2$ perovskites with orthorhombic phases.

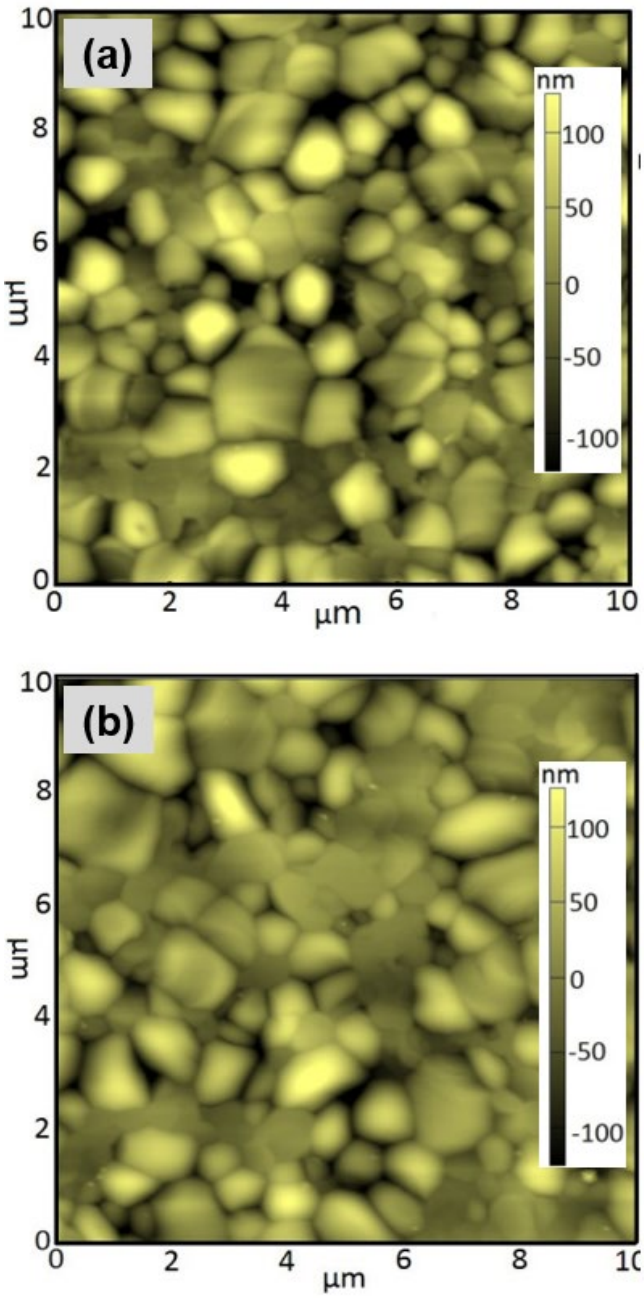

Figure A3.3. AFM top-view micrographs of (a) $CsPbI_2Br$ and (b) $CsPbI_2Br$:$CuBr_2$ (0.2 wt%) perovskite films.

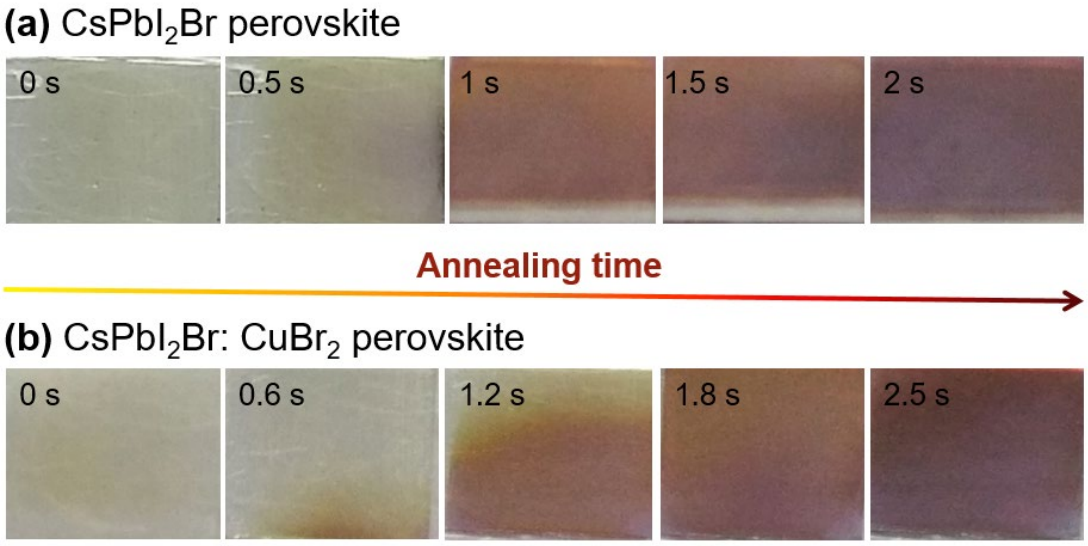

Figure A3.4. Photographs of color evolution of $CsPbI_2Br$ and $CsPbI_2Br$:$CuBr_2$ (0.2 wt%) films annealed at 260 °C.

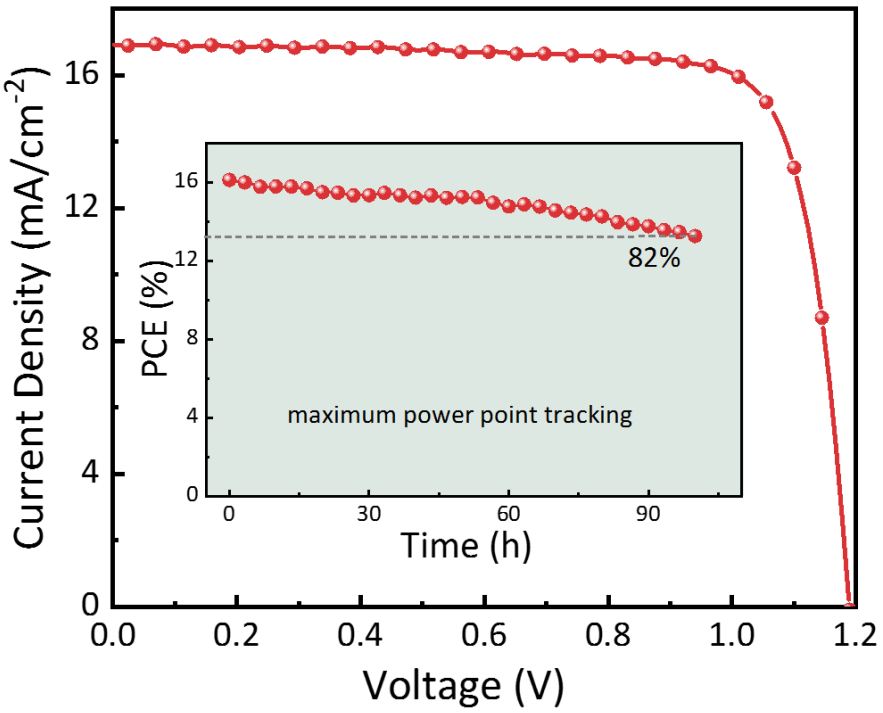

Figure A3.5. The *J-V* and maximum power point tracking (MPPT) curves of device with $CuBr_2$ (0.2 wt%) doping, aged for more than 120 hours in a nitrogen atmosphere.

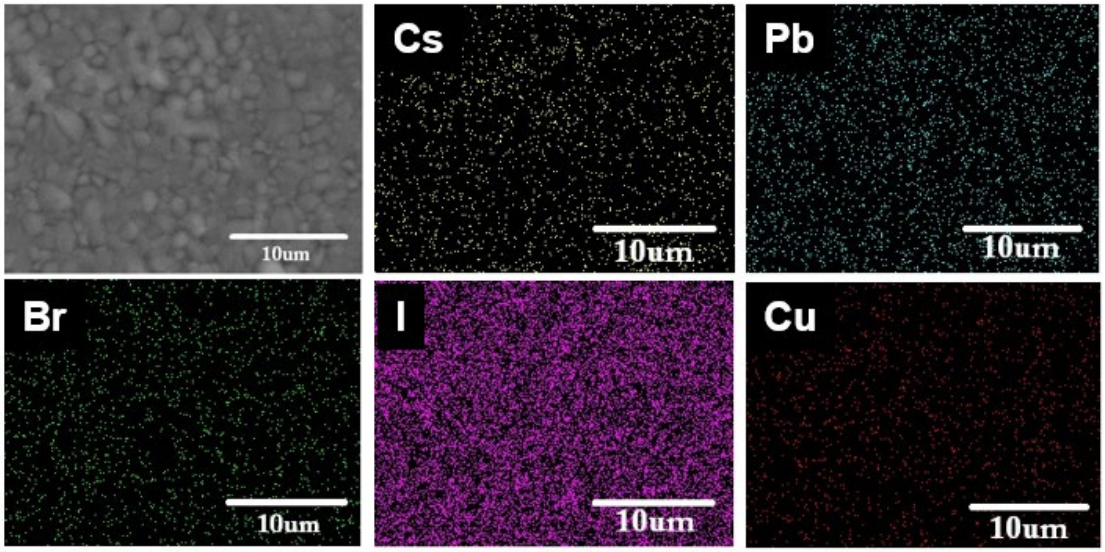

Figure A3.6. Energy-dispersive X-ray spectroscopy (EDS) mapping of $CsPbI_2Br$:$CuBr_2$ (0.2 wt%) perovskite films.

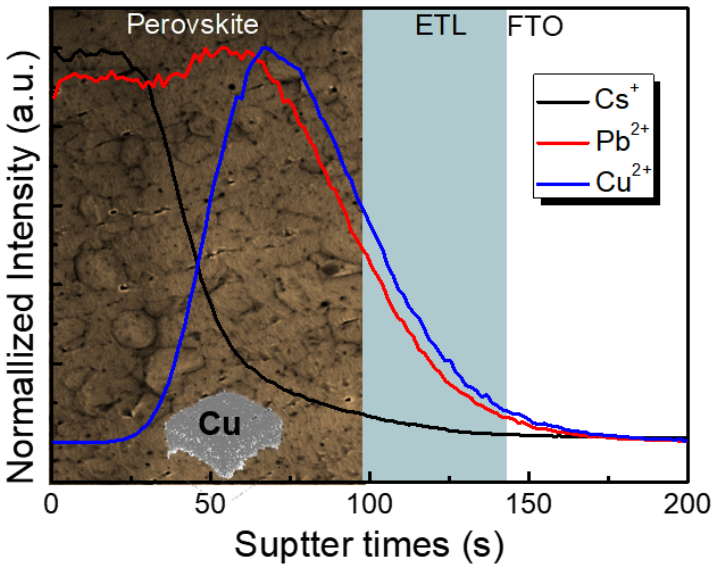

Figure A3.7. Time-of-flight secondary ion mass spectroscopy (TOF-SIMS) depth profiles of $CsPbI_2Br$:$CuBr_2$ (0.2 wt%) film as-deposited on FTO/TiO_2 substrates, exposed to 60% humidity over 24 h with a complete transformation to a yellow phase.

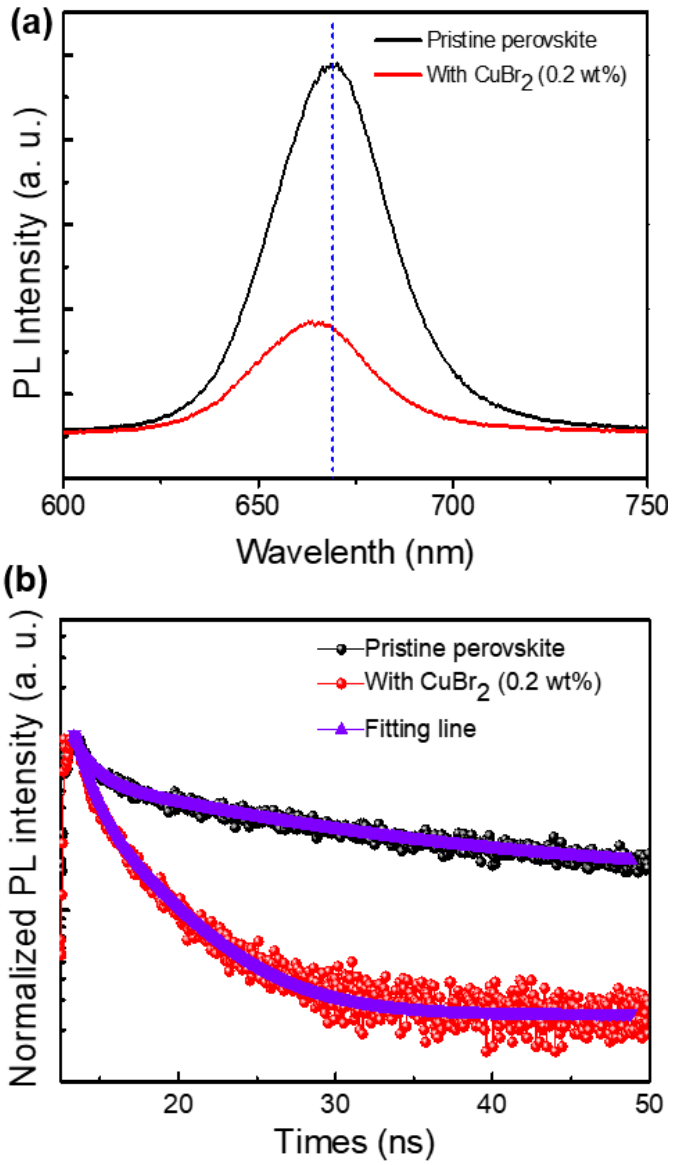

Figure A3.8. (a) Steady-state PL data and b) time-resolved photoluminescence (TRPL) of $CsPbI_2Br$ and $CsPbI_2Br$:$CuBr_2$ (0.2 wt%) perovskite films.

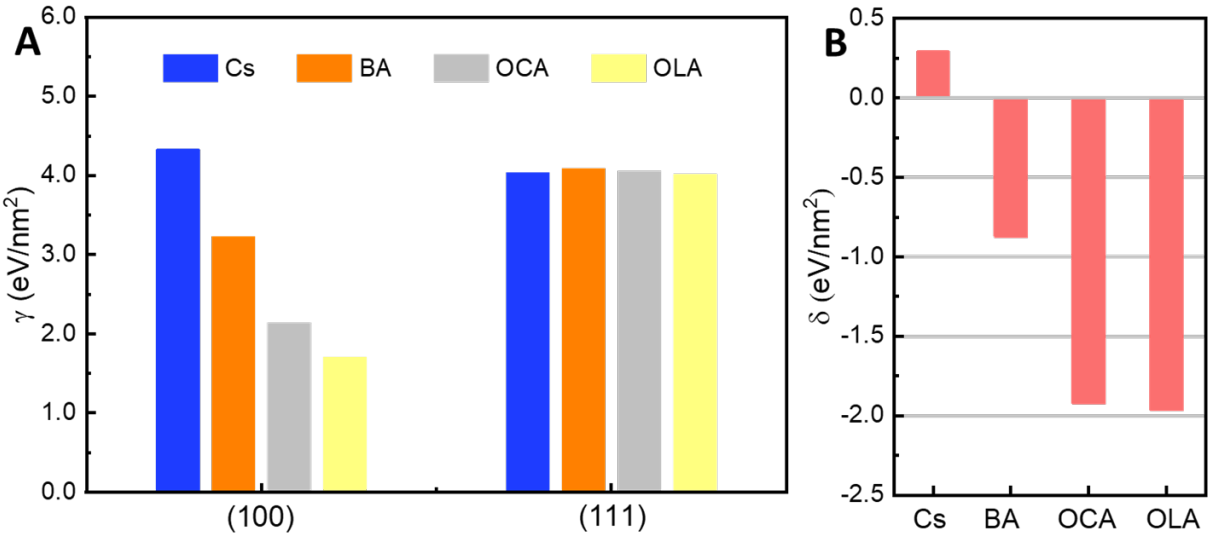

Figure A4.1. (A) The calculated surface energy γ of plane (100) and (111) for $CsPbI_2Br$ slabs terminated with Cs, BA, OCA and OLA. (B) γ_{100}- γ_{111} for $CsPbI_2Br$ slabs terminated with Cs, BA, OCA and OLA.

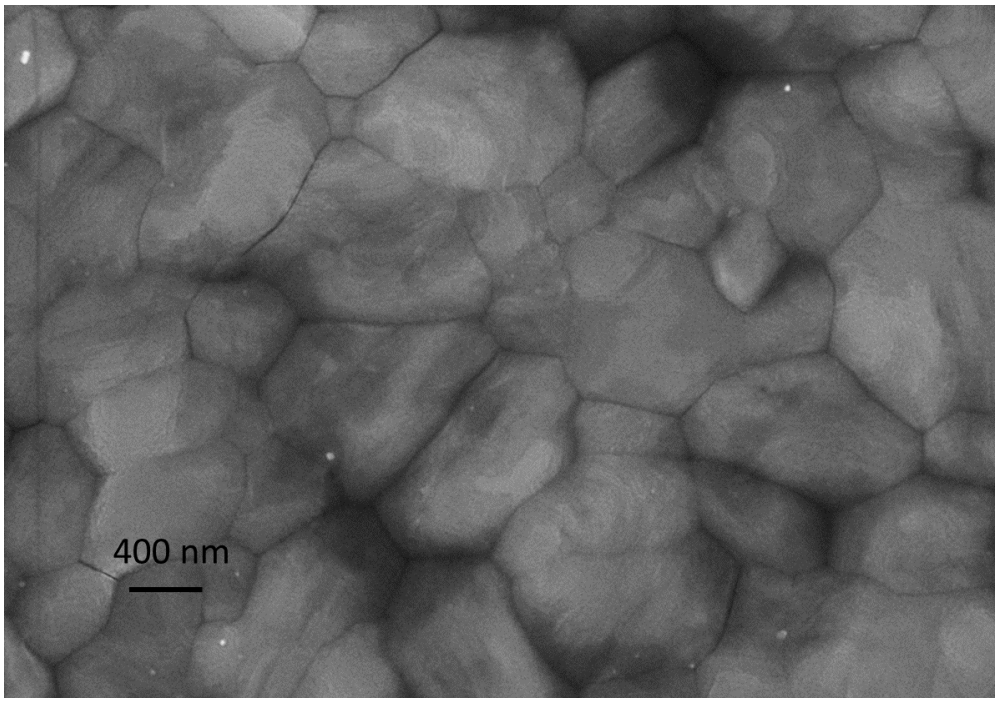

Figure A4.2. SEM image of $CsPbI_2Br$ film without IPA treatment.

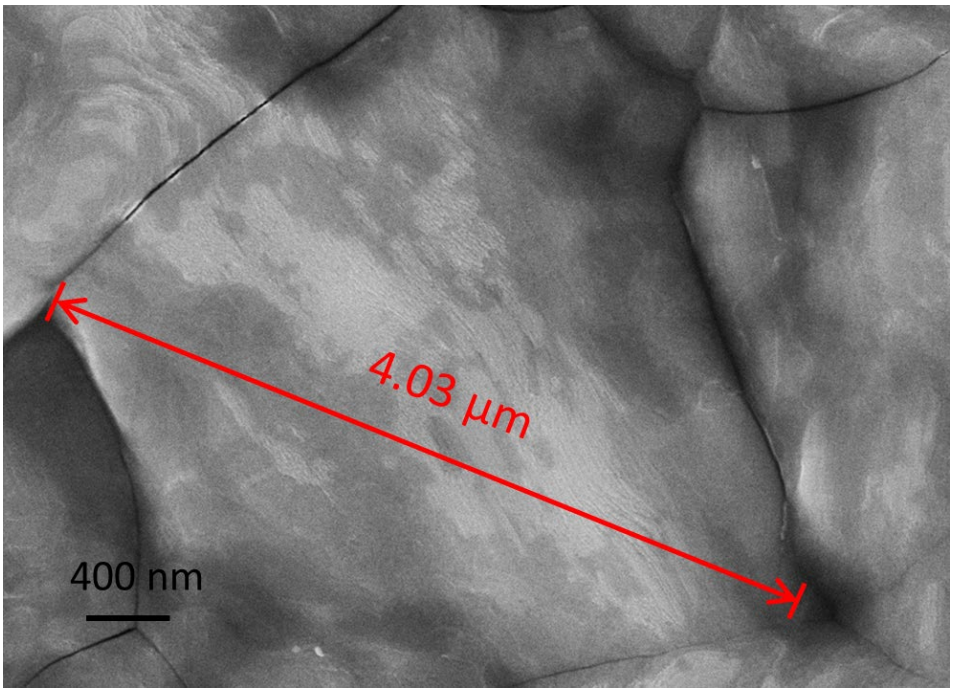

Figure A4.3 SEM image of $CsPbI_2Br$ film with OLA treatment. The grain size is as large as 4 microns.

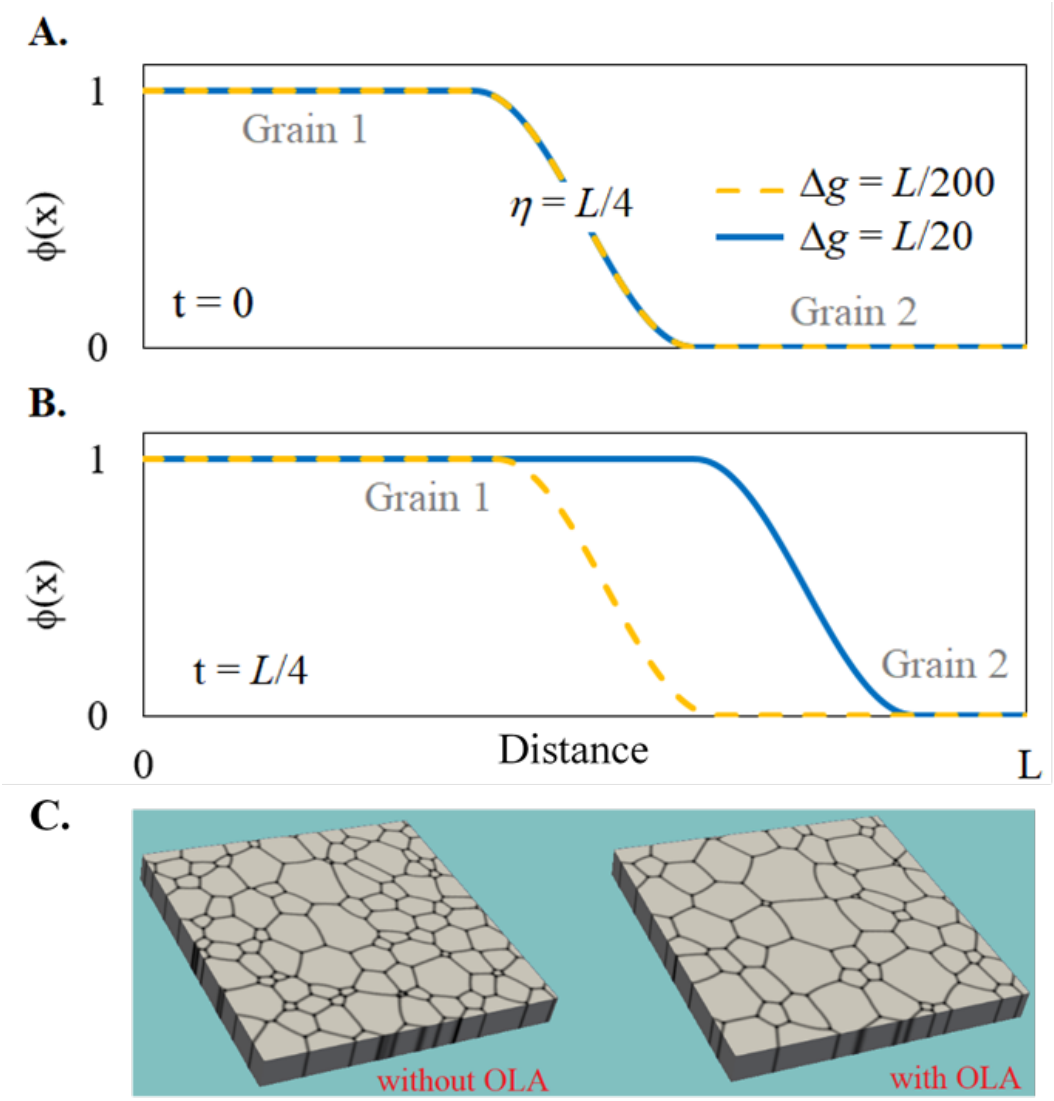

Figure A4.4. (A)-(B) A demonstration of the Phase-field model: analytical calculations of a 1D grain growth with a smooth interface and two different driving forces, $\Delta g = L/200$ and $\Delta g = L/20$, where $\Delta g = v/\mu$ and μ is taken to be unity. (A) initial condition (t=0), (B) at a later time (t=L/4). L: total length, η: interface width. (C) Snapshots of a 3D simulated grain growth of $CsPbI_2Br$ films without OLA and with OLA treatments.

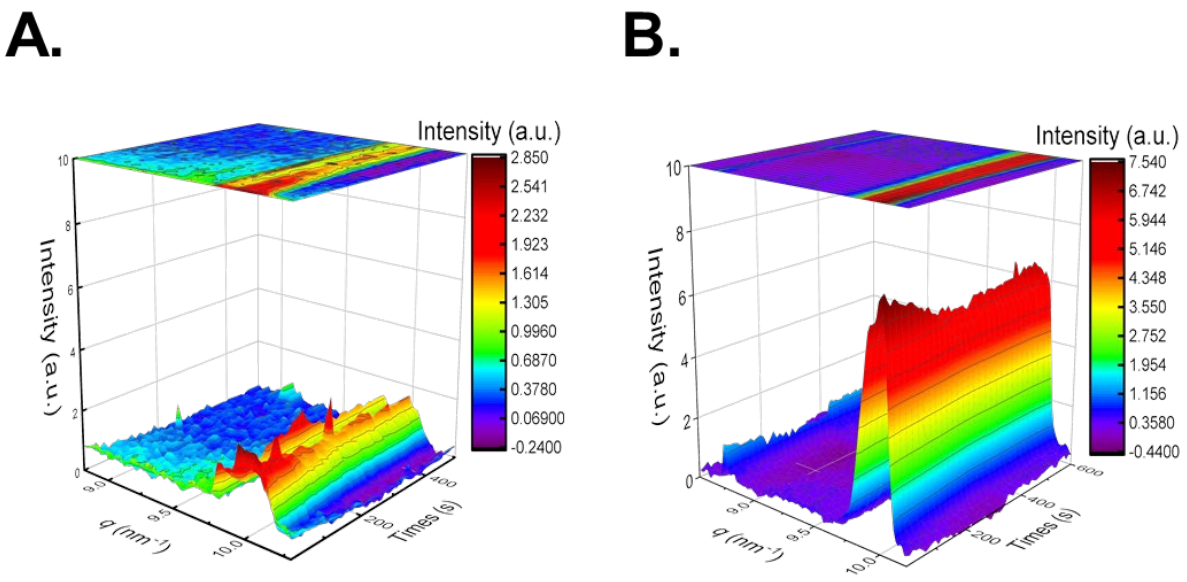

Figure A4.5 3D in-situ GIWAXS patterns of $CsPbI_2Br$ films. (A) without OLA treatment; (B) with OLA treatment.

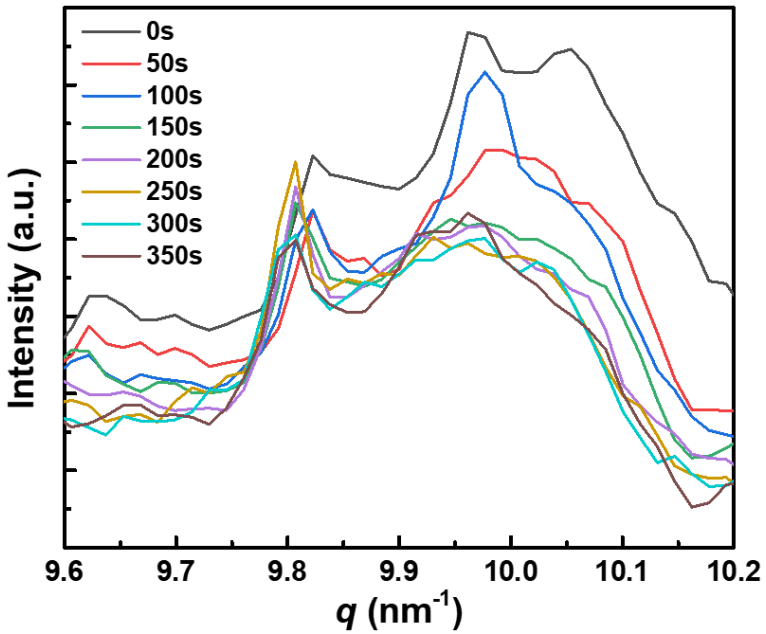

Figure A4.6 Evolution of 1D GIWAXS patterns of $CsPbI_2Br$ films without OLA treatment.

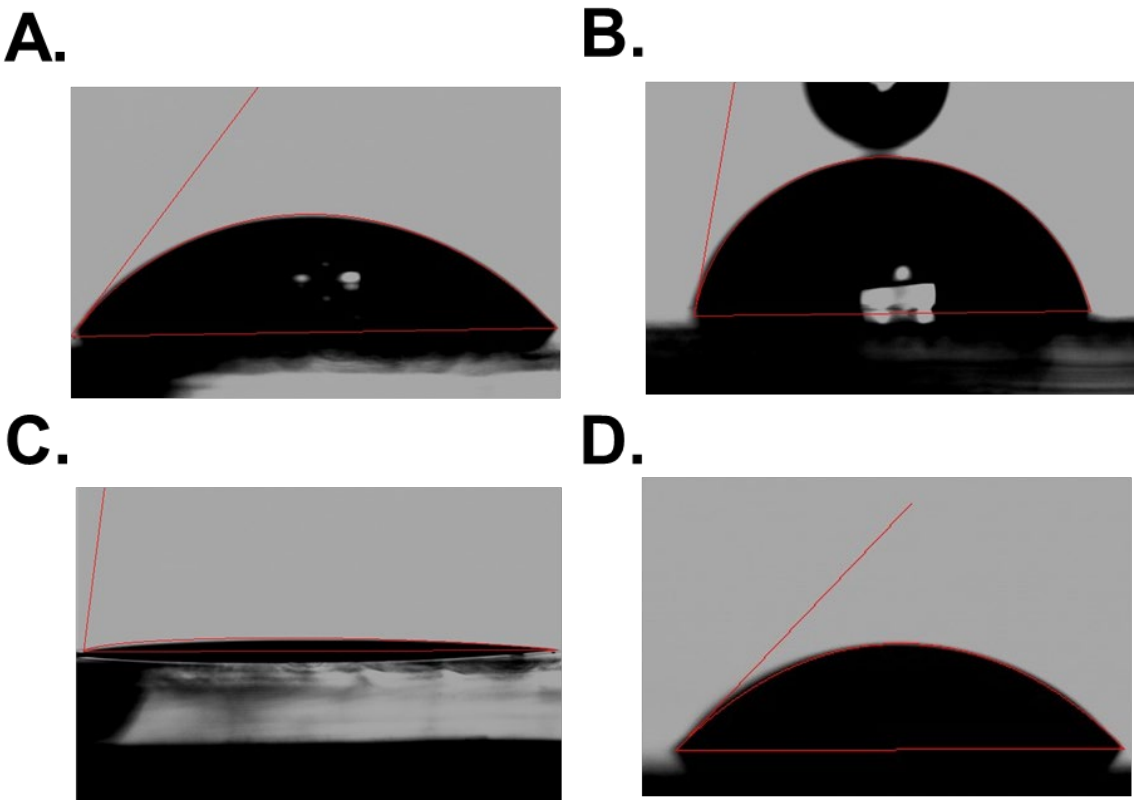

Figure A4.7 Contact angles of H_2O with $CsPbI_2Br$ films. (A) without OLA treatment and (B) with OLA treatment on H_2O; and of diiodomethane (DIM) with $CsPbI_2Br$ films (C) without OLA treatment and (D) with OLA treatment.

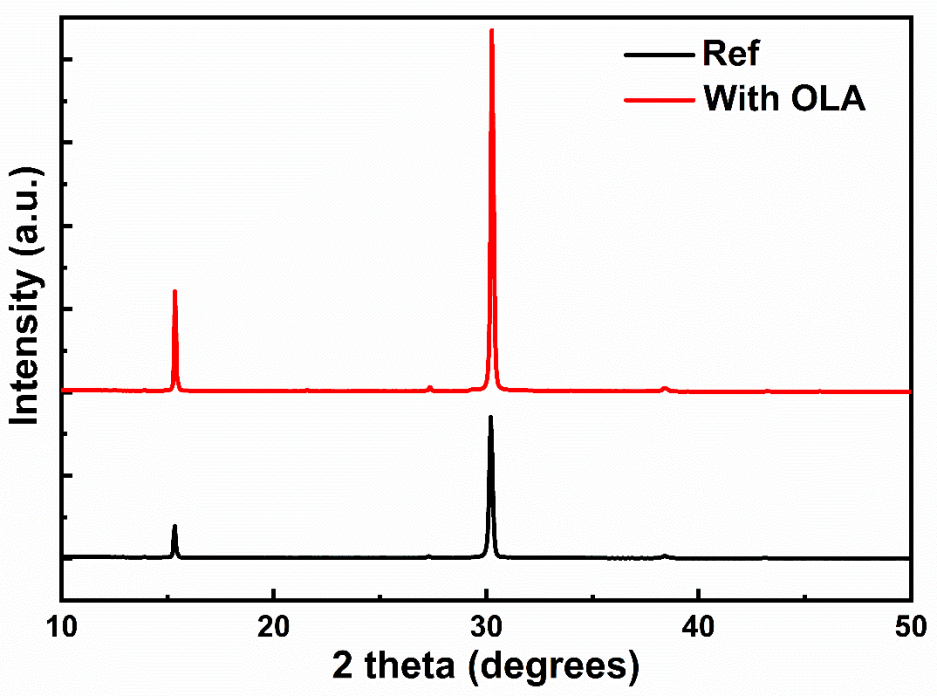

Figure A4.8 XRD patterns of $CsPbI_2Br$ films with and without OLA treatment.

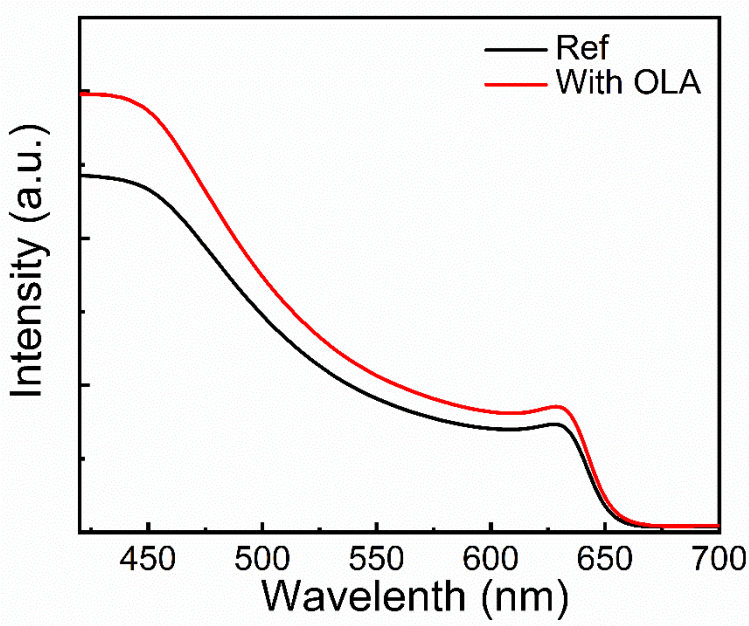

Figure A4.9. UV-Vis spectra of $CsPbI_2Br$ films with and without OLA treatment.

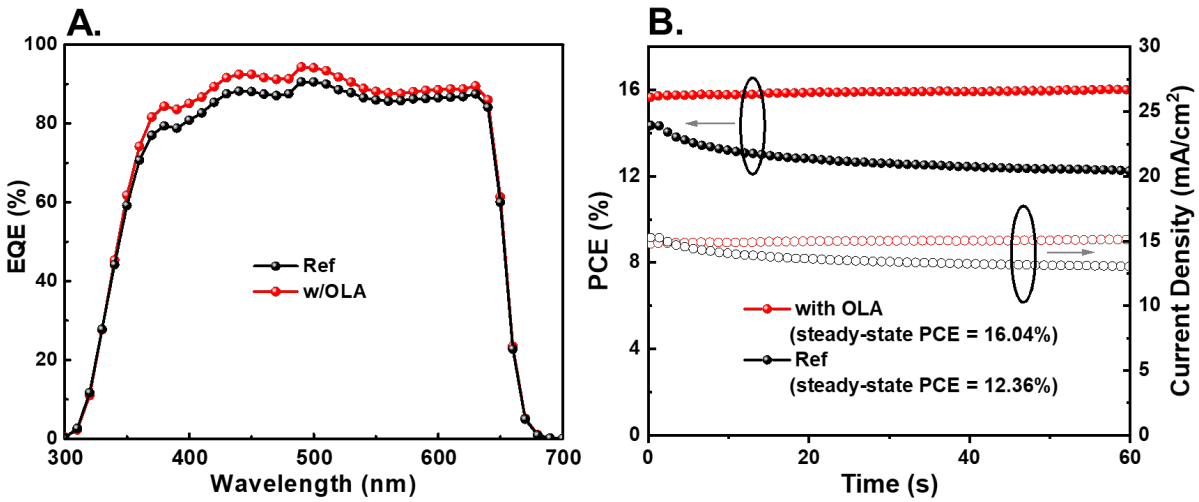

Figure A4.10 (A) EQE curves of the devices with or without OLA treatment. (B) Stabilized maximum power output and the photocurrent density at maximum power point as a function of time for the best performing perovskite solar cells with or without OLA treatment, as shown in Figure 4A, recorded under simulated one-sun AM1.5G illumination.

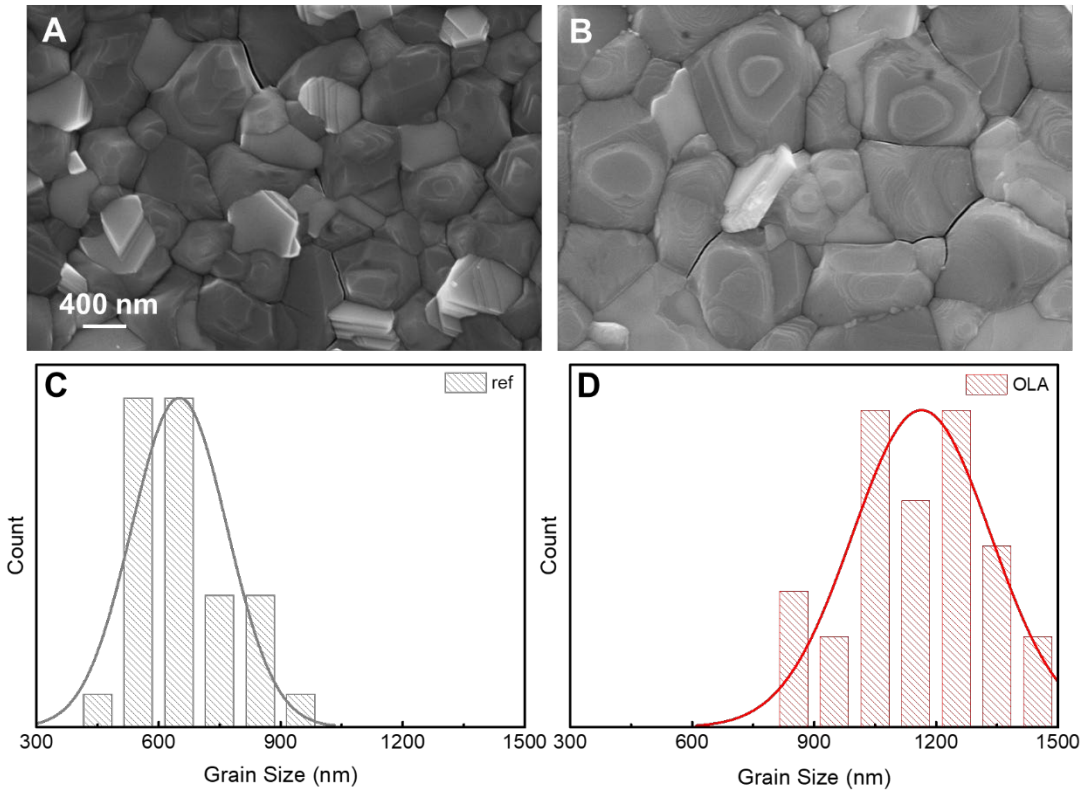

Figure A4.11 SEM image of FA-based perovskite films (A) without and (B) with OLA treatment. Grain size statistical distribution of FA-based perovskite films (C) without and (D) with OLA treatment.

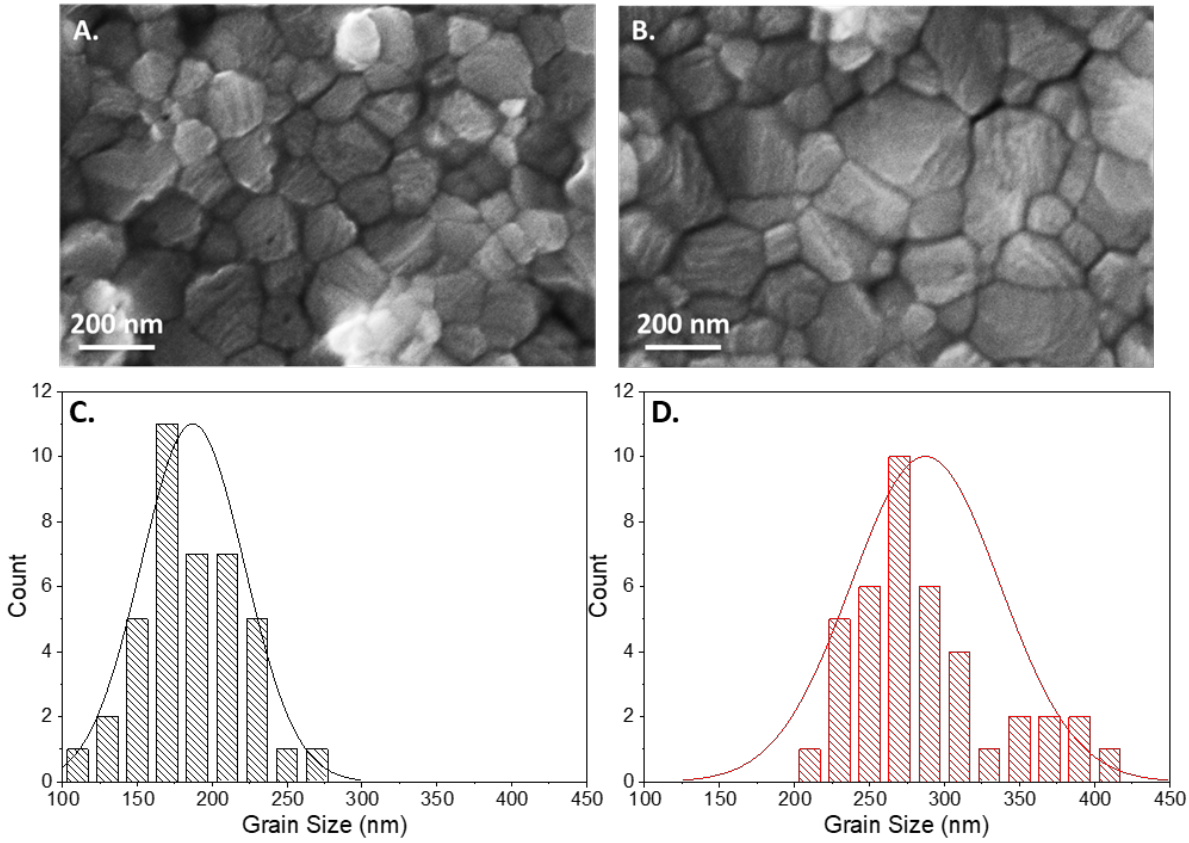

Figure A4.12. SEM image of MA-based perovskite films (A) without and (B) with OLA treatment. Grain size statistical distribution of MA-based perovskite films (C) without and (D) with OLA treatment.

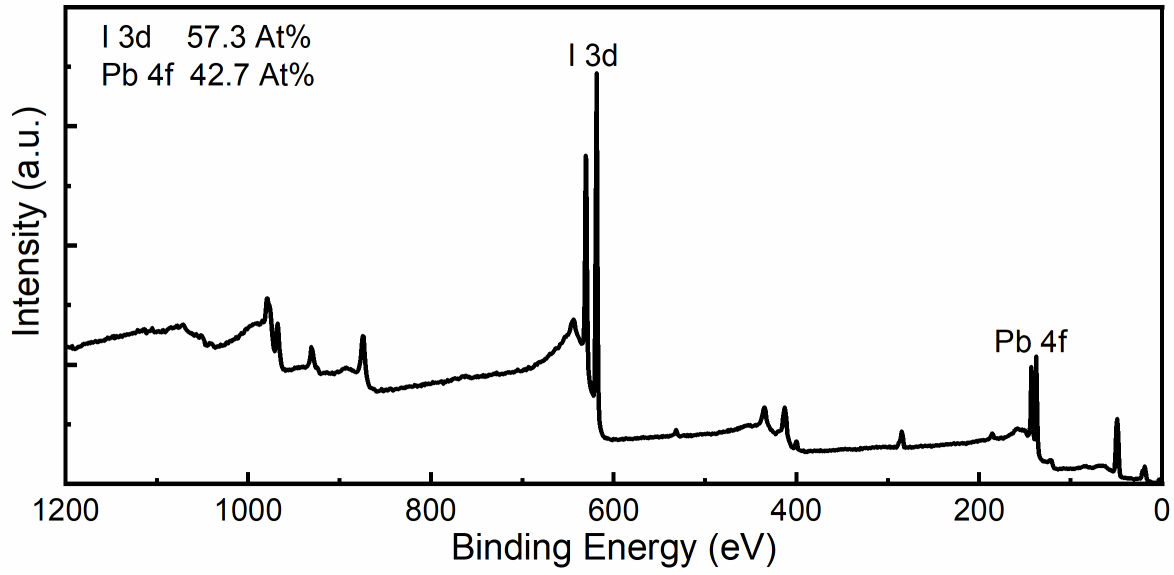

Figure A5.1 XPS full scan of the reference perovskite film, Pb 4*f* and I 3*d* peaks were integrated to determine the surface composition.

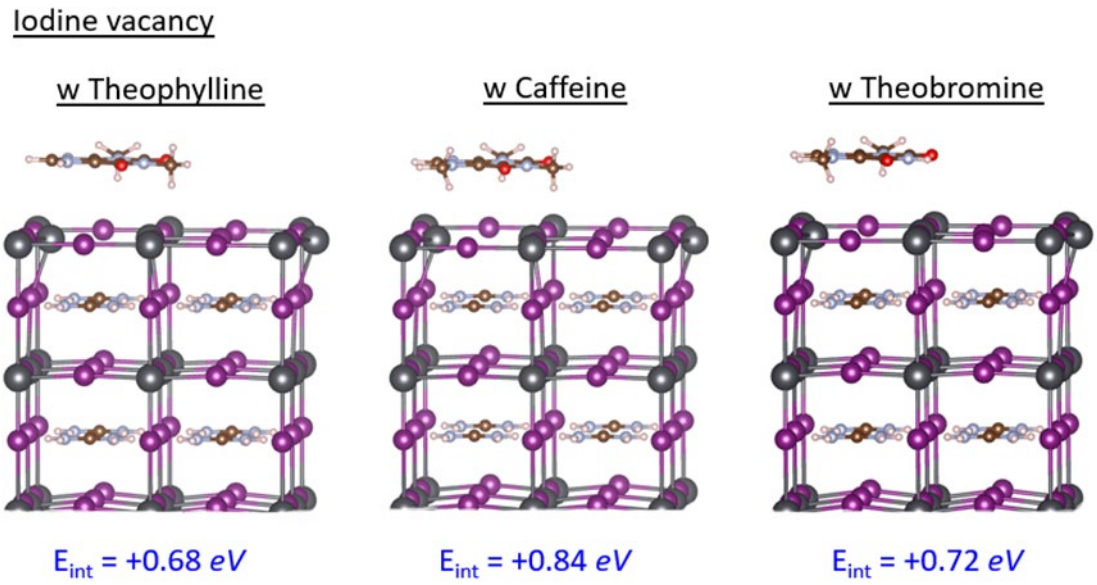

Figure A5.2 DFT-D3 predicted interaction energies between the molecule and slab complex for the V_I case.

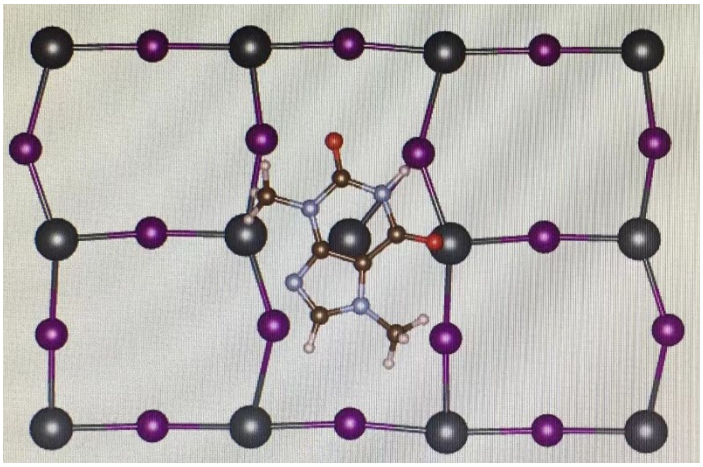

Figure A5.3 Top view of theoretical model of perovskite with theobromine surface passivation of Pb_I antisite.

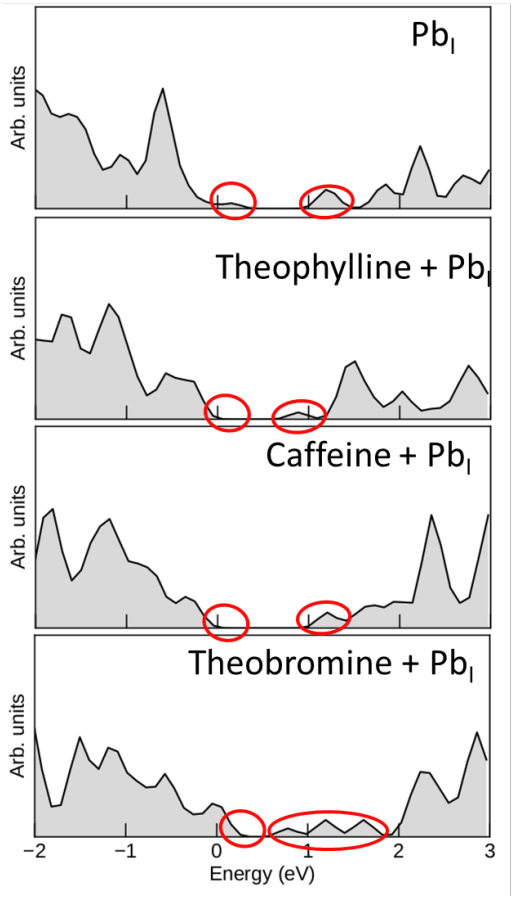

Figure A5.4 Theoretically Predicted *t*DOS of the surface Pb_I antisite defect with or without small molecule treatment.

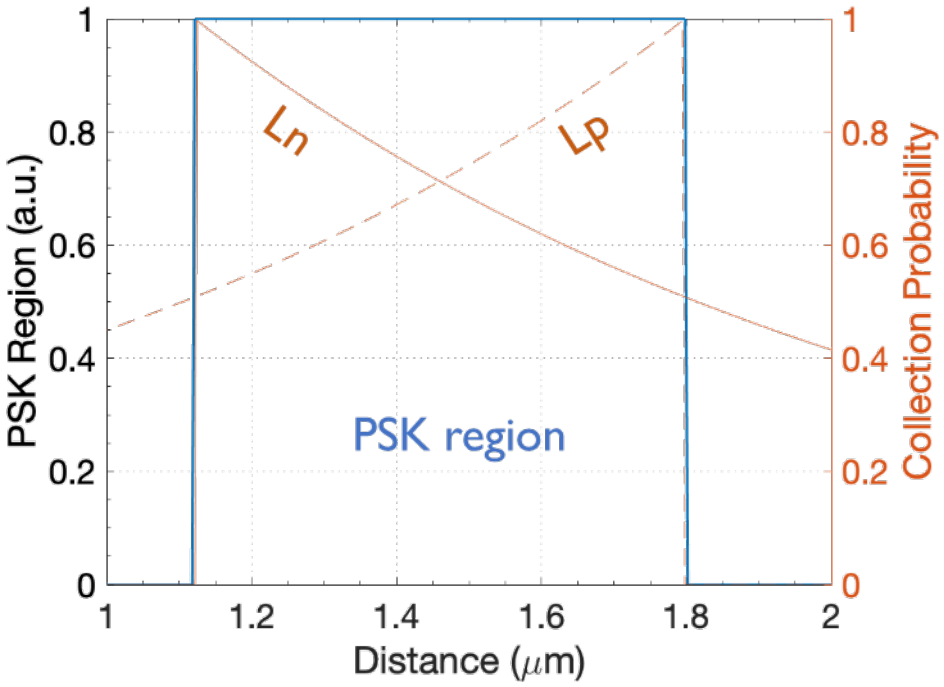

Figure A5.5 Carrier extraction probability extracted from EBIC.

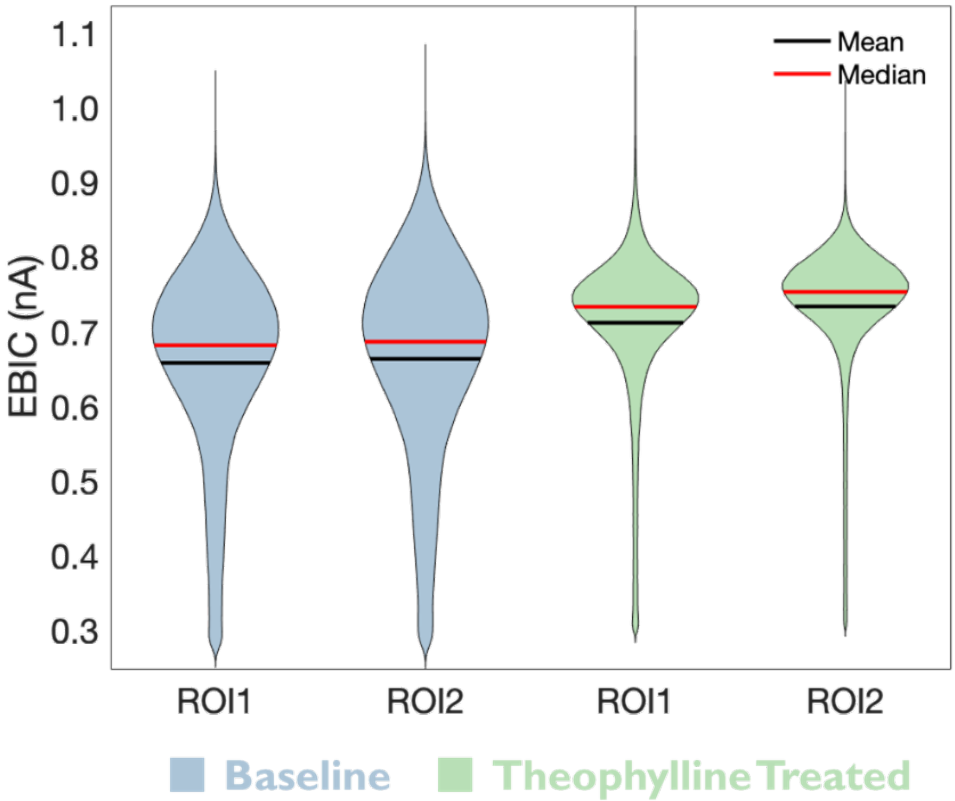

Figure A5.6 EBIC distribution profiles of perovskite active layers with or without theophylline treatment.

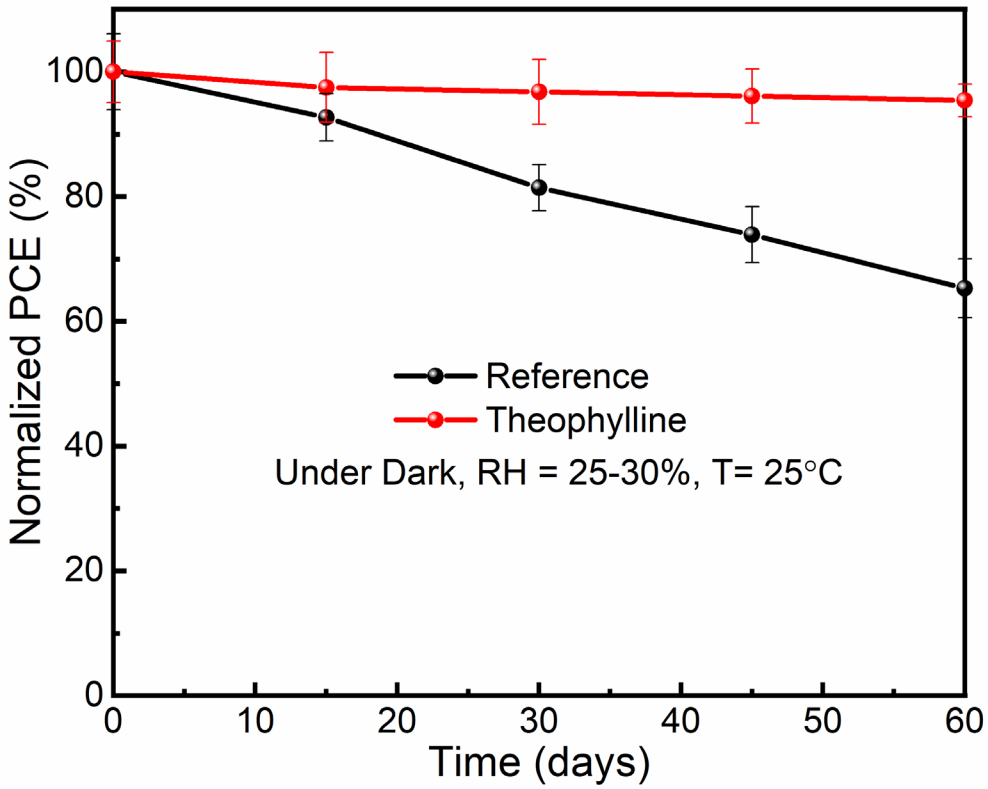

Figure A5.7 Evolution of power conversion efficiency (PCE) of perovskite solar cells with or without theophylline treatment. The devices were stored under dark with controlled humidity.

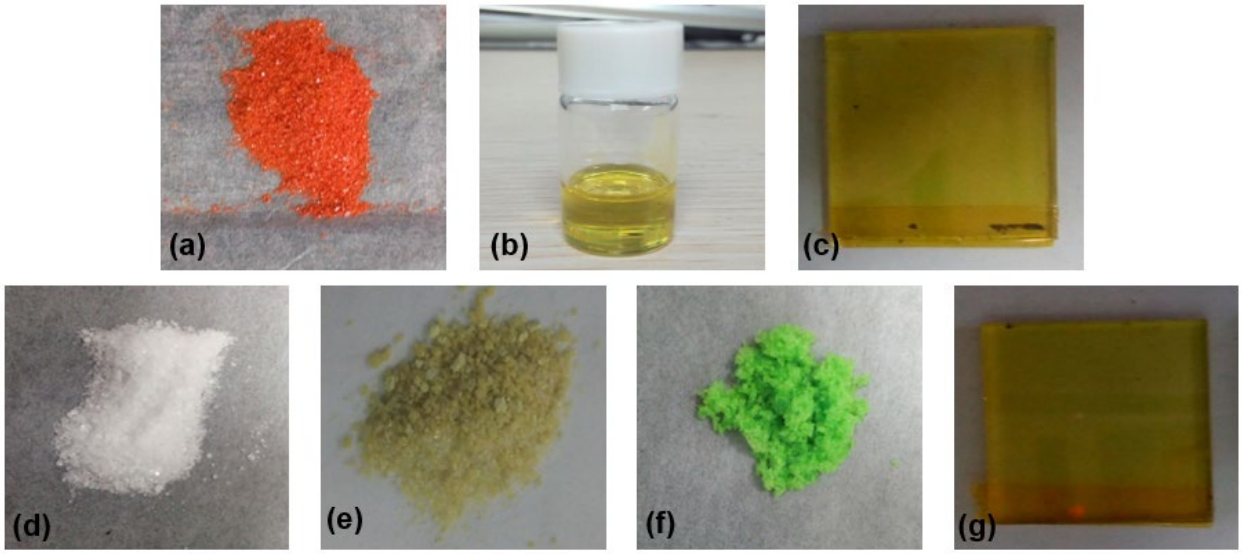

Figure A6.1. Precursor materials and thin films of solution- and vacuum-processed $Cs_2AgBiBr_6$. (a), (d), (e) and (f) are $Cs_2AgBiBr_6$, CsBr, AgBr and $BiBr_3$ powders respectively. (b) is $Cs_2AgBiBr_6$ solution in DMSO. (c) and (g) are thin films obtained by spin coating and vacuum deposition respectively.

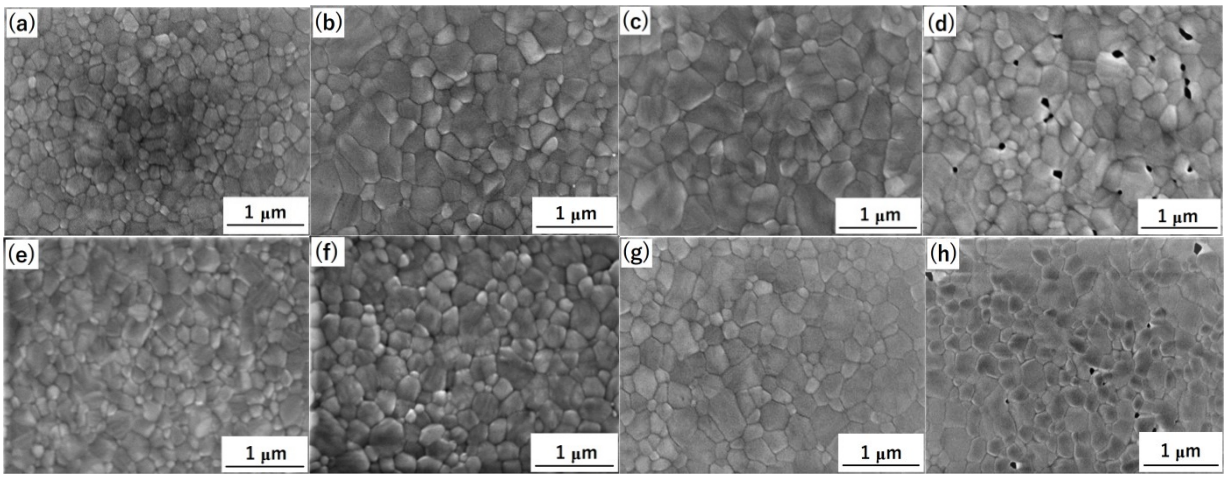

Figure A6.2. Plan view SEM images of the solution-processed films annealed at (a) 240 °C, (b) 260 °C, (c) 280 °C and (d) 300 °C and vacuum-processed films annealed at (e) 180 °C, (f) 200 °C, (g) 220 °C and (h) 240 °C.

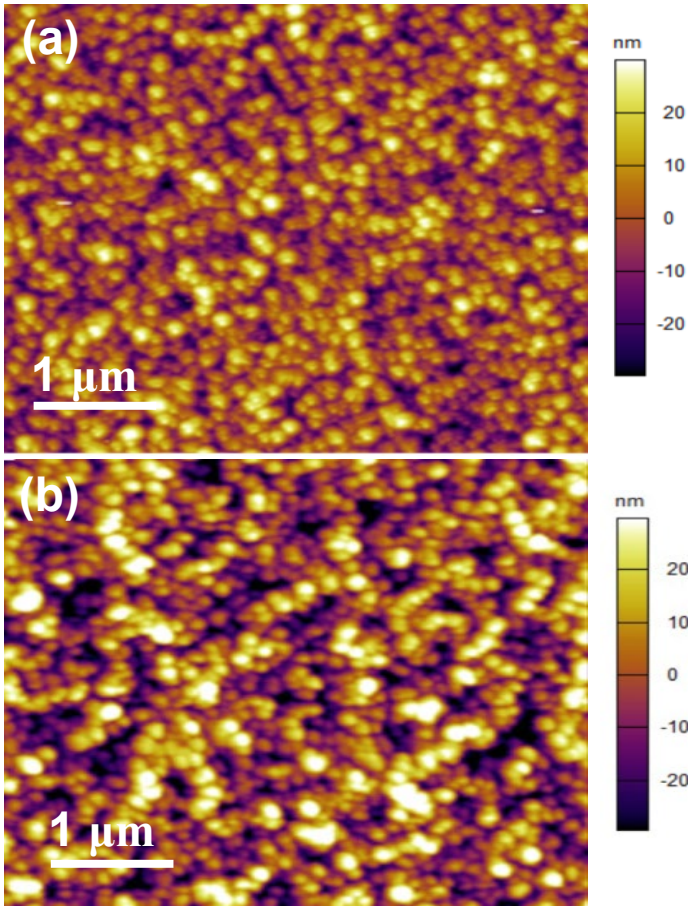

Figure A6.3. AFM images of the optimized (a) vacuum- and (b) solution-processed $Cs_2AgBiBr_6$ thin films annealed at 220 °C and 280 °C respectively.

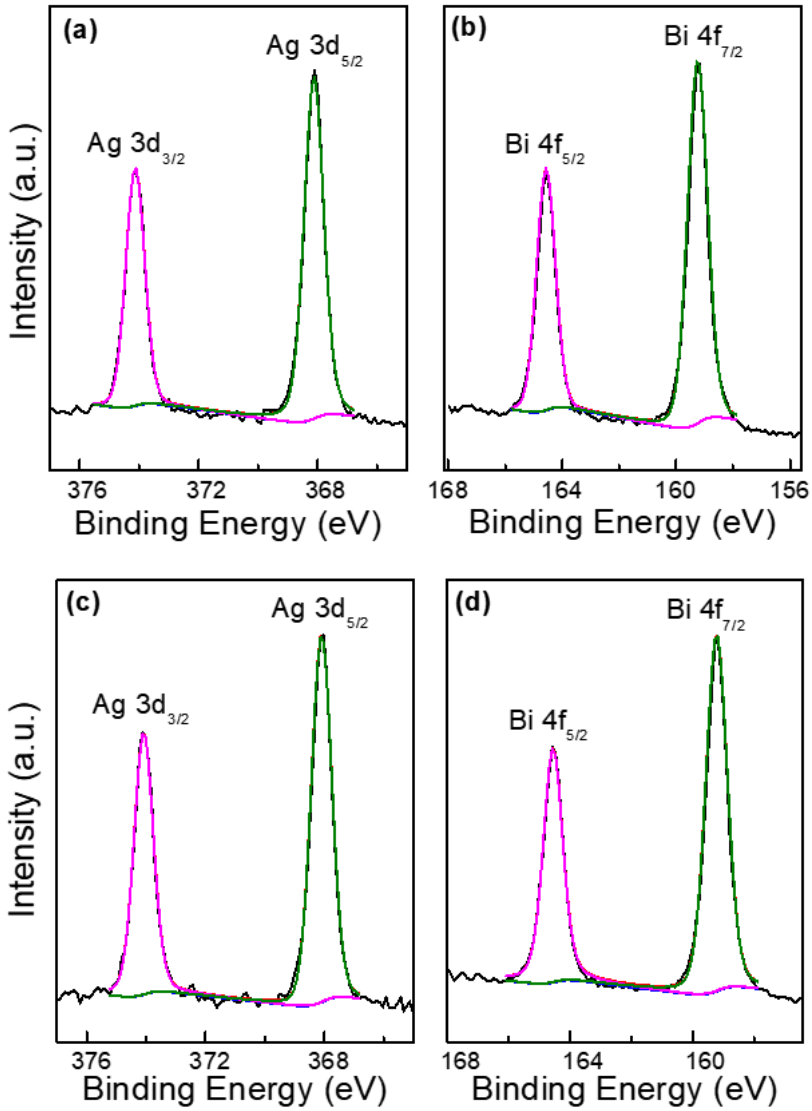

Figure A6.4. Detailed XPS scans of Ag 3d and Bi 4f core levels of (a) solution- and (b) vacuum-processed $Cs_2AgBiBr_6$ thin film.

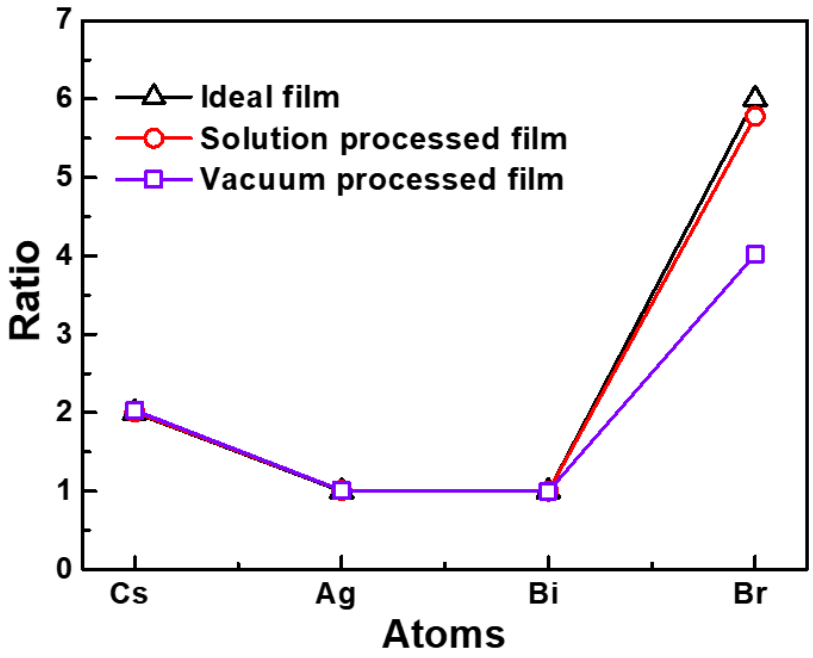

Figure A6.5. Deviation of the atomic ratios of the chemical composition of solution- and vacuum-processed $Cs_2AgBiBr_6$ thin films from ideality.

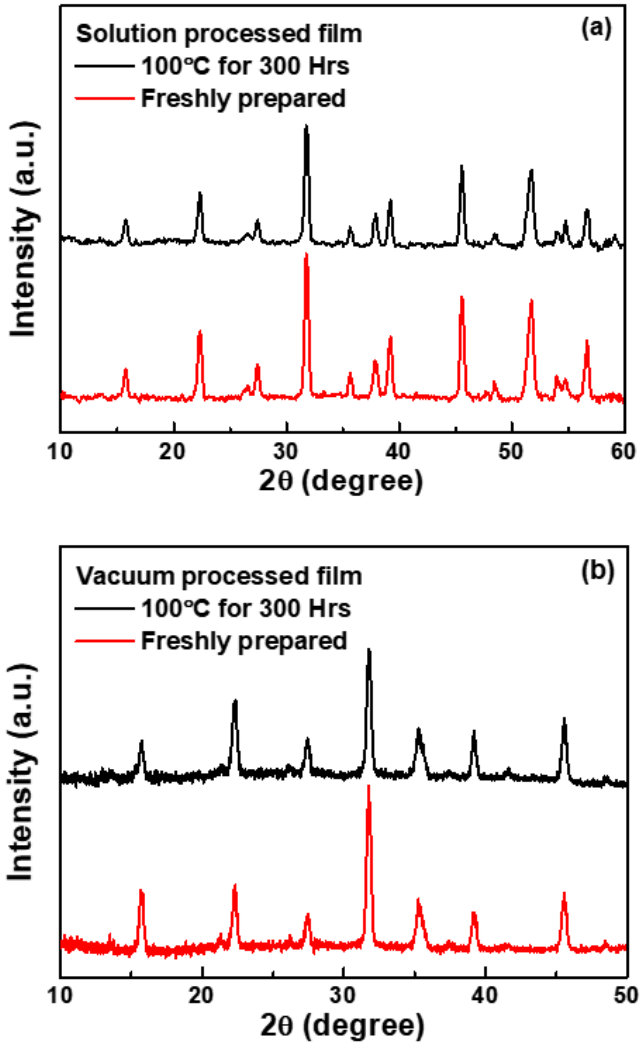

Figure A6.6. XRD patterns of freshly prepared and high temperature aged (300 hrs) $Cs_2AgBiBr_6$ thin films for (a) solution-processing and (b) vacuum-sublimation.

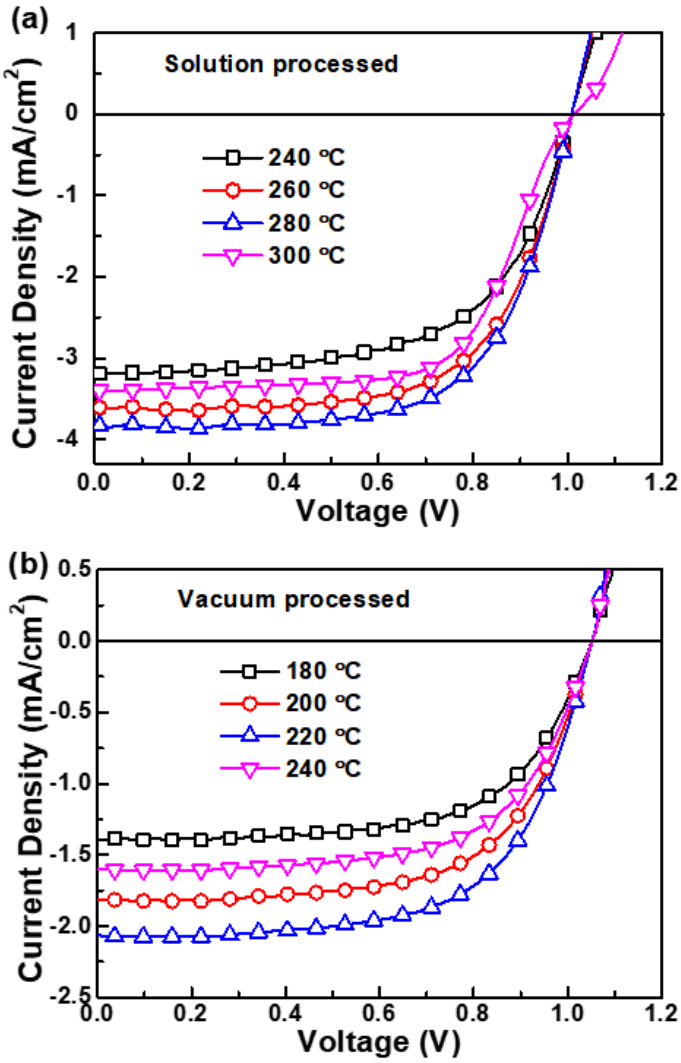

Figure A6.7. *J-V* curve of solution- and vacuum-processed devices based on the optimization of annealing temperature.

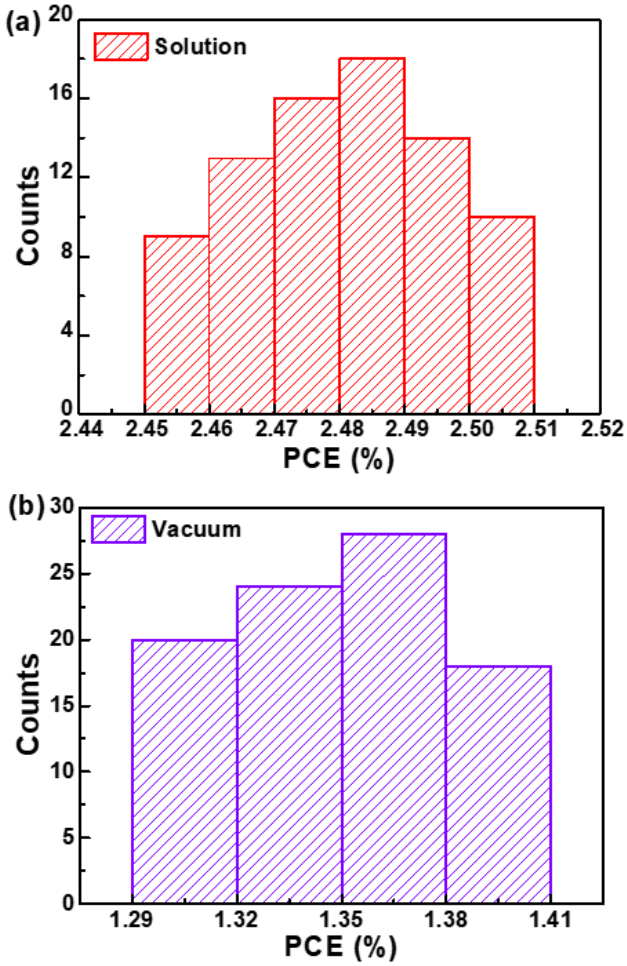

Figure A6.8. The distribution of PCEs of the (a) solution- and (b) vacuum-processed devices.

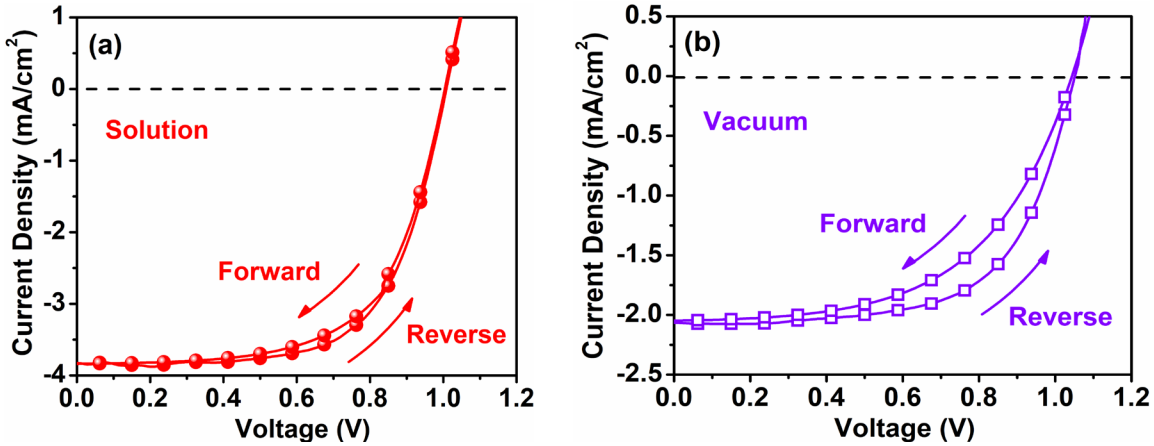

Figure A6.9. *J-V* curves showing the hysteretic responses of the (a) solution and (b) vacuum processed champion cells.

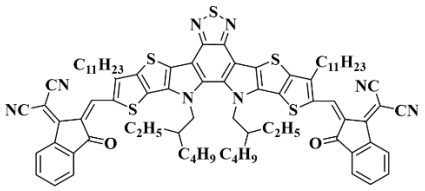

Y5

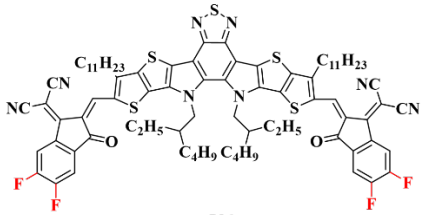

Y6

Figure A7.1. Chemical structures of acceptors (Y5, Y6).

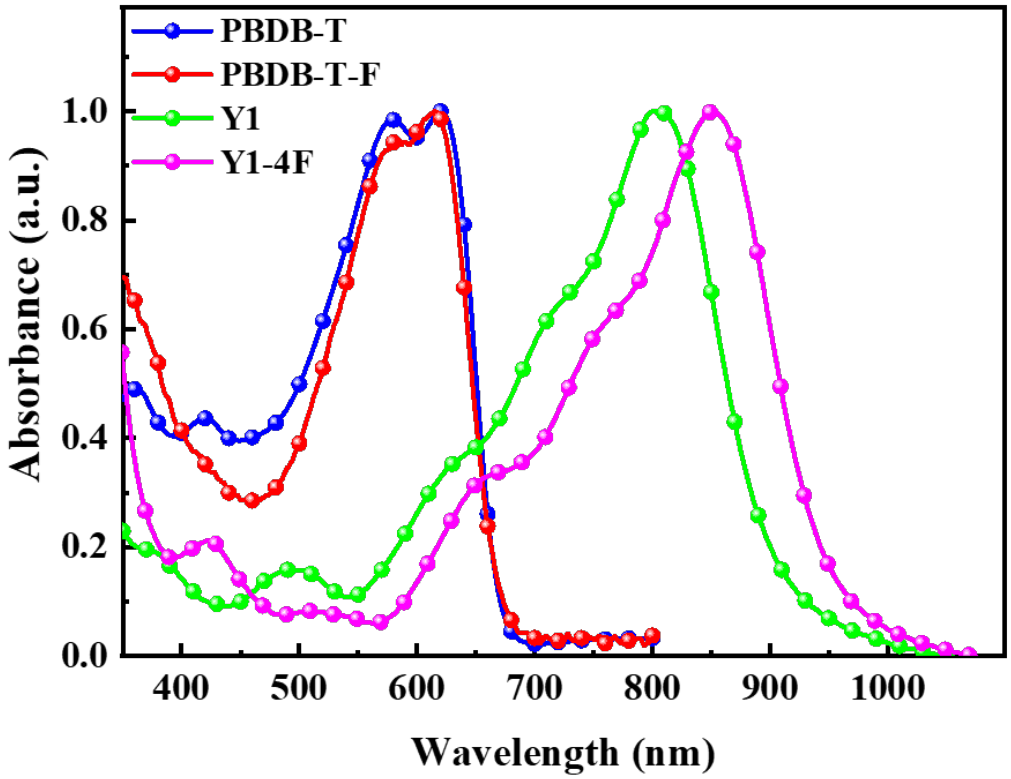

Figure A7.2 Normalized absorption spectra of polymer donors and non-fullerene acceptors in films

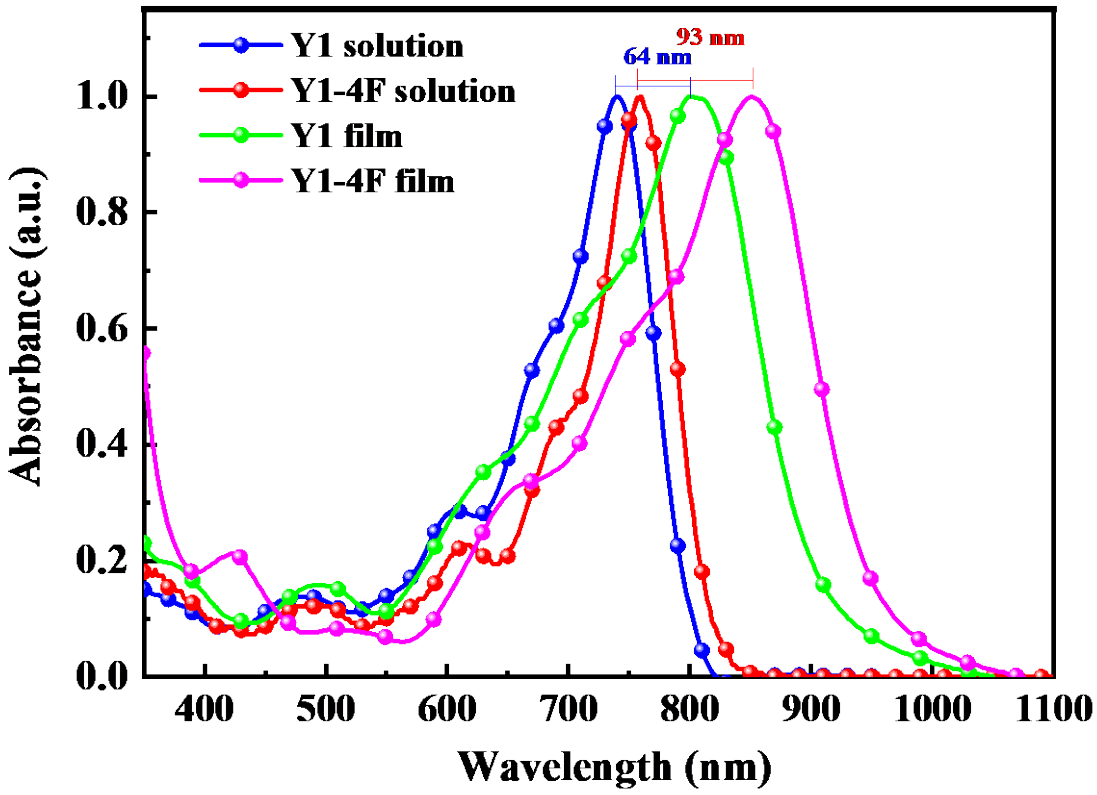

Figure A7.3 Normalized absorption spectra of non-fullerene acceptors in solution

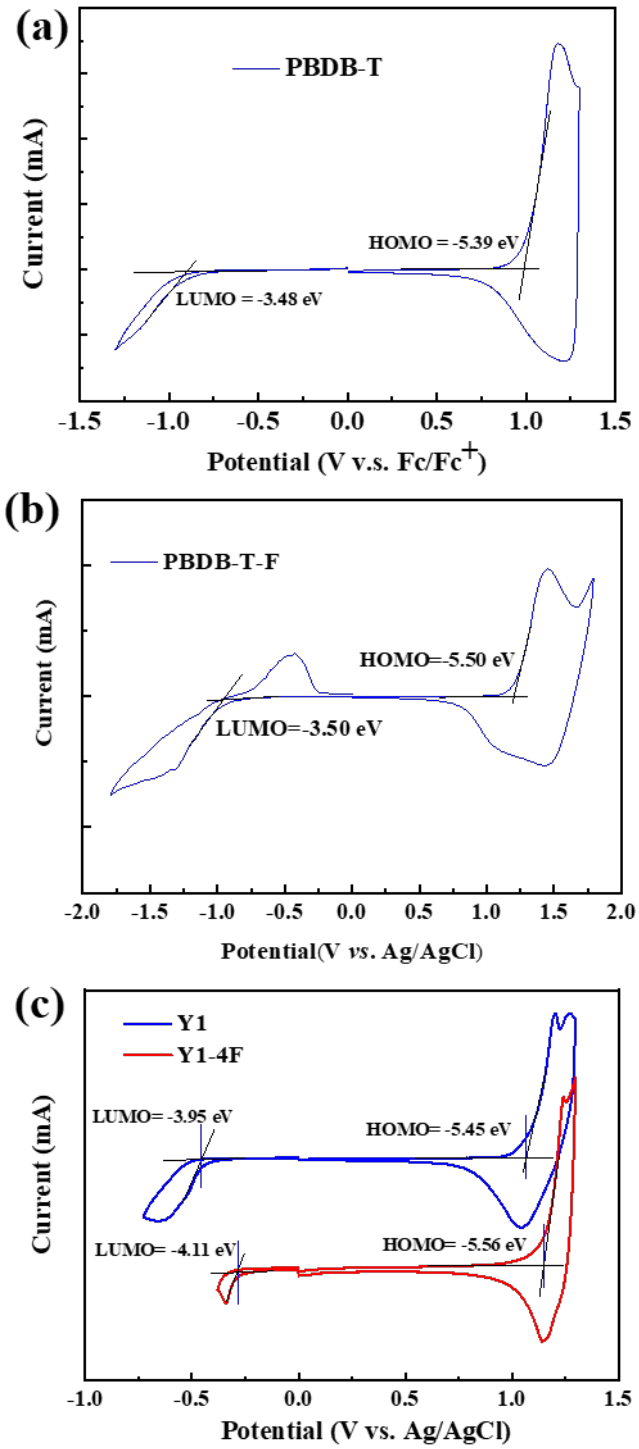

Figure A7.4. Cyclic voltammogram of (a) PBDB-T, (b) PBDB-T-F, (c) Y1 and Y1-4F in acetonitrile solution with 0.1 M Bu_4PF_6 as the supporting electrolyte with a scan speed of 50 mV s^{-1}.

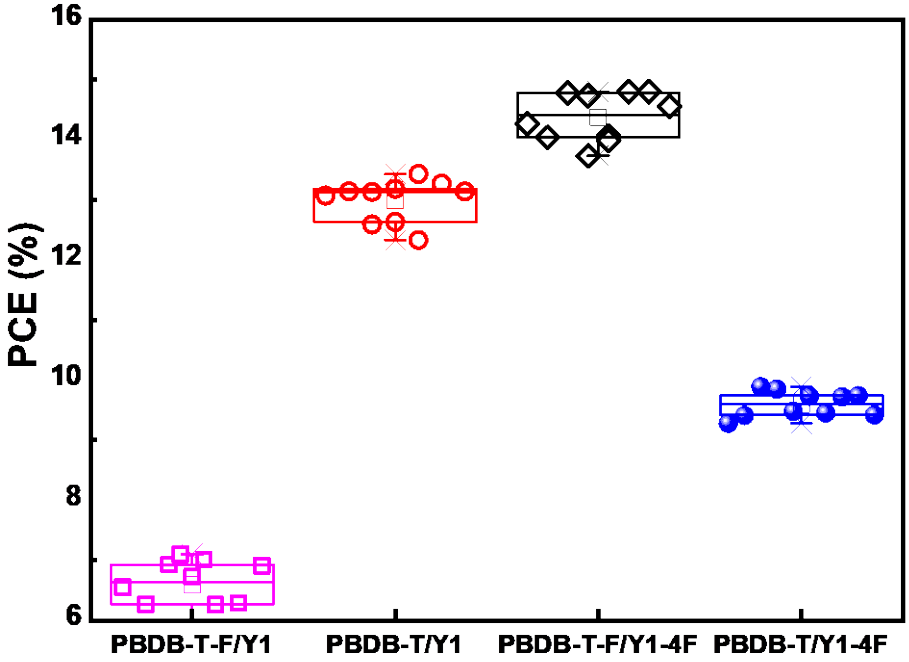

Figure A7.5 The statistic distribution of PCEs of PBDB-T/Y1, PBDB-T/Y1-4F, PBDB-T-F/Y1 and PBDB-T-F/Y1-4F.

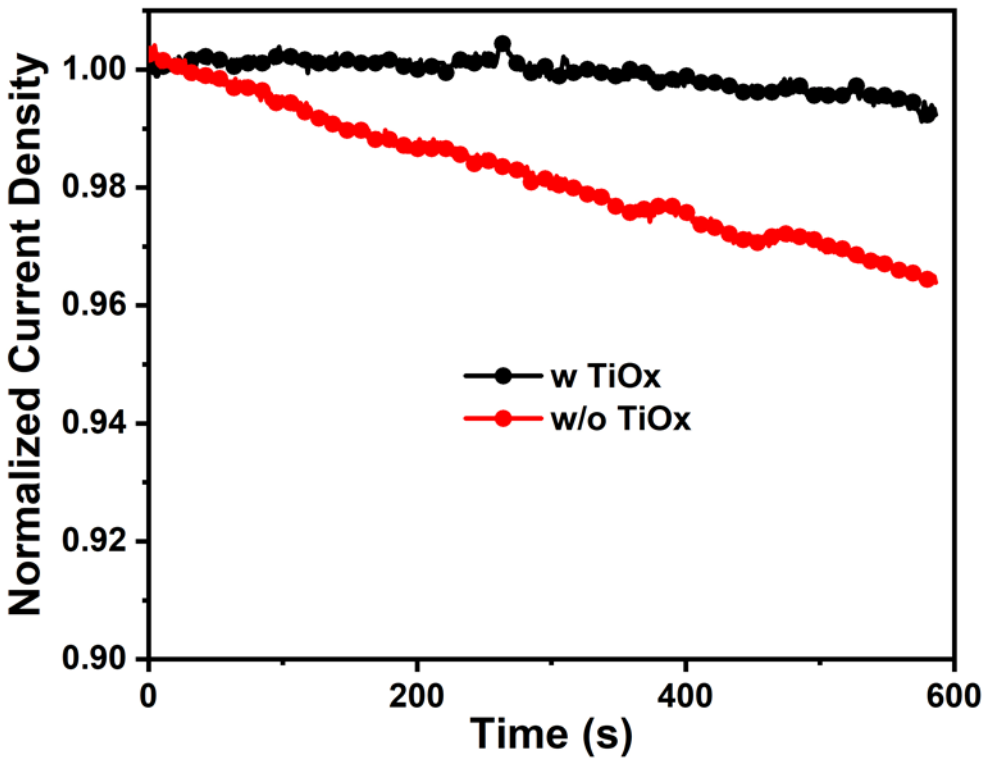

Figure A7.6 Steady state output current density of the device with or without TiOx layer.

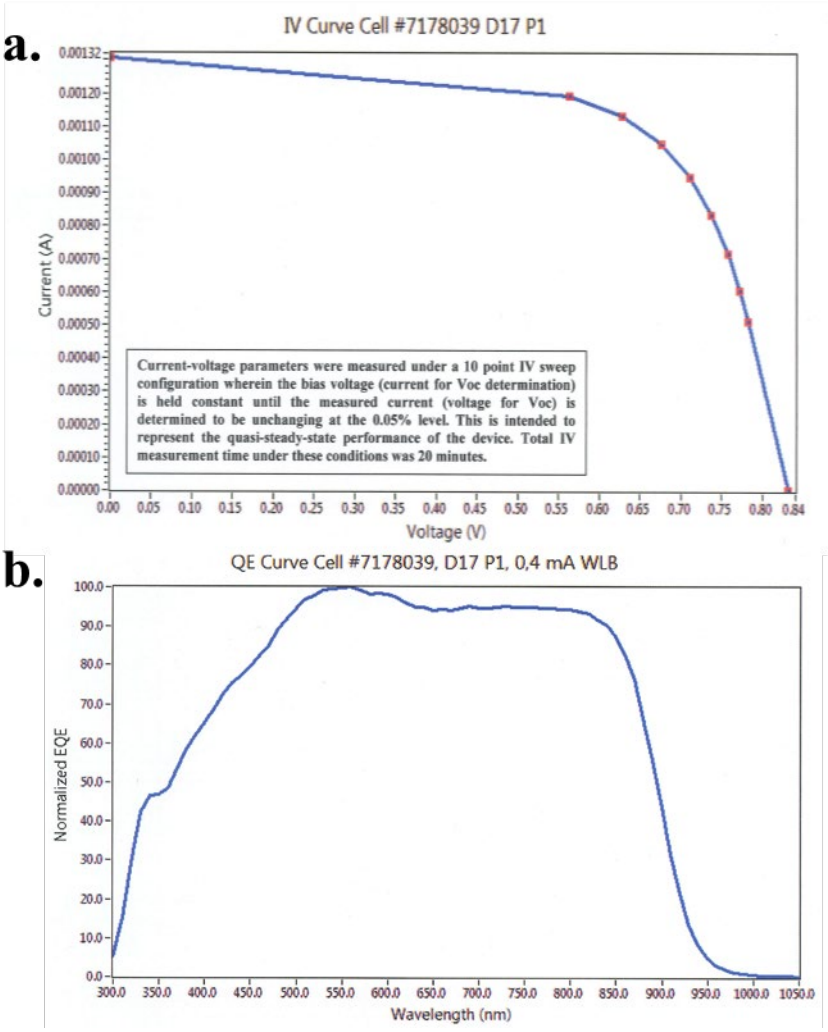

Figure A7.7 Independent certification by Newport Corporation of device based on PBDB-T-F/Y1-4F with a Quasi-Steady-State PCE of 12.86 %.

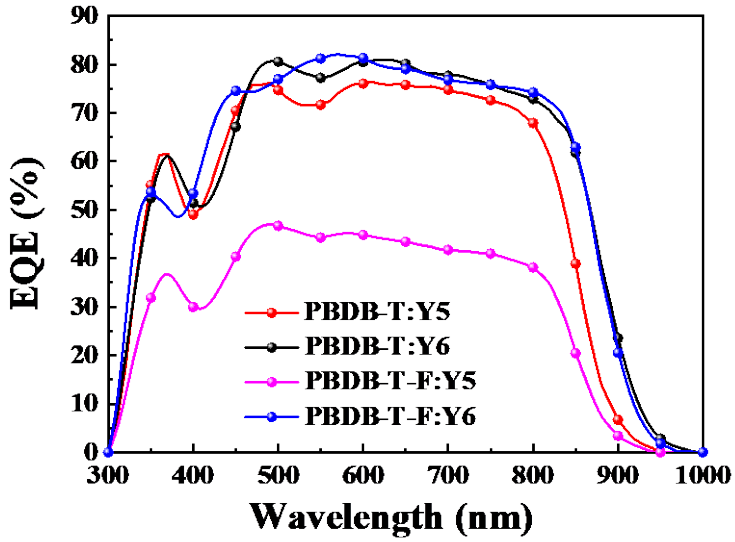

Figure A7.8 EQE spectra of devices based on PBDB-T/Y5, PBDB-T/Y6, PBDB-T-F/Y5 and PBDB-T-F/Y6 under the illumination of an AM 1.5G solar simulator, 100 mW cm^{-2}.

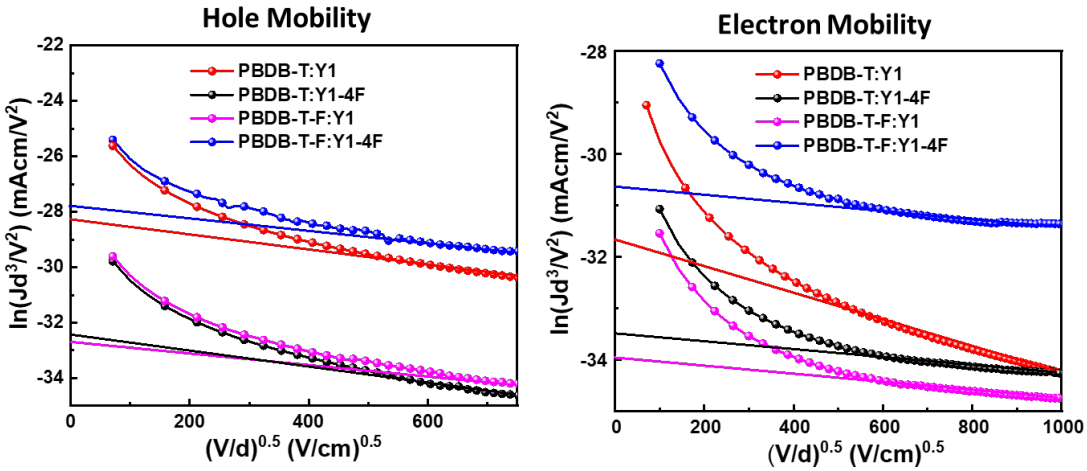

Figure A7.9 Hole-only and electron-only devices based on PBDB-T/Y1, PBDB-T/Y1-4F, PBDB-T-F/Y1 and PBDB-T-F/Y1-4F.

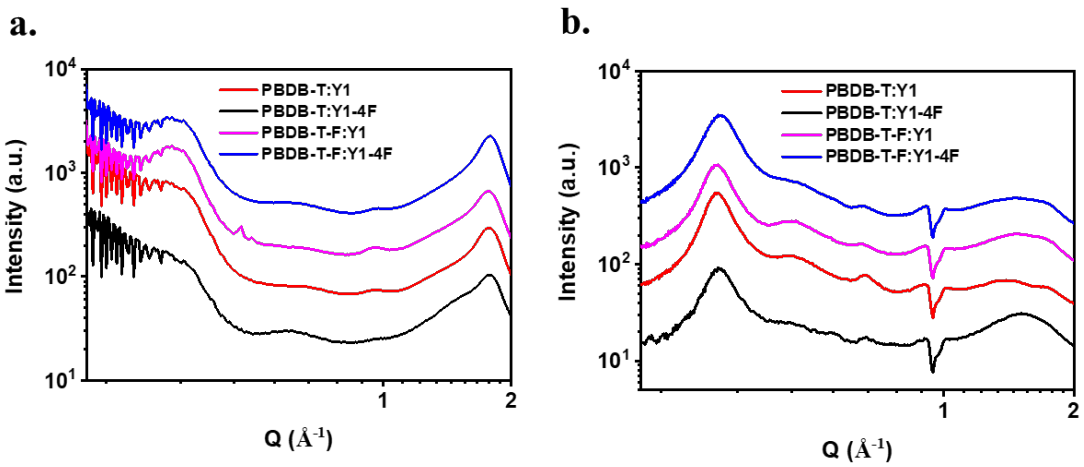

Figure A7.10 a. Out-of-plane GIWAXS profiles b. In-plane GIWAXS profiles for PBDB-T/Y1, PBDB-T/Y1-4F, PBDB-T-F/Y1 and PBDB-T-F/Y1-4F films.

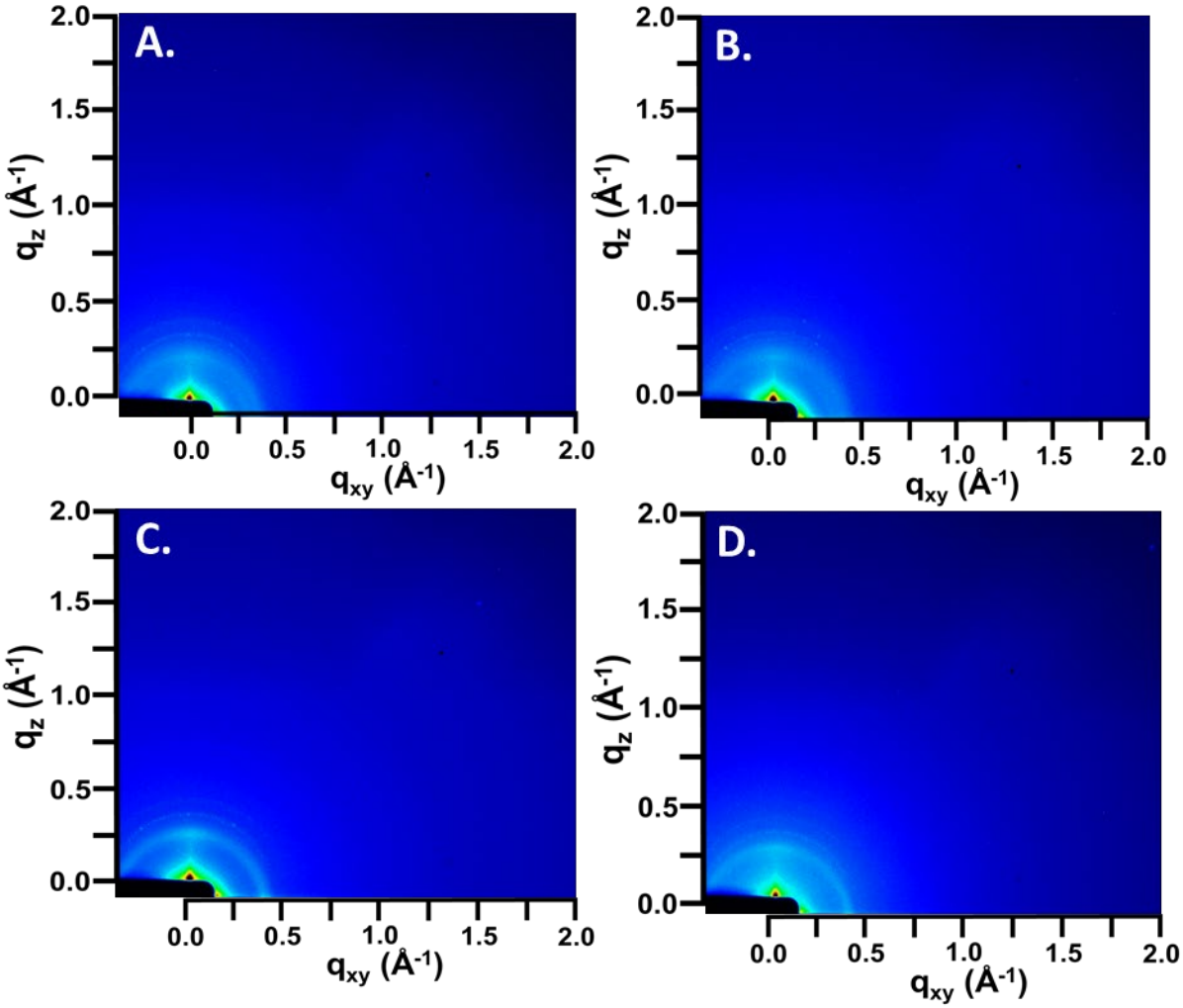

Figure A7.11. 2D GIWAXS patterns of A. PBDB-T/Y5, B. PBDB-T/Y6, C. PBDB-T-F/Y5 and D. PBDB-T-F/Y6 films.

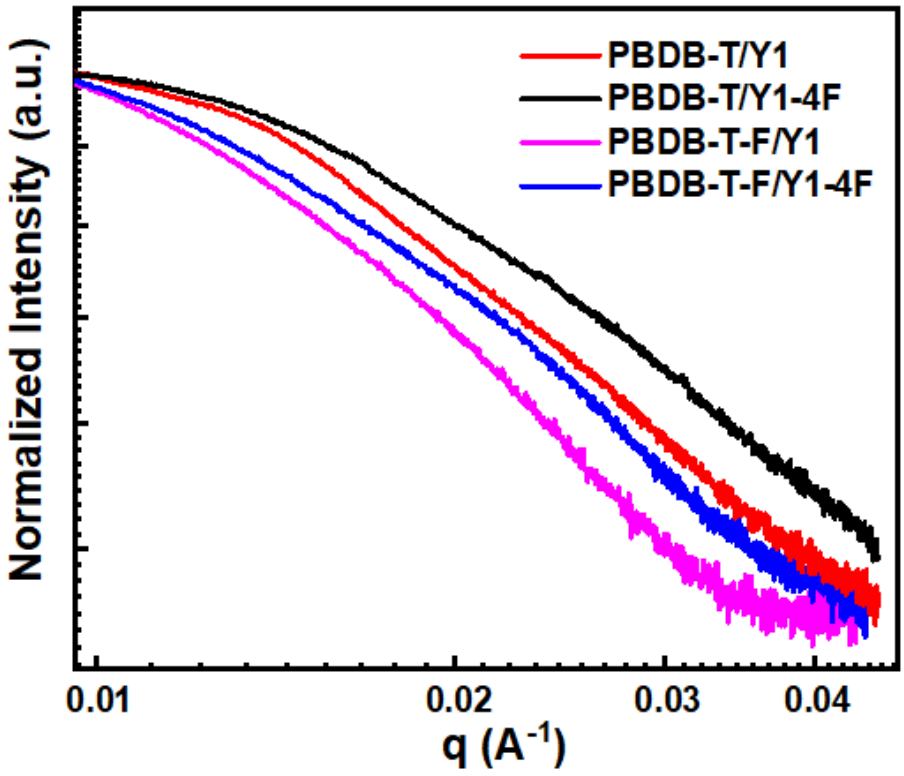

Figure A7.12 1D GISAXS profiles of PBDB-T/Y1, PBDB-T/Y1-4F, PBDB-T-F/Y1 and PBDB-T-F/Y1-4F films along in-plane.

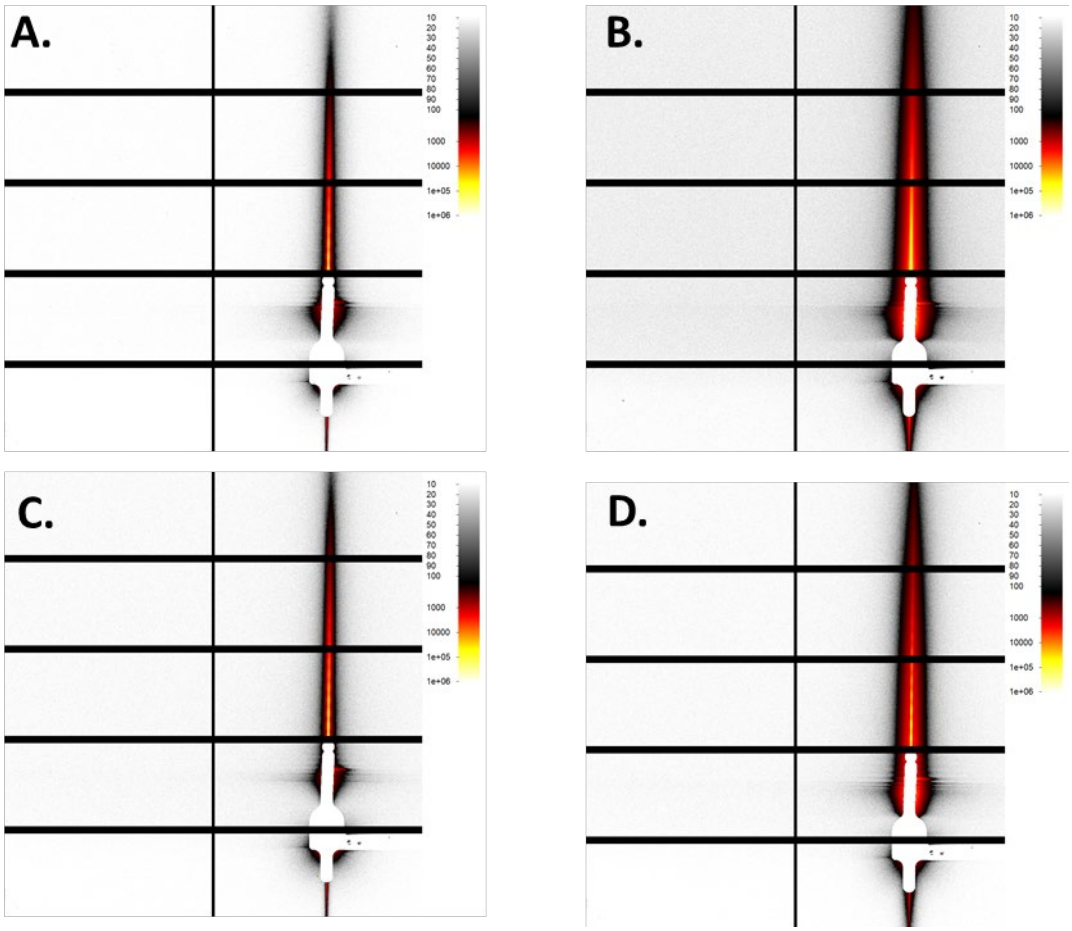

Figure A7.13. 2D GISAXS patterns of A. PBDB-T/Y5, B. PBDB-T/Y6, C. PBDB-T-F/Y5 and D. PBDB-T-F/Y6 films.

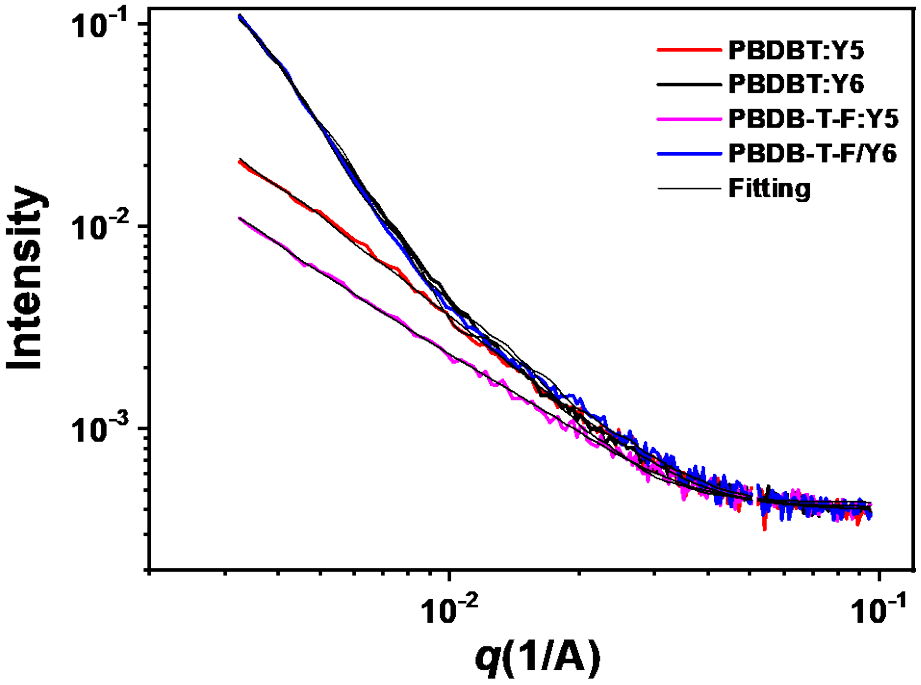

Figure A7.14 1D GISAXS profiles of PBDB-T/Y5, PBDB-T/Y6, PBDB-T-F/Y5 and PBDB-T-F/Y6 films along in-plane.

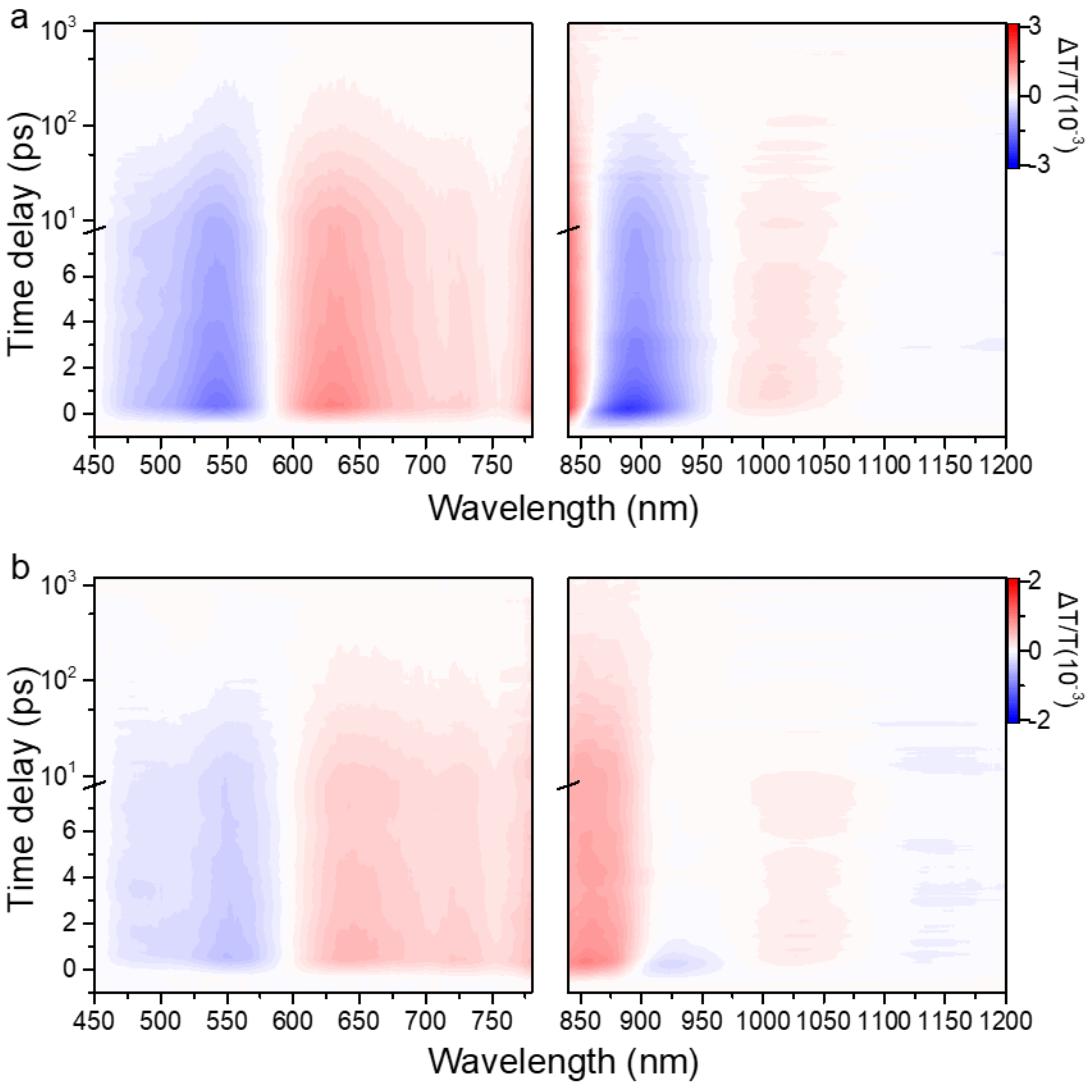

Figure A7.15. (a,b) Transient absorption spectra of Y1 and Y1-4F neat films excited at 800 nm, respectively.

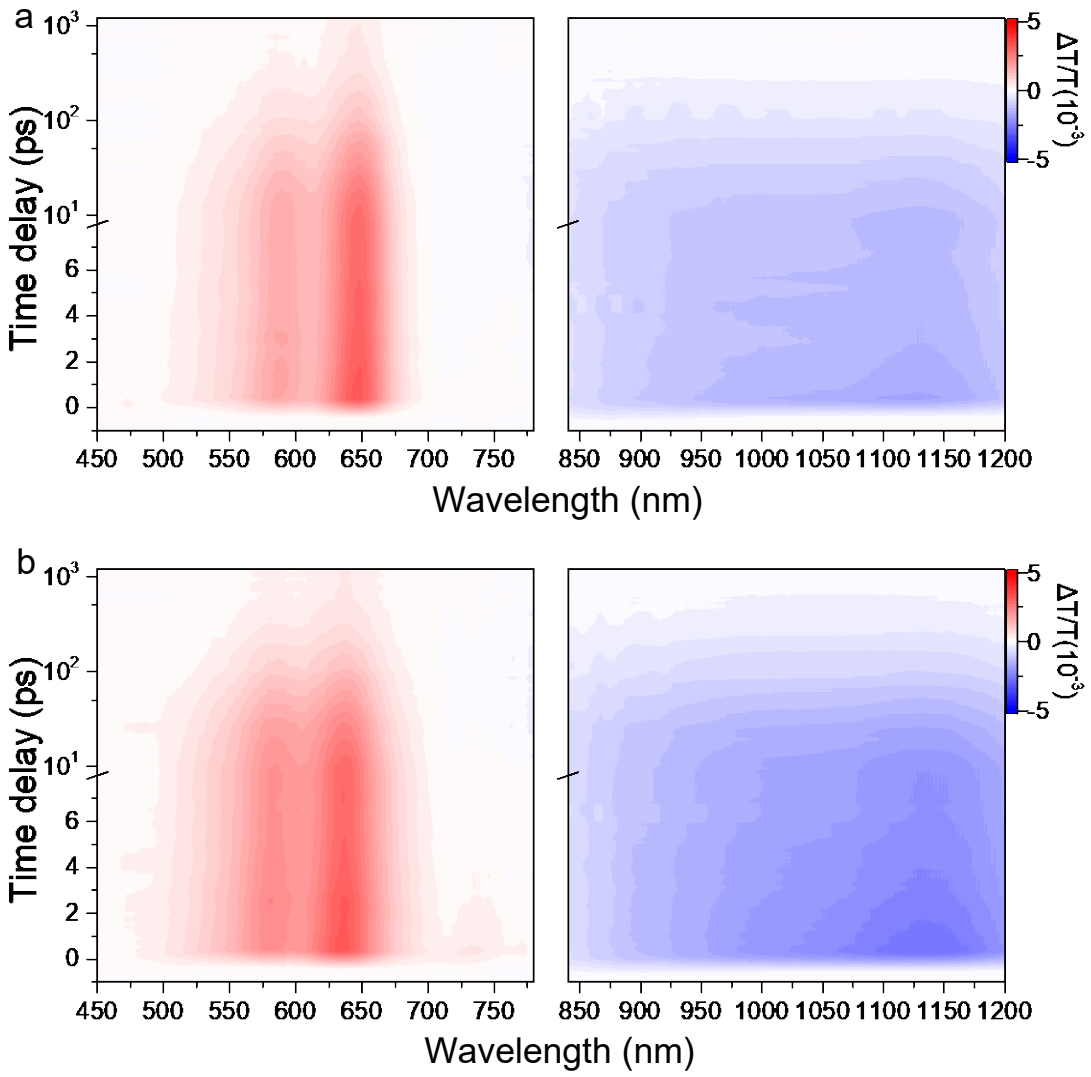

Figure A7.16. (a,b) Transient absorption spectra of PBDB-T and PBDB-T-F neat films excited at 500 nm, respectively.

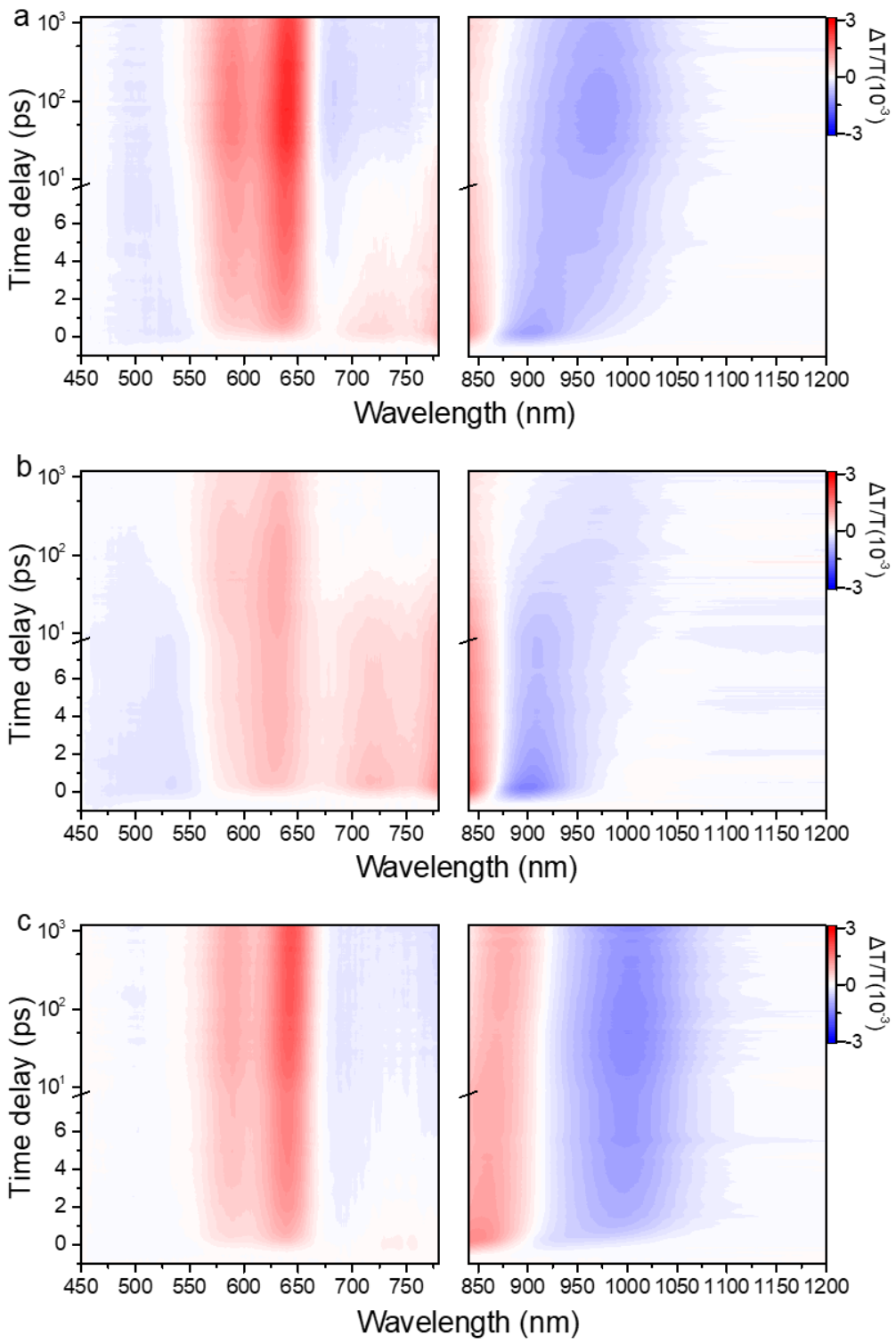

Figure A7.17. (a-c) Transient absorption spectra of the blends of PBDB-T/Y1, PBDB-T-F/Y1 and PBDB-T/Y1-4F excited at 800 nm, respectively.

Appendix B

Table B2.1. Cell parameters in the PSCs with or without scanned from forward (FS) and reverse (RS) directions.

Active layer	Scan Direction	V_{OC} (V)	J_{SC} (mA cm^{-2})	FF (%)	PCE (%)
w/o Caffeine	RS	1.067	22.08	74.29	17.50
	FS	1.051	21.80	64.85	14.85
W Caffeine	RS	1.143	22.97	77.13	20.25
	FS	1.132	22.87	70.64	18.29

Table B2.2 Summarized photovoltaic performance of perovskite devices with or without caffeine.

Devices		V_{oc} **(V)**	J_{sc} **(mA/cm^2)**	**FF (%)**	**PCE (%) (reverse)**	**PCE (%) (forward)**
CsFAMA	Average	1.11±0.02	23.06±0.36	75±1	19.45±0.47	18.05±0.33
	Best	1.13	23.30	76	19.92	18.38
CsFAMA+Caff	Average	1.14±0.01	23.54±0.43	75±1	20.45±0.37	19.26±0.26
	Best	1.14	23.97	76	20.82	19.52

Table B4.1 Calculated surface energies based on DFT-D3 method. Ref. refers to the case where Cs^+ cations are present in the top layer, whereas they are replaced by BA, OCA and OLA for the remaining cases.

Type of Treatment	γ_{100} (eV/nm^2)	γ_{111} (eV/nm^2)	δ (eV)
Ref.	4.33	4.03	+0.29
BA	3.23	4.09	-0.87
OCA	2.14	4.06	-1.92
OLA	1.71	4.01	-1.96

Table B4.2. The contact angles of H_2O and DIM on $CsPbI_2Br$ with or without OLA treatment and their respective calculated surface free energies.

i	H_2O (°)	DIM (°)	γ_s [mN m^{-1}]
Ref	46.3	7.4	59.78
OLA	76.1	46.3	38.38

Table B4.3 Surface formula, number of formula per unit cell and atomic energy term that enter γ^{clean} for the calculation of surface energies at T = 0 K. n is the number of formula units per unit cell.

Slab	Formula	n	$2A * \gamma^{clean} + nE^{bulk} - E^{slab}$
100	$Cs_nPb_nI_{2n+1}Br$	3	$-E_I$
010	$Cs_nPb_nI_{2n+1}Br$	3	$-E_I$
001	$Cs_nPb_nI_{2n}Br_{n+1}$	3	$-E_{Br}$
110	$Cs_{n-1}Pb_nI_{2n}Br_n$	4	E_{Cs}
101	$Cs_{n-1}Pb_nI_{2n}Br_n$	4	E_{Cs}
011	$Cs_{n-1}Pb_nI_{2n}Br_n$	4	E_{Cs}
111	$Cs_{n-1}Pb_nI_{2n}Br_n$	8	E_{Cs}

Table B4.4. Average and the best device data based on $CsPbI_2Br$ treated with or without various types of organic ammoniums.

Type of Treatment	V_{OC} (V)	J_{SC} (mA cm^{-2})	FF (%)	PCE (%)	
				average	best
Ref	1.103±0.02	15.15±0.25	0.73±0.05	12.17±1.05	13.13
BA	1.137±0.01	15.96±0.46	0.75±0.03	13.55±0.28	14.01
OCA	1.166±0.02	16.29±0.25	0.76±0.01	14.44±0.38	14.94
OLA	1.231±0.01	16.48±0.26	0.80±0.01	16.23±0.28	16.58

Table B5.1 ΔH_α, formation energy of neutral defects considered in this study. The energies are in eV.

Defect type	ΔH_α (eV) Surface	ΔH_α (eV) Bulk
I_{Pb}	3.15	3.89
Pb_I	0.57	1.46
V_I	0.51	0.63
V_{Pb}	3.20	2.97

Table B5.2 Photovoltaic parameters of average and the best perovskite solar cells with or without various types of surface treatments.

Type of Treatment	V_{OC} (V)	J_{SC} (mA cm^{-2})	FF	PCE (%)	
				average	best
Ref	1.153±0.02	24.19±0.35	0.73±0.07	20.36±0.53	21.02
Theophylline	1.187±0.01	24.74±0.46	0.77±0.02	22.61±0.58	23.48
Caffeine	1.168±0.02	24.63±0.39	0.75±0.01	21.58±0.69	22.32
Theobromine	1.151±0.02	24.36±0.43	0.70±0.03	19.63±0.65	20.24

Table B5.3 Photovoltaic parameters of best perovskite solar cells under reverse or forward scan with or without theophylline treatment.

Type of Treatment	V_{OC} (V)	J_{SC} (mA cm^{-2})	FF	PCE (%)
Reverse (Ref)	1.164	24.78	0.729	21.02
Forward (Ref)	1.159	24.19	0.693	19.43
Reverse (Theophylline)	1.191	25.24	0.781	23.48
Forward (Theophylline)	1.191	25.23	0.749	22.51

Table B7.1. Average and the best device data based on PBDB-T/Y5, PBDB-T/Y6, PBDB-T-F/Y5 and PBDB-T-F/Y6.

Active layer	V_{OC} (V)	J_{SC} (mA cm-2)	Calculated J_{SC} (mA cm-2)	FF (%)	PCE (%)	
					average	best
PBDB-T/Y5	0.87±0.01	22.7±0.4	22.1	70.2±1.3	13.8±0.2	14.0
PBDB-T/Y6	0.72±0.02	25.0±0.5	24.4	62.1±1.5	10.8±0.4	11.2
PBDB-T-F/Y5	0.94±0.01	13.2±0.4	12.8	59.6±2.1	7.2±0.3	7.5
PBDB-T-F/Y6	0.84±0.01	24.7±0.1	24.6	76.7±2.1	15.8±0.1	15.9

Table B7.2 Hole mobilities and electron mobilities of PBDB-T/Y1, PBDB-T/Y1-4F, PBDB-T-F/Y1 and PBDB-T-F/Y1-4F.

Active layer	μ_h (cm2 V-1 s-1)	μ_e (cm2 V-1 s-1)
PBDB-T/Y1	3.21 × 10-3	1.06 × 10-4
PBDB-T/Y1-4F	4.83 × 10-5	1.72 × 10-5
PBDB-T-F/Y1	3.64 × 10-5	1.05 × 10-5
PBDB-T-F/Y1-4F	5.25 × 10-3	3.01 × 10-4

Table B7.3 1D GISAXS Fitted Parameters of Domain Size of PBDB-T/Y1, PBDB-T/Y1-4F, PBDB-T-F/Y1 and PBDB-T-F/Y1-4F.

Active layer	Radius (Å)	Length (Å)
PBDB-T/Y1	27.80	1064.65
PBDB-T/Y1-4F	40.95	746.85
PBDB-T-F/Y1	29.35	1368.20
PBDB-T-F/Y1-4F	27.95	1126.80